FINAL REPORT

Program Title: Alliance for NanoHealth (ANH) Training Program for the development of future generations of interdisciplinary scientists and collaborative research focused upon the advancement of nanomedicine

NASA Award Number: DE-FG02-08ER64712

Name of Applicant: The University of Texas Health Science Center – Houston
(On behalf of Alliance for NanoHealth)
Department of Nanomedicine and Biomedical Engineering
1825 Pressler Street
Houston, Texas 77030

Principal Investigator: David Gorenstein, Ph.D.
1825 Pressler Street
Houston, TX 77030
713-500-2420
David.G.Gorenstein@uth.tmc.edu

PROGRAM SUMMARY

I. Accomplishments of the Program

• Offered summer internship training for three undergraduate students in alliance with MD Anderson Step-Up program.
• Awarded 2-year fellowships to two graduate students for collaborative, interdisciplinary research in specific areas of nanotechnology.
•Successfully provided three post-doctoral fellowships in the advancement of nanotechnology research. Some fellows have advanced to careers in academia and industry.
• Attracted several prominent leaders of innovation in the field of nanomedicine to engage research discussion and foster potential collaborative opportunities through the prestigious ANH Distinguished Investigator Awards.

II. Statement to the public purpose to be served by the project

Objectives:

1) To promote the mission of the Department of Energy (DOE) Science, Technology, Engineering, Math (STEM) Program by recruiting students to science and engineering disciplines with the intent of mentoring and supporting the next generation of scientists.
2) To foster interdisciplinary and collaborative research under the sponsorship of ANH for the discovery and design of nano-based materials and devices with novel structures, functions, and properties.
3) To prepare a diverse work force of scientists, engineers, and clinicians by utilizing the unique intellectual and physical resources to develop novel nanotechnology paradigms for clinical application.

A. Background

The Alliance for NanoHealth (ANH) is the first multi-disciplinary, multi-institutional collaborative research endeavor aimed solely at using nanotechnology to bridge the gaps between medicine, biology, materials science, computer technology and public policy. The ANH comprises eight world-class research institutions, scientists and clinicians located within the world's largest collection of healthcare facilities, namely the Texas Medical Center and the greater Houston region. Member institutions include the Baylor College of Medicine, The University of Texas M.D. Anderson Cancer Center, Rice University, University of Houston, The University of Texas Health Science Center at Houston, Texas A&M Health Science Center, The University of Texas Medical Branch at Galveston, and The Methodist Hospital Research Institute. This consortium of institutions forms a unique continuum that bridges Nobel-prize winning nanotechnology laboratories to outstanding basic science, technology and education programs, and to world-leading clinical establishments in cancer, cardiovascular care, infectious diseases, and many other branches of medicine. The ANH comprises an important fraction of the investigators in the Texas Medical Center area, making it by far the largest collection of nanomedicine researchers in the world.

The mission of the Alliance is to facilitate the translation of nanotechnology from the laboratory bench to clinical practice and to collectively bridge the disciplines to develop nanotechnology-based solutions to unresolved problems in medicine. The aspiration of the ANH is to lead the world in developing advances in health care that nanotechnology will engender by combining excellence in basic, applied, and clinical research, education, technology transfer, and commercialization efforts. Its principal goal is to provide new clinical approaches to saving lives through better diagnosis, treatment, and prevention. ANH institutions are committed to development and application of nanotechnology tools in the battle against heart disease, cancer, diabetes, stroke, and infection. The willingness to share strengths among the disciplines with educational and training activities as well as welcoming new scientific associations provides a rich collaborative foundation upon which the ANH has established significant research and development opportunities.

We have assembled a faculty with highly diverse expertise — mathematicians, engineers, physicians, chemists, bioscientists, and cancer biologists — to mentor students who are interested in pursuing research in nanotechnology. Our trainees provide essential bridges across disciplinary boundaries during their training and into their professional careers. Because building these connections is the essential goal of the program, we have chosen to feature a broad spectrum of faculty and research activities — all with the goal of combining in-depth exposure to new methodologies as well as modern biological and biomedical sciences.

B. Objectives

The central objective of the training program is to advance the ANH mission by integrating researchers relevant to this task as well as drawing new students into nanomedicine research. This program targets the scientific and technical areas of interest of the DOE Office of Science. These subject areas encompass the intellectual framework needed to ask insightful biological and nanotechnological questions, develop appropriate approaches to these problems, and to bring them together to advance our understanding.

C. Program Progress

This training program attracted the next generation of students to study biomedical nanotechnology, supports graduate and post-doctoral fellows interested in interdisciplinary research in a collaborative environment, and provides cutting edge nanotechnology awareness and the opportunity to create new collaborative research programs with some of the field's most prominent investigators.

Undergraduate Students: This outreach program served as a recruitment tool for attracting undergraduate students into a graduate program. This summer internship in alliance with MD Anderson Step-Up program funded three students to be trained in our cutting edge research laboratories under the mentorship and guidance of ANH investigators: faculty, postdoctoral fellows and graduate students.

Graduate Students: The overarching goal of the graduate fellowship is to develop future generations of Ph.D. level scientists in the interdisciplinary field of nanomedicine. This ANH training program recruited talented graduate students to the Texas Medical Center for their graduate training and development of

research careers in biomedical nanotechnology. See Appendix A for graduate student Awardee's progress reports and career profiles.

Postdoctoral Research Fellows: The ANH postdoctoral training program fostered a mechanism for maturing junior scientists to transition into sophisticated investigators and potential future faculty members. The ANH Program has awarded and successfully trained three postdoctoral fellows: Dev Chatterjee, Kyle Hammerick, and Elizabeth McCullum. Please see Appendix B for the individual awardee's final progress and current career profiles.

Distinguished Investigator Award Program: The Alliance supported the ANH Distinguished Investigators Award Program to attract prominent leaders of innovation in the field of nanomedicine from across the nation and abroad to be featured as Keynote Speakers and invited guests. These lecturers were engaged in ANH research laboratories, met our students, and fostered new potential collaborative efforts with ANH Investigators. See Appendix C for the invited ANH Distinguished Investigators' seminars and bio.

D. Concluding Remarks

The ANH is an outstanding individually tailored, highly multidisciplinary training program. The outcome of student participation has proven strong research support among our 8 varied institutions and a community of scholars, researchers, and clinicians. We expect the training and opportunities provided to the next generation of nanotechnology researchers will meet and address many challenging medical problems through advanced innovative methods with nanotechnology. Our goal has successfully supported the DOE mission of preparing a diverse work force of scientists, engineers, and clinicians to remain at the forefront of novel nanotechnology paradigms for clinical application.

III. Appendix

Appendix A

- Graduate Student Awardees: Laura Carpin Kennedy and Eric Frey

Alliance for NanoHealth (ANH) DOE Training Program
Graduate Student Research Training Fellowship 2009
Final Report

Name: Laura Carpin Kennedy
Institution: Rice University
Project Title: Photoablative Gold Nanoshell Therapy of Chemotherapy-Resistant Cancer Cells

I. Summary of Research:

Chemotherapy resistance continues to present a challenge in the treatment of advanced stage breast cancer patients. The development of new pharmaceuticals has done little to significantly change the problem of chemotherapy resistance, and new forms of therapy are needed that can overcome the tumor cells' ability to develop resistance. Breast cancer TICs are naturally resistant to chemo- and hormone therapy, and thus provide a logical target for battling breast cancer relapse. With traditional chemo- and hormone therapy, the non-tumorigenic cancer cells are killed, leading to tumor shrinkage, but the tumorigenic TICs are left behind to begin proliferating anew. These TICs are also thought to be the source of metastases (Morrison et al, 2008). By targeting and destroying TICs, cancer recurrence may be prevented. We proposed to target breast cancer TICs using the TVA/RCAS technology to create a surrogate marker that gold nanoshells can locate and bind. This would permit targeted destruction of the breast cancer TICs, and would demonstrate the impact of TIC destruction on tumor recurrence in the primary or distant sites. We also proposed to target trastuzumab-resistant HER2+ breast cancer for destruction with trastuzumab-conjugated gold nanoparticles. Because these cells still express the extracellular component of the HER2 receptor, we could use the HER2 receptor to locate the HER2+ breast cancer cells with the gold nanoparticles. We could then physically destroy the cells by heating the gold nanoshells with a NIR laser, overcoming any intracellular resistance mechanism.

Gold nanoparticles have great potential in the diagnosis, management, and treatment of cancer due to their versatile scattering and absorbing properties, as well as the ease with which their surfaces can be modified. Gold nanoshells usually consist of a core particle, such as silica, that is coated with a thin layer of gold. Nanoshells are "tunable" to either scattering or absorbing wavelengths by adjusting the thickness of the gold coating, making them potentially powerful as imaging contrast agents. When created to primarily absorb light, nanoshells can also efficiently convert light energy to heat energy, and kill adjacent cells via thermal ablation (Lal, Clare, & Halas, 2008). This feature of nanoshells suggests many useful applications, including cancer therapy.

Trastuzumab is a humanized monoclonal antibody pharmaceutical that is specifically targeted to the HER2 receptor, a marker that is frequently overexpressed in breast cancer. Although this drug has been approved for the adjuvant treatment of metastatic breast cancer and has shown positive clinical results, the majority of patients are intrinsically resistant (Nahta & Esteva, 2006). In 2005, Dr. Drezek's lab was the first to demonstrate that gold-silica nanoshells conjugated to HER2 antibody can be successfully used to target and ablate breast carcinoma cells in culture (Loo et al 2005). My work extended this demonstration to the clinically relevant problem of trastuzumab resistance. Trastuzumab resistance is not associated with changes in the HER2 receptor, but rather with changes in the associated intracellular signaling cascades that result in resistance (Valabrega, Montemurro, & Aglietta, 2007). We created gold-silica nanoshells with a peak optical absorbance of 780-800 nm as described by Oldenburg et al (1998). The ideal absorbing wavelengths for therapy lie in the near infrared region, as these wavelengths possess maximal transmission through tissues. The nanoshells were then conjugated to trastuzumab using a OPSS-PEG-NHS linker, and then PEGylated to block nonspecific adsorption using an optimized concentration of polyethylene glycol-thiol (PEG-SH). We used trastuzumab resistant HER2+ cell lines JIMT-1and BT474 1L, trastuzumab-sensitive HER2+ breast cancer line SKBR3 cells, and HER2- cell line MCF10A. Photothermal ablation was demonstrated by growing cells to near-confluence on a plate, incubating the trastuzumab-conjugated nanoshells with the cells for 1 hour, rinsing off the unbound

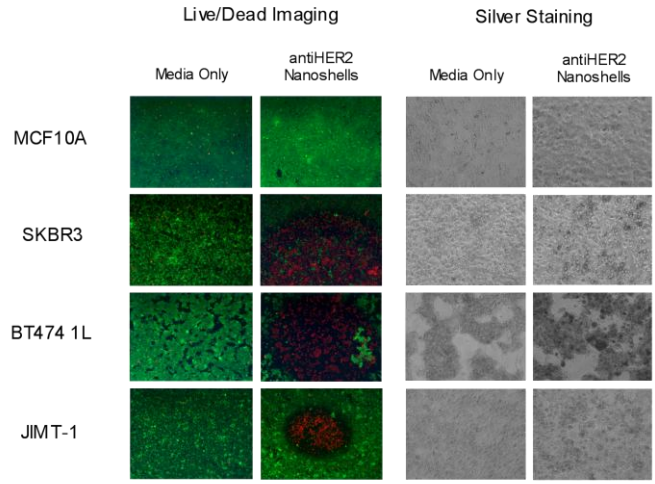

Figure 1. Photothermal therapy of trastuzumab resistant cell lines. Cells were incubated with antiHER2 immunoconjugated gold nanoshells, then irradiated with NIR laser light. Calcein stain (green) shows live cells, ethidium (red) shows dead cells. Silver staining (right column) shows nanoshells binding to HER2+ cell lines. MCF10A = HER2-; SKBR3 = HER2+, trastuzumab sensitive; BT474 1L = HER2+, trastuzumab resistant; JIMT-1 = HER2+, trastuzumab resistant. (Carpin et al, 2011)

nanoshells with PBS, and irradiating the cells with a near-infrared laser (wavelength = ~800 nm) at a power density of 80 W/cm^2 for 2 minutes with a spot size of 2 mm. After 24 hours, we visualized the cells using a live/dead stain under fluorescent microscopy to evaluate cell viability and silver staining to confirm nanoshell binding. Figure 1 shows the results of this study. We successfully ablated both the trastuzumab-sensitive and trastuzumab-resistant HER2+ breast cancer cell lines. By demonstrating that trastuzumab-conjugated nanoshells could both label and photothermally ablate both trastuzumab-sensitive and trastuzumab-resistant HER2+ breast cancer cell lines, we showed the potential for gold nanoparticle photothermal therapy to be an alternative or adjuvant treatment for chemotherapy-resistant breast cancers (Figure 1; Carpin et al, 2011).

Breast cancer TICs have become a subject of interest over the last several years as a possible therapeutic target that could have significant impact on the recurrence rates of patients with advanced breast cancer. However, to this point, they have not been targeted due to the lack of a single specific marker – most groups have targeted breast cancer TICs using at least 3 markers (Al-Hajj et al, 2003; Ponti et al, 2005, Clarke, 2005). To overcome this difficulty, the TVA/RCAS technology has been successfully utilized by Dr. Yi Li and his group to create a breast cancer model in transgenic mice that mimics tumor formation due to TIC mutations (Du et al 2006). TVA is a receptor for the avian leukosis virus, subgroup A (ALV-A). Mammalian cells usually lack this receptor, and thus cannot be infected with ALV-A. When this receptor is engineered into mammalian cells, the cells become vulnerable to infection by the virus, which becomes integrated into the genome, but does not produce sufficient levels of viral protein to permit the infection to spread or produce a host immune response. This also allows the introduction of oncogenes into the TVA+ mammalian cells using the RCAS vector (Ochsenbauer-Jambor et al, 2002). By expressing tva behind a keratin6-promoter (Bu et al, 2011), a TIC-enriched subpopulation of cells will express the TVA receptor. The presence of this single surface receptor provides a convenient target for nanoshell-based photothermal therapy and will direct nanoshells to a large percentage of the TICs present in the tumor. We proposed creating a TVA antibody-conjugated nanoshell and verifying nanoshell binding to the TVA receptor using a TVA+ 293T cell line and darkfield microscopy. We would then perform the laser ablation, imaging, and live/dead testing as described above.

We then proposed extending these in vitro studies to in vivo models and transitioning from gold-silica nanoshells to gold-gold sulfide nanoparticles, as these particles are smaller and will most likely be more effective at bulk tumor penetration. Gobin demonstrated that the gold-gold sulfide particles can be used in photothermal therapy, and actually heat faster than the gold-silica nanoshells (Gobin PhD thesis, 2007). We would prepare the antibody-conjugated gold nanoparticles in a similar manner to what was described above. To synthesize the GGS particles, we would combine aged 1 mM $Na_2S_2O_3$ and 2 mM $HAuCl_4$ and optimize the ratio for particles with a high absorbance extinction peak of approximately 800 nm. The

GGS particles will be purified of residual gold colloid by sequential centrifugation as described by Gobin (Gobin PhD thesis, 2007). We would then tag the GGS particles with either trastuzumab or anti-TVA monoclonal antibody, and pegylate to prevent non-specific binding and to increase circulation time by impairing the RE system's (RES) ability to uptake the particles. Two mouse models would be used for the in vivo testing: for the anti-TVA-conjugated GGS particles, we will use tumors from MMTV-Wnt-1 mice with K6-controlled tva expression, and for the trastuzumab-coated GGS particles, we will use mice with xenografted human ErbB2-expressing tumors. For the anti-TVA-conjugated studies, tumors will be transplanted into syngeneic mice to prevent the nanoparticles from targeting stem cells in normal tissues.

To view the accumulation of the GGS particles in the tumor in vivo, we would use diffuse optical spectroscopy (Zaman et al 2007) and 2-photon laser scanning microscope and compare the distribution of the targeted GGS particles to the non-specific antibody and PEGylated only GGS particles 48 hours after injection. We would also perform the same anti-TVA nanoparticle injections as above in tumors modified to express GFP or another reporter protein in the breast cancer TICs. Using 2-photon spectroscopy, we will evaluate the distribution of the TICs, and receive visual confirmation of calculated percentage of TICs vs. tumor somatic cells. We would also evaluate if the GGS nanoshells were reaching the TVA receptors or becoming trapped in the bulk of the tumor by comparing the positioning of the reporter protein signal to the nanoshell scattering.

Once we had confirmed that the nanoshells were binding to the targeted receptors, we would focus a NIR laser (wavelength = ~800 nm) on the tumor using 3 minutes at a power density of 4 W/cm^2 and a spot size of 5 mm as starting points for therapy (Gobin PhD thesis, 2007) and follow tumor growth for 2 weeks post-ablation. This time could then be extended to 6 weeks to evaluate for recurrence and metastases with bioluminescent imaging in mice with reporter protein-expressing tumors.

II. **Reportable Outcomes:**

a. Publications

i. Carpin LB, Bickford LR, Agollah G, Yu TK, Schiff R, Li Y, Drezek RA. Immunoconjugated gold nanoshell-mediated photothermal ablation of trastuzumab-resistant breast cancer cells. Breast Cancer Research and Treatment (2011), 125(1):27-34. doi 10.1007/s10549-010-0811-5

ii. Kennedy LC[*], Bear AS[*], Young JK, Lewinski NA, Kim J, Foster AE[+], Drezek RA[+]. "T Cells Enhance Gold Nanoparticle Delivery to Tumors in vivo." Nanoscale Research Letters (2011) 6(1):283. doi:10.1186/1556-276X-6-283

iii. Kennedy LC, Bickford LR, Lewinski NA, Coughlin AJ, Hu Y, Day ES, West JL, Drezek RA. "A New Era for Cancer Treatment: Gold nanoparticle-mediated Thermal Therapies." Small (2011) 7(2):169-183. doi 10.1002/smll.201000134

iv. Young JK, Lewinski NA, Langsner RJ, Kennedy LC, Satyanarayan A, Nammalvar V, Lin AY, Drezek RA. "Size Controlled Synthesis of Monodispersed Gold Nanoparticles via Carbon Monoxide Gas Reduction." Nanoscale Research Letters (2011) 6:428.

v. Bickford LR, Carpin LB, Sun J, Lin AWH, Loo C, Hsu K, Yu T-K, Drezek RA. **"**Optical Technologies for Noninvasive Functional and Molecular Imaging**"** in *Advanced Therapy of Breast Disease,* 3rd ed., edited by Francisco Esteva, MD,

Roman Skoracki, MD, and Gildy Babiera, MD (People's Medical Publishing House). Shelton, CT (2012): 1439-1457.

vi. Bear AS, Carpin LB, Cruz CR, Drezek RA, Foster AE. "Nanoparticles for Targeting T Cells in Allergy and Inflammatory Airway Conditions" in *Pulmonary Nanomedicine: Diagnostics, Imaging, and Therapeutics*, edited by Neeraj Vij (Pan Stanford Publishing). Singapore, Singapore (2012): 135-155.

vii. Bickford LR, Langsner RJ, Chang J, Kennedy LC[1], Agollah GD, Drezek RA. "Rapid stereomicroscopic imaging of HER2/neu overexpression in ex vivo breast tissue using topically applied silica-based gold nanoshells." Journal of Oncology (2012) 2012:291898.

viii. Bear AS[*], Kennedy LC[*], Young JK[*], Mattos JP, Lin AY, Eckels PC, Drezek RA[+], Foster AE[+]. "Elimination of Metastatic Melanoma using a Combined Therapy of Gold Nanoshell-Enabled Photothermal Therapy and Adoptive T Cell Transfer." Conditional acceptance to *PLoS ONE*, March 2013.

b. Patents

i. Foster AE, Drezek RA, Kennedy LC, Bear AS, Young JK, Lin AY. "T Cell Delivery of Gold Nanoshells for Cancer Immunotherapy." U.S. Provisional Patent Application Serial No. 61/349,319 (filed May 28, 2010)

c. Invited Presentations

i. Carpin LB*,[2] Bear AS*, Young JK, Lewinski NA, Foster A, Drezek RA. "T cell-mediated delivery of gold nanoparticles." Oral presentation at Southwestern Regional Meeting of the American Association for the Advancement of Science, April 2010.

ii. Carpin L*, Bear A*, Young J, Lewinski N, Foster A, Drezek R. "T cell vehicles enhance tumor accumulation of gold nanoparticles." Oral presentation at BMES 2010, October 2010.

iii. Kennedy L*, Bear A*, Young J, Lewinski N, Kim J, Foster A, Drezek R. "T cell vehicles enhance tumor accumulation of gold nanoparticles." Poster presentation at CPRIT 2010, November 2010.

iv. Kennedy L*, Bear A*, Young J, Lewinski N, Kim J, Foster A, Drezek R. "The Use of T cell vehicles improves gold nanoparticle tumor delivery in vivo." Poster presentation at BCM MSTP Symposium, March 2011.

[*,+] denotes equal contribution

[*,+] denotes equal contribution

III. Conclusion

We proposed targeting and ablating trastuzumab-resistant breast cancer cells and breast cancer TICs using immunoconjugated NIR-spectrum gold nanoparticles. We demonstrated the potential of trastuzumab-conjugated gold nanoparticle-mediated ablation for the treatment of chemotherapy-resistant HER2+ breast cancers in vitro. Alternative cancer therapies such as gold nanoparticle-mediated ablation may highlight a future direction for the development of cancer treatments.

IV. References

Al-Hajj M, Wicha MS, Benito-Hernandez A, Morrison SJ, Clarke MF. "Prospective identification of tumorigenic breast cancer cells." PNAS (2003) 100(7):3983-3988. doi 10.1073/pnas.0530291100

Bu, W., Chen, J., Morrison, G.D., Huang, S., Creighton, C.J., Huang, J., Chamness, G.C., Hilsenbeck, S.G., Roop, D.R., Leavitt, A.D. & Li, Y. Keratin 6a marks mammary bipotential progenitor cells that can give rise to a unique tumor model resembling human normal-like breast cancer. Oncogene Epub May 2 (2011). PMID: 21532625.

Clarke RB. "Isolation and characterization of human mammary stem cells." Cell Prolif (2005) 38:375-386.

Du Z, Podsypanina K, Huang S, McGrath A, Toneff MJ, Bogoslovskaia E, Zhang X, Moraes RC, Fluck M, Allred DC, Lewis MT, Varmus HE, Li Y. "Introduction of oncogenes into mammary glands in vivo with an avian retroviral vector initiates and promotes carcinogenesis in mouse models." PNAS (2006) 103(46):17396-17401. doi 10.1073/pnas.0608607103

Gobin, Andre Mathura. "Photothermal Therapies Using Near Infrared Absorbing Nanoparticles." (PhD thesis, Rice University, 2007), 120-161.

Gobin AM, Lee MH, Halas NJ, James WD, Drezek RA, West JL. "Near-Infrared Resonant Nanoshells for Combined Optical Imaging and Photothermal Cancer Therapy." Nano Lett (2007) 7(7):1929-1934. doi 10.1021/nl070610

Lal S, Clare SE, Halas NJ. "Nanoshell-enabled photothermal cancer therapy: impending clinical impact." Acc. Chem. Res (2008) 41(12):1842-1851. doi 10.1021/ar800150g

Loo C, Lowery A, Halas N, West J, Drezek R. "Immunotargeted nanoshells for integrated cancer imaging and therapy." Nano Lett (2005) 5(4):709-711. doi 10.1021/nl050127s

Morrison BJ, Schmidt CW, Lakhani SR, Reynolds BA, Lopez JA. "Breast cancer stem cells: implications for therapy of breast cancer." Breast Cancer Research (2008) 10:210. doi 10.1186/bcr2111

Nahta R & Esteva FJ. "Molecular mechanisms of trastuzumab resistance." Breast Cancer Research (2006) 8:215-222. doi:10.1186/bcr1612

Ochsenbauer-Jambor C, Delos SE, Accavitti MA, White JM, Hunter E. "Novel Monoclonal Antibody Directed at the Receptor Binding Site on the Avian Sarcoma and Leukosis Virus Env Complex." J Virology (2002) 76(15):7518-7527. doi 10.1128/JVI.76.15.7518-7527.2002

Oldenburg SJ, Averitt RD, Westcott SL, Halas NJ. "Nanoengineering of optical resonances." Chem Phys Lett (1998) 288:243-247.

Ponti D, Costa A, Zaffaroni N, Pratesi G, Petrangolini G, Coradini D, Pilotti S, Pierotti MA, Daidone MG. "Isolation and in vitro propagation of tumorigenic breast cancer stem cells with stem/progenitor cell properties." Cancer Res (2005) 65(13):5506-5511.

Valabrega G, Montemurro F, Aglietta M. "Trastuzumab: mechanism of action, resistance and future perspectives in HER2-overexpressing breast cancer." Ann Oncol (2007) 18:977-984. doi 10.1093/annonc/mdl475

Zaman RT, Diagaradjane P, Wang JC, Schwartz J, Rajaram N, Gill-Sharp KL, Cho SH, Rylander III HG, Payne JD, Krishnan S, Tunnell JW. "*In vivo* detection of gold nanoshells in tumors using diffuse optical spectroscopy." IEEE J Sel Top Quant (2007) 13(6):1715-1720. doi 10.1109/JSTQE.2007.910804

Breast Cancer Res Treat (2011) 125:27–34
DOI 10.1007/s10549-010-0811-5

PRECLINICAL STUDY

Immunoconjugated gold nanoshell-mediated photothermal ablation of trastuzumab-resistant breast cancer cells

Laura B. Carpin · Lissett R. Bickford · Germaine Agollah · Tse-Kuan Yu · Rachel Schiff · Yi Li · Rebekah A. Drezek

Received: 4 February 2010 / Accepted: 13 February 2010 / Published online: 10 March 2010

Abstract Trastuzumab is a FDA-approved drug that has shown clinical efficacy against HER2+ breast cancers and is commonly used in combination with other chemotherapeutics. However, many patients are innately resistant to trastuzumab, or will develop resistance during treatment. Alternative treatments are needed for trastuzumab-resistant patients. Here, we investigate gold nanoparticle-mediated photothermal therapies as a potential alternative treatment for chemotherapy-resistant cancers. Gold nanoshell photothermal therapy destroys the tumor cells using heat, a physical mechanism, which is able to overcome the cellular adaptations that bestow trastuzumab resistance. By adding anti-HER2 to the gold surface of the nanoshells as a targeting modality, we increase the specificity of the nanoshells for HER2+ breast cancer. Silica–gold nanoshells conjugated with anti-HER2 were incubated with both trastuzumab-sensitive and trastuzumab-resistant breast cancer cells. Nanoshell binding was confirmed using two-photon laser scanning microscopy, and the cells were then ablated using a near-infrared laser. We demonstrate the successful targeting and ablation of trastuzumab-resistant cells using anti-HER2-conjugated silica–gold nanoshells and a near-infrared laser. This study suggests potential for applying gold nanoshell-mediated therapy to trastuzumab-resistant breast cancers in vivo.

Keywords Nanoshells · Photothermal therapy · Chemotherapy resistance · Breast cancer · Trastuzumab

L. B. Carpin · L. R. Bickford · T.-K. Yu · R. A. Drezek (✉)
Department of Bioengineering, Rice University, 6100 Main St., MS-142, Houston, TX 77005, USA
e-mail: drezek@rice.edu

G. Agollah
Nanospectra Biosciences Inc., Houston, TX 77054, USA

T.-K. Yu
Department of Radiation Oncology, The University of Texas M.D. Anderson Cancer Center, Houston, TX 77030, USA

R. Schiff · Y. Li
Breast Center, Baylor College of Medicine, Houston, TX 77030, USA

R. A. Drezek
Department of Electrical and Computer Engineering, Rice University, Houston, TX 77005, USA

Introduction

Despite the advances in the treatment of early-stage breast cancer, patients with advanced Stage III and IV disease have 5-year survival rates of only 57% and 20%, respectively [1]. Although many new chemotherapy drugs and regimens have been developed, little improvement has been seen in the ultimate outcome of these cancer patients. Epidermal growth factor 2 receptor (Erb2 or HER2) is amplified in 20–25% of human breast cancer, and is known to be a marker of poorer prognosis due to HER2+ breast cancers aggressive nature and tendency to recur [2, 3]. In 2006, a therapeutic antibody against HER2 (Trastuzumab) was developed as part of a new class of drugs. Trastuzumab binds to the HER2 receptor and halts tumor cell growth through suppression of HER2 signaling and subsequent elevation of the levels of $p27^{KIP1}$ protein [2]. Trastuzumab showed positive clinical results as a treatment for HER2+ metastatic breast cancer in clinical trials [4, 5], and after subsequent studies was approved as a treatment for patients with HER2+ metastatic breast

cancer. Despite the initial success of trastuzumab, the development of drug resistance has presented a major barrier. The majority of patients are intrinsically resistant to trastuzumab prior to starting therapy [6], and most initially responsive patients develop resistance to treatment within a year [2]. Second generation agents like lapatinib, which is small molecule-based tyrosine kinase inhibitor, have been developed for trastuzumab-resistant patients, but chemotherapy resistance continues to be problematic [7]. The development of gold nanoparticle-mediated photothermal cancer therapy presents a new and minimally invasive treatment possibility for chemotherapy-resistant cancers [8]. To date, gold nanoparticle-mediated treatment has only been applied to chemotherapy-sensitive cell lines. Here, we demonstrate the targeting and photothermal ablation of trastuzumab-resistant breast cancer cells in vitro using anti-HER2-conjugated silica–gold nanoshells.

The development of trastuzumab resistance has been attributed to a variety of mechanisms, including overexpression of glycoprotein MUC4 [9], overexpression of insulin-like growth factor 1 (IGF-1) [10], and constitutive P13K/Akt activity [11]. However, even in cases where there is obstructed binding of the extracellular component of the HER2 receptor, the receptor itself remains unchanged. In addition, although a mutation of the extracellular component of the HER2 receptor that results in trastuzumab resistance is theoretically possible, in most cases of resistance this does not occur [2]. This presents the possibility of using an antibody generated against the HER2 receptor as a targeting modality for an alternative form of therapy, such as gold nanoparticle-mediated photothermal therapy.

Gold nanoparticles have great potential in the diagnosis, management, and treatment of cancer due to their versatile scattering and absorbing properties, as well as the ease with which their surfaces can be modified. For therapy applications, a variety of gold nanoparticles can be used, including gold colloid [12], silica–gold nanoshells [8], gold nanorods [13], and gold nanocages [14]. For this study, silica–gold nanoshells are used due to their low cytotoxicity profile and demonstrated efficacy as a therapeutic against HER2+ breast cancer cells [8, 15, 16]. Gold nanoshells usually consist of a dielectric core, such as silica, which is coated with a thin layer of gold. The unique optical properties of nanoshells are due to the localized surface plasmon resonance of the gold metal electrons, and these properties can be modulated by controlling the thickness of the gold coating during synthesis. When designed to primarily absorb light, nanoshells can efficiently convert light energy to heat energy, destroying adjacent cells via thermal ablation [15, 17–19]. Unlike conventional hyperthermia treatments, the use of nanoshells as an absorptive agent has the added benefit of decreasing the laser intensity requirements for therapy, which prevents inadvertent ablation of normal cells.

To further enhance therapy, ligands such as antibodies, polymers, or DNA, can be conjugated to the gold nanoparticle surface. This modification has demonstrated increased target specificity in vitro [8, 17, 20]. In the case of HER2+ breast cancer, Loo et al. demonstrated that gold–silica nanoshells conjugated to anti-HER2 can be successfully used to target and ablate chemotherapy-sensitive breast cancer cells in culture [16]. Here, we demonstrate that anti-HER2-conjugated silica–gold nanoshells can mediate effective targeting and photothermal ablation of two cultured anti-HER2-resistant breast cancer cell lines—JIMT-1 has a lower level of anti-HER2 binding due to overexpression of MUC4 [9], and BT474 AZ LR is resistant to both trastuzumab and lapatinib. Using photothermal therapy, the cancer cells can be destroyed by the conversion of nanoshell-absorbed energy to heat. This physical mechanism of cell ablation effectively evades any developed intracellular resistance mechanism, presenting a new possibility for the treatment of trastuzumab-resistant breast cancers.

Methods

Breast cancer cell lines

Three HER2-overexpressing breast cancer cell lines were chosen for this study: SK-BR-3, JIMT-1, and BT474 AZ LR. The MCF10A cell line, which is an immortalized, HER2 negative breast epithelial cell line, was used as a control. The SK-BR-3 and MCF10A cell lines were purchased from American Type Culture Collection. The SK-BR-3 cell line is trastuzumab sensitive. The JIMT-1 cell line was purchased from DSMZ (Germany), and is trastuzumab resistant. The BT474 AZ LR cell line, a subculture of BT474, is resistant to both trastuzumab and lapatinib. The SK-BR-3 and JIMT-1 cell lines were both cultured in McCoy's 5A and Dulbecco's Modified Essential Medium, respectively, supplemented with 10% fetal bovine serum (FBS) and 1% penicillin–streptomycin. The BT474 AZ LR cell line was cultured in Dulbecco's Modified Essential Medium High Glucose supplemented with 10% FBS and 1% penicillin–streptomycin–glutamine and with 1 μM of lapatinib to maintain HER2 therapy resistance. The MCF10A cells were cultured in Mammary Epithelial Basal Medium (MEBM) supplemented with a BulletKit (Clonetics). All cells were maintained at 37°C in a 5% CO_2 atmosphere.

Quantification of HER2 receptor antigens on cell surface

Quantification of HER2 surface receptors was performed as described by Bickford et al. [21]. Cells were grown to confluence, trypsinized, counted, and incubated with either media alone, PE antihuman CD340 (erbB2/HER-2) antibody (BioLegend, San Diego, CA), or PE mouse IgG1 isotype control antibody (BioLegend, San Diego, CA) for 30 min on ice in the dark. The IgG1 isotype serves as background signal correction. The cells were then washed in 1 × PBS, resuspended in 500 µl of cell staining buffer (BioLegend, San Diego, CA, USA), and stored on ice until analysis. Immunofluorescence intensity was determined by flow cytometry at The University of Texas M.D. Anderson Cancer Center (MDACC) flow cytometry core. To correlate the immunofluorescence intensity with the quantity of HER2 antigens available for binding on each cell, a Quantum Simply Cellular anti-Mouse IgG kit (Bangs Laboratories, Inc., Technology Drive Fishers, IN, USA) was used. This kit has four different sets of microbeads possessing a known number of antigen binding sites, which permits the development of a calibration curve correlating immunofluorescence intensity with the quantity of antigen binding sites. The curve is then used to calculate the number of antigen binding sites per cell.

Silica–gold nanoshells and antibody conjugation

The silica–gold nanoshells were synthesized using previously described methods [15–17, 22]. In brief, silica cores were created using the Stöber method [23], and the silica core surface was functionalized with amine groups. These amine groups were then used to seed 4–7-nm gold colloid onto the silica surface. The size of the silica cores was determined to be 120 nm by scanning electron microscopy (SEM) prior to gold seeding. The gold shell was then completed by adding additional gold solution, potassium carbonate, and formaldehyde. After synthesis, the UV–Vis spectrum of the nanoshells was correlated with Mie Theory to determine the absorption, extinction, and scattering coefficients of the nanoshells, and subsequently the approximate concentration. The average nanoshell diameter was confirmed to be 150 ± 10 nm by SEM. The nanoshell peak absorbance was determined to be 780 nm with a concentration of 3.85×10^9 nanoparticles/ml (Fig. 1).

To modify the surfaces of the nanoshells with anti-HER2 antibody, the methods of Loo et al. were employed [16]. The anti-HER2 antibody (C-erbB-2/HER-2/*neu* Ab-4, Lab Vision Corporation) was incubated with a custom orthopyridyl-disulfide-polyethylene glycol-*N*-hydroxysuccinimide ester (OPSS-PEG-NHS, MW = 2kD, CreativeBiochem Laboratories, Winston Salem, NC, USA) linker at a molar ratio of

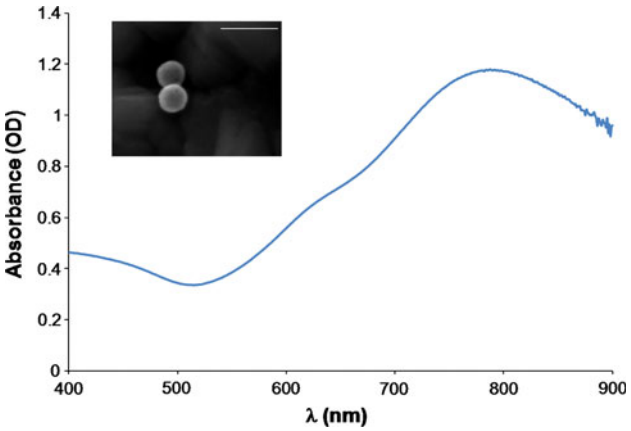

Fig. 1 Absorbance spectrum of the silica–gold nanoshells (silica core radius = 60 nm, total radius = 75 nm). Inset shows SEM image of the nanoshells; scale bar is 300 nm

3:1 in sodium bicarbonate (100 mM, pH 8.5) overnight on ice at 4°C. Aliquots were then stored at −80°C until use, when they were thawed on ice. The antibody binds to the OPSS-PEG-NHS linker via the amide group, and adsorbs to the gold surface of the nanoshell via the thiols of the OPSS group. To attach the antibody-linker to the gold nanoshells, nanoshells were incubated with the antibody-linker at 4°C for 2 h, then 1 mM polyethylene glycol-thiol (PEG-SH, MW = 5kD, Nektar) was added and the nanoshells were incubated overnight at 4°C for further stabilization. After nanoshell conjugation, the unreacted PEG-linker and PEG-SH were removed by centrifugation of the nanoshell solution and removal of the supernatant. The anti-HER2 nanoshells were then resuspended in cell-line appropriate media prior to use in cell studies.

Two-photon laser scanning microscopy to confirm binding efficiency

For in vitro two-photon nanoshell binding studies, 5×10^5 cells in suspension from each cell line (MCF10A, SK-BR-3, JIMT-1, and BT474 AZ LR), were incubated with 1.73×10^9 nanoshells in 1 ml of media for 1 h at 37°C with rotation in a hybridization oven. Cells incubated with media alone were used as a control. After the incubation, the cell lines were washed three times with 1 ml of 1 × phosphate-buffered saline (PBS) to remove unbound nanoshells, and resuspended in 0.5 ml of cell line appropriate media. Each treatment and control group was then seeded onto an inverted coverslip and allowed to attach overnight. A Zeiss Laser Scanning Microscope 510 META multiphoton system (Zeiss, Thornwood, NY, USA) was used in combination with a Coherent Chameleon femtosecond mode locked Ti:sapphire laser (Coherent, Santa Clara, CA, USA) for imaging.

Nanoshell-mediated photothermal therapy

For in vitro photothermal ablation studies, 5×10^5 cells in suspension from each cell line (MCF10A, SK-BR-3, JIMT-1, and BT474 AZ LR) were incubated with 1.71×10^{10} nanoshells as described above. Media alone was again used as a control. Cells were washed with PBS and seeded in coverslips as described above.

Laser irradiation of the cells was performed in a similar manner to previous photothermal therapy studies [16–18]. After the cells were attached, each well was uncovered, placed on top of a glass microscope slide, and exposed to an 808-nm NIR diode laser (Coherent Inc., Santa Clara, CA, USA) at 80 W/cm^2 with a 1.5-mm spot size for 5 min. Following laser irradiation, the cells were returned to the 37°C incubator with 5% CO_2 for several hours. Live/dead viability staining was then performed using an Invitrogen Live/Dead viability/cytotoxicity kit (Carlsbad, CA, USA), and cells were imaged using a Zeiss Axiovert 135 Fluorescence microscope (Zeiss, Thornwood, NY, USA). To confirm nanoshell binding, silver staining was performed using Sigma–Aldrich Silver Enhancement solutions (St. Louis, MO, USA), followed by brightfield imaging.

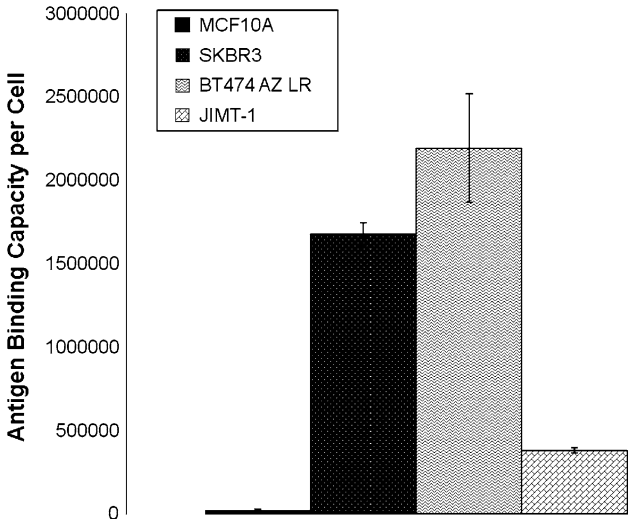

Fig. 2 Anti-HER2 binding capacity of each breast cancer cell line, determined by flow cytometry. The HER2+ cell lines (SK-BR-3, JIMT-1, BT474 AZ LR) show a significantly higher binding capacity than the HER2-cell line (MCF10A). Data for MCF10A, SK-BR-3, and JIMT-1 reused with permission from [21]. Copyright 2009 from Springer

Results

Quantification of antigen binding for each cell line

Using flow cytometry, the number of antigen binding sites for each cell line was determined, as displayed in Fig. 2. Data for the MCF10A, SK-BR3, and JIMT-1 cell lines are being reused with permission from [21]. A one-factor ANOVA test indicated significant differences between cell lines in the number of binding sites ($P < 0.01$). Each of the HER2+ breast cancer lines used in this study had a larger number of anti-HER2 binding sites than the normal epithelial cell line, MCF10A ($2.43 \times 10^4 \pm 3.77 \times 10^3$ receptors), by the Tukey comparison test ($P < 0.01$). The BT474 AZ LR cell line had the greatest anti-HER2 binding capacity ($2.19 \times 10^6 \pm 3.25 \times 10^5$ receptors), followed by the SK-BR-3 ($1.68 \times 10^6 \pm 6.78 \times 10^4$ receptors) and then the JIMT-1 ($3.82 \times 10^5 \pm 1.47 \times 10^4$ receptors) cell lines. Notably, the JIMT-1 cell line has a significantly lower HER2 binding site expression when compared to the SK-BR-3 and BT474 AZ LR cell lines ($P < 0.01$).

Two-photon microscopy of nanoshell–cell binding

Nanoshell binding is evaluated through two-photon laser scanning microscopy in Fig. 3. The figure shows phase-

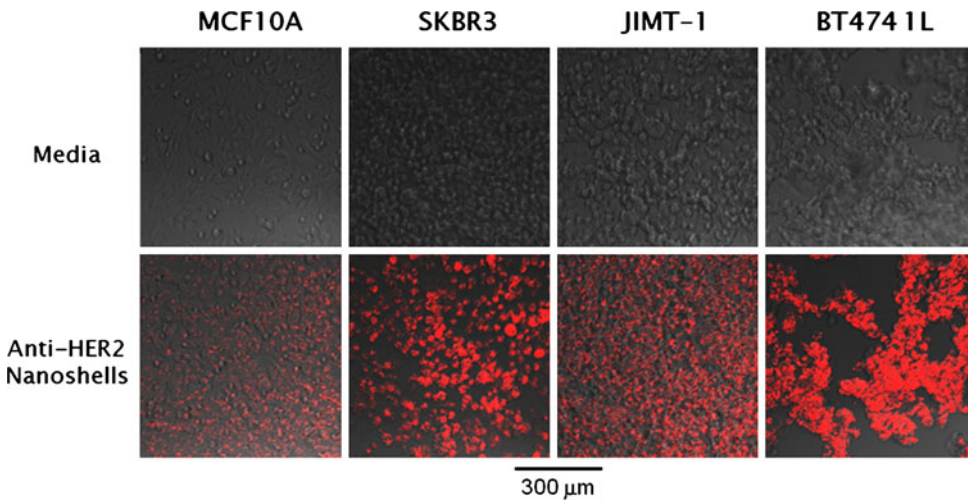

Fig. 3 Verification of nanoshell binding using two-photon laser scanning microscopy. Images depicted are phase contrast images overlaid with two-photon images. SK-BR-3, JIMT-1, and BT474 AZ LR cell lines, all HER2+, show greater binding of the anti-HER2 nanoshells than the MCF10A normal epithelial cell line

contrast images overlaid with the two-photon images. The cells incubated with media only demonstrate no nanoshell signal. The HER2+ cell lines incubated with nanoshells each show nanoshell signal, while the HER2-cell line shows significantly less. The SK-BR-3 and BT474 AZ LR cell lines show the most nanoshell binding. The JIMT-1 cell line demonstrates less nanoshell binding than the SK-BR-3 and BT474 AZ LR cell lines, but greater nanoshell binding than the MCF10A cell line. There is some degree of binding seen with the MCF10A cell line, but this binding is still significantly less than the HER2+ breast cancer cells.

Nanoshell-mediated cell destruction of trastuzumab-resistant cell lines

Figure 4 shows the live/dead imaging and silver staining for the treatment and media control group of each cell line. None of the media alone groups show evidence of cell death on the live/dead images or evidence of nanoshell binding on the silver stain. The silver staining confirms that nanoshells are bound to each of the HER2+ cell lines (SK-BR-3, BT474 AZ LR, JIMT-1), with minimal nanoshell binding to the MCF10A cell line. The MCF10A-nanoshell group does not demonstrate localized area of cell death, while each of the HER2+ breast cancer-nanoshell groups show a clearly defined region of dead cells (red) corresponding to the laser spot surrounded by non-irradiated, nanoshell-bound live cells (green).

Discussion

Anti-HER2 resistance continues to be a challenge for clinicians treating advanced cancers. Gold nanoparticle-mediated photothermal therapy could present new possibilities for cancers that are currently resistant to conventional chemotherapy and radiation treatments. The objective of this study was to demonstrate that immunoconjugated silica–gold nanoshells can effectively destroy both chemotherapy-sensitive and chemotherapy-resistant breast cancer cell lines. Two trastuzumab-resistant breast cancer cell lines were selected for testing, JIMT-1 and BT474 AZ LR. A trastuzumab-sensitive breast cancer cell line, SK-BR-3, and a HER2 negative normal epithelial cell line, MCF10A, were also chosen as positive and negative binding controls. Each of the HER2+ breast cancer cell lines selected was effectively ablated using nanoshell-mediated photothermal therapy. These results suggest gold nanoparticle-mediated photothermal therapy may have potential to be employed against chemotherapy-resistant breast cancers in vivo.

As the first step of this study, we evaluated nanoshell binding efficiency using two-photon laser scanning

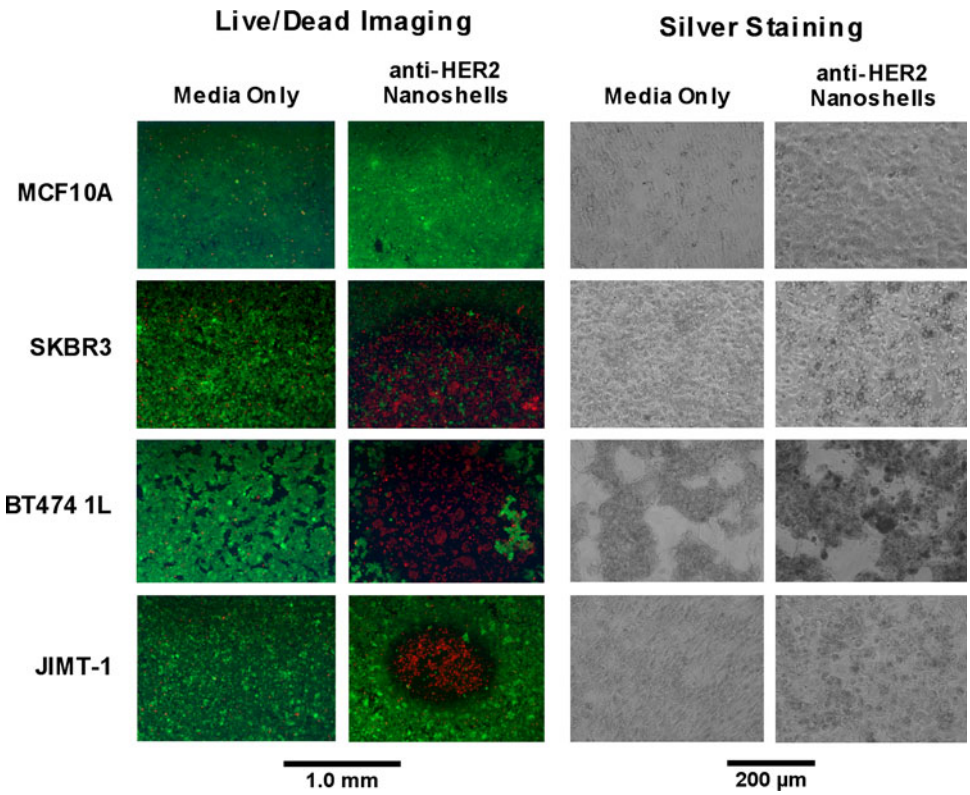

Fig. 4 Photothermal therapy results. Live/dead imaging demonstrates cell ablation in HER2+ cell lines (SK-BR-3, JIMT-1, BT474 AZ LR) treated with anti-HER2 nanoshells and NIR laser irradiation. Silver staining shows nanoshell binding for each of the HER2+ cell lines

microscopy. Silica–gold nanoshells have demonstrated two-photon properties, and can be used to label HER2+ breast cancer cells in vitro [24, 25]. Nanoshell binding has also been demonstrated using darkfield microscopy [15] and optical coherence tomography [26], which depends on the enhanced scattering of the nanoshells for contrast. However, for future in vivo studies, two-photon luminescence may prove superior in bulk tissue to these scatter-based techniques. This is due to the improved signal to noise ratio of two-photon microscopy, as well as its demonstrated ability to more effectively investigate the nanoshell distribution within the tumor with the assistance of software [25]. In Fig. 3, we observe that the anti-HER2 conjugated silica–gold nanoshells bind specifically to trastuzumab-resistant HER2+ breast cancer cell lines, with very little binding to the normal breast epithelial cell line, MCF10A (Figs. 3, 4). The degree of nanoshell binding shown by both the two-photon and silver stain images seems to correlate with the HER2 antigen binding capacity of the breast cancer cell lines. The JIMT-1 cell line has the lowest anti-HER2 binding capacity of the three breast cancer lines studied. Nagy et al. found that only 20% of HER2 receptors are available for trastuzumab binding due to obstruction of the extracellular component of the HER2 receptor by MUC4 [9]. Despite this, anti-HER2 nanoshell binding is still clearly seen in both the two-photon and silver stain images, though to a lesser degree than the other two HER2+ lines. Importantly, this lesser degree of binding is still sufficient for the photothermal destruction of the JIMT-1 cells, while the action of trastuzumab is impaired against these cells [9]. In the case of the BT474 AZ LR cell line, the nanoshell binding is more than adequate to ensure cell death upon NIR laser irradiation. Photothermal therapy is also effective against the BT474 AZ LR cell line, while the action of both trastuzumab and lapatinib is impaired against these cells.

Using silica–gold nanoshells as a mediating absorptive agent for photothermal therapy has advantages over conventional hyperthermia treatments. In Fig. 4, the ablated areas (red) are surrounded by living, healthy cells (green), and cell lines with minimal or no nanoshell binding show no regions of cell death. Only HER2+ cells with bound nanoshells with in the region of the laser spot are ablated. Targeting the gold nanoparticles with an antibody or peptide permits single cell specificity in vitro [27, 28]. This specificity is important during in vivo studies, when healthy tissues such as skin will be in the laser path to cancerous tissue. Because nanoshells efficiently absorb the irradiating laser energy and convert it to heat, the laser power requirements to induce cell death are lowered. In conventional hyperthermia treatments, this specificity is lacking, as the power of the irradiating energy source must be high enough to kill cells without the assistance of a mediating agent. Thus, using nanoshells as part of photothermal therapy in vitro lowers the power requirements of the irradiating energy, as well as increasing the specificity of therapy for malignant cells.

Figure 4 does demonstrate some variation in the size of the ablated regions. This variation was seen consistently among several replicate experiments. These differences are likely due to variations in the laser intensity distribution, the degree of cell confluence, and density of HER2 receptors on the cell surfaces. In order for cell death to occur, a temperature of 70–80°C must be achieved for approximately 4 min [13]. The net temperature increase of the cells within the laser spot is dependent on a combination of variables, including: the absorptive cross-section of the silica–gold nanoshells, the physical distribution of the nanoshells among the cells, the intensity and duration of the laser illumination, and the heat transfer and dissipation properties of the cells and media [29]. Nonuniform laser intensity could lead to cells at the periphery of the spot receiving less laser power [30], resulting in the minimum temperature and duration needed for cell death not being achieved. However, the laser spot size, power, and duration were held consistent throughout each of the treatment groups and experiments, so it is unlikely that this is a large contributor. The nanoshell binding density could also be playing a significant role, and, based on the information in Figs. 2 and 3, is a likely contributor to the variation in ablated area size.

The low anti-HER2 binding capacity of the JIMT-1 cell line versus the higher binding capacities of the SK-BR-3 and BT474 AZ LR cell lines correlates with the small ablated area for the JIMT-1 cells and the larger ablated areas for the SK-BR-3 and BT474 AZ LR cells. This supports the nanoshell binding density being a major contributor to the variation in ablation size. However, although the SK-BR-3 cell line has a lower anti-HER2 binding capacity than the BT474 AZ LR cell line, the size of the ablated area for this cell line is larger. This could be due to several factors. Some of this variation may be due to the differences in how the SK-BR-3 and BT474 AZ LR cell lines tend to grow. The SK-BR-3 cells grow in a monolayer, while the BT474 AZ LR cell line tends to grow in conglomerates. These growth differences may have resulted in different heating profiles between the two cell lines, affecting the sizes of the ablated regions. Another possible contributing factor is differences in thermal sensitivity between the SK-BR-3 and BT474 AZ LR cell lines, which has been seen in response to conventional hyperthermia treatments in tumors resected from breast cancer patients [31]. Regardless of variation in the size of the ablated regions, each of the HER2+ breast cancer cell lines was successfully ablated using nanoshell-mediated photothermal therapy. Each of these variables (laser intensity profile,

nanoshell binding density, the tumor cell density/tumor shape, the thermal sensitivity of the tumor) will need to be considered in applying and optimizing nanoshell-mediated therapy to trastuzumab-resistant cancers in vivo.

The successful application of gold nanoshell-mediated photothermal therapy to trastuzumab-resistant breast cancer cells in vitro suggests a promising new approach for the treatment of advanced HER2+ breast cancers. By virtue of its physical means of destroying cancer, nanoshell-mediated thermal ablation of these types of cancer has an innate advantage over trastuzumab, lapatinib, and other antibody or small molecule-based therapies. Gold nanoparticle-mediated photothermal therapies also have demonstrated synergistic cell killing in combination with chemotherapy in vitro [32]and radiation in vivo [33], suggesting that the combination of conventional treatments and this technology could also be beneficial for cancer therapy. In vivo studies with xenografted trastuzumab-resistant breast cancers are currently underway to further confirm the efficacy and applicability of this nanotechnology to anti-HER2-resistant breast cancers.

Acknowledgments We would like to thank Wendy Schober at MDACC for performing the flow cytometry on each cell line. This study was supported by a Department of Defense Congressionally Directed Breast Cancer Research Program Era of Hope Scholar Award to Rebekah Drezek and Tse-Kuan Yu, the Center for Biological and Environmental Nanotechnology (EEC-0118007 and EEC-0647452), the NCI breast cancer SPORE P50 (CA58183), and the Nancy Owens Memorial Foundation (Y. Li). L. Carpin would also like to thank the Medical Scientist Training Program at Baylor College of Medicine for training support.

References

1. American Cancer Society: Breast Cancer Facts and Figures (2007–2008) In: breast cancer facts and figures 2007–2008. American Cancer Society, Atlanta
2. Nahta R, Yu D, Hung MC, Hortobagyi GN, Esteva FJ (2006) Mechanisms of disease: understanding resistance to HER2-targeted therapy in human breast cancer. Nat Clin Pract 3(5):269–280
3. Slamon DJ, Clark GM, Wong SG, Levin WJ, Ullrich A, McGuire WL (1987) Human breast cancer: correlation of relapse and survival with amplification of the HER-2/neu oncogene. Science 235(1):177–182
4. Cobleigh MA, Vogel CL, Tripathy D, Robert NJ, Scholl S, Fehrenbacher L, Wolter JM, Paton V, Shak S, Lieberman G et al (1999) Multinational study of the efficacy and safety of humanized anti-HER2 monoclonal antibody in women who have HER2-overexpressing metastatic breast cancer that has progressed after chemotherapy for metastatic disease. J Clin Oncol 17(9):2639–2648
5. Vogel CL, Cobleigh MA, Tripathy D, Gutheil JC, Harris LN, Fehrenbacher L, Slamon DJ, Murphy M, Novotny WF, Burchmore M et al (2002) Efficacy and safety of trastuzumab as a single agent in first-line treatment of HER2-overexpressing metastatic breast cancer. J Clin Oncol 20(3):719–726
6. Nahta R, Esteva FJ (2006) HER2 therapy: molecular mechanisms of trastuzumab resistance. Breast Cancer Res 8(6):215
7. Valabrega G, Montemurro F, Aglietta M (2007) Trastuzumab: mechanism of action, resistance and future perspectives in HER2-overexpressing breast cancer. Ann Oncol 18(6):977–984
8. Hirsch LR, Stafford RJ, Bankson JA, Sershen SR, Rivera B, Price RE, Hazle JD, Halas NJ, West JL (2003) Nanoshell-mediated near-infrared thermal therapy of tumors under magnetic resonance guidance. Proc Natl Acad Sci USA 100(23):13549–13554
9. Nagy P, Friedlander E, Tanner M, Kapanen AI, Carraway KL, Isola J, Jovin TM (2005) Decreased accessibility and lack of activation of ErbB2 in JIMT-1, a herceptin-resistant, MUC4-expressing breast cancer cell line. Cancer Res 65(2):473–482
10. Lu Y, Zi X, Zhao Y, Mascarenhas D, Pollak M (2001) Insulin-like growth factor-I receptor signaling and resistance to trastuzumab (Herceptin). J Natl Cancer Inst 93(24):1852–1857
11. Yakes FM, Chinratanalab W, Ritter CA, King W, Seelig S, Arteaga CL (2002) Herceptin-induced inhibition of phosphatidylinositol-3 kinase and Akt Is required for antibody-mediated effects on p27, cyclin D1, and antitumor action. Cancer Res 62(14):4132–4141
12. Huang X, Qian W, El-Sayed IH, El-Sayed MA (2007) The potential use of the enhanced nonlinear properties of gold nanospheres in photothermal cancer therapy. Lasers Surg Med 39(9):747–753
13. Huang X, El-Sayed IH, Qian W, El-Sayed MA (2006) Cancer cell imaging and photothermal therapy in the near-infrared region by using gold nanorods. J Am Chem Soc 128(6):2115–2120
14. Skrabalak SE, Chen J, Au L, Lu X, Li X, Xia Y (2007) Gold nanocages for biomedical applications. Adv Mater 19(20):3177–3184
15. Loo C, Lin A, Hirsch L, Lee MH, Barton J, Halas N, West J, Drezek R (2004) Nanoshell-enabled photonics-based imaging and therapy of cancer. Technol Cancer Res Treat 3(1):33–40
16. Loo C, Lowery A, Halas N, West J, Drezek R (2005) Immunotargeted nanoshells for integrated cancer imaging and therapy. Nano Lett 5(4):709–711
17. Bernardi RJ, Lowery AR, Thompson PA, Blaney SM, West JL (2008) Immunonanoshells for targeted photothermal ablation in medulloblastoma and glioma: an in vitro evaluation using human cell lines. J Neurooncol 86(2):165–172
18. Gobin AM, Moon JJ, West JL (2008) EphrinA I-targeted nanoshells for photothermal ablation of prostate cancer cells. Int J Nanomed 3(3):351–358
19. Stern JM, Stanfield J, Lotan Y, Park S, Hsieh JT, Cadeddu JA (2007) Efficacy of laser-activated gold nanoshells in ablating prostate cancer cells in vitro. J Endourol/Endourol Soc 21(8):939–943
20. Elghanian R, Storhoff JJ, Mucic RC, Letsinger RL, Mirkin CA (1997) Selective colorimetric detection of polynucleotides based on the distance-dependent optical properties of gold nanoparticles. Science 277(5329):1078–1081
21. Bickford LR, Agollah G, Drezek R, Yu TK (2009) Silica-gold nanoshells as potential intraoperative molecular probes for HER2-overexpression in ex vivo breast tissue using near-infrared reflectance confocal microscopy. Breast cancer research and treatment [Epub ahead of print]
22. Oldenburg SJ, Averitt RD, Westcott SL, Halas NJ (1998) Nanoengineering of optical resonances. Chem Phys Lett 288(2–4):243–247
23. Stober W, Fink A, Bohn E (1968) Controlled growth of monodisperse silica spheres in micron size range. J Colloid Interf Sci 26(1):62–69
24. Bickford L, Sun J, Fu K, Lewinski N, Nammalvar V, Chang J, Drezek R (2008) Enhanced multi-spectral imaging of live breast

cancer cells using immunotargeted gold nanoshells and two-photon excitation microscopy. Nanotechnology 19(31): 315102
25. Park J, Estrada A, Sharp K, Sang K, Schwartz JA, Smith DK, Coleman C, Payne JD, Korgel BA, Dunn AK et al (2008) Two-photon-induced photoluminescence imaging of tumors using near-infrared excited gold nanoshells. Opt Express 16(3):1590–1599
26. Gobin AM, Lee MH, Halas NJ, James WD, Drezek RA, West JL (2007) Near-infrared resonant nanoshells for combined optical imaging and photothermal cancer therapy. Nano Lett 7(7):1929–1934
27. Black KC, Kirkpatrick ND, Troutman TS, Xu L, Vagner J, Gillies RJ, Barton JK, Utzinger U, Romanowski M (2008) Gold nanorods targeted to delta opioid receptor: plasmon-resonant contrast and photothermal agents. Mol Imaging 7(1):50–57
28. Tong L, Zhao Y, Huff TB, Hansen MN, Wei A, Cheng JX (2007) Gold nanorods mediate tumor cell death by compromising membrane integrity. Adv Mater 19:3136–3141
29. Cheong SK, Krishnan S, Cho SH (2009) Modeling of plasmonic heating from individual gold nanoshells for near-infrared laser-induced thermal therapy. Med Phys 36(10):4664–4671
30. de Lange DF, Hofman JT, Meijer J (2005) Influence of intensity distribution on the meltpool and clad shape for laser cladding. In: Third international WLT-conference on lasers in manufacturing: 2005; Munich, Germany
31. Rofstad EK (1990) Heat sensitivity and thermotolerance in vitro of human breast carcinoma, malignant melanoma and squamous cell carcinoma of the head and neck. Br J Cancer 61(1):22–28
32. Hauck TS, Jennings TL, Yatsenko T, Kumaradas JC, Chan WCW (2008) Enhancing the toxicity of cancer chemotherapeutics with gold nanorod hyperthermia. Adv Mater 20(20):3832–3838
33. Diagaradjane P, Shetty A, Wang JC, Elliott AM, Schwartz J, Shentu S, Park HC, Deorukhkar A, Stafford RJ, Cho SH et al (2008) Modulation of in vivo tumor radiation response via gold nanoshell-mediated vascular-focused hyperthermia: characterizing an integrated antihypoxic and localized vascular disrupting targeting strategy. Nano Lett 8(5):1492–1500

Nanoscale Research Letters
a SpringerOpen Journal

NANO EXPRESS Open Access

T cells enhance gold nanoparticle delivery to tumors *in vivo*

Laura C Kennedy[1†], Adham S Bear[2†], Joseph K Young[3], Nastassja A Lewinski[1], Jean Kim[1], Aaron E Foster[2*†] and Rebekah A Drezek[1,3*†]

Abstract

Gold nanoparticle-mediated photothermal therapy (PTT) has shown great potential for the treatment of cancer in mouse studies and is now being evaluated in clinical trials. For this therapy, gold nanoparticles (AuNPs) are injected intravenously and are allowed to accumulate within the tumor via the enhanced permeability and retention (EPR) effect. The tumor is then irradiated with a near infrared laser, whose energy is absorbed by the AuNPs and translated into heat. While reliance on the EPR effect for tumor targeting has proven adequate for vascularized tumors in small animal models, the efficiency and specificity of tumor delivery *in vivo*, particularly in tumors with poor blood supply, has proven challenging. In this study, we examine whether human T cells can be used as cellular delivery vehicles for AuNP transport into tumors. We first demonstrate that T cells can be efficiently loaded with 45 nm gold colloid nanoparticles without affecting viability or function (e.g. migration and cytokine production). Using a human tumor xenograft mouse model, we next demonstrate that AuNP-loaded T cells retain their capacity to migrate to tumor sites *in vivo*. In addition, the efficiency of AuNP delivery to tumors *in vivo* is increased by more than four-fold compared to injection of free PEGylated AuNPs and the use of the T cell delivery system also dramatically alters the overall nanoparticle biodistribution. Thus, the use of T cell chaperones for AuNP delivery could enhance the efficacy of nanoparticle-based therapies and imaging applications by increasing AuNP tumor accumulation.

Introduction

Gold nanoparticles (AuNPs) have been successfully used to enable photothermal therapy (PTT) for the treatment of cancer in small animal studies [1-5], and has recently moved towards clinical application [6]. A variety of AuNPs have been examined for PTT, including silica-gold nanoshells [2], gold nanorods [7], gold nanocages [8], gold-gold sulfide nanoparticles [9], and hollow gold nanoshells [3]. These particles can be engineered to absorb light in the near infrared (NIR) range, where light is maximally transmissive and minimally absorbed by tissue. AuNP delivery can be accomplished by systemic administration (intravenous injection). The nanoparticles, depending on their shape, hydrodynamic size, and surface charge, will accumulate within the tumor via its irregular vasculature; this passive accumulation is known as the enhanced permeability and retention (EPR) effect [10,11]. Polyethylene glycol (PEG)-coated particles with a hydrodynamic diameter of approximately 60 nm have demonstrated the most efficient delivery to the tumor using the EPR effect [11], and more recently, the use of smaller hollow gold [3] and gold-gold sulfide nanoshells [12] (20-40 nm diameter) has further improved nanoparticle half-life in the blood. However, even with these smaller particles, the percentage of the injected dose (ID) delivered to the tumor is low [13,14], and accumulation in non-target sites such as the liver and spleen is comparatively high [13,15]. Thus, new methods aimed at improving tumor delivery and specificity may increase the tumor concentration of gold nanoparticles and ultimately the efficacy of anti-tumor PTT and enhance nanoparticle mediated imaging techniques.

Attempts at augmenting gold nanoparticle tumor delivery have included a variety of nanoparticle surface modifications, including conjugation with antibodies [3]

* Correspondence: aefoster@txccc.org; drezek@rice.edu
† Contributed equally
[1]Department of Bioengineering, Rice University, Houston, TX 77005, USA
[2]Center for Cell and Gene Therapy, Baylor College of Medicine, The Methodist Hospital and Texas Children's Hospital, Houston, TX 77030, USA
Full list of author information is available at the end of the article

and hormone analogs [16]; however, inclusion of targeting ligands has only modestly improved tumor accumulation and specificity. This is likely due to the reliance of these nanoparticles on passive accumulation through EPR, which is highly dependent on adequate blood flow to the tumor. Therefore, tumors or tumor regions that exhibit poor vasculature and hypoxia are less likely to be effectively targeted using nanoparticles, ultimately limiting their therapeutic use. Choi et al. [17] recently demonstrated that macrophages could be used as a cellular delivery vehicle to deposit AuNPs in tumors and hypoxic tumor tissues, facilitating delivery through active cellular migration and extravasation in response to chemotactic factors produced by malignant cells. These encouraging results suggested that other immune cells might be used as cellular delivery vehicles. In this study, we assessed the capacity of activated T cells to function as chaperones for AuNPs. Unlike macrophage, T cells are readily isolated and expanded *in vitro*, and upon infusion, circulate throughout the body and migrate into tumors in response to tumor-associated chemokines. This tumor-tropic property permits their use as cellular vehicles for the delivery of molecular therapeutics [18-21].

Combining the advantages of T cells with nanotechnology has the potential to generate innovative new approaches to cancer therapy. Several studies have demonstrated that T cells may serve as efficient drug delivery vehicles for the treatment of cancer, including transport of magnetic particles bearing doxorubicin and for use in boron neutron capture therapy [22,23]. Here we have explored whether T cells can be used as AuNP carriers to increase delivery to tumor sites *in vivo* using gold colloidal nanospheres (40-45 nm), comparable in size to hollow gold nanoshells and gold-gold sulfide nanoparticles used for PTT. Although gold colloid in this size range has maximal absorbance in the visible wavelengths, there are several variants of AuNPs that are of similar size (25-60 nm) and absorb optimally in the NIR region, permitting translation of this delivery method for PTT. These gold nanoparticle variants include gold-gold sulfide nanoparticles, hollow gold nanoshells, and gold nanocubes, all of which have demonstrated efficacy as PTT-mediating agents in mouse studies [24]. Additionally, there have been studies demonstrating photothermal therapy using gold colloid that has been strategically aggregated to red-shift the peak absorbance into the NIR [25,26]. The possible applications of a AuNP-T cell delivery system could further be extended to imaging and drug delivery applications, as gold nanoparticles also have demonstrated potential as scatter- and absorption-based imaging contrast agents [27-30] and drug delivery agents [31]. In this study, we demonstrate that gold colloid is readily taken up by activated human T cells without impairing their viability or cellular functions, and that following intravenous infusion into tumor bearing micecan more efficiently deliver AuNPs to distant tumor sites.

Results

Loading of activated human T cells with AuNPs

Synthesized gold colloid was determined to be 40-45 nm in diameter by transmission electron microscopy (TEM) (Figure 1a and Figure S1 in Additional file 1). Activated and expanded human T cells were cultured in the presence of AuNPs for a period of 1 to 24 h to permit AuNP internalization. AuNP loading was confirmed using bright field and dark field microscopy demonstrating that T cells co-localize with AuNPs (Figure 1b). We further optimized loading conditions by altering AuNP concentration (per cell) and time of incubation. To determine the number of nanoparticles present per T cell, an inductively coupled plasma optical emission spectrometry (ICP-OES) analysis was used. T cells from three different human donors were first cultured with concentrations of AuNPs ranging from 0.05 to 0.5 nM for a period of 24 h to evaluate for variability in gold nanoparticle loading due to differences in T cells from different donors (Figure 1c). A maximum of 14,900 ± 2,400 AuNPs was internalized per T cell using a AuNP loading concentration of 0.5 nM (Figure 1c). We then performed a time course study using T cells from a single donor to determine the minimum amount of time required to load the T cells with the maximum number of AuNPs (Figure 1d). For this study, we incubated T cells with nanoparticle concentrations ranging from 0.05 to 1 nM. At 24 h, the 0.5 and 1 nM groups have similar gold content, suggesting that there is a maximum amount of AuNPs that can be internalized by T cells. These results demonstrate that maximal AuNP loading of T cells can be achieved using a concentration of 0.5 nM AuNP and an incubation period of 24 h.

AuNP-loading does not affect T cell viability or function

We next measured T cell viability and function post-AuNP loading to assess potential toxicity that may inhibit T cell performance as an *in vivo* delivery vehicle. Loading T cells with AuNPs had no immediate effect on T cell viability as determined by Annexin-V/7-AAD staining (Figure 2a) and did not alter the phenotype of the cells (Figure S2 in Additional file 1). Furthermore, there were no prolonged effects on T cell proliferation as measured by thymidine incorporation (Figure 2b). Importantly, AuNPs did not affect migration when tested in a transwell chemotaxis assay against supernatant produced from human LCL tumors, suggesting that T cells retain their migratory behavior post-AuNP

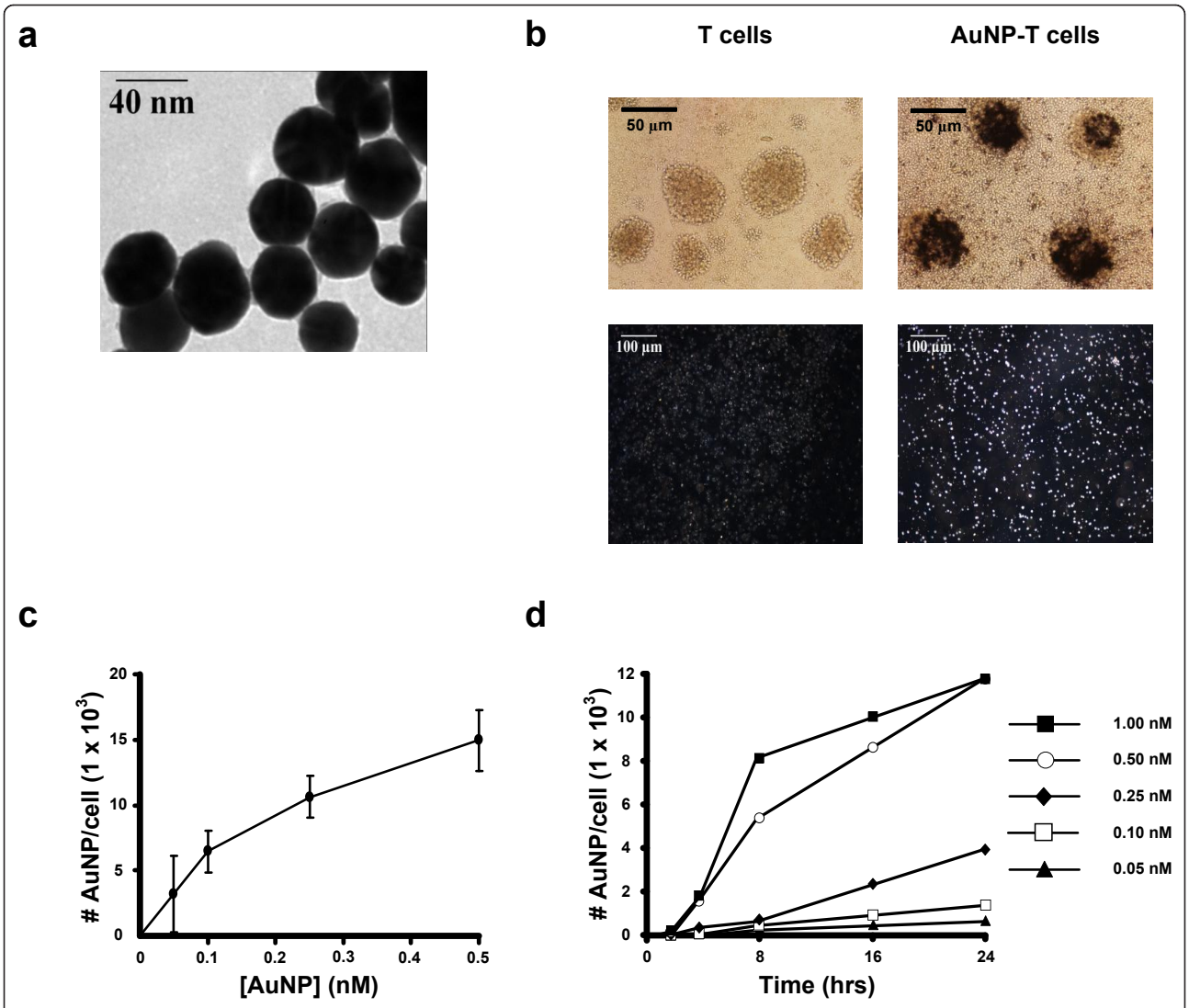

Figure 1 Gold nanoparticle uptake by human T cells. **(A)** TEM imaging of gold colloid (diameter = 40-45 nm). **(B)** Brightfield (upper) and darkfield (lower) images of human T cells demonstrate gold nanoparticle uptake by the increased light scattering seen in the AuNP-T cell group compared to T cells alone. **(C)** ICP-OES analysis of T cell gold content at 24 h using different nanoparticle loading concentrations. Each point is a composite of data acquired from three different T cell donors. **(D)** Time course data for T cells from a single donor loaded with different concentrations of gold nanoparticles. Optimal loading occurred after 24 h at a concentration between 0.5 and 1.0 nM.

loading (Figure 2c). Finally, production of IFN-γ following mitogen activation (PMA-I) was not impaired by AuNPs (Figure 2d). These results show that AuNPs have no detrimental effects on T cell viability and function *in vitro* and indicate that T cell migration *in vivo* will likely be retained following loading.

T cells migrate and transport AuNPs to tumors *in vivo*

In vivo AuNP-T cell migration to tumor sites was first examined using bioluminescent imaging and histology. T cells were first genetically modified to express firefly luciferase and then subsequently loaded with AuNPs. Bioluminescent imaging 48 h post-intravenous injection of AuNP-T cells demonstrate specific migration of the T cells to subcutaneous LCL tumors in immune deficient SCID mice (Figure 3a). This timepoint was selected based on previous studies that have demonstrated T cell localization to tumor sites 48 h post-infusion [32,33]. We next resected the tumors and performed histology to determine if AuNPs and T cells co-localized within the tumor. Immunohistochemical staining using CD3 antibody (a pan-T cell marker) demonstrated infiltration of T cells into the tumor (Figure 3b). In addition, areas of increased scatter in the darkfield images correlated well with areas of $CD3^+$ staining. This observation demonstrates that the T cells maintain internalized AuNPs during *in vivo* migration to the tumor site.

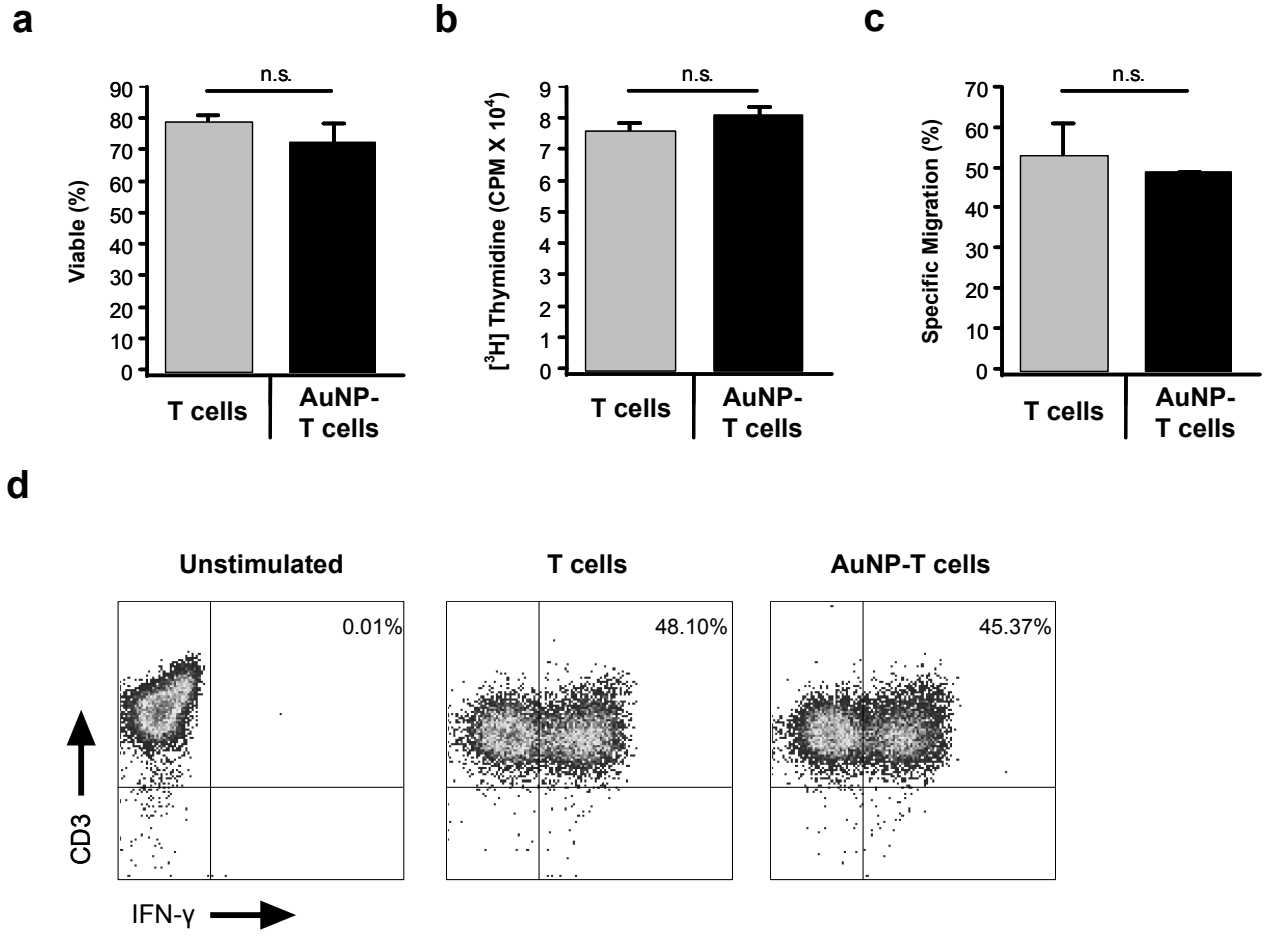

Figure 2 AuNP loading has no significant effect on T cell viability or function. T cells were loaded in the presence of 0.5 nM AuNPs for 24 h or cultured in medium alone and then measured for viability using Annexin-V/PI staining **(A)**, proliferation using thymidine incorporation **(B)**, migration through a transwell membrane in response to tumor (LCL) produced supernatant **(C)** and intracellular analysis of IFN-γ cytokine production following mitogen stimulation **(D)**.

Delivery of AuNPs by T cells alters nanoparticle biodistribution

We next performed a comprehensive *in vivo* biodistribution study using inductively coupled plasma mass spectrometry (ICP-MS) and ICP-OES to map the location of free PEGylated AuNPs (40-45 nm gold colloid coated with 5000 MW PEG) and AuNPs delivered by T cells. Prior to injection, ICP-OES was performed to determine the absolute gold dose for PEG-AuNPs and AuNP-T cells. Following intravenous injection with PEG-AuNPs or AuNP-T cells, tumors, and organs (bone, brain, heart, intestine, kidney, liver, lungs, muscle, plasma, and spleen) were harvested and analyzed for gold levels using ICP-MS. For PEG-AuNP treated mice, organs were harvested at 4, 8, 24, and 48 h post-injection, while for AuNP-T cell treated mice, organs were harvested at 24 and 48 h (Figure 4a). Predictably, the biodistribution of AuNP-T cells is altered when compared to that of the PEG-AuNPs. As observed in previous studies [13,15], the highest percentages of AuNPs using PEG coating were delivered to the liver and spleen (5.65 and 17.03%, respectively, at 48 h, Figure 4b,c). In comparison, T cells delivered AuNPs to the lung, liver, and spleen, which received 4.76, 33.5, and 2.69% at 48 h, respectively (Figure 4b and 4c). The plasma half-life of the PEG-AuNPs was calculated to be 6.05 h, and no gold was detected in the plasma for the AuNP-T cell group, suggesting no significant AuNP leakage from the T cells during *in vivo* migration. The AuNP-T cell biodistribution over time correlates with the normal biodistribution of human T cells, suggesting that the presence of internalized AuNPs does not significantly change the T cell biodistribution [32]. These data suggest that cellular delivery of AuNP will result in a unique biodistribution pattern that is dependent on the cell type used for delivery.

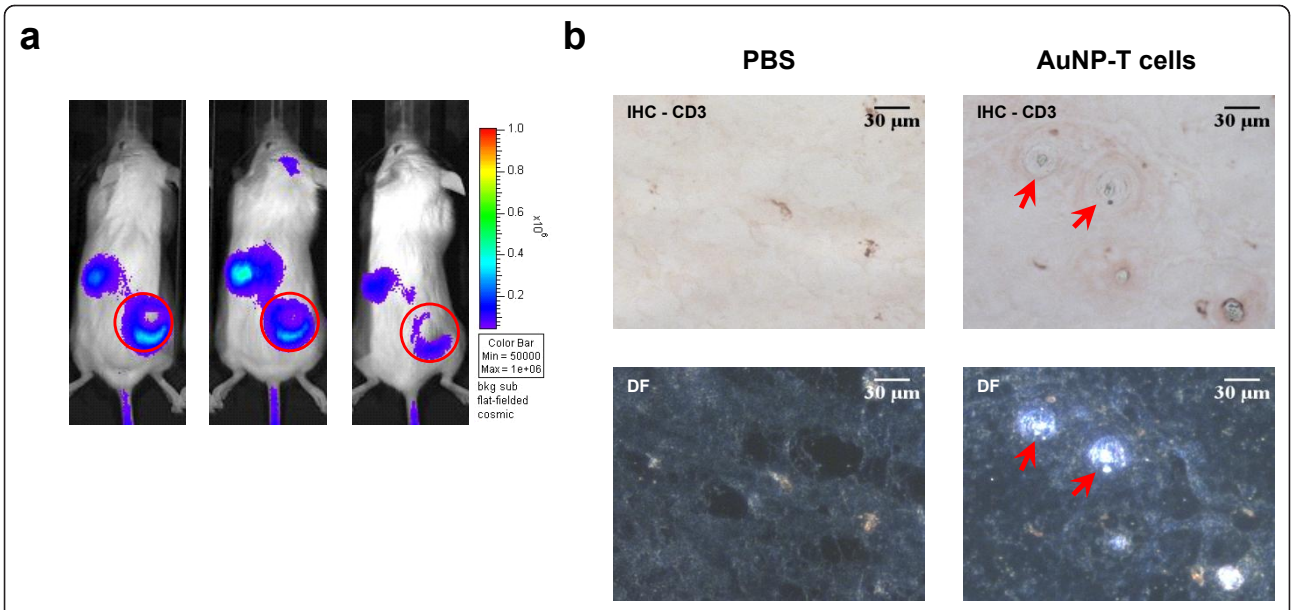

Figure 3 AuNP-loaded T cells migrate to tumors *in vivo*. (A) T cells were retrovirally modified to express firefly luciferase then loaded in the presence of 0.5 nM AuNP for 24 h. Cells were subsequently injected intravenously into SCID mice bearing subcutaneous xenografted LCL tumors. Bioluminescent imaging of AuNP-T cell biodistribution at 48 h post-injection showing AuNP-T cell localization at the tumor site (red circle) and within the spleen. **(B)** Resected tumors were analyzed by bright field imaging (top row) and immunohistochemistry for human CD3 expression and dark field imaging (bottom row) to indicate the presence of AuNPs. Red arrows indicate the colocalization of $CD3^+$ T cells and AuNPs within the tumor.

T cell delivery increases tumor accumulation of AuNPs

Closer examination of LCL tumors following treatment with either PEG-AuNPs or AuNP-T cells showed an increase in AuNP delivery to tumors following cellular transport. For PEG-AuNPs, the highest level of accumulation in tumors was observed at 24 h post-injection, while peak tumor gold accumulation following T cell delivery was seen at 48 h. Using PEG-AuNP, ICP-MS analysis of gold content of excised tumor tissue showed that 0.39 ± 0.33% of ID reached the tumor at 24 h. Whereas, using AuNP-T cells, 1.55 ± 0.72% of the ID localized to the tumor at 48 h ($P < 0.01$) (Figure 5). This represents a four-fold increase in the efficiency of AuNP delivery to the tumor site using T cells as vehicles.

Discussion

One of the greatest challenges of translating nanotechnologies to the clinical realm is optimizing *in vivo* delivery. Maximizing AuNP accumulation at the tumor site has the potential to enhance photothermal cancer therapy, as well as other applications such as optical imaging. In this study, we show that human T cells can be used to transport AuNPs to distant tumor sites following intravenous administration. Following short term incubation with AuNPs, T cells can be efficiently loaded with over 14,000 AuNPs per cell without affecting cell viability, proliferation, and cytokine production. Importantly, T cells loaded with AuNPs retain their ability to migrate *in vitro*, and demonstrate tumor-specific homing in mice. Using T cells as a vehicle to deliver AuNPs resulted in a four-fold increase in the efficiency of AuNP tumor accumulation, demonstrating that active transport of AuNPs by cellular chaperones is superior to that of passive accumulation through the EPR effect.

Stephan et al. [33] recently demonstrated that synthetic drug-carrier nanoparticles could be stably conjugated to the surface of immune cells, including T cells, for delivery of therapeutic molecules. In these studies, T cells efficiently carried surface-tethered nanoparticles to tumors in mice, and when loaded with cytokines to support T cell growth, dramatically increased antitumor efficacy. However, our study conclusively demonstrates *in vivo* that internal loading of AuNPs in T cells can improve tumor localization, and thus may be a useful technology for a variety of nanoparticle based therapies.

In this study, we elect to use AuNPs. AuNPs are known to have low cytotoxicity, and gold has been used in humans for the treatment of arthritis for over 50 years [34], which makes AuNPs a logical choice in the pursuit of clinical applications. For this study, 40-45 nm gold colloidal nanospheres were selected for internalization by activated human T cells. The internalization of nanoparticles by cells is believed to be accomplished predominantly by receptor-mediated endocytosis, and particle size is an important variable in determining the kinetics

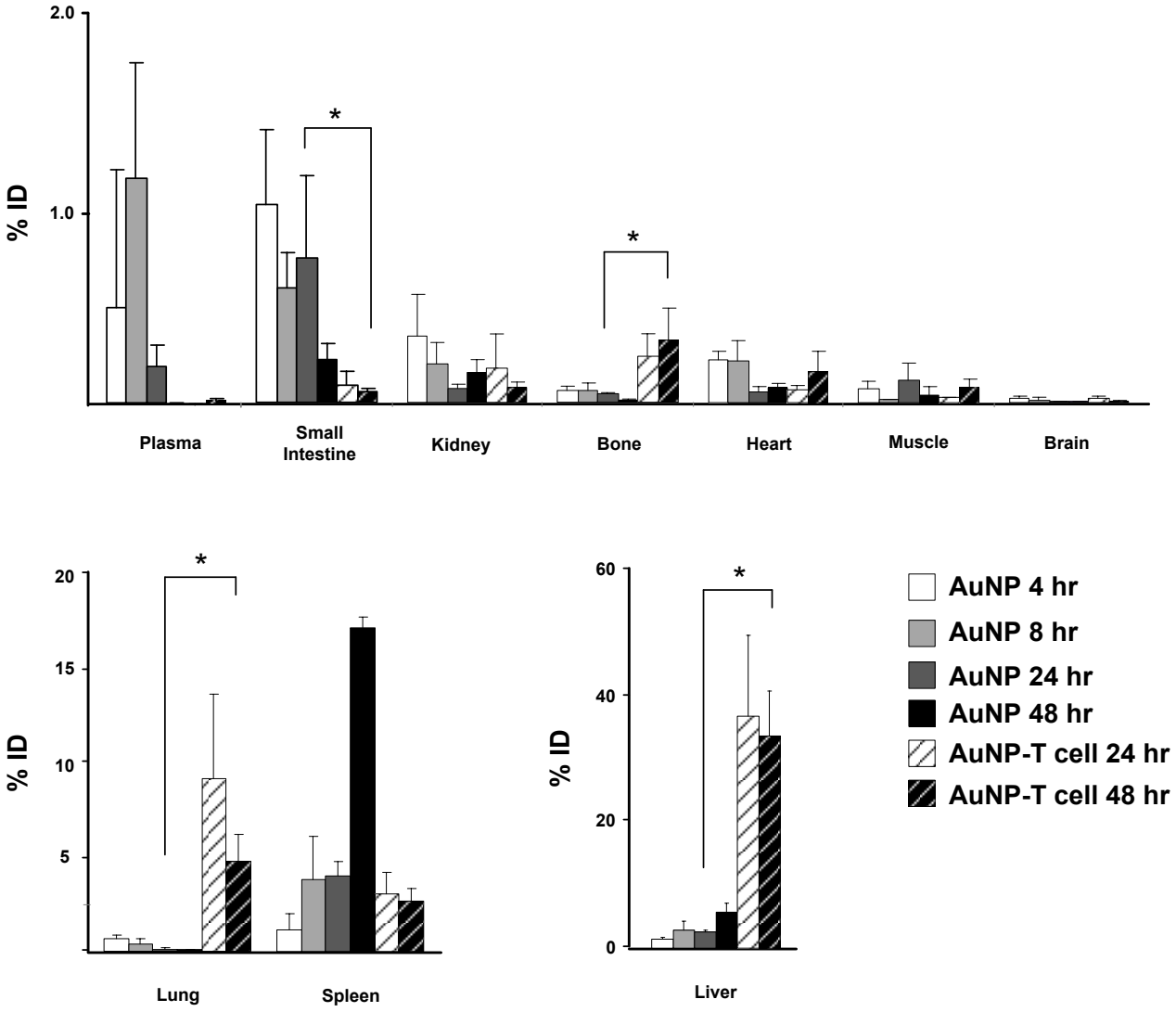

Figure 4 Biodistribution comparison of AuNPs and AuNP-T cells in mice. Mice were injected with PEG-AuNPs (60-65 nm hydrodynamic diameter), AuNP-T cells, or PBS and subsequently sacrificed at various time points to determine biodistribution. PBS gold levels were negligible in comparison to AuNP and AuNP-T cell groups for all organs. Values are percentage of the injected gold dose (%ID) were calculated from ICP-MS and are normalized for dry weight differences. The AuNP-T cell group exhibited significantly higher gold delivery to the lungs, liver, and bone, while the AuNP group demonstrated higher gold levels within the small intestine. No significant differences were seen in the spleen, kidney, muscle, or brain. An asterisk indicates statistically significant ($P < 0.05$) differences.

of cellular uptake, with maximal uptake in a size range of 40-50 nm [35,36]. We selected the size of our AuNPs for this proof-of-concept delivery study to optimize nanoparticle cellular uptake. We modulated the degree of nanoparticle internalization by altering the concentration of nanoparticles incubated with the T cells (Figure 1c). We also evaluated nanoparticle uptake using T cells isolated from three different human donors (Figure 1c) and saw only small variation, suggesting that this technique could be extrapolated to the T cells of any patient.

The internalized gold colloid used in this study also had no detrimental impact on the viability or function of activated human T cells in vitro (Figure 2), and the T cells were able to migrate to tumors *in vivo* while maintaining their AuNP payload (Figure 3). In addition to their ability to carry AuNPs to tumors, T cells can be selected for tumor-specificity for adoptive immunotherapy studies [37-39]. Furthermore, T cells may be genetically engineered to improve their function [40,41] or enhance their ability to migrate to tumors *in vivo* [42,43]. It has been demonstrated that systemically administered AuNPs tend to accumulate mainly in the perivascular regions of the tumor [11], limiting passive accumulation of nanoparticles by the EPR effect to well-

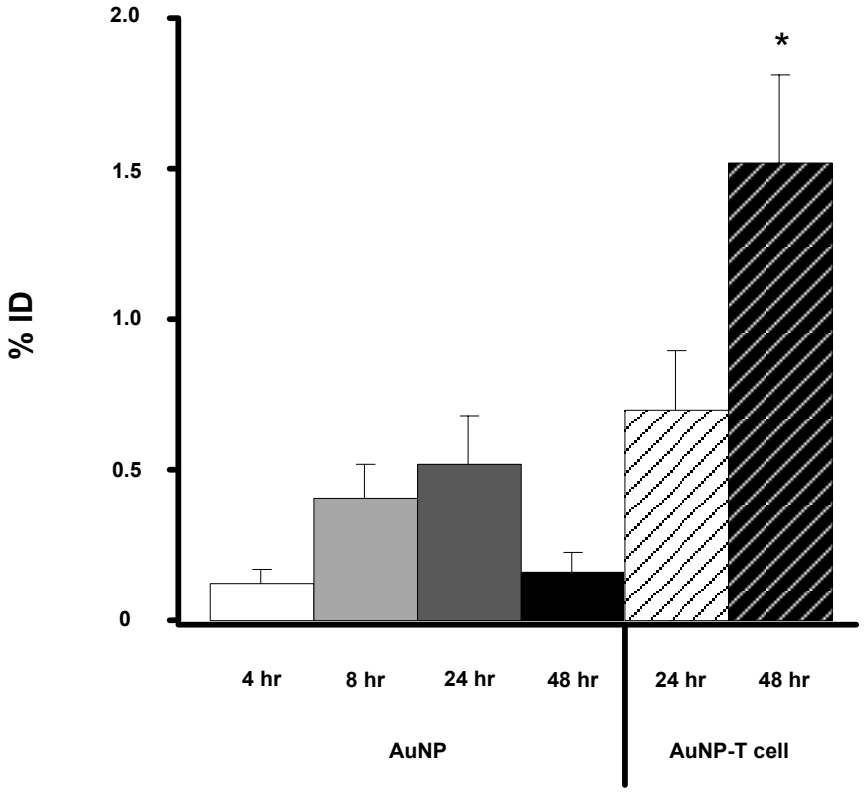

Figure 5 AuNP-T cells enhance the delivery of gold nanoparticles to the tumor site *in vivo*. Tumor-bearing mice were injected i.v. with PEG-AuNPs or AuNP-T cells. Tumors were subsequently resected at various time points and measured for AuNP content using ICP-MS. Values displayed represent the percentage of injected gold normalized for tumor dry weight differences (mean ± SEM). The percentage of gold delivered by the AuNP-T cells at 48 h represents a significant, four-fold increase over the PEG-AuNP group at 24 h ($P < 0.01$).

vascularized regions of the tumor. T cells may naturally localize to tumors, and tumor-specific T cell clones have been demonstrated to penetrate into the hypoxic cores of the tumors *in vivo* [44]. The more extensive infiltration of tumor sites by antigen-specific T cells may permit enhanced penetration of the tumor when compared to freely-injected nanoparticles, potentially augmenting therapeutic efficacy.

The use of T cell vehicles also significantly affects nanoparticle biodistribution (Figure 4). Freely injected nanoparticles (40-45 nm gold colloidal nanospheres coated with 5000 MW PEG) accumulate most significantly in well-vascularized organs such as the liver, spleen, kidney, and gut (Figure 4). Maximal AuNP tumor accumulation for the freely injected PEG-AuNP group is seen at 24 h (Figure 5). After 24 h, increased gold content for the PEG-AuNP group is seen in the spleen, liver, and kidney with a corresponding decrease in gold content within the tumor and other organs, which represents a shift towards AuNP clearance.

AuNP-T cells present a much different biodistribution from the systemically administered nanoparticles that correlates with the expected biodistribution of T cells. After adoptive transfer of AuNP-T cells, a large percentage of the ID is seen within the liver and lungs at 24 h. T cells are known to accumulate within the liver and lungs after administration due to the vascularity and number of adhesion molecules present in these organs [45]. This pattern of T cell migration is consistent with the biodistribution of adoptively transferred T cells seen in previous studies [33,45]. AuNP-T cells are also seen accumulating in the spleen and bone of the mice; these locations are also normal reservoirs of T cells [46]. The large number of AuNP-T cells seen in the liver likely represents apoptotic T cells. This large accumulation is not observed by bioluminescence imaging in Figure 3, and the liver is a known site where apoptotic T cells are entrapped [47]. Tumor accumulation of AuNP-T cells increases from 24 to 48 h as T cells escape from the lungs and migrate to the tumor (Figure 5). The biodistribution of AuNP-T cells matches the expected biodistribution of normal activated T cells, suggesting that AuNP biodistribution can be modulated based on the selection of the cellular vehicle. In the case of T cells, it is possible that the biodistribution may be altered to to further favor tumor accumulation and persistence by

manipulating cell culture conditions [45] or by genetic modification of T cells [43].

Using T cells as cellular vehicles for AuNP delivery, we achieve a four-fold increase in tumor delivery efficiency at 48 h when compared to freely injected PEG-coated AuNPs at 24 h (Figure 5). This represents a significant increase in delivery efficiency ($P < 0.01$, Student's *t*-test) using T cells. These results demonstrate for the first time that T cells can be used to enhance AuNP delivery to a tumor *in vivo*. The use of AuNPs and T cells together combines the photothermal therapy and imaging advantages of AuNPs with the immunotherapy and biodistribution advantages of T cells. Future directions will focus on utilizing the AuNP-T cell system for cancer therapy by modifying the T cells to further enrich AuNP tumor accumulation and enhance anti-tumor effects.

Conclusions

In this study we demonstrate the internalization of AuNPs into activated human T cells for the delivery of nanoparticles *in vivo*. AuNP uptake has no negative impact on T cell viability, proliferation, or immune function, and T cells are able to transport the AuNP payload to tumor sites *in vivo*. Furthermore, the use of T cells as a AuNP vehicle enhances *in vivo* delivery efficiency by four-fold. This delivery method alters the biodistribution of gold compared to freely injected AuNPs, and demonstrates that the selection of a particular cellular vehicle may dictate AuNP biodistribution.

Methods

AuNP synthesis and PEGylation

Gold(III) chloride trihydrate ($HAuCl_4$ $3H_2O$ 99%) and potassium carbonate anhydrous (K_2CO_3 99%) were purchased from Sigma-Aldrich (St. Louis, MO). Deionized water was provided by a Milli-Q system. In this synthesis method, Au^{3+} is reduced to Au^0 using CO as a reducing agent. A 0.38 mM $HAuCl_4$ solution was prepared and aged in an amber bottle at 4°C for a minimum of 72 h prior to use. After aging the chloroauric acid solution, the temperature was allowed to gradually rise to 16°C. A 1.8 mM K_2CO_3 solution was then prepared by adding 75 mg of K_2CO_3 to the aged 200 mL $HAuCl_4$ solution. This solution was aged for 30 min prior to aeration with CO gas. A 40 mL volume of the aged solution was added to the beaker and stirred continuously prior to aeration. CO gas (Matheson-Trigas) was injected into the continuously stirring solution at a flow rate of 30.5 mL/min. The CO flow was controlled via a flow rate control valve. A visible color change from clear to dark purple to red is observed during synthesis, indicating formation of AuNPs. TEM images were taken to confirm size and monodispersity. Particles were sterilized by filtration through a 0.22 μm polyethersulfone filter. To stabilize the particles in preparation for mouse injection, 0.5 mM polyethylene glycol-thiol (PEG-SH, MW = 5 kD, Nektar) was added to the particles. After a 24-h incubation, excess PEG-SH was removed by centrifugation and PEGylated particle stability was confirmed by increasing solution tonicity with 1 M NaCl. Dynamic light scattering measurements were taken to assess the hydrodynamic diameter of the PEGylated gold colloid.

T cell isolation and preparation

Peripheral blood was obtained with informed consent from willing healthy donors using a Baylor College of Medicine Institutional Review Board approved protocol. Peripheral blood mononuclear cells (PBMC) were isolated by Ficoll gradient centrifugation (Lymphoprep, Nycomed, Oslow, Norway). PBMC were used to generate EBV-transformed B cells lines (LCL) and T cell lines. LCL and T cells were maintained in RPMI 1640 supplemented with 10% fetal calf serum (FCS; Hyclone, Logan, UT) and 2 mM GlutaMAX (Invitrogen, Carlsbad, CA). For T cell expansion, non-tissue culture treated 24-well plates were coated with OKT3 (1 μg/mL; Ortho Pharmaceuticals, Raritan, NJ) and anti-CD28 antibody (1 μg/mL; BD Biosciences, San Diego, CA) overnight at 4° C. Plates were washed and 2×10^6 PBMC were plated per well in complete RPMI supplemented with 100 U/mL recombinant human interleukin-2 (IL-2). On day 3, T cell blasts were harvested and further expanded or transduced in IL-2 supplemented media.

T cell internalization of AuNPs

Day 7 OKT3 blasts were harvested and suspended in complete RPMI supplemented with IL-2 and 0, 0.05, 0.1, 0.25, 0.5, or 1 nM of AuNPs for 24 h (1 mole = 6.022×10^{23} nanoparticles). Cells were harvested and washed a minimum of three times using 1 × phosphate-buffered saline (PBS) prior to subsequent experiments. To confirm loading, T cells were imaged using darkfield microscopy. To quantitatively characterize loading, 2×10^6 T cells per sample were prepared for ICP-OES analysis by digesting the cells in three parts trace metal grade hydrochloric acid (Fisher Scientific, Pittsburgh, PA) and one part trace metal grade nitric acid (EMD Chemicals, Gibbstown, NJ) overnight. Samples were then diluted to 10 mL in distilled water and filtered. T cells incubated with media alone were used as a control.

T cell viability and functionality after AuNP loading

To determine the effect of AuNP loading on T cell phenotype, we used the following monoclonal antibodies conjugated to FITC, PE, PerCP, or APC (BD Biosciences): CD3, CD4, CD8, CD45RA, CD45RO, CD56,

CD62L, CCR5, and CCR7. An Annexin V apoptosis detection kit (BD Biosciences) was used to determine T cell viability post-AuNP loading. Cells were analyzed using a FACSCalibur flow cytometer (BD Biosciences) and FCSExpress software (De Novo Software, Los Angeles, CA). A [^{3}H] thymidine incorporation assay was used to assess the effects of AuNP loading on T cell proliferation. Following AuNP loading, T cells were seeded in triplicate into 96-well round bottom plates at 1×10^5 cells per well in complete RPMI containing 100 U/mL IL-2 for 24 h. T cells were then pulsed with 5 μCi [^{3}H] thymidine (Amersham Pharmacia Biotech, Piscataway, NJ) overnight. Cells were then harvested onto glass filter strips and analyzed using a TriCarb 2500 RT β-counter (Packard Biosciences, Downers Grove, IL). To determine if AuNP-loaded T cells retain the ability to migrate *in vitro*, we used a transwell migration assay. T cells were labeled with 50 μCi Chromium^{51} (Cr^{51}; MP Biomedicals, Solon, OH) and 1.5×10^5 cells were placed in the upper chamber of 24-well 6.5 mm diameter, 5 μm pore size transwell chambers (Costar Transwell, Corning, NY). Media alone or LCL tumor supernatant was placed in the bottom chamber. Plates were then incubated for 3 h at 37°C. Cells in the bottom chamber were then harvested and analyzed using a γ-counter (Cobra Quantum, Perkin Elmer, Shelton, CT). Specific migration was calculated using the following equation: Specific Migration (%) = (Experimental [LCL supernatant] - Spontaneous [media alone])/(Maximum [1.5×10^5 cells] - Spontaneous [media alone]) × 100. To measure the ability of AuNP-loaded T cells to secrete IFN-γ following mitogenic stimulation, 2×10^5 T cells were seeded into 96-well round bottom plates for 24 h. T cells were then stimulated with 25 ng/mL phorbol myristate acetate (PMA; Sigma-Aldrich, St. Louis, MO) and 1 μg/mL Ionomycin (I; Sigma-Aldrich). Following 2 h of PMA-I stimulation, Brefeldin A (Sigma) was added to allow for intracellular cytokine retention. Four hours later, cells were permeabilized using 1% Saponin (Sigma) and IFN-γ expression was detected by intracellular cytokine staining using PE-conjugated anti-IFN-γ monoclonal antibody (BD Biosciences).

In vivo delivery studies

SCID xenograft model

In vivo migration, AuNP delivery, and biodistribution studies were performed using severe combined immune deficient mice (SCID [strain ICR-Prkdc(scid)]; Taconic, Hudson, NY). All mouse experiments were performed under a Baylor College of Medicine Institutional Animal Care and Use Committee (IACUC) approved protocol. 1×10^7 LCL tumor cells were resuspended in Matrigel (BD Biosciences) and injected subcutaneously (s.c.) into the shaved right flanks of mice. Tumors were allowed to establish and grow to at least 0.5 mm × 0.5 mm in size (2-3 weeks) before use.

Mouse injections and sample collection

To prepare AuNP-T cell injections, T cells were prepared as above and incubated with 0.5 nM AuNPs for 24 h. Cells were harvested and washed extensively using 1 × PBS prior to injection. For delivery studies, mice received either PBS, 1×10^7 AuNP-T cells, or 1×10^{11} PEGylated AuNPs via the tail vein in a 200 μL bolus. These dosages were selected based on previous *in vivo* studies using AuNPs and adoptively transferred T cells. To determine optimal time points for delivery analysis, tumors were resected at either 4, 8, 24, or 48 h for the PEGylated AuNP group and 24 or 48 h for the AuNP-T cell group. In addition, plasma as well as portions of the liver, spleen, kidneys, small intestine, muscle, heart, lung, bone, and brain were also collected for analysis at 4, 8, or 24 h for the PEGylated AuNP group and 24 or 48 h for the AuNP-T cell group. All tissues, including tumors, were flash frozen with liquid nitrogen after collection and stored at -80°C until analysis.

Bioluminescent imaging

To determine if AuNP-loaded T cells can migrate to tumors *in vivo* and thereby deliver AuNP to the tumor site, T cells were transduced with retrovirus encoding GFP*luc* as previously described by our group [48]. Transduced cells were then loaded with AuNPs for 24 h then injected intravenously (i.v.) via the tail vein (1×10^7 T cells per mouse). Forty-eight hours post-T cell infusion, the biodistribution of T cells was visualized using the *In Vivo* Imaging System (IVIS; Xenogen) following intraperitoneal (i.p.) injection of 150 mg/kg D-luciferin (Xenogen, Alameda, CA).

Ex vivo tissue analysis and imaging

To image AuNP-T cells within the tumor, tumors were thawed in a 37°C water bath and embedded in optimal cutting temperature (O.C.T.) compound (Sakura Finetek USA, Inc., Torrence, CA) using dry ice. The embedded tissue was then sectioned into 8 μm slices using a cryostat, dried overnight at room temperature, and stored at -80°C. Tissue sections were then fixed with acetone and stained for CD3 using anti-CD3 (Abcam ab5690, Cambridge, MA) as the primary antibody and the Invitrogen Histostain® Plus Broad Spectrum (AEC) kit. Slides were coverslipped with immunomount (Thermo Scientific, Pittsburgh, PA) and imaged by bright field and dark field microscopy. Resected mouse tissues were prepared and analyzed for gold content using ICP-MS and ICP-OES. Samples were lyophilized and weighed, then digested and prepared as previously described. Samples of the AuNP-T cell and AuNP boluses were also analyzed to confirm the amount of gold systemically administered.

Statistical methods

For the biodistribution analysis, we performed a one-way ANOVA followed by Tukey's method. Each organ was examined individually at various time points for each treatment group (n = 3 for all time points and treatment groups). Significance was set at $P < 0.05$. An asterisk indicates significant differences between every possible AuNP:AuNP-T cell comparison pair at all time points for each organ. For the tumor delivery analysis, we used a Student's t-test to compare AuNP systemic administration to AuNP-T cell delivery. For this study, n = 8 for the AuNP group, while n = 11 for the AuNP-T cell group.

Additional material

Additional file 1: Figure S1 Gold colloid size distribution. Particle sizes were determined using TEM. A total of 585 particles were examined over multiple images to generate the histogram. **Figure S2 AuNP-loading does not affect T cell phenotype**. T cells were loaded in the presence of 0.5 nM AuNP for 24 h and subsequently stained with a panel of antibodies and analyzed by flow cytometry.

Abbreviations

AuNPs: gold nanoparticles; EPR: enhanced permeability and retention; FCS: fetal calf serum; ICP-MS: inductively coupled plasma mass spectrometry; ICP-OES: inductively coupled plasma optical emission spectrometry; ID: injected dose; i.p., intraperitoneal; i.v., intravenous; NIR: near infrared; O.C.T.: optimal cutting temperature; PBMC: peripheral blood mononuclear cells; PMA: phorbol myristate acetate; PBS: phosphate-buffered saline; PTT: photothermal therapy; PEG: polyethylene glycol; s.c., subcutaneous; TEM: transmission electron microscopy.

Acknowledgements

We thank Dr. Hao Liu for his statistical expertise. We also gratefully acknowledge the John Dunn Foundation, the Cancer Prevention Research Institute of Texas (CPRIT), the Alliance for NanoHealth, the Medical Scientist Training Program at Baylor College of Medicine, and the McNair Foundation for funding and training support.

Author details

[1]Department of Bioengineering, Rice University, Houston, TX 77005, USA
[2]Center for Cell and Gene Therapy, Baylor College of Medicine, The Methodist Hospital and Texas Children's Hospital, Houston, TX 77030, USA
[3]Department of Electrical and Computer Engineering, Rice University, Houston, TX 77005, USA

Authors' contributions

LK and AB performed the *in vitro* and *in vivo* characterizations of the AuNPs, the mouse studies, the tumor histology, the ICP-MS and ICP-OES analyses, and drafted the manuscript. JY synthesized and characterized the AuNPs. NL assisted with the ICP-OES and ICP-MS analyses. JK assisted with the tumor histology and ICP-MS and ICP-OES analyses. AF and RD participated in the design and coordination of the study, as well as assisted in the drafting of the manuscript.

Competing interests

The authors declare that they have no competing interests.

Received: 4 January 2011 Accepted: 4 April 2011 Published: 4 April 2011

References

1. Dickerson EB, Dreaden EC, Huang X, El-Sayed IH, Chu H, Pushpanketh S, McDonald JF, El-Sayed MA: **Gold nanorod assisted near-infrared plasmonic photothermal therapy (PPTT) of squamous cell carcinoma in mice.** *Cancer Lett* 2008, **269**:57-66.
2. Hirsch LR, Stafford RJ, Bankson JA, Sershen SR, Rivera B, Price RE, Hazle JD, Halas NJ, West JL: **Nanoshell-mediated near-infrared thermal therapy of tumors under magnetic resonance guidance.** *Proc Natl Acad Sci USA* 2003, **100**:13549-13554.
3. Melancon MP, Lu W, Yang Z, Zhang R, Cheng Z, Elliot AM, Stafford J, Olson T, Zhang JZ, Li C: **In vitro and in vivo targeting of hollow gold nanoshells directed at epidermal growth factor receptor for photothermal ablation therapy.** *Mol Cancer Therap* 2008, **7**:1730-1739.
4. O'Neal DP, Hirsch LR, Halas NJ, Payne JD, West JL: **Photo-thermal tumor ablation in mice using near infrared-absorbing nanoparticles.** *Cancer Lett* 2004, **209**:171-176.
5. Schwartz JA, Shetty AM, Price RE, Stafford RJ, Wang JC, Uthamanthil RK, Pham K, McNichols RJ, Coleman CL, Payne JD: **Feasibility study of particle-assisted laser ablation of brain tumors in orthotopic canine model.** *Cancer Res* 2009, **69**:1659-1667.
6. **Nanospectra.** [http://www.nanospectra.com/index.html].
7. Tong L, Zhao Y, Huff TB, Hansen MN, Wei A, Cheng JX: **Gold Nanorods Mediate Tumor Cell Death by Compromising Membrane Integrity.** *Adv Mater* 2007, **19**:3136-3141.
8. Chen J, Wang D, Xi J, Au L, Siekkinen A, Warsen A, Li ZY, Zhang H, Xia Y, Li X: **Immuno gold nanocages with tailored optical properties for targeted photothermal destruction of cancer cells.** *Nano Lett* 2007, **7**:1318-1322.
9. Cole JR, Mirin NA, Knight MW, Goodrich GP, Halas NJ: **Photothermal efficiencies of nanoshells and nanorods for clinical therapeutic applications.** *J Phys Chem C* 2009, **113**:12090-12094.
10. Jain RK: **Transport of molecules, particles, and cells in solid tumors.** *Annu Rev Biomed Eng* 1999, **1**:241-263.
11. Perrault SD, Walkey C, Jennings T, Fischer HC, Chan WC: **Mediating tumor targeting efficiency of nanoparticles through design.** *Nano Lett* 2009, **9**:1909-1915.
12. Gobin AM, Watkins EM, Quevedo E, Colvin VL, West JL: **Near-infrared-resonant gold/gold sulfide nanoparticles as a photothermal cancer therapeutic agent.** *Small* 2010, **6**:745-752.
13. James W, Hirsch L, West J, O'Neal P, Payne J: **Application of INAA to the build-up and clearance of gold nanoshells in clinical studies in mice.** *J Radioanal Nucl Chem* 2007, **271**:455-459.
14. von Maltzahn G, Park JH, Agrawal A, Bandaru NK, Das SK, Sailor MJ, Bhatia SN: **Computationally guided photothermal tumor therapy using long-circulating gold nanorod antennas.** *Cancer Res* 2009, **69**:3892-3900.
15. Niidome T, Yamagata M, Okamoto Y, Akiyama Y, Takahashi H, Kawano T, Katayama Y, Niidome Y: **PEG-modified gold nanorods with a stealth character for in vivo applications.** *J Control Release* 2006, **114**:343-347.
16. Lu W, Xiong C, Zhang G, Huang Q, Zhang R, Zhang JZ, Li C: **Targeted photothermal ablation of murine melanomas with melanocyte-stimulating hormone analog-conjugated hollow gold nanospheres.** *Clin Cancer Res* 2009, **15**:876-886.
17. Choi MR, Stanton-Maxey KJ, Stanley JK, Levin CS, Bardhan R, Akin D, Badve S, Sturgis J, Robinson JP, Bashir R, *et al*: **A cellular Trojan Horse for delivery of therapeutic nanoparticles into tumors.** *Nano Lett* 2007, **7**:3759-3765.
18. Cole C, Qiao J, Kottke T, Diaz RM, Ahmed A, Sanchez-Perez L, Brunn G, Thompson J, Chester J, Vile RG: **Tumor-targeted, systemic delivery of therapeutic viral vectors using hitchhiking on antigen-specific T cells.** *Nature Med* 2005, **11**:1073-1081.
19. Harrington K, Alvarez-Vallina L, Crittenden M, Gough M, Chong H, Diaz RM, Vassaux G, Lemoine N, Vile R: **Cells as vehicles for cancer gene therapy: the missing link between targeted vectors and systemic delivery?** *Human Gene Ther* 2002, **13**:1263-1280.
20. Qiao J, Kottke T, Willmon C, Galivo F, Wongthida P, Diaz RM, Thompson J, Ryno P, Barber GN, Chester J, Selby P, Harrington K, Melcher A, Vile RG: **Purging metastases in lymphoid organs using a combination of antigen-nonspecific adoptive T cell therapy, oncolytic virotherapy and immunotherapy.** *Nat Med* 2008, **14**:37-44.
21. Yotnda P, Savoldo B, Charlet-Berguerand N, Rooney C, Brenner M: **Targeted delivery of adenoviral vectors by cytotoxic T cells.** *Blood* 2004, **104**:2272-2280.
22. Mortensen MW, Kahns L, Hansen T, Sorensen PG, Bjorkdahl O, Jensen MR, Gundersen HJ, Bjornholm T: **Next generation adoptive immunotherapy–**

human T cells as carriers of therapeutic nanoparticles. *J Nanosci Nanotechnol* 2007, **7**:4575-4580.
23. Steinfeld U, Pauli C, Kaltz N, Bergemann C, Lee HH: **T lymphocytes as potential therapeutic drug carrier for cancer treatment.** *Int J Pharm* 2006, **311**:229-236.
24. Kennedy LC, Bickford LR, Lewinski NA, Coughlin AJ, Hu Y, Day ES, West JL, Drezek RA: **A New Era for Cancer Treatment: Gold-Nanoparticle-Mediated Thermal Therapies.** *Small* 2011, **7**:169-183.
25. Huang X, Qian W, El-Sayed IH, El-Sayed MA: **The potential use of the enhanced nonlinear properties of gold nanospheres in photothermal cancer therapy.** *Lasers Surg Med* 2007, **39**:747-753.
26. Zharov VP, Galitovskaya EN, Johnson C, Kelly T: **Synergistic enhancement of selective nanophotothermolysis with gold nanoclusters: potential for cancer therapy.** *Lasers Surg Med* 2005, **37**:219-226.
27. Gobin AM, Lee MH, Halas NJ, James WD, Drezek RA, West JL: **Near-infrared resonant nanoshells for combined optical imaging and photothermal cancer therapy.** *Nano Lett* 2007, **7**:1929-1934.
28. Huang X, El-Sayed IH, Qian W, El-Sayed MA: **Cancer cell imaging and photothermal therapy in the near-infrared region by using gold nanorods.** *J Am Chem Soc* 2006, **128**:2115-2120.
29. Park J, Estrada A, Sharp K, Sang K, Schwartz JA, Smith DK, Coleman C, Payne JD, Korgel BA, Dunn AK, Tunnell JW: **Two-photon-induced photoluminescence imaging of tumors using near-infrared excited gold nanoshells.** *Opt Exp* 2008, **16**:1590-1599.
30. Sokolov K, Follen M, Aaron J, Pavlova I, Malpica A, Lotan R, Richards-Kortum R: **Real-time vital optical imaging of precancer using anti-epidermal growth factor receptor antibodies conjugated to gold nanoparticles.** *Cancer Res* 2003, **63**:1999-2004.
31. Han G, Ghosh P, Rotello VM: **Functionalized gold nanoparticles for drug delivery.** *Nanomedicine* 2007, **2**:113-123.
32. Foster AE, Dotti G, Lu A, Khalil M, Brenner MK, Heslop HE, Rooney CM, Bollard CM: **Antitumor activity of EBV-specific T lymphocytes transduced with a dominant negative TGF-beta receptor.** *J Immunother* 2008, **31**:500-505.
33. Stephan MT, Moon JJ, Um SH, Bershteyn A, Irvine DJ: **Therapeutic cell engineering with surface-conjugated synthetic nanoparticles.** *Nat Med* 2010, **16**:1035-1041.
34. Lewinski N, Colvin V, Drezek R: **Cytotoxicity of nanoparticles.** *Small* 2008, **4**:26-49.
35. Chithrani BD, Ghazani AA, Chan WCW: **Determining the size and shape dependence of gold nanoparticle uptake into mammalian cells.** *Nano Lett* 2006, **6**:662-668.
36. Jiang W, Kim BY, Rutka JT, Chan WC: **Nanoparticle-mediated cellular response is size-dependent.** *Nature Nanotechnol* 2008, **3**:145-150.
37. Bollard CM, Aguilar L, Straathof KC, Gahn B, Huls MH, Rousseau A, Sixbey J, Gresik MV, Carrum G, Hudson M, Dilloo D, Gee A, Brenner MK, Rooney CM, Heslop HE: **Cytotoxic T lymphocyte therapy for Epstein-Barr virus+ Hodgkin's disease.** *J Exp Med* 2004, **200**:1623-1633.
38. Dudley ME, Wunderlich JR, Robbins PF, Yang JC, Hwu P, Schwartzentruber DJ, Topalian SL, Sherry R, Restifo NP, Hubicki AM, Robinson MR, Raffeld M, Duray P, Seipp CA, Rogers-Freezer L, Morton KE, Mavroukakis SA, White DE, Rosenberg SA: **Cancer regression and autoimmunity in patients after clonal repopulation with antitumor lymphocytes.** *Science* 2002, **298**:850-854.
39. Rooney CM, Smith CA, Ng CY, Loftin SK, Sixbey JW, Gan Y, Srivastava DK, Bowman LC, Krance RA, Brenner MK, Heslop HE: **Infusion of cytotoxic T cells for the prevention and treatment of Epstein-Barr virus-induced lymphoma in allogeneic transplant recipients.** *Blood* 1998, **92**:1549-1555.
40. Leen AM, Rooney CM, Foster AE: **Improving T cell therapy for cancer.** *Annu Rev Immunol* 2007, **25**:243-265.
41. Pule MA, Savoldo B, Myers GD, Rossig C, Russell HV, Dotti G, Huls MH, Liu E, Gee AP, Mei Z, Yvon E, Weiss HL, Liu H, Rooney CM, Heslop HE, Brenner MK: **Virus-specific T cells engineered to coexpress tumor-specific receptors: persistence and antitumor activity in individuals with neuroblastoma.** *Nat Med* 2008, **14**:1264-1270.
42. Craddock JA, Lu A, Bear A, Pule M, Brenner MK, Rooney CM, Foster AE: **Enhanced tumor trafficking of GD2 chimeric antigen receptor T cells by expression of the chemokine receptor CCR2b.** *J Immunother* 2010, **33**:780-788.
43. Di Stasi A, De Angelis B, Rooney CM, Zhang L, Mahendravada A, Foster AE, Heslop HE, Brenner MK, Dotti G, Savoldo B: **T lymphocytes coexpressing CCR4 and a chimeric antigen receptor targeting CD30 have improved homing and antitumor activity in a Hodgkin tumor model.** *Blood* 2009, **113**:6392-6402.
44. Boissonnas A, Fetler L, Zeelenberg IS, Hugues S, Amigorena S: **In vivo imaging of cytotoxic T cell infiltration and elimination of a solid tumor.** *J Exp Med* 2007, **204**:345-356.
45. Kolen S, Dolstra H, van de Locht L, Braakman E, Schattenberg A, de Witte T, van de Wiel-van Kemenade E: **Biodistribution and retention time of retrovirally labeled T lymphocytes in mice is strongly influenced by the culture period before infusion.** *J Immunother* 2002, **25**:385-395.
46. Beck BH, Kim HG, Kim H, Samuel S, Liu Z, Shrestha R, Haines H, Zinn K, Lopez RD: **Adoptively transferred ex vivo expanded gammadelta-T cells mediate in vivo antitumor activity in preclinical mouse models of breast cancer.** *Breast Cancer Res Treat* 2010, **122**:135-144.
47. Crispe IN, Dao T, Klugewitz K, Mehal WZ, Metz DP: **The liver as a site of T-cell apoptosis: graveyard, or killing field?** *Immunol Rev* 2000, **174**:47-62.
48. Vera J, Savoldo B, Vigouroux S, Biagi E, Pule M, Rossig C, Wu J, Heslop HE, Rooney CM, Brenner MK, Dotti G: **T lymphocytes redirected against the kappa light chain of human immunoglobulin efficiently kill mature B lymphocyte-derived malignant cells.** *Blood* 2006, **108**:3890-3897.

doi:10.1186/1556-276X-6-283
Cite this article as: Kennedy *et al.*: T cells enhance gold nanoparticle delivery to tumors *in vivo*. *Nanoscale Research Letters* 2011 **6**:283.

Nanoscale Research Letters
a SpringerOpen Journal

NANO EXPRESS Open Access

Size-controlled synthesis of monodispersed gold nanoparticles via carbon monoxide gas reduction

Joseph K Young[1], Nastassja A Lewinski[2†], Robert J Langsner[2†], Laura C Kennedy[2], Arthi Satyanarayan[3], Vengadesan Nammalvar[2], Adam Y Lin[2] and Rebekah A Drezek[1,2*]

Abstract

An in depth analysis of gold nanoparticle (AuNP) synthesis and size tuning, utilizing carbon monoxide (CO) gas as a reducing agent, is presented for the first time. The sizes of the AuNPs are tunable from ~4 to 100 nm by altering the concentration of $HAuCl_4$ and inlet CO gas-injection flow rate. It is also found that speciation of aqueous $HAuCl_4$, prior to reduction, influences the size, morphology, and properties of AuNPs when reduced with CO gas. Ensemble extinction spectra and TEM images provide clear evidence that CO reduction offers a high level of monodispersity with standard deviations as low as 3%. Upon synthesis, no excess reducing agent remains in solution eliminating the need for purification. The time necessary to synthesize AuNPs, using CO, is less than 2 min.

Background

Metallic nanoparticles have attracted substantial attention due to their distinctive properties and various applications. AuNPs can exhibit a strong optical response to the extinction of surface plasmons by an alternating electromagnetic field [1]. By simply adjusting the size of the gold nanoparticles, this optical resonance can be positioned over hundreds of nanometers in wavelength across the visible into the near infrared spectrum [1,2]. Since these oscillations are located on the boundary of the metal and the external medium, these waves are very sensitive to changes in this boundary, such as the absorption of molecules to the metal surface [3]. These features render AuNPs useful as building blocks, and pave the way for fabricating biological labels, biological sensors, environmental detection of biological reagents, and clinical diagnostic technologies [4-6]. Many researchers have also exploited the unique optical properties of AuNPs for biomedical applications, such as thermal ablative cancer therapy and gene therapy [7-9].

Since the plasmon-derived optical resonance of gold nanoparticles is strongly related to the dimensions and morphology of the nanoparticles, the ability to synthesize monodispersed AuNPs is essential. The most popular and reliable method of producing AuNPs is an aqueous phase synthesis, which relies on the reduction of tetrachloroauric acid in the presence of a reducing agent to form colloid [10-15]. A number of different reducing agents can be used for the tetrachloroauric acid reduction. These agents have a significant influence on the morphology of the final product, and most of them lead to polydispersed nanoparticle solutions. To date, only a few methods have been established to synthesize AuNPs from about one nanometer to several hundred nanometers in diameter. A widely used method is based on the reduction of tetrachloroaurate ions in water using sodium citrate as a reductant to obtain AuNPs with diameters ranging from 16 to 147 nm [2,16,17]. While this method has demonstrated good quality control over particle size, a high level of monodispersity is limited to the synthesis of larger particles typically in the range of 22 to 120 nm. Another disadvantage to this synthesis method is that excess citrate remains in the solution. The residual citrate, which acts as a passivation layer on the surface of the nanoparticles, can reduce the effectiveness of surface functionalization with other biological markers [18].

Smaller-sized AuNPs, 1 to 5 nm, are usually prepared by borohydride reduction in the presence of thiol capping agents [19]. Disadvantages of this method include the use of toxic organic solvents and the potential presence of impurities introduced by using capping agents, which can also hinder the surface modification and functionality of particles for particular applications [20]. Also, AuNPs have been synthesized using formaldehyde as a reducing

* Correspondence: drezek@rice.edu
† Contributed equally
[1]Department of Electrical and Computer Engineering, Rice University, MS-366, 6100 Main St., Houston, TX 77005, USA
Full list of author information is available at the end of the article

agent. One disadvantage is that formaldehyde is toxic, and the excess formaldehyde in the solution leads to solution instability and eventual particle aggregation [13].

Non-chemical based reduction methods, to synthesize AuNPs, have also been employed. Size-selected AuNPs have been synthesized by use of laser irradiation in a surfactant based aqueous environment [21]. Yet this method limits AuNPs sizes to sub 10 nm diameters. Meunier et al. were able to synthesize gold nanoparticles from 3 to ~80 nm via a femtosecond laser-assisted method [22]. An involved multi-step process, including a seeding step, was necessary to produce the larger particles. This process requires a complicated femtosecond laser setup and nanoparticle synthesis was also dependent on polymer utilization. Dispersed AuNPs were also synthesized using glow discharge plasma [23-26]. Researchers showed that this method can produce particles in less than 5 min yet these particles were limited to ~4 nm diameters [26]. Takai et al. used discharge plasma to produce larger AuNPs of irregular shapes [24]. Polydispersed spherical AuNPs, ~20 nm in diameter, were only produced after exposure times greater than 45 min.

As compared to the current synthesis methods, CO has an advantage in that no excess reducing agent remains in solution. This eliminates the need for purification via multiple centrifugation steps. The reduction of $HAuCl_4$ with CO can also take place at room temperature, unlike other methods such as citrate reduction that require boiling of the solution. The time necessary to produce AuNPs using CO is less than 2 min compared to 20 min for comparable particle sizes using citrate reduction and 45 min for discharge plasma synthesis. CO reduction offers a cheap and flexible alternative to femtosecond laser-based AuNP synthesis processes while eliminating the need for surfactants and polymers to tune the nanoparticle sizes. To the best of our knowledge, there has never been an in depth study of AuNP synthesis, utilizing CO as a reducing agent, to enable size tuning from sub 5 to 100 nm diameters.

In this paper, an in depth analysis of AuNP synthesis utilizing CO gas as a reducing agent is presented. After synthesis, AuNP mono- and polydispersity was examined. The size and monodispersity of the AuNPs were tunable by controlling variables such as $HAuCl_4$ concentration and gas flow during synthesis. The CO reduction method offered excellent tunability over a broad range of sizes while maintaining a high level of monodispersity. Ensemble extinction spectra and TEM images provide clear evidence that CO reduction offers excellent AuNP tunability and is a viable alternative to other synthesis methods.

Results and discussion

AuNPs, synthesized by CO reduction, with average diameter ranging from 4 to 52 nm, were prepared as described below. A set of solutions consisting of $HAuCl_4$ concentrations ranging from 0.01 mM up to 0.09 mM was used. Each $HAuCl_4$ concentration was duplicated to ensure reproducibility. For each $HAuCl_4$ concentration, five 40 mL samples were prepared. Each sample was aerated at different flow rates controlled by a control valve. The five solutions were exposed to CO gas at flow rates of 16.9, 25.45, 31.59, 37.0, and 42.9 mL/min, respectively. The effect of stirring speed was examined, and it was found that the number of revolutions per minute (rpm), by which the solution was stirred, played a role in particle size and morphology. The optimal stir speed, for producing the most monodispersed particles, was found to be 500 rpm. For the following discussion, each solution was constantly stirred at a rate of 500 rpm during synthesis unless noted otherwise. Additionally, the effect of gas-injection flow rates and diffuser pore size on nanoparticle monodispersity and reaction completion times were investigated. It was found that a 60-μm average diffuser pore size was sufficient for producing monodispersed particles. The solution temperature, prior to aeration, was maintained between 20 and 22°C.

Formation of colloidal gold

The Au^{3+} reduction, by CO, to Au^0 takes place via a number of redox reactions. When the CO gas is introduced into the aqueous $HAuCl_4$ solution, electrons are donated to the $[AuCl_4]^-$ ions. For $[AuCl_4]^-$ ions to be reduced to gold atoms, a series of redox reactions take place. This includes the liberations of Cl^- ions and is described by Equations 1 and 2.

$$AuCl_4^- + 2e^- \rightarrow AuCl_2^- + 2Cl^- \quad (1)$$

$$AuCl_2^- + e^- \rightarrow Au^0 + 2Cl^- \quad (2)$$

The electrons are contributed from the reaction of CO and dihydrogen monoxide and the reducing half reactions are given in Equations 3 and 4.

$$CO(g) + H_2O \rightarrow CO_2(aq) + 2e^- + 2H^+ \quad (3)$$

$$CO(g) + 2H_2O \rightarrow HCO_3^- + 2e^- + 3H^+ \quad (4)$$

The thermodynamics of $HAuCl_4$ reduction in aqueous solutions using CO is presented (see Additional file 1).

Synthesis of AuNPs

To illustrate the effects of CO gas flow injection rates on nanoparticle synthesis, nanoparticles were synthesized from an aqueous solution of $HAuCl_4$ acid at a concentration of 0.01 mM. Even at this lower concentration, which is normally not used for the synthesis of AuNPs, the extinction spectra is clearly visible and well

formed as evident in Figure 1. A smoother, more pronounced spectrum was generated at the minimum flow rate of 16.9 mL/min when compared to the other injection flow rates. As the flow rate was increased from 16.9 to 42.9 mL/min the change in spectral symmetry was clearly visible. TEM micrographs of the corresponding nanoparticles are displayed in Figure 1. The gas-injection flow rate of 16.9 mL/min produced individual nanoparticles compared to the other injection rates. The nanoparticles produced by the 16.9 mL/min flow rate ranged in size from 5 to 11 nm in diameter. A flow rate of 25.45 mL/min, Figure 1B, produced nanoparticle aggregates and irregularly shaped particulate matter. Nanoparticles synthesized at a flow rate of 31.59 mL/min consisted of aggregated particle chains. A CO flow rate of 37 mL/min (Figure 1C) resulted in aggregated particle chains similar to that of nanoparticles produced at a flow rate of 25.45 mL/min. The particle aggregation in Figure 1B, D was evident by the broad spectral band. As the flow rate increased to 42.9 mL/min, the nanoparticles became elliptical in shape and very polydispersed. The nanoparticle sizes, when aerated at 42.9 mL/min, ranged from 5 to 40 nm in diameter with some aggregated particles; this size distribution is reflected in the broad spectral band.

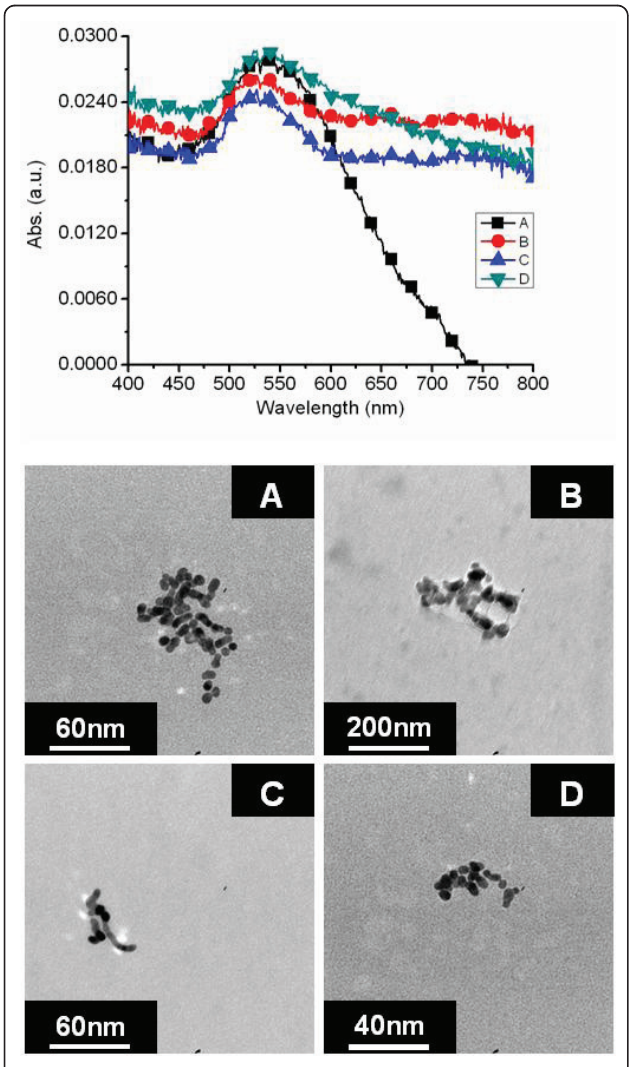

Figure 1 Effect of CO flow rate on nanoparticle morphology. UV-visible extinction spectra of nanoparticles synthesized from a chloroauric acid concentration of 0.01 mM aerated at flow rates of 16.9, 25.5, 37.0, and 42.9 mL/min corresponding to A, B, C, and D, respectively, with accompanying TEM micrographs. A smoother, more pronounced spectrum was generated at the minimum flow rate of 16.9 mL/min when compared to the other injection flow rates. As the flow rate was increased from 16.9 to 42.9 mL/min the change in spectral symmetry was clearly visible.

Increasing the chloroauric acid concentration reduced the polydispersity of the nanoparticles, yet the gas-injection flow rate continued to influence the AuNP size distribution profiles. Figure 2 shows the UV-visible spectra of AuNPs synthesized from a chloroauric acid concentration of 0.03 mM at flow rates of 16.9, 25.5, and 37.0 mL/min (Figure 2A, B, C). The polydispersity of the AuNPs aerated at 16.9 mL/min (Figure 2A) is represented by a broad particle distribution curve. The particle sizes for Figure 2A ranged from 2.5 to 17 nm in diameter. Increasing the CO flow reduced the width of the particle distribution curve where an optimum inlet gas flow was obtained at 25.5 mL/min (Figure 2B). The standard deviation for 2B was 7%, well below the 13 to 15% normally obtained for comparable sizes via citrate reduction [3]. To confirm the formation of Au atoms from $HAuCl_4$, the valence state of Au was identified by X-ray photoelectron spectroscopy (XPS). Figure 3 shows an XPS spectrum of AuNPs synthesized via CO gas reduction. The Au $4f_{7/2}$ peak appeared at a binding energy of 83.98 eV and the Au $4f_{5/2}$ peak appeared at a binding energy of 87.71 eV. This indicates the formation of metallic gold [27,28]. These particles remained stable in excess of 12 months when stored at 4°C.

A better understanding of the effect of the gas flow rates and chloroauric acid concentrations on nanoparticle synthesis can be obtained by considering the mechanisms involved in nanoparticle nucleation and growth. When aerating the aqueous $HAuCl_4$ solution with CO gas, the precursor concentration increases continuously with increasing time. As the concentration reaches supersaturation, nucleation takes place and leads to a decrease in concentration. The continued decrease of the concentration is due to the growth of the particles. During the growth process, two growth mechanisms could take place or a combination of the two. The first growth mechanism is due to the formation of particles from coalescence of the nuclei only. The second growth mechanism is due to the coalescence of nuclei into simple and multiple twins with further growth from monomer attachment of Au atoms on the surface [16].

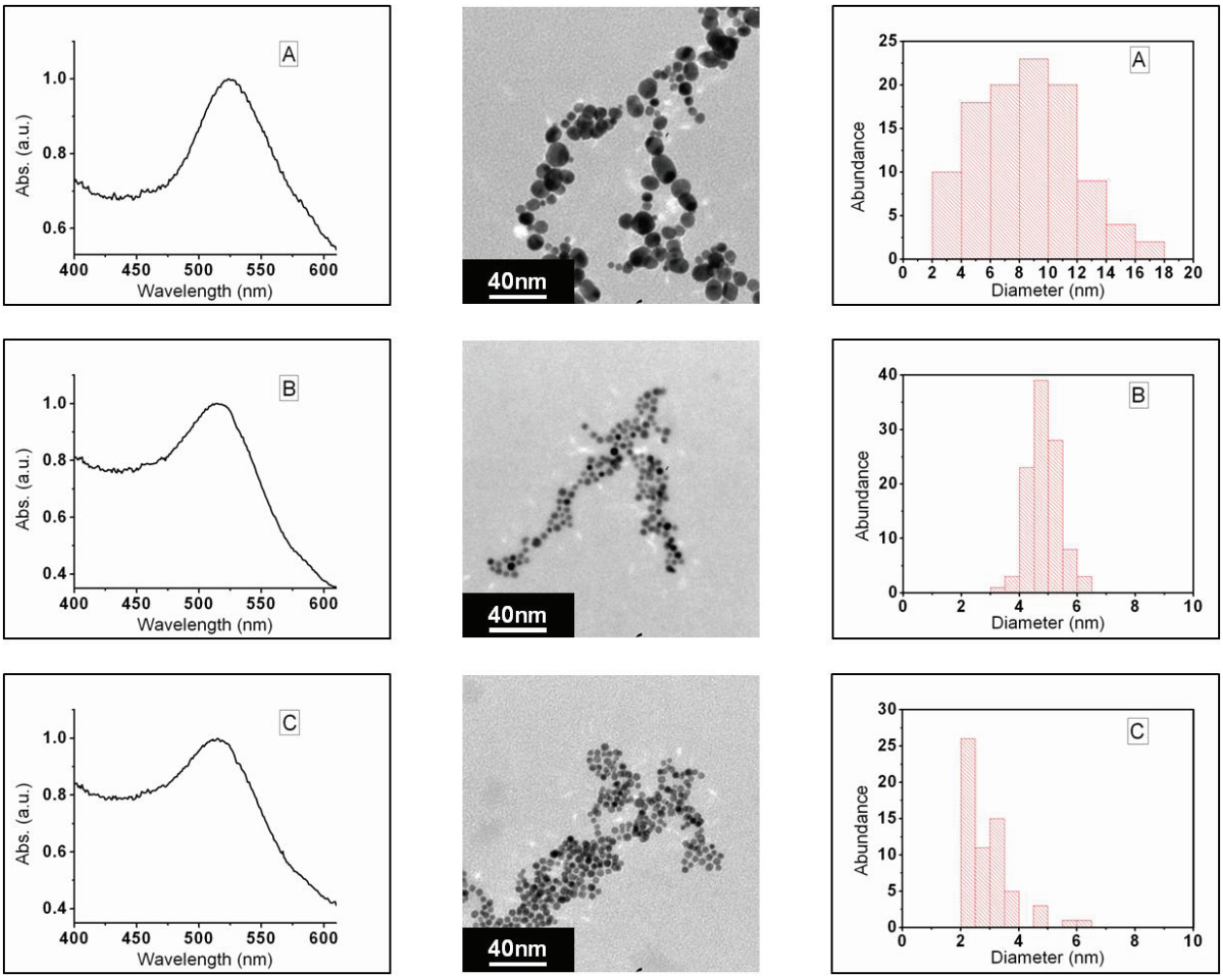

Figure 2 Effect of CO flow rate on nanoparticle distribution. UV-visible extinction spectra of nanoparticles synthesized from a chloroauric acid concentration of 0.03 mM aerated at flow rates of 16.9, 25.5, and 37.0 mL/min corresponding to A, B, and C, respectively, with accompanying TEM micrographs and histograms.

To produce monodispersed AuNPs with CO gas, the rate of nucleation must be high enough so that the precursor concentration does not continue to climb. Instead a large amount of nuclei are formed in a short period. Turkevich et al. found that the nucleation process consists of a polymerization step [29]. When the aqueous $HAuCl_4$ solution is neutral or acidic, the nucleus is formed by gold organic polymer. While the aqueous $HAuCl_4$ solution is alkaline, a polymerization of gold hydroxide takes place [16,30]. The rate of growth of these nuclei should be fast enough to decrease the concentration below the nucleation concentration rapidly. This results in the creation of a limited number of seed particles. The rate of growth must be slow enough that the growth period is long compared with the nucleation period. This produces AuNPs with narrowed size distributions which are the result of the limited nucleation period.

Factors affecting AuNP synthesis

Since the morphology is found to depend strongly on injection flow rates and $HAuCl_4$ concentrations, a relationship between the $HAuCl_4$ concentration and gas-injection flow rates on particle monodispersity can be found. Solution stir speeds during synthesis were examined and it was found that stir speeds had an effect on synthesis and played a role in nanoparticle size disparities. Slow solution stir speeds had the biggest affect on solutions aerated at a flow rate of 16.9 mL/min or below. Increasing the stir speed of the solution aided in the solubility and dispersal of the CO gas molecules during synthesis. It was found that adjusting the gas-injection flow rate compensated for a reduction or increase in solution stir speed. The gas diffuser pore size affected the synthesis process considerably when the solution was at a standstill or stirred at a relatively slow speed below

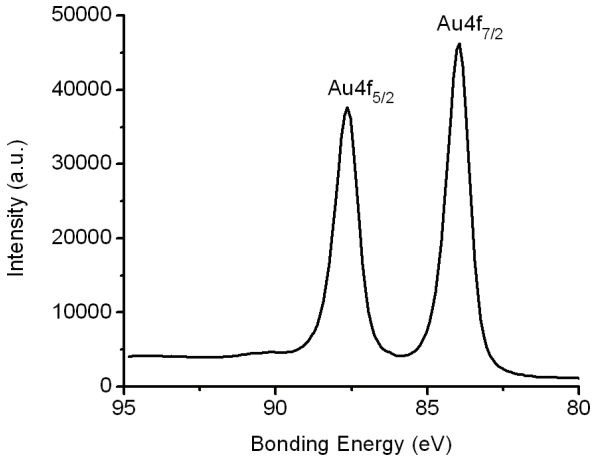

Figure 3 XPS spectrum of AuNPs synthesized via CO gas reduction. The Au $4f_{7/2}$ peak appeared at a binding energy of 83.98 eV and the Au $4f_{5/2}$ peak appeared at a binding energy of 87.71 eV. This indicates the formation of metallic gold [27,28].

75 rpm. Once the solution stir speed approached and/or crossed the 75 rpm threshold, injection-hole size produced only small variances. Once the stir speed reached 500 rpm, there was no difference between samples produced with different diffuser pore sizes, and only the Au concentration or gas-injection flow rates affected particle sizes. Therefore, the solution stirring speed was maintained at 500 rpm to isolate the gas-injection flow rate and Au concentration effect on nanoparticle synthesis.

A chloroauric concentration of 0.03 mM and an inlet gas flow of 16.9 mL/min stirred at 500 rpm resulted in coalescence and growth of nanoparticles before the nucleation reached equilibrium. In essence, the induction period was initiated with a slow autocatalytic rise in the number of nuclei due to the lack of sufficient reducing agent in the solution. Because of this slow nucleus formation, new nuclei were being formed while existing nuclei had already undergone coalescence resulting in polydispersity. Increasing the flow rate to 25.5 mL/min increased the autocatalytic rise in the number of nuclei. Particle growth took place after cessation of the nucleation process resulting in monodispersity. This is illustrated by the fact that the particle distribution curve for Figure 2B consisted of particle sizes in the range of 4 to 6 nm as opposed to the range of 2 to 17 nm (Figure 2A). By increasing the flow rate further (Figure 2C), rapid coalescence of the nuclei takes place. The resulting polydispersity of the sol at increased gas-injection flow rates is still marginal compared to the lower flow rate of 16.9 mL/min. When comparing the spectra of Figure 2A, B, C the more polydispersed sample possesses a broadened spectrum. This is illustrated in more detail (see Additional file 2).

Increasing $HAuCl_4$ concentration

When the chloroauric acid concentration approached 0.2 mM, the gas-injection flow rate had a less pronounced effect on the spectra symmetry yet the flow rate continued to dictate the monodispersity of the particles. When particles were synthesized from a chloroauric acid concentration of 0.3 mM, the most monodispersed sample was produced at a flow rate of 25.5 mL/min. The mean diameter for this sample was 9 nm with a standard deviation of 11%.

As the concentration increased to 0.5 mM, 20 to 25 nm particles were produced. Continual increase of the chloroauric acid concentration beyond 0.5 to 0.6 mM only produced small changes in nanoparticle size with increased absorbance. The standard deviation for the AuNPs produced at 0.6 mM was 8% indicating monodispersity. As the concentration was increased to 1 mM, nanoparticles approaching 30 nm in diameter were produced but the standard deviation approached 20%. Further doubling the concentration to 2 mM had no uniform effect on particle growth, with the majority of the particles in the 30 nm size regime and some of the particles in the 40 to 55 nm size regime with a standard deviation approaching 35%. The UV-visible spectra of the sol prepared at different concentrations (Figure 4), increasing from 0.02 to 1 mM, shows an increase in absorbance which correlates to an increase in particle concentration and volume. Figure 5 shows the pronounced red shifting of the plasmon, which is associated with increased nanoparticle size. The red shift of the plasmon is further illustrated (see Additional file 3). This shifting effect is in line with the prediction described by Mie theory [1,2]. The statistical analysis of

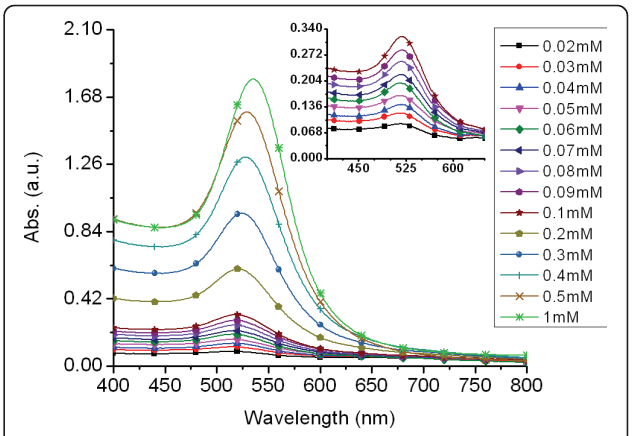

Figure 4 Effect of increasing chloroauric acid concentrations on nanoparticle spectral profile. UV-visible spectra of gold nanoparticles with increasing chloroauric acid concentrations from 0.02 to 0.05 mM in 0.01 mM increments, from 0.1 to 0.5 mM in .1 mM increments, and at 1 mM. The inset is the absorbance spectra of gold nanoparticles produced from concentrations of 0.02 to 0.1 mM.

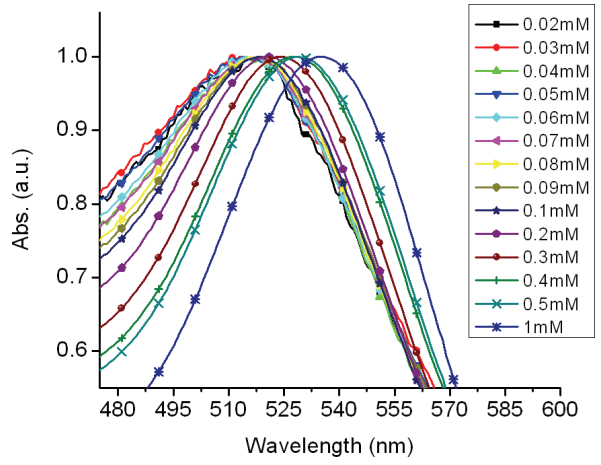

Figure 5 Spectral shift based on chloroauric acid concentrations. Normalized UV-visible spectra of gold nanoparticles with increasing chloroauric acid concentrations from 0.02 to 0.05 mM in 0.01 mM increments, from 0.1 to 0.5 mM in 0.1 mM increments, and at 1 mM. A red-shifting of the plasmon is observed as the chloroauric acid concentration is increased.

the particles synthesized from aqueous solutions of $HAuCl_4$ ranging from 0.02 to 0.6 mM revealed an average standard deviation of approximately 11%.

Influence of pH on AuNP synthesis

It is known that pH is a factor influencing the nucleation and growth of AuNPs [13,16,30]. Since the synthesis process takes place in an acidic environment, the particle is formed from gold polymer with a small contribution from gold hydroxide polymer reduction. As the concentration of chloroauric acid increases, the pH of the solution decreases (see Additional file 4) resulting in particle formation solely by gold polymer reduction. In an acidic environment, the effective monodispersed particle size threshold was reached at approximately 25 nm. The effective monodispersed threshold was defined as a standard deviation below 13%. As previously mentioned, continual increase of the chloroauric concentration eventually resulted in adverse affects on nanoparticle monodispersity. To further grow particles and maintain monodispersity, $HAuCl_4$ hydrolysis was explored. The addition of potassium carbonate (K_2CO_3) to generate an alkaline solution for gold hydroxide polymer reduction was systematically investigated. It was found that the speciation of $HAuCl_4$ had great influence on the size and monodispersity of the AuNPs. As the pH increased, speciation of aqueous $HAuCl_4$ occurred.

Adding K_2CO_3 raised the pH of the solution by allowing hydrolysis of $HAuCl_4$ to take place to form gold hydroxide solution. A 200 mL aqueous $HAuCl_4$ solution, with a concentration of 0.1 mM, was prepared by adding fresh gold to 200 mL of DI water. This solution was aged in an amber bottle, and light protected in a 4°C environment for a minimum of 72 h prior to use. A 0.5 N stock solution of K_2CO_3 was prepared and stirred for a minimum of 1 h. After aging, the chloroauric acid solution was allowed to gradually rise to 22°C. The pH was measured to be 3.6. $HAuCl_4$ (0.1 mM) aqueous solution with various pH values were prepared by the addition of K_2CO_3 aqueous solution into 20 mL of $HAuCl_4$ aqueous solution and shaken vigorously for a minimum of 1 min. This solution was allowed to age for 15 min before introduction of CO gas. The pH values of the aqueous solutions, measured prior to reduction, ranged from 4.25 to 11.4.

Figure 6 shows UV-visible absorption spectra of AuNPs prepared by reduction of hydrolyzed $HAuCl_4$ at various pH. At pH = 4.25, the acquired AuNPs exhibited a symmetric spectrum with a surface plasmon resonance (SPR) peak at 512 nm. When the pH increased to 6.6, there was a SPR shift to 527 nm. When the pH increased to 7.45, the SPR peak position did not change much at 528 nm, and the SPR peak remained symmetric. The SPR feature changed abruptly when the pH was 9.34 showing a broad feature originating at 559 nm. The SPR peak red-shifted further when the pH increased to 10.3. Absorption in the NIR region also gained significant intensity.

Previous experimental and theoretical results demonstrated that $AuCl_4$ undergoes a pH-dependant stepwise hydrolysis which gives way to $[AuCl_x(OH)_{4-x}]^-$ [30,31]. The extent of hydrolysis in turn depends on the pH which gives an indication of the amount of OH^- available for hydrolysis. When the pH is low, $[AuCl_4]^-$ ions dominate the solution. As the pH is increased to 4.25, $[AuCl_4]^-$ concentration is lowered and the contribution

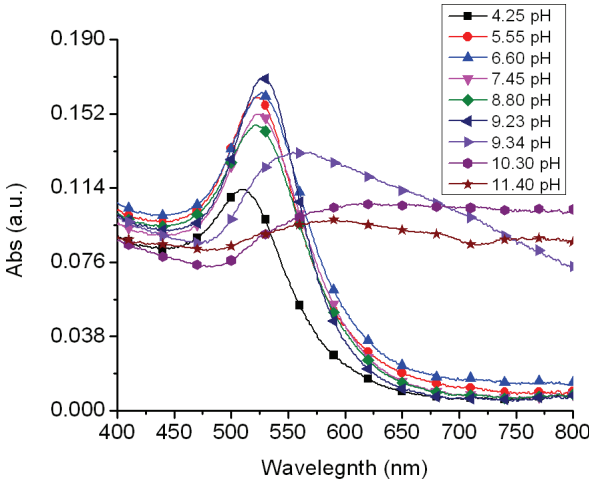

Figure 6 Effect of pH on nanoparticle spectrum. UV-visible spectra of AuNPs produced from a 0.1 mM $HAuCl_4$ aqueous solution synthesized at varying pH values.

from $[AuCl_3(OH)]^-$ ions is increased. Raising the pH of the solution to 6.66 reduced the concentration of $[AuCl_4]^-$ and $[AuCl_3(OH)]^-$ significantly, and the ionic composition was primarily made up of $[AuCl_2(OH)_2]^-$ ions. Further increasing the pH to 8.8 resulted in large ion contribution from $[AuCl(OH)_3]^-$ ions. Additional increase to 10.3 resulted in an overwhelming ion contribution from $[Au(OH)_4]^-$ ions with an appreciable contribution from $[AuCl(OH)_3]^-$ ions. This was because $[Au(OH)_4]^-$ is amphoteric. Its solubility increased due to the formation of $[Au(OH)_4]^-$ at higher pH, thus making the soluble $[Au(OH)_4]^-$ the most dominant species at high pH instead of the precipitating $[AuCl(OH)_3]^-$ [30]. It is the control of hydrolysis to tune the speciation of $[AuCl_x(OH)_{4-x}]^-$ that subsequently influenced the nanoparticle size.

It was observed that amongst the six species of $[AuCl_x(OH)_{4-x}]^-$ discussed earlier, $[Au(OH)_4]^-$ seems to have the lower tendency to be reduced in solution to form colloidal gold. This was evident from its slow and gradual color change when reduced, taking approximately 7 min for complete reduction to occur. This was in contrast to the reduction of other $[AuCl_x(OH)_{4-x}]^-$ species formed at lower pH where it was observed that the addition of CO gas caused a color change within seconds and total reduction within approximately 2 min. This observation may possibly be attributed to a weaker reduction potential of $[Au(OH)_4]^-$ compared to other species. It was found that adjustment to pH < 10 by addition of smaller amounts of K_2CO_3 resulted in the formation of other dominant species that had greater tendency to be reduced in solution to form colloidal gold. It was observed that the synthesis environment also affected nanoparticle stability. The stability of the nanoparticles was monitored for approximately 2 months to examine the pH effect on nanoparticle stability. As the pH increased, prior to synthesis, the nanoparticles became less stable. Table 1 illustrates the stability of the AuNP solutions produced at varying pH.

It was observed that hydrolysis of $[AuCl_4]^-$ started to occur within minutes after the addition of K_2CO_3 indicating immediate formation of the $[AuCl_x(OH)_{4-x}]^-$ species. It was further observed that Au colloid, of varying sizes, were produced when K_2CO_3 and $HAuCl_4$ concentrations and gas-injection flow rates remained constant and only aging times varied. This indicated that aging the gold hydroxide solution, before the addition of CO gas, had a strong influence on the outcome of the reaction.

By controlling the development of the $[AuCl_x(OH)_{4-x}]^-$ species, colloids of various sizes can be synthesized using CO as a reducing agent. When the pH is sufficiently high, the resultant aging process can generate coalescence of $Au(OH)_4$ initiating a limited nucleation process absent of a reducing agent. This nucleation process is out of favor with the requirements necessary for generating monodispersed nanoparticles. Thus proper aging times must be determined to synthesize monodispersed nanoparticles of a particular size from a given K_2CO_3 and $HAuCl_4$ concentration. Exploiting the control of $[AuCl_x(OH)_{4-x}]^-$ species development, by addition of K_2CO_3 and aging of the solution, Au colloid in the ranges of 15 to 100 nm in diameter were produced. Spectra A and B in Figure 7 show the UV-visible spectra of Au colloid produced from a mixture of 200 mL 0.38 mM $HAuCl_4$ aqueous solution and K_2CO_3 (2.71 mM) aged at 30 and 40 min, respectively, in solution reduction volumes of 40 mL. Both SPR peaks were well ordered with a SPR peak at 536 nm for the 30-min aged solution and 546 nm for the 40-min aged solution. Both solutions were aerated with CO gas at an inlet gas flow rate of 25.5 mL/min. The red-shift and dampening of the SPR peak indicated an increase in particle size. The effect of the solution volume being aerated was explored to determine if the amount of solution being aerated had an effect on nanoparticle size and monodispersity. Spectra C, D, and E in Figure 7 were produced from AuNPs synthesized from a 200 mL 0.38 mM $HAuCl_4$ aqueous solution with K_2CO_3 (3.62 mM) aged for

Table 1 Influence of pH upon stability of AuNPs

pH Before synthesis	pH After synthesis	Color	Stability After 1 h stored at 22°C	Stability After 6 h stored at 22°C	Stability After 2 months Stored at 4°C
4.25	3.72	Light pink	Stable	Stable	Small aggregation
4.25	3.72	Light pink	Stable	Stable	Small aggregation
5.55	4.75	Light red	Stable	Stable	Small aggregation
6.6	5.92	Light red	Stable	Stable	Stable
7.45	6.11	Light red	Stable	Stable	Stable
8.8	6.42	Light red	Stable	Stable	Stable
9.23	6.55	Medium red	Stable	Stable	Stable
9.34	6.32	Purple	Stable	Stable	Medium aggregation
10.3	8.10	Blue	Stable	Some aggregation	Heavy aggregation
11.4	10.96	Light blue	Crashed	Crashed	Crashed

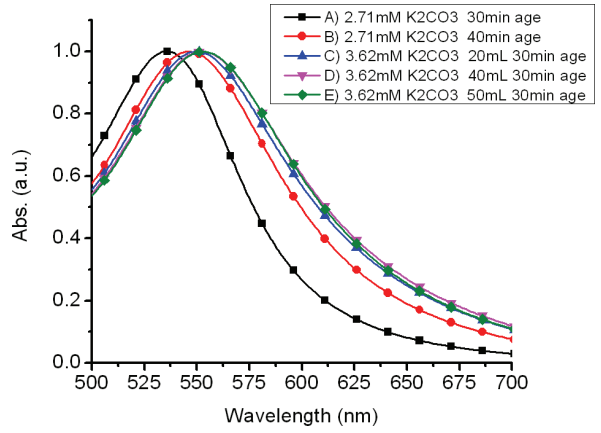

Figure 7 Nanoparticle spectra as a function of K_2CO_3 concentration and aging. UV-visible spectra of AuNPs produced from a mixture of 0.38 mM $HAuCl_4$ aqueous solution with 2.71 mM or 3.62 mM K_2CO_3. A and B are 2.71 mM K_2CO_3 aged at 30 and 40 min, respectively, at an aeration volume of 40 mL. C, D, and E are 3.62 mM K_2CO_3 aged for 30 min each at aeration volumes of 20, 40, and 50 mL, respectively. All samples were aerated at a gas flow rate of 25.5 mL/min.

30 min. The aeration volumes were 20, 40, and 50 mL, respectively. The amount of solution aerated had a small but noticeable effect on SPR peak position. The resulting SPR peak positions were 550, 553, and 554 nm for aeration volumes of 20, 40, and 50 mL, respectively. Increasing the amount of K_2CO_3, in a $HAuCl_4$ aqueous solution of known concentration, while decreasing the aging time, produced larger AuNPs while still maintaining monodispersity. Aqueous solutions of 200 mL 0.38 mM $HAuCl_4$ with 2.71 and 3.62 mM of K_2CO_3 aged for 30 min each produced AuNPs with SPR peak positions at 536 and 553 nm, respectively.

By employing a combination of gold polymer reduction and gold hydrolyzed polymer reduction, particles sizes from ~4 to 100 nm can be synthesized. Figure 8 shows a TEM micrograph illustrating the different sizes available using CO as a reducing agent. Figures 8A, B, C, D are TEM images of AuNPs synthesized without the addition of K_2CO_3. Figures 8E, F are AuNPs synthesized from a hydrolyzed solution of aqueous $HAuCl_4$ via the addition of K_2CO_3. The corresponding sizes of the AuNPs are 4, 6, 15, 25, 50, and ~100 nm with standard deviations of 7, 13, 8, 8, 10, and 11%, respectively.

Conclusions

These results indicate that AuNPs can be synthesized using CO as a reducing agent. CO offers tunability of nanoparticle sizes via altering $HAuCl_4$ concentration and flow rate. The fast synthesis rates, ease of tunability, and absence of cytotoxic by products allow for these CO-based AuNPs to be optimized and readily produced for biomedical and industrial applications. The manipulation of the solution pH and speciation of $HAuCl_4$ to control particle morphology may also be used as a means to tune the particle size. TEM micrographs and UV-visible spectral analysis confirm that the CO-based AuNPs are monodispersed upon synthesis. Future work will focus on how temperatures, upon synthesis, affect morphology. Nanoparticle surface chemistry and functionalization will also be explored. Cytotoxicity of the CO-based AuNPs in human cell lines will subsequently be investigated and compared against citrate-based nanoparticles.

Methods

Chemicals and materials

Hydrogen tetrachloroaurate III trihydrate ($HAuCl_4{\cdot}3H_2O$, 99.99%), and absolute ethanol (C_2H_5OH, 99.5%) where purchased from Sigma Aldrich and used as received. Carbon monoxide (CO, 99%) was supplied by Matheson-Trigas. All solutions were prepared using ultrapure water (18 Mohm Millipore Milli-Q water).

Pre-synthesis

All chloroauric acid solutions were aged in individual amber bottles under 4°C and light protected for a minimum of 3 days prior to use. All glassware used in the following procedures were cleaned in a bath of freshly prepared aqua regia solution (3 parts HCL acid to 1 part HNO_3 acid) and rinsed thoroughly with ethanol three times and then rigorously rinsed four times with copious amounts of pure grade water and oven dried prior to use. Stirring was conducted by a PTFE-coated magnetic stir bar which was cleaned and dried in the same manner as the glassware.

Carbon monoxide-based synthesis of pure aqueous $HAuCl_4$ solution

Several chloroauric acid solutions were prepared for utilization with CO reduction. Various weights of fresh chloroauric acid were dissolved in individual amber bottles containing water (200 mL). At least two separate batches of all solution concentrations were employed to confirm reproducibility. One set of solutions consisted of varying concentrations of chloroauric acid (0.01 to 0.09 mM in 0.01 mM increments) and $HAuCl_4$ (1 mM) and $HAuCl_4$ (2 mM) solutions were prepared. A solution of $HAuCl_4$ (1 wt%) was also prepared. Gold nanoparticles synthesized by CO reduction, with average diameter nanoparticles ranging from 4.5 to 52 nm were prepared as described below. For each $HAuCl_4$ concentration five volumes (40 mL) were prepared. Each sample was aerated at different flow rates controlled by a control valve. The gas entered the solution via a 60 um pore gas diffuser (Fisher Scientific) attached to the end of the gas supply line downstream of the control valve. The five solutions were exposed to CO

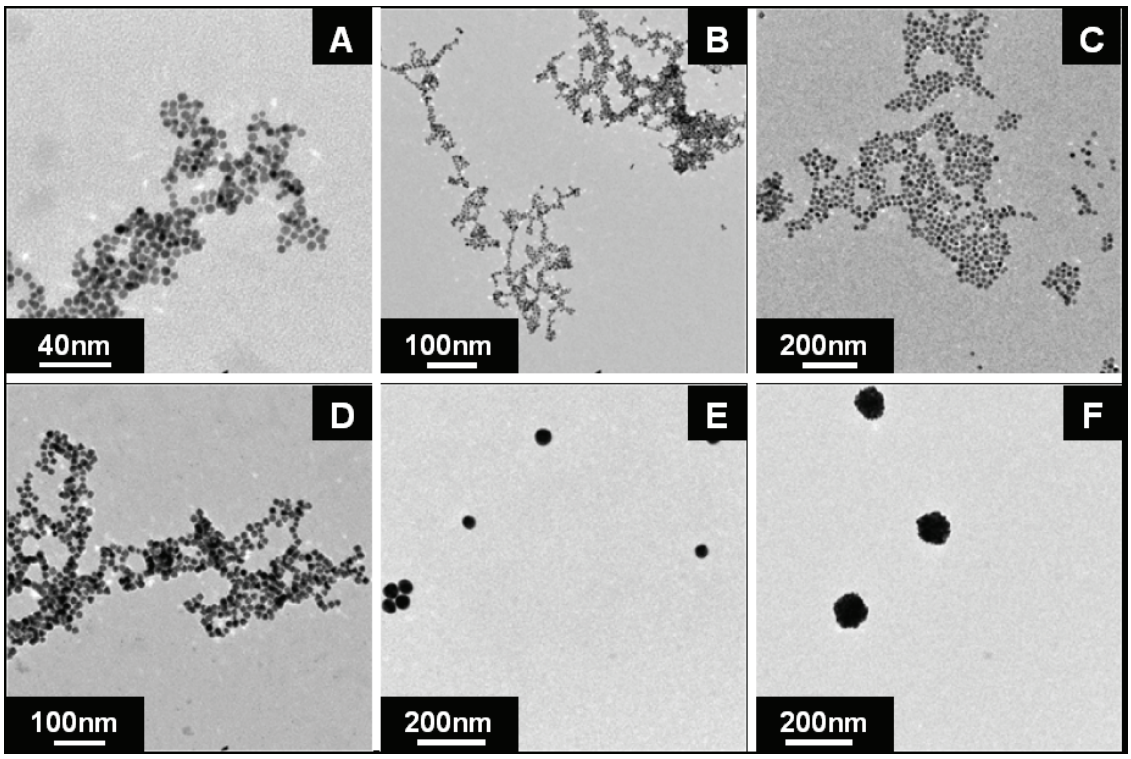

Figure 8 TEM images of AuNPs synthesized by CO reduction of $HAuCl_4$. A, B, C, and D are TEM images of AuNPs synthesized without the addition of K_2CO_3. E and F are AuNPs synthesized from a hydrolyzed solution of aqueous $HAuCl_4$ via the addition of K_2CO_3. The corresponding sizes of the AuNPs are 4, 6, 15, 25, 50, and ~100 nm respectively.

gas at flow rates of 16.9, 25.45, 31.59, 37.0, and 42.9 mL/min, respectively. The solution temperature, prior to aeration, was maintained between 20 and 22°C.

Carbon monoxide-based synthesis of pH adjusted $HAuCl_4$ solution and hydrolyzed $HAuCl_4$ solution

A 200 mL aqueous $HAuCl_4$ solution, with a concentration of 0.1 mM, was prepared by adding fresh gold to 200 mL of ultrapure Milli-Q water. This solution was aged in an amber bottle in light protected 4°C environment for a minimum of 72 h prior to use. After aging, the chloroauric acid solution was allowed to gradually rise to 22°C. A fresh stock solution of potassium carbonate (0.5 N) was prepared and stirred for a minimum of 1 h. $HAuCl_4$ aqueous solutions with various pH values were prepared by the addition of certain amounts of K_2CO_3 aqueous solution into of $HAuCl_4$ (0.1 mM) aqueous solution (20 mL) and shaken vigorously for a minimum of 1 min. This solution was allowed to age for 15 min before introduction of CO gas. The pH values of the aqueous solutions, measured prior to reduction, ranged from 4.25 to 11.4. Additionally several aqueous $HAuCl_4$ (0.38 mM) solutions (200 mL) were prepared by adding fresh gold to ultrapure Milli-Q water (200 mL). These solutions were allowed to age for a minimum of 72 h. K_2CO_3 (75 mg, 2.71 mM) was added to two $HAuCl_4$ (0.38 mM) solutions (200 mL) and aged for 30 and 40 min, respectively. K_2CO_3 (100 mg, 3.62 mM) was added to a $HAuCl_4$ (0.38 mM) solution (200 mL) and aged for 30 min. All solutions were aerated with CO gas at an inlet flow rate of 25.5 mL/min.

Nanoparticle characterization

Sample size distributions were determined by transmission electron microscopy (TEM) performed using a JEOL 1230 High Contrast-Transmission Electron Microscope (HC-TEM) operating between 80 and 100 kV. Samples were prepared for both instruments by contacting a AuNP (10 μL) drop with a carbon film coated 200 mesh copper grid. The grids were placed in a spotlessly clean container, covered and allowed to dry completely before use.

The optical response of the gold nanoparticles was determined by examining the optical extinction spectra of aqueous samples in 1 cm path length polystyrene cuvettes using a Varian Cary 300 UV-visible spectrophotometer. The UV-visible spectra were acquired at wavelengths between 400 to 800 nm. Distilled water was used as the reference and the blank for baseline subtraction.

XPS was carried out using a PHI Quantera SXM system. The soft X-ray source consisted of aluminum with

source energy of 1486.7 eV. The take off angle was set at 45°. Precut silicon wafers 4.5 mm × 5 mm were cleaned by immersion in a 3:1 H_2SO_4:H_2O_2 (piranha) solution for 15 min and rinsed with ultrapure Milli-Q water then dried. The sample was prepared by concentrating the AuNPs and dropping colloidal solution on precut silicon wafers. They were placed in a spotlessly clean container, covered and allowed to dry.

Additional material

Additional file 1: Thermodynamics of $HAuCl_4$ reduction in aqueous solutions using carbon monoxide as a reducing agent. The entire process is performed between 20 and 22°C and a pressure of 1 atm. The pH of the solution varies as a function of $HAuCl_4$ concentration. Nernst equation describes potential of electrochemical cell as a function of concentrations of ions taking part in the reaction:

$$E = E^0 - \frac{RT}{nF}\ln(Q) \quad \text{(M1a)}$$

where E^0 is the standard reduction potential, R is the absolute gas constant = 8.31441 J/(mol K), F is Faraday constant = 96484.6 C/mol, T is the absolute temperature = 295.15 K, n is number or electrons, and Q is the reaction quotient. RT/F can be considered constant.

$$Q = \frac{\{C\}^c\{D\}^d}{\{A\}^a\{B\}^b} \quad \text{(M2a)}$$

$$E = E^0 - \frac{RT}{nF} * 2.303 * \log(Q) \quad \text{(M3a)}$$

The CO gas is injected at a flow rate of 25.45 mL/min in 40 mL aqueous sample volumes. A water saturation constant of 0.26 g per 1 kg at 22°C is used.

$$Au^{3+} + 2e^- \rightarrow Au^0 \quad E^0(V) = 1.52 \quad \text{(M4a)}$$

$$AuCl_4^- + 2e^- \rightarrow AuCl_2^- + 2Cl^- \quad E^0(V) = 0.926 \quad \text{(M5a)}$$

$$AuCl_2^- + e^- \rightarrow Au^0 + 2Cl^- \quad E^0(V) = 1.154 \quad \text{(M6a)}$$

$$AuCl_4^- + 3e^- \rightarrow Au^0 + 4Cl^- \quad E^0(V) = 1.002 \quad \text{(M7a)}$$

$$CO(g) + H_2O \rightarrow CO_2(aq) + 2e^- + 2H^+ \quad E^0(V) = 0.11 \quad \text{(M8a)}$$

$$CO(g) + 2H_2O \rightarrow HCO_3^- + 2e^- + 3H^+ \quad E^0(V) = -0.101 \quad \text{(M9a)}$$

Redox potentials (7) and (8) are given at pH 0. The redox potentials are pH-dependent and must be adjusted for the varying pH values.

Additional file 2: Effect of CO flow rate on nanoparticle spectral profile. Normalized UV-visible spectra of nanoparticles synthesized from a chloroauric acid concentration of 0.03 mM aerated at flow rates of 16.9, 25.5, and 37.0 mL/min corresponding to A, B, and C, respectively. The effect of the gas flow rate during synthesis is illustrated by a comparison of the three spectra.

Additional file 3: Plasmon peak position and absorbance value as a function of chloroauric acid concentration. The chloroauric acid concentration ranging from 0.01 to 1 mM. The data is plotted on a logarithmic scale. As the $HAuCl_4$ concentration increases the absorbance intensity increases with an accompanying red-shift of the plasmon peak position.

Additional file 4: pH values before and after AuNP synthesis. pH values for given $HAuCl_4$ concentrations ranging from 0.02 to 0.1 mM in 0.01 mM increments and from 0.1 to 0.5 mM in 0.1 mM increments. The *x*-axis is plotted on a logarithmic scale. The inset shows the pH values of the AuNP solutions from 0.01 to 0.1 mM and is plotted on a linear scale. As the reduction of $HAuCl_4$ by CO takes place, H^+ ions are liberated decreasing the pH of the solution. All pH measurements were taken at room temperature.

Abbreviations

CO: carbon monoxide; AuNP: gold nanoparticle; HC-TEM: high contrast-transmission electron microscope; rpm: revolutions per minute; SPR: surface plasmon resonance; TEM: transmission electron microscopy; XPS: X-ray photoelectron spectroscopy.

Acknowledgements

This work was supported by a DoD Era of Hope Scholar Award, Welch Foundation Grant C-1598. We thank Lissett Bickford and Oara Neumann for their assistance and helpful suggestions.

Author details

[1]Department of Electrical and Computer Engineering, Rice University, MS-366, 6100 Main St., Houston, TX 77005, USA [2]Department of Bioengineering, Rice University, MS-142, 6100 Main St., Houston, TX 77005, USA [3]Department of Biochemistry and Cell Biology, Rice University, MS-140, 6100 Main St., Houston, TX 77005, USA

Authors' contributions

JKY is the primary author and conceived of the study, carried out the conception and design, synthesis and experiments, characterization, acquisition of data, analysis and interpretation of data, and drafting of the manuscript. NAL and RJL equally contributed as secondary authors by conducting cytotoxicity studies, data analysis and manuscript revisions. LCK carried out experiments, performed particle characterizations and aided in the drafting of the manuscript. AS participated in the design of the study, carried out synthesis and experiments and helped draft the manuscript. AYL and VN participated in the design of the study and coordination. RAD is the principal investigator.

Competing interests

The authors declare that they have no competing interests.

Received: 24 November 2010 Accepted: 16 June 2011
Published: 16 June 2011

References

1. Hovel H, Fritz S, Hilger A, Kreibig U: **Width of cluster plasmon resonance: Bulk dielectric functions and chemical interface damping.** *Phys Rev B* 1993, **48**:18178-18188.
2. Link S, El-Sayed MA: **Size and temperature dependence of the plasmon absorption of colloidal gold nanoparticles.** *J Phys Chem B* 1999, **103**:4212-4217.
3. Jain PK, Qian W, El-Sayed MA: **Ultrafast cooling of photexcited electrons in gold nanoparticle-thiolated DNA conjugates involves the dissociation of the gold-thiol bond.** *J Am Chem Soc* 2006, **128**:2426-2433.
4. Bickford L, Agollah G, Drezek R, Yu TK: **Silica-gold nanoshells as potential intraoperative molecular probes for HER2- overexpression in ex vivo breast tissue using near-infrared reflectance confocal microscopy.** *Breast Cancer Res Treat* 2009, **120**:547-555.
5. Yu L, Banerjee IA, Matsu H: **Direct growth of shape-controlled nanocrystals on nanotubes via biologicalrecognition.** *J Am Chem Soc* 2003, **125**:14837-14840.

6. Turner APF: **Biosensors-sense and sensitivity.** *Science* 2000, **290**:1315-1317.
7. Yeh C, Hung C, Chang TC, Lin HP, Lin YC: **An immunoassay using antibody-gold nanoparticle conjugate, silver enhancement and flatbed scanner.** *Microfluid Nanofluid* 2009, **6**:85-91.
8. Yang W, Wang J, Zhao S, Sun Y, Sun C: **Multilayered construction of glucose oxidase and gold nanoparticles on Au electrodes based on layer-by-layer covalent attachment.** *Electrochem Commun* 2006, **8**:665-672.
9. Wu ZS, Zhou GZ, Jiang JH, Shen GL, Yu RQ: **Gold colloid-bienzyme conjugates for glucose detection utilizing surfaced-enhanced raman scattering.** *Talanta* 2006, **70**:533-539.
10. Duff DG, Baiker A, Edwards PP: **A new hydrosol of gold clusters 1. Formation and particle size variation.** *Langmuir* 1993, **9**:2301-2309.
11. Brinson BE, Lassiter JB, Levin CS, Bardhan R, Mirin N, Halas NJ: **Nanoshells made easy: improving Au layer growth on nanoparticle surfaces.** *Langmuir* 2008, **24**:14166-14171.
12. Hu J, Wang Z, Li J: **Gold nanoparticles with special shapes: controlled synthesis, surface-enhanced raman scattering, and the application in biodetection.** *Sensors* 2007, **7**:3299-3311.
13. Park SE, Park MY, Han PK, Lee SW: **The effect of pH-adjusted gold colloids on the formation of gold clusters over APTMS-coated silica cores.** *Bull Korean Chem Soc* 2006, **27**:1341.
14. Polte J, Erler R, Thunemann AF, Sokolov S, Ahner TT, Rademann K, Emmerling F, Kraehnert R: **Nucleation and growth of gold nanoparticles studied via in situ small angle x-ray scattering at millisecond time resolution.** *ACS Nano* 2010, **4**:1076-1082.
15. Beattie JK: **Monodispersed colloids of transition metal and lanthanide compounds.** *Pure Appl Chem* 1989, **61**:937-941.
16. Turkevich J, Stevenson PC, Hillier J: **Formation of colloidal gold.** *J Phys Chem* 1953, **57**:670-673.
17. Sakai T, Alexandridis P: **Size and shape-controlled synthesis of colloidal gold through autoreduction of the auric cation by poly(ethylene oxide)-poly(propylene oxide) block copolymers in aqueous solutions at ambient conditions.** *Nanotechnology* 2005, **16**:S344-S353.
18. Majzik A, Patakfalvi R, Hornok V, Dekany I: **Growing and stability of gold nanoparticles and their functionalization by cysteine.** *Gold Bull* 2009, **42**:113-123.
19. Jana NR, Gearheart L, Murphy CJ: **Seeding growth for size control of 5-40 nm diameter gold nanoparticles.** *Langmuir* 2001, **17**:6782-6786.
20. Shan C, Li F, Yaun F, Yang G, Niu L, Zhang Q: **Size-controlled synthesis of monodispersed gold nanoparticles stabilized by polyelectrolyte-functionalized ionic liquid.** *Nanotechnology* 2008, **19**:285601.
21. Mafune F, Kohno J, Takeda Y, Kondow T: **Full physical preparation of size-selected gold nanoparticles in solution: laser ablation and laser-induced size control.** *J Phys Chem B* 2002, **106**:7575-7577.
22. Besner S, Kabashin AV, Winnik FM, Meunier M: **Synthesis of size-tunable polymer-protected gold nanoparticles by femtosecond laser-based ablation and seed growth.** *J Phys Chem C* 2009, **113(22)**:9526-9531.
23. Takai O: **Solution plasma processsing (SSP).** *Pure Appl Chem* 2008, **80**:2003-2011.
24. Saito N, Hieda J, Takai O: **Synthesis process of gold nanoparticles in solution plasma.** *Thin Solid Films* 2009, **518**:912-917.
25. Ashkarran AA, Iraji A, Mahbavi SM, Ahadian MM, Nezhad MRH: **Rapid and efficient synthesis of colloidal gold nanoparticles by arc discharge method.** *Appl Phys A* 2009, **96**:423-428.
26. Liang X, Wang ZJ, Liu CJ: **Size-controlled synthesis of colloidal gold nanoparticles at room temperature under the influence of glow discharge.** *Nanoscale Res Lett* 2010, **5**:124-129.
27. Thomas TD, Weightman P: **Valance electron structure of AuZn and AuMg alloys derived from a new way of analyzing Auger-parameter shifts.** *Phys Rev B* 1986, **33**:5406.
28. Seah MP, Smith GC, Anthony MT: **AES: energy calibration of electron spectrometers. I-an absolute, traceable energy calibration and the provision of atomic reference line energies.** *Surf Interface Anal* 1990, **15**:293-308.
29. Turkevich J: **Colloidal gold, part I.** *Gold Bull* 1985, **18**:86-91.
30. Wang S, Qian K, Bi X, Huang W: **Influence of speciation of aqueous HAuCl4 on the synthesis, structure, and property of Au colloids.** *J Phys Chem C* 2009, **113**:6505-6510.
31. Lemire C, Meyer R, Shaikhutdinov S, Freund HJ: **Do quantum size effects control CO adsorption on gold nanoparticles?** *Surface Chem Angew Chem Int Ed* 2004, **43**:118-121.

doi:10.1186/1556-276X-6-428
Cite this article as: Young *et al.*: Size-controlled synthesis of monodispersed gold nanoparticles via carbon monoxide gas reduction. *Nanoscale Research Letters* 2011 **6**:428.

Hindawi Publishing Corporation
Journal of Oncology
Volume 2012, Article ID 291898, 10 pages
doi:10.1155/2012/291898

Research Article

Rapid Stereomicroscopic Imaging of HER2 Overexpression in *Ex Vivo* Breast Tissue Using Topically Applied Silica-Based Gold Nanoshells

Lissett R. Bickford,[1,2,3] Robert J. Langsner,[1] Joseph Chang,[4] Laura C. Kennedy,[1,5] Germaine D. Agollah,[6] and Rebekah Drezek[1,7]

[1] *Department of Bioengineering, Rice University, 6100 Main Street, MS 142, Houston, TX 77005, USA*
[2] *School of Biomedical Engineering and Sciences, Virginia Polytechnic Institute and State University, Blacksburg, VA 24061, USA*
[3] *Department of Mechanical Engineering, Virginia Polytechnic Institute and State University, Blacksburg, VA 24061, USA*
[4] *School of Medicine, University of California San Francisco, San Francisco, CA 94143, USA*
[5] *School of Medicine, Baylor College of Medicine, Houston, TX 77030, USA*
[6] *Department of Chemistry and Process Development, Nanospectra Biosciences, Inc., Houston, TX 77054, USA*
[7] *Department of Electrical and Computer Engineering, Rice University, Houston, TX 77005, USA*

Correspondence should be addressed to Rebekah Drezek, drezek@rice.edu

Received 5 April 2012; Accepted 11 September 2012

Academic Editor: José María Benlloch

Tumor margin detection for patients undergoing breast conservation surgery primarily occurs postoperatively. Previously, we demonstrated that gold nanoshells rapidly enhance contrast of HER2 overexpression in *ex vivo* tissue sections. Our ultimate objective, however, is to discern HER2 overexpressing tissue from normal tissue in whole, nonsectioned, specimens to facilitate rapid diagnoses. Here, we use targeted nanoshells to quickly and effectively visualize HER2 receptor expression in intact *ex vivo* human breast tissue specimens. Punch biopsies of human breast tissue were analyzed after a brief 5-minute incubation with and without HER2-targeted silica-gold nanoshells using two-photon microscopy and stereomicroscopy. Labeling was subsequently verified using reflectance confocal microscopy, darkfield hyperspectral imaging, and immunohistochemistry to confirm levels of HER2 expression. Our results suggest that anti-HER2 nanoshells used in tandem with a near-infrared reflectance confocal microscope and a standard stereomicroscope may potentially be used to discern HER2-overexpressing cancerous tissue from normal tissue in near real time and offer a rapid supplement to current diagnostic techniques.

1. Introduction

Currently, breast cancer is the second leading cause of cancer-related deaths in women, and it accounts for approximately one-third of all cancers diagnosed in women in the United States [1]. To reduce cancer recurrence and progression, cancerous tissue must be completely eliminated, regardless of grade [2]. Surgical breast cancer therapy focuses on removing the primary tumor and identifying the possibility of metastatic disease from the evaluation of sentinel lymph nodes. Although some patients may require modified radical mastectomy, many patients with less-advanced breast cancer elect breast-conserving surgery. The presence of a positive surgical margin during these surgeries has been associated with lower rates of patient survival [3]. Due to residual cancer cells being left in many patients that undergo breast conservation therapy, as many as 40% of patients have experienced local breast cancer recurrence near the site of the original tumor [4]. Intraoperative treatment decisions are, therefore, absolutely critical.

Presently, intraoperative tumor margin detection occurs primarily in specialized tertiary centers, such as The University of Texas M.D. Anderson Cancer Center (MDACC). In these centers, the resected tissue receives a preliminary evaluation by a pathologist while the patient remains in the operating room; if necessary, additional tissue can be

removed until the pathologist determines that the tumor margins are negative. In community hospitals, however, pathologic analysis of excised tissue only occurs postoperatively [5]. Patients who consequently have positive tumor margins must return for surgical reexcision and receive increased doses of adjuvant radiation therapy [6, 7]. Thus, the existence of positive tumor margins portends additional risks and costs to the patient. Due to the existing limitations of current intraoperative tumor margin detection, there is an opportunity to develop superior diagnostic tools to assist in reducing the recurrence and progression of cancer due to inadequate tissue removal during primary surgery.

While histologic analysis remains the gold standard for tumor margin assessment, the macroscopic evaluation of whole, nonsectioned tissue specimens may also be used to provide an intraoperative estimate of tumor margin status prior to subsequent processing. This would be an invaluable tool in hospitals without onsite pathology suites. Macroscopic visualization of questionable tissue is attractive for enhancing the sensitivity and specificity of tumor margin delineation: if the number of suspicious regions that require further microscopic processing can be reduced, surgeons and pathologists can focus their attention and resources on areas that remain inconclusive. Currently, macroscopic evaluation only occurs for breast cancer specimens that involve microcalcifications or nonpalpable masses and does not occur for palpable breast masses [8]. For nonpalpable masses that have been resected, radiographic images are used to determine the extent of the breast disease and the proximity to the resected margins. Although specimen radiography appears to increase the accuracy of tumor margin detection, limitations have been noted. For instance, microcalcifications that appear as tumor on radiographic images may actually be areas of lymphocytic accumulation [9]. The use of contrast agents targeted to specific biomarkers associated with disease may present an opportunity to increase the sensitivity and specificity of macroscopic evaluations.

In preceding studies, we confirmed that silica-based gold nanoshells targeted to the Human Epidermal growth factor Receptor 2 (HER2) could be used for the rapid contrast enhancement of both cells [10] and tissue sections [11] which overexpress HER2 biomarkers. While gold nanoshells can be conjugated to a variety of biomarkers [12, 13], we have selected HER2 due to its association with increased cancer aggression, recurrence, and progression when amplified [14, 15]. Amplification of this cell-surface bound tyrosine kinase receptor occurs in up to a quarter of all human breast cancer cases [16]. Importantly, using biomarkers for tumor margin detection has recently been shown to better identify patients at high risk of cancer recurrence over standard histological analysis [17].

To facilitate prompt tumor margin detection intraoperatively, the ability to assess tumor margins without physical sectioning is highly desirable as sectioning may incur significant time to the surgical procedure [5]. Thus, in this study, we advance our previous findings by examining the ability to rapidly target HER2 receptors in intact *ex vivo* human breast tissue specimens without sectioning. We first confirm the predominance of the surface targeting needed to identify the tumor margins and preferential labeling of HER2-positive tissue using two photon and hyperspectral imaging. Then, we demonstrate that anti-HER2-targeted gold nanoshells can be used as rapid diagnostic imaging agents for HER2 overexpression in intact breast tissue specimens using a standard stereomicroscope and confirm these results through reflectance confocal microscopy and immunohistochemistry.

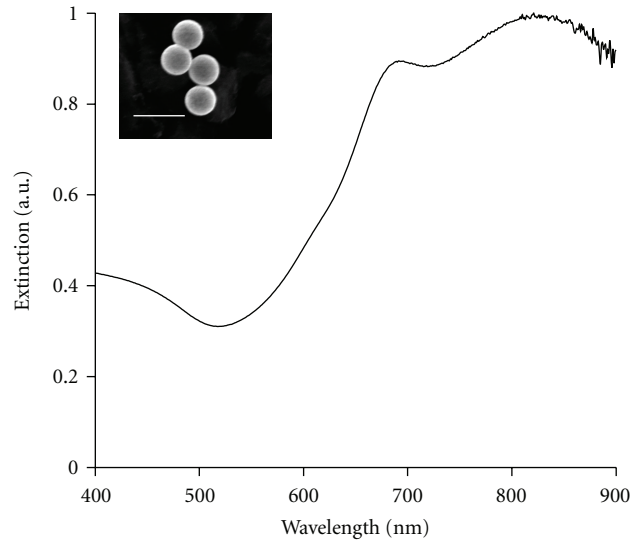

Figure 1: Measured extinction spectra of nanoshells with an average core diameter of 276 nm and average shell thickness of 19 nm. Insert depicts corresponding image from scanning electron microscopy. Scale bar represents 500 nm.

2. Materials and Methods

2.1. Nanoshell Fabrication and Antibody Conjugation. Nanoshells were fabricated as formerly described [18–20], and only a brief summary will be provided here. Silica cores were made using the Stöber method [21], in which tetraethyl orthosilicate was reduced in the presence of ammonium hydroxide dissolved in 200 proof ethanol. The surfaces of the cores were then modified by reaction with aminopropyltriethoxysilane (APTES) to functionalize reactive amine groups on the surface. The final particles were measured by dynamic light scattering (DLS) to have an average diameter of 276 nm. Next, gold colloid (~1–3 nm diameter) was fabricated and adsorbed onto the surface of the silica cores via the amine groups to form gold nucleation sites [22]. To fully cover the surface of the silica cores, additional gold was added to these nucleation sites via a reduction reaction in which hydrogen tetrachloroaurate trihydrate ($HAuCl_4 3H_2O$) was dissolved in potassium carbonate and then added with formaldehyde to help reduce the gold. After the gold layer over the silica cores was formed, the spectrum of the final nanoshell solution was visualized using a UV-VIS spectrophotometer (Varian Cary 300) (Figure 1).

To determine the concentration of nanoshells in solution, the absorption, scattering, and extinction coefficients were

determined using Mie theory. The average nanoshell diameter, as validated by scanning electron microscopy (SEM), was 314 nm with a peak surface plasmon resonance at 840 nm. The concentration of the working nanoshell solution was approximately 2.0×10^9 particles/mL.

Nanoshells were targeted to biological HER2 antigens by linking the surfaces of the nanoshells to anti-HER2 antibodies using previously described methods [18]. Prior to beginning experimental studies, nanoshells were incubated with an anti-HER2-linker cocktail [18] for 2 hours at 4°C. To ensure nanoparticle stabilization in biological media, the nanoshells were next incubated with a 1 mM polyethylene glycolthiol solution (PEG-SH, MW = 5 kD, Nektar) for 12–16 hours at 4°C. Next, unbound antibodies and excess PEG-SH were removed from the nanoshells by centrifugation. Prior to experimental studies, the nanoshells were resuspended in antibody diluent (IHC World, pH 7.4) by gentle pipetting to a final volume of 165 μL.

2.2. Ex Vivo Human Breast Tissue Specimens. Normal and cancerous (HER2-negative and HER2-positive) breast tissue specimens were supplied by the Cooperative Human Tissue Network (CHTN) through a protocol approved by the Institutional Review Board (IRB). Tissues were designated as normal or cancerous by pathologists at the medical centers where the tissue samples were obtained. Additionally, HER2 status was previously determined by pathologists at the respective medical centers prior to the patients undergoing any form of medical treatment.

Before use, samples were thawed briefly in a 37°C water bath and cut on a disposable cutting board using a 5 mm punch biopsy to maintain size consistency. At least two punch biopsies were taken from each specimen for control and experimental conditions. Each cut specimen used was 5 mm in diameter with an average thickness of 1 mm. Tissue samples were subsequently incubated in prewarmed antibody diluent for 1 minute at room temperature with gentle agitation in a 24-well plate. After prerinsing, the samples were incubated in either antibody diluent or the aforementioned targeted-nanoshell cocktail in polyethylene sample vials (Sigma Aldrich). The vials were placed on a nutator in an incubator at 37°C for 5 minutes. After incubation, the tissue samples were removed from the vials and rinsed 3 times in 1x PBS briefly in a 24-well plate. Samples were moved to a clean well of 1x PBS prior to imaging.

2.3. Two-Photon Imaging of Human Breast Tissue Specimens. Both HER2-positive and HER2-negative cancerous samples were evaluated for surface labeling of HER2-targeted nanoshells by employing two-photon imaging of intact breast tissue specimens. Samples were placed directly on a glass coverslip (Fisher Scientific), and an additional coverslip was placed on top of the tissue in order to facilitate moderate tissue compression. For image acquisition, a Zeiss multiphoton confocal microscope (LSM 510 META NLO) was used in tandem with a Coherent Chameleon femtosecond-pulsed, mode-locked Ti: sapphire laser. This system was set to operate as formerly described [23]. Specifically, an excitation wavelength of 780 nm and a power setting of 10% maximum excitation power were used. The collected emission wavelength range was 451–697 nm. Images were collected at a magnification of 20x and a z-stack (depth) increment of 5 μm. In order to calculate the percentage of area covered by nanoshells, ImageJ imaging software was implemented after image acquisition. Recent research has shown that ImageJ can be used to analyze signal intensity of silica-gold nanoshells under different imaging systems [11, 24]. Each pixel in the images had an intensity value in the range of 0–255. To determine the nanoshell level in each image, an intensity threshold of 30 was used to separate areas that did not have nanoshells ($\leq$30) from those that did have nanoshells (>30). The value of 30 was chosen because images of negative controls were found to have a maximum intensity of 30. The number of pixels that were above the threshold value was then used to calculate the area of each image that contained nanoshells.

2.4. Darkfield Hyperspectral Imaging of Human Breast Tissue Slices. To confirm the presence of nanoshells on the surface of the tissues, HER2-positive cancerous, HER2-negative cancerous and normal tissue samples were incubated with nanoshells as previously described. A thin layer of pathological ink was placed on the tissue surface for orientation. The tissues were embedded in OCT media (BBC chemical) and frozen rapidly over dry ice. The specimens were cut at a section thickness of 8 μm using a Leica CM1850 UV cryostat. Cancerous specimens were sectioned at -20°C and normal specimens at -30°C. The different temperatures were used to maintain optimal tissue morphology as recommended by Leica. Additionally, Magalhães et al. reported on the use of different temperatures to slice normal and cancerous tissue [25]. The sections were immediately placed on superfrost slides (Fisher Scientific) and allowed to dry overnight. The next day the tissue slices were imaged with a 10x objective on an Olympus darkfield microscope equipped with a Cytoviva high-resolution illuminator. Hyperspectral images of the tissue slices were taken using a hyperspectral camera that provides both spatial and spectral data for each image.

Spectral data of each field of view (FOV) was used to determine if nanoshells were present on each slice of tissue. Comparisons were made between tissue surfaces and tissue beyond the surfaces to determine the presence of nanoshells; spectral data from tissue that was not incubated with nanoshells was also used as a negative control.

2.5. Macroscopic Imaging of Human Breast Tissue Specimens. Normal and HER2-positive cancerous breast tissue specimens (from patients who had and had not received neoadjuvant chemotherapy) were imaged using a Zeiss Discovery. V8 stereomicroscope equipped with a VisiLED MC1000 light source. For macroscopic imaging of breast tissue specimens, a thin plastic black stage was placed beneath a glass coverslip to enable ease of tissue placement and to provide a consistent black background among all samples. The specimens (controls and respective nanoshell-labeled counterparts) were placed alongside each other on top of the coverslip. Images were taken at both 1x and 2x magnification under the same lighting conditions.

2.6. Reflectance Confocal Microscopy Imaging of Human Breast Tissue Specimens. Following widefield imaging, the aforementioned samples were prepared for microscopic analysis under reflectance confocal microscopy. For this component of the study, a Lucid VivaScope 2500 inverted confocal microscope was used. Samples were placed directly on glass slides that were modified by the addition of an adhesive 1 mm deep, 20 mm diameter silicon isolator (Invitrogen). To compress the tissue slightly and consistently among samples, an adhesive tissue cassette (Lucid, Inc.) was placed directly on top of the silicone isolators above the tissue specimens. Multiple images were taken at a power of 0.4 mW and at the same distance from the glass surface for both samples and controls. After reflectance imaging, the samples were prepared for histological processing. Additionally, reflectance intensity measurements were recorded using ImageJ processing software as formerly described [11].

2.7. Immunohistochemistry and Histology. Once images were collected under both stereomicroscopy and RCM imaging systems, normal and HER2-positive cancerous samples (with and without previous neoadjuvant chemotherapy) were embedded in OCT media and sectioned to a thickness of 5 μm. Multiple sections from each specimen were prepared for either immunohistochemistry (IHC) or hematoxylin and eosin (H&E) staining. IHC for the HER2 antigen was executed using the Histostain Plus AEC Broad Spectrum Kit (Invitrogen) per manufacturer's instructions. H&E staining was also performed per manufacturer's instructions (Sigma Aldrich) for the alcoholic Eosin Y solution. For image acquisition, a standard brightfield microscope (Zeiss Axioskop 2 equipped with a Zeiss Axiocam MRc5 color camera) was used at a magnification of 20x.

3. Results

3.1. Distribution and Penetration of Gold Nanoshells in Intact Human Breast Tissue. The goal of this study was to evaluate the distribution of anti-HER2-conjugated gold nanoshells on resected intact tissue specimens. For comparison, the nanoshell labeling between HER2-positive and HER2-negative tissue samples was evaluated using a two-photon imaging system. As previously reported, this imaging system is capable of enhancing and capturing the luminescence signature of the gold nanoshells [23] while also collecting a stack of images taken through the depth of the tissue of interest. Figure 2 represents such images of HER2-positive and HER2-negative cancerous tissue samples incubated with HER2-targeted nanoshells. Each sequential increment in the z-direction represents 5 μm into the tissue. Qualitatively, the first image (taken at the surface or at 0 μm) in Figure 2 demonstrates that the nanoshells preferentially label HER2 receptors on the surface of the tissue. Additionally, Figure 2 displays decreased signal as the focal spot from the confocal microscope penetrates further into the tissue. This is believed to be due to a minimal number of nanoshells being able to penetrate the tissue in the limited amount of incubation time, thus decreasing signal collected beyond the surface. A quantitative difference of the nanoshell signal at the surface of the HER2-positive and HER2-negative tissue was calculated. Using ImageJ imaging software, it was determined that approximately 66% of the FOV for HER2-positive tissue was covered in nanoshells versus just 2% for the FOV of the HER2-negative tissue. This confirms the preferential labeling and visualization of HER2-positive tissue using anti-HER2 nanoshells.

To further validate the surface binding of the nanoshells, hyperspectral images of different tissue sections were also acquired. Figure 3(a) shows a representative surface of a HER2-positive tissue section after incubation with anti-HER2 nanoshells. Figure 3(b) illustrates tissue 24 μm beyond the surface of the same tissue. Spectra from multiple ($n = 3$) specimens that were incubated with anti-HER2 nanoshells were acquired, and analysis showed that tissues without nanoshells had very similar spectra across different patients. Figure 3(c) displays the respective spectral information of each FOV shown in Figures 3(a) and 3(b). Additionally, the spectra of HER2-positive tissue without nanoshells have been included as a control. As can be seen in this graph, the spectra of the surface of the HER2-positive tissue incubated with anti-HER2 nanoshells are distinctive from that of the same tissue 24 μm beyond the surface. In fact, the spectra of the tissue beyond the surface of the nanoshell-labeled specimen are very similar to the spectra of the surface of the control. These results support our findings that the targeted nanoshells primarily localized to the surface of the tissue.

3.2. Enhanced Optical Imaging of Intact Ex Vivo Human Breast Cancer Tissue Using Gold Nanoshells. Based on previous results demonstrating the preferential labeling of HER2-targeted nanoshells on the surface of intact *ex vivo* HER2-positive tissue specimens, we assessed the potential of using a standard stereomicroscope to visualize this enhanced contrast. For this component of the study, human breast tissue specimens that overexpressed HER2 receptors at the time of patient diagnosis were evaluated and compared to normal breast tissue. Due to the ultimate goal of utilizing gold nanoshells to rapidly label tumor margins intraoperatively in diverse patient populations, we examined tissue from patients who had and had not undergone neoadjuvant chemotherapy. All tissue samples were incubated with either antibody diluent buffer or the anti-HER2-targeted nanoshells for 5 minutes at 37°C. As shown in Figure 4, which represents raw images taken with a stereomicroscope, intact tissue specimens incubated with antibody diluent alone showed no markings or features characteristic of nanoshells. However, tissue specimens incubated with the anti-HER2-targeted nanoshells demonstrate numerous particles on the surfaces of the tissues. Qualitatively, the HER2-positive tissue from the patient who did not undergo previous chemotherapy shows the greatest labeling with the targeted nanoshells. The HER2-positive tissue from the patient who did undergo neoadjuvant chemotherapy does demonstrate enriched nanoshell labeling when compared to normal tissue, though not to the same extent as the patient without previous chemotherapy. In contrast, the normal tissue shows the least amount of nanoshell labeling, and only a few areas of nanoshells can be visually perceived.

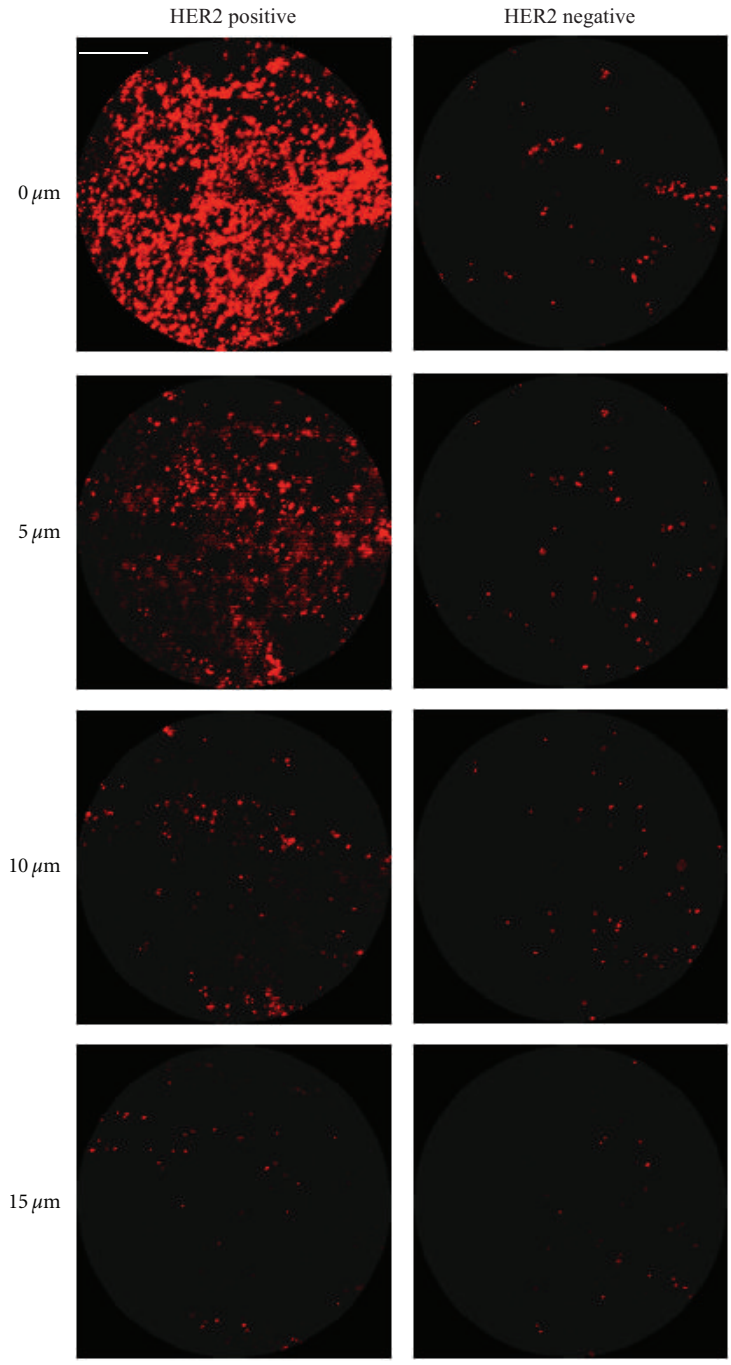

Figure 2: *Z*-stack two-photon luminescence images of HER2-positive and HER2-negative tissue incubated with HER2-targeted nanoshells for 5 minutes at 37°C. Each progressive image represents an increase in depth penetration of 5 μm. Magnification = 20x. Scale bar = 50 μm.

While the degree of nanoshell labeling can be visualized without image adjustments under a standard stereomicroscope, the superior extent of this labeling can be seen more clearly after a simple contrast enhancement using imaging software (ImageJ). As seen in Figure 5(a), the nanoshells are even more discernable against the tissue background regardless of inherent tissue constituents.

To validate the enhanced nanoshell labeling seen by macroscopic imaging, the surfaces of the same tissue samples were also imaged using reflectance confocal microscopy (Figure 5(b)). Concurring with the stereomicroscopic images, we see dramatic nanoshell surface labeling when using targeted nanoshells with previously untreated HER2-positive tissue. For the HER2-positive sample that had formerly undergone chemotherapy, we also see enhanced nanoshell labeling, though to a lesser degree than the untreated sample as suggested by the stereomicroscopy results. The normal breast tissue displays the least amount of

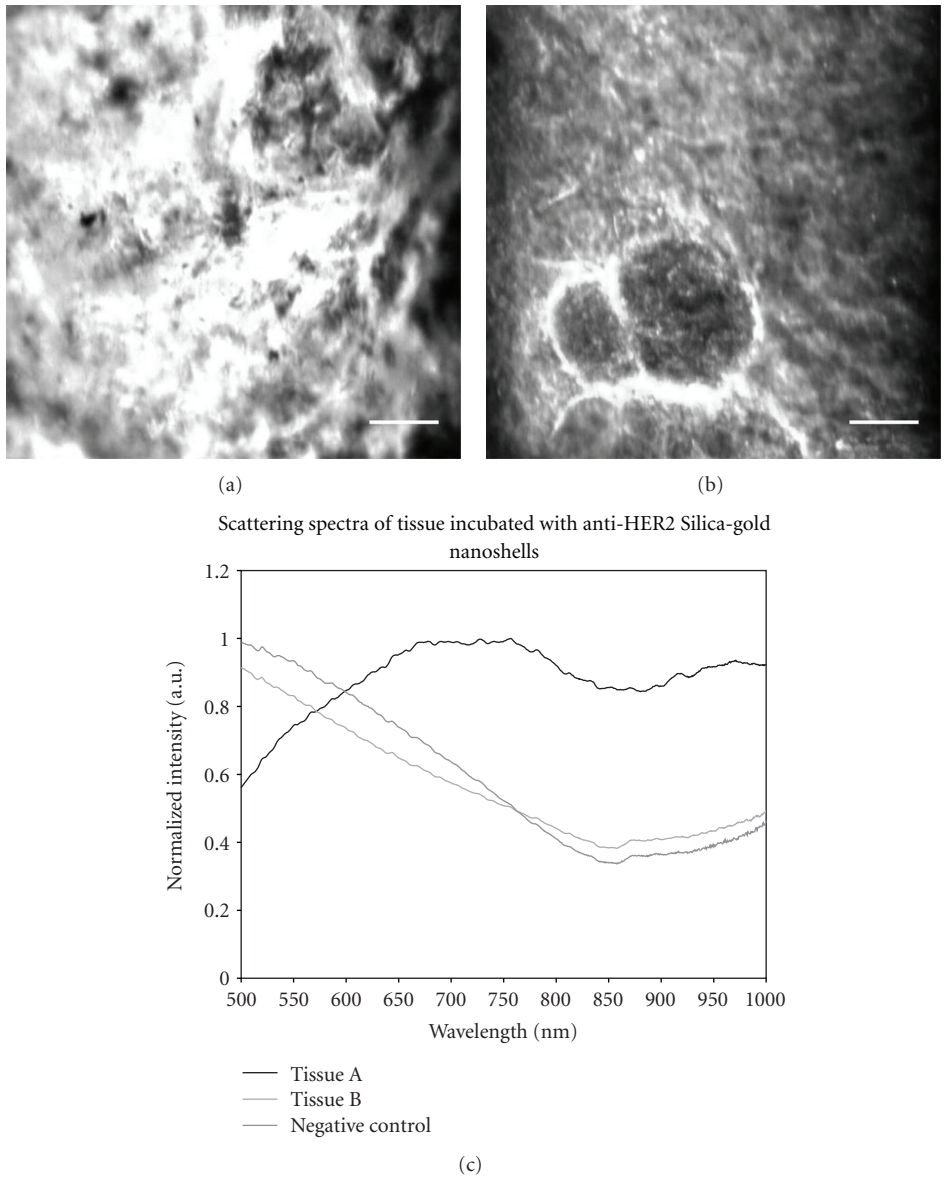

Figure 3: Darkfield images of HER2-positive tissue sectioned after incubation with anti-HER2-targeted silica-gold nanoshells. (a) Surface of HER2-positive tissue, (b) 24 μm beyond the surface of the same tissue. (c) Scattering spectra of the fields of view depicted in (a) and (b). Additionally, spectra from the surface of HER2-positive tissue not incubated with silica-gold nanoshells are shown as a negative control. Scale bar = 50 μm.

surface labeling with only minimal nanoshells evident with either imaging system. Reflectance intensity measurements (data not shown) were ~2.5 to 3 times greater for both the HER2-positive tissue sample receiving chemotherapy and for the HER2-positive tissue not receiving chemotherapy when compared to the normal tissue sample.

Subsequent histological analysis shown in Figure 5(c) reveals that the distribution of HER2 receptors seen with nanoshell-enabled contrast corresponds to that seen with IHC against HER2. The HER2 expression seen by IHC is greater for the previously untreated HER2-positive tissue sample than for the sample that had undergone neoadjuvant chemotherapy. This is believed to be due to the effects of chemotherapy. Rasbridge et al. previously demonstrated that patient response to chemotherapy is highly variable, with patients previously negative for HER2 overexpression occasionally becoming positive after treatment and patients previously positive for HER2 overexpression subsequently becoming negative [26]. Although patient response to chemotherapy varies, tissues previously identified as overexpressing HER2 receptors during initial diagnosis, regardless of chemotherapy exposure, demonstrate enhanced nanoshell labeling over normal tissue. Additionally, H&E-stained sections of all tissue samples have been included (Figure 5(d)) to illustrate the microscopic characteristics and differences associated with cancerous versus noncancerous conditions.

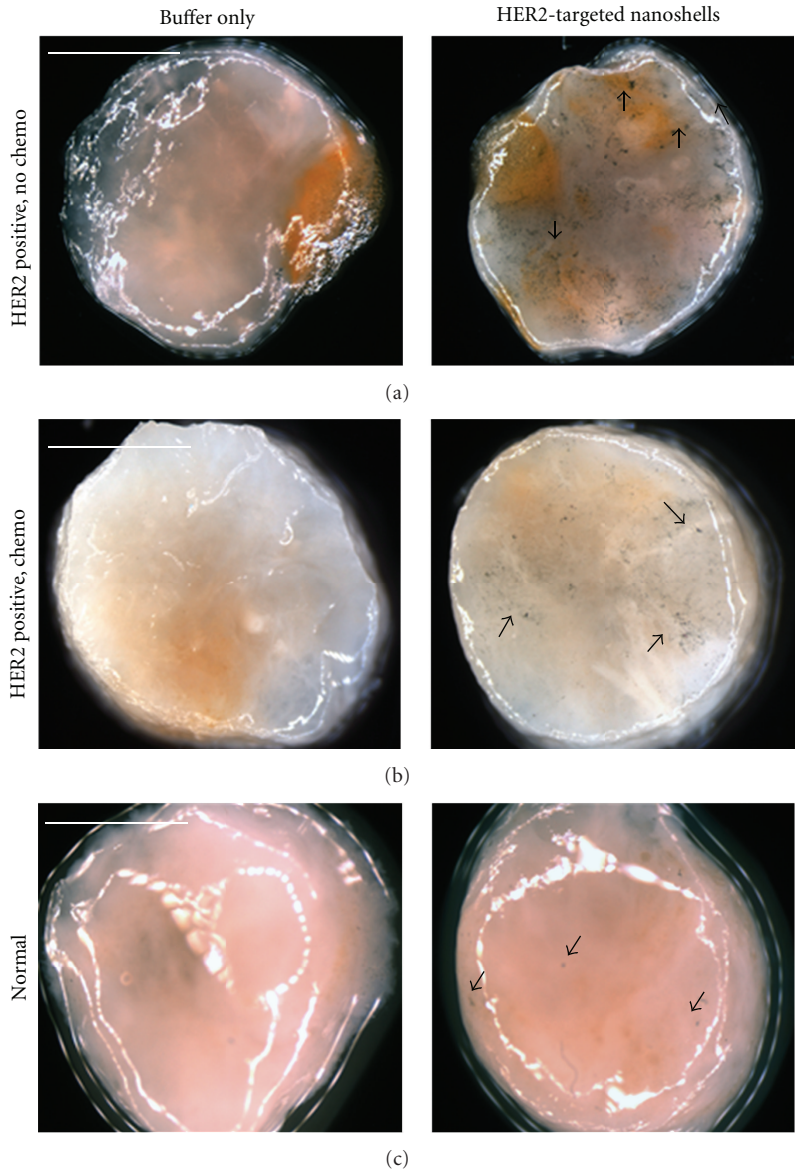

Figure 4: Raw stereomicroscope images of (a) and (b) HER2-overexpressing cancerous and (c) normal tissue incubated with either buffer or HER2-targeted nanoshells for 5 minutes at 37°C. Cancerous tissue taken from a patient (a) without chemotherapy and (b) following neoadjuvant chemotherapy. Arrows represent nanoshells. Images taken at 2x. Scale bars = 2.5 mm.

4. Discussion

In this study we demonstrated the ability to use targeted gold nanoshells to rapidly improve visualization of a specific biomarker associated with disease aggression and progression (HER2) in intact *ex vivo* human breast tissue and confirmed binding location via confocal and darkfield hyperspectral microscopy. By utilizing silica-gold nanoshells designed as rapid diagnostic imaging agents, surgeons and pathologists may be able to realize tumor margin status directly in the operating room after both macroscopic and microscopic assessment. While multiple methods of intraoperative tumor margin detection are currently under investigation [27–31], we are developing an inexpensive and portable system for rapidly analyzing *ex vivo* specimens based on the desire to enhance current methodologies without delay in clinical translation due to regulatory concerns associated with *in vivo* systems.

The ability to enhance contrast of malignancy using topically applied agents has previously been demonstrated for oral and breast tissue using fluorescently labeled deoxyglucose and epidermal growth factor (EGF) conjugates [32–34] as well as cervical tissue using fluorescently labeled gold nanoparticles targeted to EGF receptors [35]. However, these studies employed incubation times ranging from 20–45 minutes, which exceeds the length of time currently needed to obtain tumor margin status using frozen section histology. Additionally, the aforementioned studies utilized

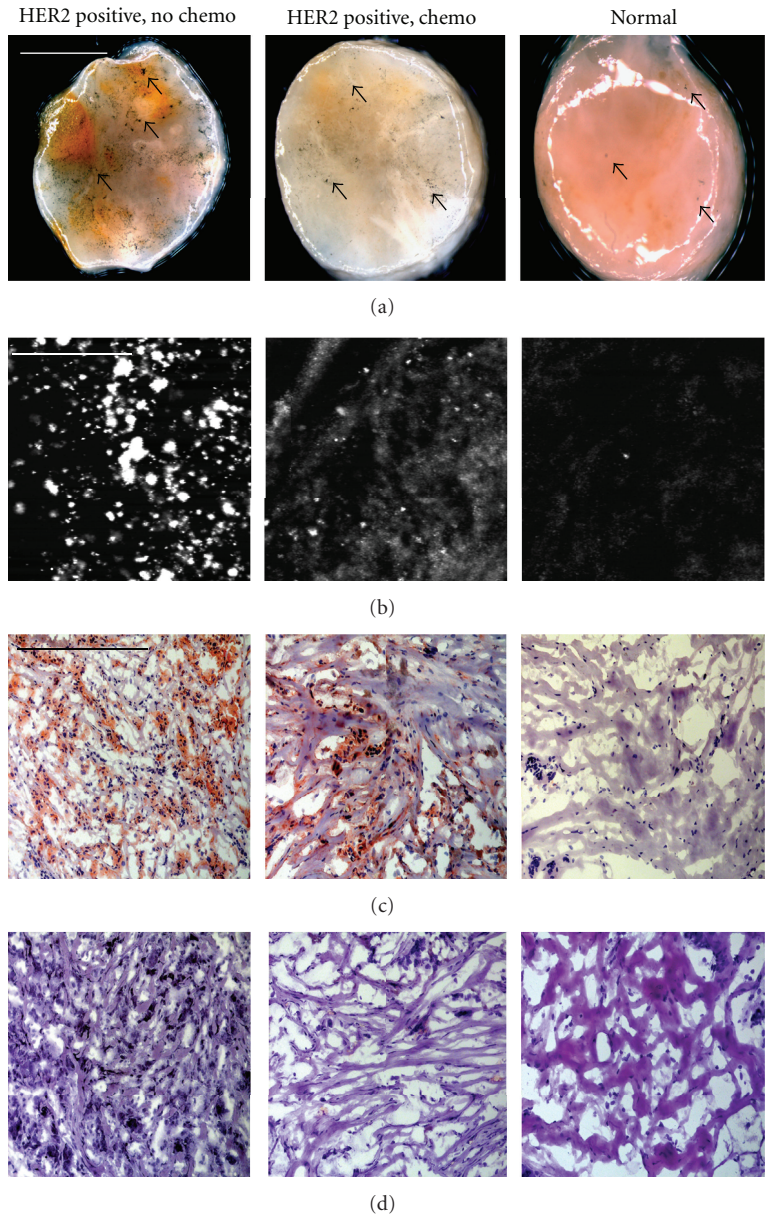

Figure 5: (a) Stereomicroscopic images of HER2-overexpressing breast tissue (with and without neoadjuvant chemotherapy) and normal breast tissue incubated with HER2-targeted nanoshells for 5 minutes at 37°C after contrast enhancement. Magnification at 2x; scale bar = 2.5 mm. Arrows represent nanoshells. (b) Respective reflectance confocal microscopy images of tissue samples from (a). Power = 0.4 mW and scale bar = 75 μm. Respective (c) HER2 immunohistochemistry and (d) H&E results taken under brightfield microscopy under 20x magnification. Scale bar = 0.35 mm.

optical clearing agents, which may be necessary for particles that target intracellular biomarkers [36, 37]. Nevertheless, gold nanoshells targeted to extracellular biomarkers may offer more favorable opportunities for *ex vivo* intraoperative tumor margin detection without the need for lengthy incubation times or the use of optical clearing agents.

Recently, we verified that silica-based gold nanoshells could be used to enhance contrast of both HER2-overexpressing cells and tissue sections within 5 minutes of incubation time [10, 11]. However, translating this technology towards clinical relevancy requires the ability to assess whole, unsectioned specimens. Here, we confirm that gold nanoshells, when targeted to HER2 receptors, can be used to distinguish intact HER2-overexpressing *ex vivo* tissue from normal tissue within the same incubation time, and we demonstrate that this difference can be observed macroscopically. These results are supported by microscopic imaging and immunohistochemistry against HER2.

By employing macroscopic imaging intraoperatively, clinicians may be better able to distinguish cancerous and normal breast tissue prior to further microscopic analysis and subsequent histological processing. Ultimately, this system could also be used for other diagnostic applications, for other anatomical locations, and for other biomarkers

associated with disease. By facilitating fast and accurate tumor margin results intraoperatively as a supplement to current diagnostic methods, we expect to reduce the amount of time spent in surgery due to inadequate tissue removal.

To translate these findings more readily to the clinic, we are presently developing a low-cost widefield imaging system that can be used to detect the overexpression of HER2 (and other extracellular biomarkers) through contrast enhancement provided by gold nanoshells. In addition, we plan to collect data from diverse patient populations and assess results with fresh tissue samples. In this way, the use of gold nanoshells may demonstrate widespread efficacy or be limited only to specific patient subsets.

Authors' Contributions

Bickford and Langsner contributed equally to this work.

Acknowledgments

The authors thank the Cooperative Human Tissue Network for providing fresh frozen tissue samples. The authors thank Glenn P. Goodrich and Nanospectra Biosciences, Inc. for providing nanoshells used in the studies. The authors also thank Nadhi Thekkek for assistance with ImageJ data acquisition. This work was supported by a Department of Defense Congressionally Directed Breast Cancer Research Program Era of Hope Scholar Award to Rebekah Drezek, the Center for Biological and Environmental Nanotechnology (EEC-0118007 and EEC-0647452). L. Bickford thanks the Department of Defense (DoD) for training support through the National Defense Science & Engineering Graduate Fellowship (NDSEG) Program.

References

[1] A. C. Society, "Breast Cancer Facts and Figures 2005-2006," American Cancer Society, Inc., 2010, http://www.cancer.org/Research/CancerFactsFigures/BreastCancerFactsFigures/breast-cancer-facts–figures-2005-2006.

[2] R. G. Steen, *A Conspiracy of Cells*, Plenum Press, New York, NY, USA, 1993.

[3] C. M. Mojica, R. Bastani, W. J. Boscardin, and N. A. Ponce, "Low-income women with breast abnormalities: system predictors of timely diagnostic resolution," *Cancer Control*, vol. 14, no. 2, pp. 176–182, 2007.

[4] B. Fisher, S. Anderson, J. Bryant et al., "Twenty-year follow-up of a randomized trial comparing total mastectomy, lumpectomy, and lumpectomy plus irradiation for the treatment of invasive breast cancer," *The New England Journal of Medicine*, vol. 347, no. 16, pp. 1233–1241, 2002.

[5] R. G. Pleijhuis, M. Graafland, J. de Vries, J. Bart, J. S. de Jong, and G. M. van Dam, "Obtaining adequate surgical margins in breast-conserving therapy for patients with early-stage breast cancer: current modalities and future directions," *Annals of Surgical Oncology*, vol. 16, no. 10, pp. 2717–2730, 2009.

[6] A. Oouchi, K. I. Sakata, H. Masuoka et al., "The treatment outcome of patients undergoing breast-conserving therapy: the clinical role of postoperative radiotherapy," *Breast Cancer*, vol. 16, no. 1, pp. 49–57, 2009.

[7] C. S. Melanie, W. N. Kent, J. Z. Mark et al., "The importance of the lumpectomy surgical margin status in long term results of breast conservation," *Cancer*, vol. 76, pp. 259–267, 1995.

[8] N. Cabioglu, K. K. Hunt, A. A. Sahin et al., "Role for intraoperative margin assessment in patients undergoing breast-conserving surgery," *Annals of Surgical Oncology*, vol. 14, no. 4, pp. 1458–1471, 2007.

[9] R. A. Graham, M. J. Homer, C. J. Sigler et al., "The efficacy of specimen radiography in evaluating the surgical margins of impalpable breast carcinoma," *American Journal of Roentgenology*, vol. 162, no. 1, pp. 33–36, 1994.

[10] L. R. Bickford, J. Chang, K. Fu et al., "Evaluation of immunotargeted gold nanoshells as rapid diagnostic imaging agents for HER2-overexpressing breast cancer cells: a time-based analysis," *Nanobiotechnology*, vol. 4, no. 1–4, pp. 1–8, 2008.

[11] L. R. Bickford, G. Agollah, R. Drezek, and T.-K. K. Yu, "Silica-gold nanoshells as potential intraoperative molecular probes for HER2-overexpression in ex vivo breast tissue using near-infrared reflectance confocal microscopy," *Breast Cancer Research and Treatment*, vol. 120, no. 3, pp. 547–555, 2010.

[12] K. Sokolov, M. Follen, J. Aaron et al., "Real-time vital optical imaging of precancer using anti-epidermal growth factor receptor antibodies conjugated to gold nanoparticles," *Cancer Research*, vol. 63, no. 9, pp. 1999–2004, 2003.

[13] X. Liu, Q. Dai, L. Austin et al., "A one-step homogeneous immunoassay for cancer biomarker detection using gold nanoparticle probes coupled with dynamic light scattering," *Journal of the American Chemical Society*, vol. 130, no. 9, pp. 2780–2782, 2008.

[14] R. Nahta, D. Yu, M. C. Hung, G. N. Hortobagyi, and F. J. Esteva, "Mechanisms of disease: understanding resistance to HER2-targeted therapy in human breast cancer," *Nature Clinical Practice. Oncology*, vol. 3, no. 5, pp. 269–280, 2006.

[15] D. J. Slamon, G. M. Clark, S. G. Wong, W. J. Levin, A. Ullrich, and W. L. McGuire, "Human breast cancer: correlation of relapse and survival with amplification of the HER-2/neu oncogene," *Science*, vol. 235, no. 4785, pp. 177–182, 1987.

[16] D. G. Hicks and S. Kulkarni, "HER2+ breast cancer," *American Journal of Clinical Pathology*, vol. 129, pp. 263–273, 2008.

[17] S. Vosoughhosseini, M. Lotfi, A. Fakhrjou et al., "Analysis of epidermal growth factor receptor in histopathologically tumor-free surgical margins in patients with oral squamous cell carcinoma," *African Journal of Biotechnology*, vol. 11, pp. 516–520, 2012.

[18] C. Loo, A. Lin, L. Hirsch et al., "Nanoshell-enabled photonics-based imaging and therapy of cancer," *Technology in Cancer Research and Treatment*, vol. 3, no. 1, pp. 33–40, 2004.

[19] C. Loo, L. Hirsch, M. H. Lee et al., "Gold nanoshell bioconjugates for molecular imaging in living cells," *Optics Letters*, vol. 30, no. 9, pp. 1012–1014, 2005.

[20] C. Loo, A. Lowery, N. Halas, J. West, and R. Drezek, "Immunotargeted nanoshells for integrated cancer imaging and therapy," *Nano Letters*, vol. 5, no. 4, pp. 709–711, 2005.

[21] W. Stöber, A. Fink, and E. Bohn, "Controlled growth of monodisperse silica spheres in the micron size range," *Journal of Colloid and Interface Science*, vol. 26, no. 1, pp. 62–69, 1968.

[22] D. G. Duff, A. Baiker, and P. P. Edwards, "A new hydrosol of gold clusters. 1. Formation and particle size variation," *Langmuir*, vol. 9, no. 9, pp. 2301–2309, 1993.

[23] L. Bickford, J. Sun, K. Fu et al., "Enhanced multi-spectral imaging of live breast cancer cells using immunotargeted gold nanoshells and two-photon excitation microscopy," *Nanotechnology*, vol. 19, no. 31, Article ID 315102, 2008.

[24] E. S. Day, L. R. Bickford, J. H. Slater, N. S. Riggall, R. A. Drezek, and J. L. West, "Antibody-conjugated gold-gold sulfide nanoparticles as multifunctional agents for imaging and therapy of breast cancer," *International Journal of Nanomedicine*, vol. 5, no. 1, pp. 445–454, 2010.

[25] T. Magalhães, A. von Bohlen, M. L. Carvalho, and M. Becker, "Trace elements in human cancerous and healthy tissues from the same individual: a comparative study by TXRF and EDXRF," *Spectrochimica Acta B*, vol. 61, no. 10-11, pp. 1185–1193, 2006.

[26] S. A. Rasbridge, C. E. Gillett, A. M. Seymour et al., "The effects of chemotherapy on morphology, cellular proliferation, apoptosis and oncoprotein expression in primary breast carcinoma," *British Journal of Cancer*, vol. 70, no. 2, pp. 335–341, 1994.

[27] A. Haid, M. Knauer, S. Dunzinger et al., "Intra-operative sonography: a valuable aid during breast-conserving surgery for occult breast cancer," *Annals of Surgical Oncology*, vol. 14, no. 11, pp. 3090–3101, 2007.

[28] T. Karni, I. Pappo, J. Sandbank et al., "A device for real-time, intraoperative margin assessment in breast-conservation surgery," *American Journal of Surgery*, vol. 194, no. 4, pp. 467–473, 2007.

[29] L. Tafra, R. Fine, P. Whitworth et al., "Prospective randomized study comparing cryo-assisted and needle-wire localization of ultrasound-visible breast tumors," *American Journal of Surgery*, vol. 192, no. 4, pp. 462–470, 2006.

[30] M. Bakhshandeh, S. O. Tutuncuoglu, G. Fischer, and S. Masood, "Use of imprint cytology for assessment of surgical margins in lumpectomy specimens of breast cancer patients," *Diagnostic Cytopathology*, vol. 35, no. 10, pp. 656–659, 2007.

[31] N. Nitin, L. C. Alicia, M. Tim et al., "Molecular imaging of glucose uptake in oral neoplasia following topical application of fluorescently labeled deoxy-glucose," *International Journal of Cancer*, vol. 124, no. 11, pp. 2634–2642, 2009.

[32] V. E. Strong, J. Humm, P. Russo et al., "A novel method to localize antibody-targeted cancer deposits intraoperatively using handheld PET beta and gamma probes," *Surgical Endoscopy and Other Interventional Techniques*, vol. 22, no. 2, pp. 386–391, 2008.

[33] R. J. Langsner, L. P. Middleton, J. Sun et al., "Wide-field imaging of fluorescent deoxy-glucose in ex vivo malignant and normal breast tissue," *Biomedical Optics Express*, vol. 2, no. 6, pp. 1514–1523, 2011.

[34] N. Nitin, K. J. Rosbach, A. El-Naggar, M. Williams, A. Gillenwaterand, and R. R. Richards-Kortum, "Optical molecular imaging of epidermal growth factor receptor expression to improve detection of oral neoplasia," *Neoplasia*, vol. 11, no. 6, pp. 542–551, 2009.

[35] J. Aaron, N. Nitin, K. Travis et al., "Plasmon resonance coupling of metal nanoparticles for molecular imaging of carcinogenesis in vivo," *Journal of Biomedical Optics*, vol. 12, no. 3, Article ID 034007, 2007.

[36] A. L. van de Ven, K. Adler-Storthz, and R. Richards-Kortum, "Delivery of optical contrast agents using Triton-X100, part 1: reversible permeabilization of live cells for intracellular labeling," *Journal of Biomedical Pptics*, vol. 14, no. 2, Article ID 021012, 2009.

[37] A. L. van de Ven, K. Adler-Storthz, and R. Richards-Kortum, "Delivery of optical contrast agents using Triton-X100, part 2: enhanced mucosal permeation for the detection of cancer biomarkers," *Journal of biomedical optics*, vol. 14, no. 2, Article ID 021013, 2009.

Alliance for NanoHealth (ANH) DOE Training Program
Graduate Student Research Training Fellowship 2009
Final Report

Name: Eric W. Frey
Institution: Rice University
Project Title: Single-Molecule Manipulation Studies of Single-Stranded DNA Overstretching Transitions

I. **Summary of Research:** Free energy landscapes provide the conceptual framework for understanding how proteins and nucleic acids fold, unfold, and interact with each other [1]. We reconstructed free energy landscapes of bio-molecules of biological and medical interest, by using atomic force microscopy nano-scale imaging and single-molecule manipulation, combined with non-equilibrium statistical physics [2]. Tracts of poly(dA:dT) in the genome are major determinants of nucleosome organization, due to their unique dynamic and mechanical properties [3]. We showed that as single-stranded poly(dA) is extended under force, its free energy landscape branches into multiple pathways, with the higher pathway representing a kinetically trapped state and the lower pathway representing an equilibrium state [4-5]. We also studied the nanomechanical behavior of von Willebrand factor, a multimeric blood-clotting protein involved in bleeding disorders [6]. Under a pathophysiological level of fluid shear stress known to activate von Willebrand factor that initiates blood clotting [7], we found that this protein adopts a meta-stable state that is more resistant to force-induced unfolding, and that the protein was in the activated state for much longer than previously expected [8].

II. **Reportable Outcomes:**

a. Publications

i. E. W. Frey and C.-H. Kiang, "Using the Crooks fluctuation theorem to determine the free energy profile of overstretching single-stranded DNA through multiple pathways," (2013) *in preparation*.

ii. S. S. Wijeratne, J. Martinez, E. W. Frey, M. Farach-Carson, and C.-H. Kiang, "Single-molecule mechanics of perlecan in the cartilage extracellular matrix," (2013) *in preparation*.

iii. C. Guo, N. C. Harris, S. S. Wijeratne, E. W. Frey, and C.-H. Kiang, "Multiscale mechanobiology: mechanics and the molecular, cellular, and tissue levels," *Cell & Bioscience* (2013) *submitted*.

iv. S. S. Wijeratne, E. Botello, H.-C. Yeh, Z. Zhou, A. Bergeron, E. W. Frey, J. M. Patel, J. Moake, J.-F. Dong, and C.-H. Kiang, "Mechanical activation of a multimeric adhesive protein through domain conformational change," *Physical Review Letters* 110 (2013).

v. Eric W. Frey, Ashton A. Gooding, Sitara Wijeratne, and Ching-Hwa Kiang, "Understanding the physics of DNA using nanoscale single-molecule manipulation," *Front. Phys.***7** (2012).

vi. Eric W. Frey, *Experimental Free Energy Landscape Reconstruction of DNA Unstacking Using Crooks Fluctuation Theorem*, Rice University M.S. Thesis (2012).

b. Contributed Presentations

i. 21st Keck Annual Research Conference, *poster* (2011)
ii. Meeting of the Texas section of the American Physical Society, *oral presentation* (2011)
iii. Brockman Hall for Physics dedication, *poster* (2011)
iv. The Physics of Evolution, UCSD workshop, *poster* (2010)
v. Rice Quantum Institute, *oral presentation* (2010)
vi. Alliance for NanoHealth symposium, *poster* (2010)
vii. BioScience Research Collaborative grand opening, *poster* (2010)

III. **Conclusion:** The interdisciplinary training provided by this fellowship has opened the door to new collaborations between physicists such as myself and biomedical researchers. Experience applying atomic force microscopy and equilibrium and non-equilibrium physics to the fundamental properties of disease-associated biological molecules has enabled contributions to additional projects on the perlecan protein, and DNA and protein p53 interactions, projects which are currently underway. Recently, in collaboration with colleagues at Baylor College of Medicine, we have designed and imaged a novel 2D nano-grid self-assembled from a single RNA monomer, making it potentially suitable for delivery and growth *in vivo*. The research supported by this fellowship lead to the achievement of PhD candidacy in 2012 and the expected completion of my PhD thesis by the end of 2013.

IV. **References:**

[1] Bryngelson et al., "Theory of Protein Folding: the Energy Landscape Perspective," *Annu. Rev. Phys. Chem.* 48 (1997).

[2] Alemany et al., "Experimental Free-Energy Measurements of Kinetic Molecular States using Fluctuation Theorems," *Nat. Phys.* 8 (2012).

[3] Segal et al., "Poly(dA:dT) Tracts: Major Determinants of Nucleosome Organization," *Curr. Opin. Struct. Biol.* 1 (2009).

[4] Eric W. Frey, *Experimental Free Energy Landscape Reconstruction of DNA Unstacking Using Crooks Fluctuation Theorem*, Rice University M.S. Thesis (2012).

[5] E. W. Frey and C.-H. Kiang, "Using the Crooks fluctuation theorem to determine the free energy profile of overstretching single-stranded DNA through multiple pathways," (2013) *in preparation*.

[6] Moake et al., "Unusually Large Plasma Factor VIII: von Willebrand Factor Multimers in Chronic Relapsing Thrombotic Thrombocytopenic Purpura," *N. Engl. J. Med.* 307 (1982).

[7] Moake et al., "Involvement of Large Plasma von Willebrand Factor (vWF) Multimers and Unusually Large vWF Forms from Endothelial Cells in Shear-Stress Induced Platelet Aggregation," *J. Clin. Invest.* 78 (1986).

[8] S. S. Wijeratne, E. Botello, H.-C. Yeh, Z. Zhou, A. Bergeron, E. W. Frey, J. M. Patel, J. Moake, J.-F. Dong, and C.-H. Kiang, "Mechanical activation of a multimeric adhesive protein through domain conformational change," *Physical Review Letters* (2013) *in press*.

V. **Appendices**

Current Career Profile (optional):

- Briefly describe your career profile:
  - I received an MS in physics and PhD candidacy at Rice University in 2012, after obtaining an undergraduate degree in physics at Miami University in 2008. As an undergraduate I worked in a biological physics lab and co-authored three publications on fluorescence microscopy under high pressure. In graduate school, I continued research in biological physics, but changed focus to the nano-scale and health-related aspects of biomolecules, and began several interdisciplinary collaborations with medical researchers in the Houston medical center. I expect to complete my PhD in December 2013.
- Include how the NASA/DOE Fellowship helped advance your career:
  - This fellowship has provided the interdisciplinary training needed for me, as a physicist, to make meaningful contributions to the field of nano-health. The research on poly(dA) and von Willebrand factor resulted in an MS thesis and PhD candidacy, and lead to further collaborations on perlecan, DNA and protein p53, and the self-assembly of RNA nano-structures. As a result, I was awarded a grant from the Nanobiology Interdisciplinary Graduate Training Program (NIGTP) for 2012-2013, which has similar objectives as the Alliance for NanoHealth fellowship. By the end of 2013, I expect to have completed my PhD in physics with a focus on interdisciplinary, nano-scale research of medically-relevant biological systems.

Published in final edited form as:
Front Phys. 2012 October ; 7(5): 576–581. doi:10.1007/s11467-012-0261-0.

Understanding the physics of DNA using nanoscale single-molecule manipulation

Eric W. Frey, **Ashton A. Gooding**, **Sitara Wijeratne**, and **Ching-Hwa Kiang**†
Department of Physics and Astronomy, Rice University, Houston, TX 77005, USA

Abstract

Processes for decoding the genetic information in cells, including transcription, replication, recombination and repair, involve the deformation of DNA from its equilibrium structures such as bending, stretching, twisting, and unzipping of the double helix. Single-molecule manipulation techniques have made it possible to control DNA conformation and simultaneously detect the induced changes, revealing a rich variety of mechanically-induced conformational changes and thermodynamic states. These single-molecule techniques helped us to reveal the physics of DNA and the processes involved in the passing on of the genetic code.

Keywords

single-molecule manipulation; the physics of DNA

1 Introduction

DNA is the carrier of genetic information and is involved in biomolecular processes such as transcription and replication. Many of these processes are governed by the mechanics and thermodynamics of bending, stretching, twisting, and unzipping the double helix [1-6]. Double-stranded DNA (dsDNA) is a semi-flexible polymer, with its base-stacking architecture and negative charges along its phosphate backbone. In physiological conditions, thermal fluctuations do not bend it significantly on length scales below 50 nm, which is equivalent to 150 base pairs (bp) [7]. The 10 μm-long DNA of a viral genome can be packed inside a capsid of 50 nm in diameter [8-10], and in eukaryotic cells, histones bend DNA into loops of 10 nm in diameter. The latter serves as the first step in the hierarchical packaging of the genome in eukaryotes (Fig. 1), and it regulates gene expression by obstructing access to base pairs [11]. Histones, helicases, topoisomerases, and RNA and DNA polymerases are examples of proteins that generate or relieve tension and torque in DNA to enable its biochemical functions [5, 12-15]. With advances in single-molecule techniques, it has been possible to examine the physics of DNA directly. By providing control and measurement of force of a single molecule, these techniques have revealed a variety of DNA conformations and much of DNA's complex behavior.

2 Single-molecule manipulation experiments

Single-molecule manipulation techniques using atomic force microscopy (AFM), optical tweezers, and magnetic tweezers are illustrated in Fig. 2. These techniques have been used to manipulate a variety of biological molecules. In each of these methods, a single DNA molecule is attached between a substrate and a force probe, either an AFM tip or a micron-

†chkiang@rice.edu.

sized bead, in an aqueous solution. The change in molecular end-to-end distance is determined from the change in probe and substrate positions. The force on the molecule is determined from displacement of the probe relative to its equilibrium position. Nonspecific attachment, typically used in AFM, is achieved by adsorption of DNA to the substrate surface or the probe surface. Specific attachment, employed by optical and magnetic tweezers, is achieved by functionalization of probe and substrate surfaces. These modifications exploit the high affinity and specificity of binding among ligand-receptor, antibody-antigen pairs and DNA hybridization. Other techniques elongate DNA by confining the molecule within micro or nano-sized obstacles. Such techniques include driving DNA electrophoretically through microlithographic arrays [17], nanochannels [18, 19], and nanopores [20].

In AFM [Fig. 2(a)], the force probe is an AFM tip attached to a cantilever, and the substrate is mounted on a piezoelectric scanner. Moving the substrate toward the AFM tip allows nonspecific or specific molecular attachment between the substrate and cantilever. When the molecule is attached to the tip and the substrate, moving the substrate away from the cantilever produces force on the attached molecule, and the resulting bending of the cantilever is detected by the deflection of the laser beam reflecting off the back of the cantilever onto a position-sensitive detector. The force exerted on the molecule, F, is determined by Hooke's law, $F = -Kz$, where K is the cantilever's spring constant and z is the cantilever displacement from its equilibrium position. Using the equipartition theorem, the spring constant is determined using $\frac{1}{2}k_{\mathrm{B}}T = \frac{1}{2}K\left\langle z^2\right\rangle$, where k_{B} is Boltzmann's constant and T is temperature [23]. AFM cantilevers used for single-molecule manipulation typically have a spring constant $K = 10$ pN/nm or higher. This results in unloaded cantilever fluctuations of at least 5 pN at room temperature, which sets the limit of the noise level in the force on an attached molecule measurable by AFM. AFM is able to measure high forces up to a few nanoNewtons, the limit usually being set by the strength of the attachment [24-26].

In a typical optical tweezers setup [Fig. 2(b)], the force probe is a micrometer-sized dielectric bead captured in an optical trap. The substrate may be the side of a translatable fluid chamber or a second bead held by either a micropipette or a second optical trap [4, 12. 14]. The optical trap consists of a tightly-focused laser, which exerts a three-dimensional restoring force on a dielectric bead trapped near the laser focus. To minimize photo-damage to the trapped biomolecules, near-infrared wavelengths are used [27-29]. The displacement of the bead from the trap center can be measured by video tracking via an optical microscope. For small displacements of the bead, the force is determined using Hooke's law, and the trap stiffness is determined using the equipartition theorem, as in the case of AFM. Optical traps typically have spring constants ranging from 0.005–1 pN/nm, which is smaller than the AFM cantilevers. The low noise level allows measurement of forces on the molecule as low as 0.1 pN. Optical tweezers are generally used to probe forces less than 100 pN, where the ligand-receptor or antibody-antigen pairs used to attach the DNA unbind [30].

Magnetic tweezers [Fig. 2(c)] are similar to optical tweezers, except that the force probe consists of a super-paramagnetic bead in an applied magnetic field. The force on the bead is proportional to the gradient of the square of the magnetic field. In addition, a torque is applied to the bead due to its small magnetic polarization anisotropy, which tends to align the bead with the applied magnetic field. Thus, by rotating the applied field, the attached molecule can be twisted as well as stretched [31, 32]. Magnetic tweezers have miniscule stiffness as low as 10^{-6} pN/nm, allowing them to probe forces as low as 10^{-3} pN. Like optical tweezers, they can probe up to 100 pN until the DNA handles break [33-35].

Each of these single-molecule manipulation techniques has advantages and disadvantages. While AFM is capable of probing large forces up to a few nanoNewtons, it is generally not sensitive for probing forces less than 5 pN. Optical tweezers and magnetic tweezers, on the other hand, can measure forces as small as 0.1 pN and 10^{-3} pN, respectively. However, these techniques have an upper limit for the forces that can be studied, since the DNA handles usually break around 100 pN. Other considerations include spatial and temporal resolution, and stability and drift control. For high spatial resolution, subnanometer precision is routinely obtained using AFM [36], and optical tweezers has achieved high spatial resolution in a recent work [37]. Video tracking of beads in optical tweezers and magnetic tweezers offers a simple method for measuring position, but with less resolution (around 5 nm) and sampling rate limited to 500 Hz for fast cameras [38], while greater resolution and sampling rates are possible using more sophisticated methods [39]. Dynamic position control is implemented in AFM and optical tweezers using a piezoelectric scanner with capacitive position detection in a feedback loop, with an accuracy of 1 nm or better. This enables force-clamping, a mode in which the extension of the molecule is measured over time while maintaining a constant applied force. Magnetic tweezers are uniquely suited to high-bandwidth force-clamping at low cost, without the need for sophisticated feedback loops, since large magnet displacements change the applied force only slightly (typically 1 pN for a displacement of 1 mm).

Recent efforts have been made to combine fluorescence imaging with single-molecule manipulation [40, 41]. For example, by using fluorescent dyes which bind to specific conformations of DNA, this combination of methods can distinguish different structures of DNA under applied force [42]. In addition, fluorescence can be used to pinpoint the location where an applied force has the largest effect on DNA [43]. Finally, the large forces obtainable in an AFM experiment enabled direct fluorescence imaging of DNA strand rupture [44].

3 Polymer physics models of DNA

Single-molecule manipulation experiments measure the force-extension curve of DNA, and the data are fitted to polymer physics models to determine parameters that define its mechanical properties (Fig. 3). In solution, DNA adopts a random coil conformation which minimizes free energy. Extending the molecule imposes a constraint limiting the number of accessible conformations, thus the work done on the molecule is mainly used to offset the reduced entropy. For dsDNA, at forces less than 10 pN the force-extension curve is dominated by this entropic elasticity. At higher forces, dsDNA begins to exceed its contour length and, consequently, its double-helix structure is disrupted. The polymer elasticity models which best describe the force-extension curves of single-stranded DNA (ssDNA) and dsDNA are the freely-jointed chain (FJC) and wormlike chain (WLC) models, respectively.

In the FJC model, the polymer consists of a chain of freely rotating segments of characteristic Kuhn length. The extensible FJC assumes that the polymer is stretchable, and the force is related to extension x by [30, 46]

$$x = b_{ss}\left[\coth(2\beta P_{ss}F) - \frac{1}{2\beta P_{ss}F}\right]\left(1+\frac{F}{K_{ss}}\right) \quad (1)$$

where P_{ss}, b_{ss}, and K_{ss} are the persistence length, contour length, and stretch modulus of ssDNA, respectively, and $\beta = 1/(k_B T)$. The persistence length is a measure of bending stiffness. The K_{ss} accounts for the extensibility of the molecule. For ssDNA, $P_{ss} = 0.75$ nm and $K_{ss} = 800$ pN [30, 47-49].

The WLC models a polymer as a flexible rod characterized by a bending stiffness. In an extensible WLC model, force can be related to extension by [45, 50]

$$x = b_{ds}\left(1 - \frac{1}{\sqrt{4\beta P_{ds} F}} + \frac{F}{K_{ds}}\right) \quad (2)$$

where P_{ds}, b_{ds}, and K_{ds} are the persistence length, contour length, and elastic stretch modulus of dsDNA, respectively. For dsDNA, P_{ds} = 50 nm and K_{ds} = 1200 pN [30, 47-49].

4 The overstretching transitions and force-induced melting

Figure 4(a) is a typical force-extension curve of dsDNA. At low forces, the molecule behaves like a WLC. When the force reaches 65 pN, the force-extension curve shows a plateau, indicating a cooperative transition of the molecular conformation [30, 51]. Recent experiments demonstrate that both melting and a B-DNA to S-DNA transition occurs at this force, depending on environmental factors [52-54]. At forces around 150 pN, dsDNA melts into ssDNA, where the force-extension curve is best described by the extensible FJC model [Eq. (1)] with a persistence length and stretch modulus consistent with ssDNA [30, 47, 48]. Another example is poly(dA) (ssDNA composed only of adenine bases), where distinct plateaus and multiple force-extension pathways have been observed [21, 55]. One poly(dA) pathway is similar to that of random-sequence ssDNA, whereas the other pathway has an additional, energetically favored transition [Fig. 4(b)], possibly to a state in which the bases are weakly stacked. The multiple pathways suggest that poly(dA) has two conformational states when stretched close to twice its contour length. Further study is required to elucidate the structures responsible for these transitions and whether they can be tuned by changing environmental conditions, such as salt concentration and temperature.

Pulling single DNA molecules has been found to unzip as well as stretch DNA. Unzipping occurs when the secondary structure, i.e., the double helix of dsDNA is disrupted, resulting in unpairing of the bases. The dynamics of unzipping are sequence-dependent, as evidenced by higher observed forces in GC-rich regions [56] and good reproducibility for unzipping/rezipping molecules of the same sequence [57, 58].

5 Conclusion

The response of the DNA molecule to a force is crucial in many biochemical functions, including transcription, replication, recombination, and packaging. Fundamental DNA properties are being revealed as melting and complex reactions are being probed. Understanding quantitatively the detailed mechanical property of single- and double-stranded DNA allows us to characterize different DNA conformational states and their associated energetics. This quantitative information will help us predict DNA behavior and interactions that are important in biological and medical systems.

Acknowledgments

We thank NSF DMR-0907676, Welch Foundation No. C-1632, Hamill Innovation Fund, NIH/NIBIB T32EB009379-03, and the Alliance for NanoHealth, NASA/DOE DE-FG02-08ER64712 for support.

References

1. Hogan ME, Austin RH. Nature. 1987; 329(6136):263. [PubMed: 3627268]
2. Goodman SD, Nash HA. Nature. 1989; 341(6239):251. [PubMed: 2528697]
3. Stasiak A, Capua ED. Nature. 1982; 299(5879):185. [PubMed: 7050731]

4. Hegner M, Smith SB, Bustamante C. Proc Natl Acad Sci USA. 1999; 96(18):10109. [PubMed: 10468570]
5. Johnson DS, Bai L, Smith BY, Patel SS, Wang MD. Cell. 2007; 129(7):1299. [PubMed: 17604719]
6. Bloomfield, VA.; Crothers, DM.; Tinoco, I, Jr. Nucleic Acids: Structures, Properties, and Functions. Sausalito, California: University Science Books; 2000.
7. Baumann CG, Smith SB, Bloomfield VA, Bustamante C. Proc Natl Acad Sci USA. 1997; 94(12): 6185. [PubMed: 9177192]
8. Smith DE, Tans SJ, Smith SB, Grimes S, Anderson DL, Bustamante C. Nature. 2001; 413(6857): 748. [PubMed: 11607035]
9. Fuller DN, Raymer DM, Kottadiel VI, Rao VB, Smith DE. Proc Natl Acad Sci USA. 2007; 104(43): 16868. [PubMed: 17942694]
10. Fuller DN, Rickgauer JP, Jardine PJ, Grimes S, Anderson DL, Smith DE. Proc Natl Acad Sci USA. 2007; 104(27):11245. [PubMed: 17556543]
11. Felsenfeld G, Groudine M. Nature. 2003; 421(6921):448. [PubMed: 12540921]
12. Brower-Toland BD, Smith CL, Yeh RC, Lis JT, Peterson CL, Wang MD. Proc Natl Acad Sci USA. 2002; 99(4):1960. [PubMed: 11854495]
13. Strick TR, Croquette V, Bensimon D. Nature. 2000; 404(6780):901. [PubMed: 10786800]
14. Abbondanzieri EA, Greenleaf WJ, Shaevitz JW, Landick R, Block SM. Nature. 2005; 438(7067): 460. [PubMed: 16284617]
15. Wuite GJL, Smith SB, Young M, Keller D, Bustamante C. Nature. 2000; 404(6773):103. [PubMed: 10716452]
16. Luger K, Mäder AW, Richmond RK, Sargent DF, Richmond TJ. Nature. 1997; 389(6648):251. [PubMed: 9305837]
17. Volkmuth WD, Austin RH. Nature. 1992; 358(6387):600. [PubMed: 1501715]
18. Tegenfeldt JO, Prinz C, Cao H, Chou S, Reisner WW, Riehn R, Wang YM, Cox EC, Sturm JC, Silberzan P, Austin RH. Proc Natl Acad Sci USA. 2004; 101(30):10979. [PubMed: 15252203]
19. Reisner W, Morton KJ, Riehn R, Wang YM, Yu Z, Rosen M, Sturm JC, Chou SY, Frey E, Austin RH. Phys Rev Lett. 2005; 94(19):196101. [PubMed: 16090189]
20. Sauer-Budge AF, Nyamwanda JA, Lubensky DK, Branton D. Phys Rev Lett. 2003; 90(23): 238101. [PubMed: 12857290]
21. Chen W-S, Chen W-H, Chen Z, Gooding AA, Lin K-J, Kiang C-H. Phys Rev Lett. 2010; 105(21): 218104. [PubMed: 21231359]
22. Lionnet T, Joubaud S, Lavery R, Bensimon D, Croquette V. Phys Rev Lett. 2006; 96(17):178102. [PubMed: 16712339]
23. Hutter JL, Bechhoefer J. Rev Sci Instrum. 1993; 64(7):1868.
24. Rief M, Clausen-Schaumann H, Gaub HE. Nat Struct Biol. 1999; 6(4):346. [PubMed: 10201403]
25. Staple DB, Loparic M, Kreuzer HJ, Kreplak L. Phys Rev Lett. 2009; 102(12):128302. [PubMed: 19392329]
26. Lv S, Dudek DM, Cao Y, Balamurali MM, Gosline J, Li H. Nature. 2010; 465(7294):69. [PubMed: 20445626]
27. Neuman KC, Chadd EH, Liou GF, Bergman K, Block SM. Biophys J. 1999; 77(5):2856. [PubMed: 10545383]
28. Koirala D, Dhakal S, Ashbridge B, Sannohe Y, Rodriguez R, Sugiyama H, Balasubramanian S, Mao H. Nat Chem. 2011; 3(10):782. [PubMed: 21941250]
29. Gibaud T, Barry E, Zakhary MJ, Henglin M, Ward A, Yang Y, Berciu C, Oldenbourg R, Hagan MF, Nicastro D, Meyer RB, Dogic Z. Nature. 2012; 481(7381):348. [PubMed: 22217941]
30. Smith SB, Cui YJ, Bustamante C. Science. 1996; 271(5250):795. [PubMed: 8628994]
31. Strick T, Allemand J, Croquette V, Bensimon D. Prog Biophys Mol Biol. 2000; 74(1-2):115. [PubMed: 11106809]
32. Lipfert J, Wiggin M, Kerssemakers JW, Pedaci F, Dekker NH. Nat Commun. 2011; 2:439. [PubMed: 21863006]

33. Strick TR, Allemand J-F, Bensimon D, Croquette V. Biophys J. 1998; 74(4):2016. [PubMed: 9545060]
34. Yan J, Skoko D, Marko JF. Phys Rev E. 2004; 70(1) 011905.
35. Chen H, Fu H, Zhu X, Cong P, Nakamura F, Yan J. Biophys J. 2011; 100(2):517. [PubMed: 21244848]
36. Welker J, Giessibl FJ. Science. 2012; 336(6080):444. [PubMed: 22539715]
37. Stigler J, Ziegler F, Gieseke A, Gebhardt JCM, Rief M. Science. 2011; 334(6055):512. [PubMed: 22034433]
38. Bérut A, Arakelyan A, Petrosyan A, Ciliberto S, Dillenschneider R, Lutz E. Nature. 2012; 483(7388):187. [PubMed: 22398556]
39. Shank EA, Cecconi C, Dill JW, Marqusee S, Bustamante C. Nature. 2010; 465(7298):637. [PubMed: 20495548]
40. del Rio A, Perez-Jimenez R, Liu R, Roca-Cusachs P, Fernandez JM, Sheetz MP. Science. 2009; 323(5914):638. [PubMed: 19179532]
41. Deng Y, Sun M, Shaevitz JW. Phys Rev Lett. 2011; 107(15):158101. [PubMed: 22107320]
42. van Mameren J, Gross P, Farge G, Hooijman P, Modesti M, Falkenberg M, Wuite GJL, Peterman EJG. Proc Natl Acad Sci USA. 2009; 106(43):18231. [PubMed: 19841258]
43. Lang MJ, Fordyce PM, Engh AM, Neuman KC, Block SM. Nat Methods. 2004; 1(2):1.
44. Hards A, Zhou C, Seitz M, Bräuchle C, Zumbusch A. Chem Phys Chem. 2005; 6(3):534. [PubMed: 15799480]
45. Marko JF, Siggia ED. Macromolecules. 1995; 28(26):8759.
46. Wang MD, Yin H, Landick R, Gelles J, Block SM. Biophys J. 1997; 72(3):1335. [PubMed: 9138579]
47. Clausen-Schaumann H, Rief M, Tolksdorf C, Gaub HE. Biophys J. 2000; 78(4):1997. [PubMed: 10733978]
48. Cocco S, Yan J, Léger J-F, Chatenay D, Marko J. Phys Rev E. 2004; 70(1) 011910.
49. Calderon CP, Chen W-H, Lin K-J, Harris NC, Kiang C-H. J Phys: Condens Matter. 2009; 21(3) 034114.
50. Odijk T. Macromolecules. 1995; 28(20):7016.
51. Cluzel P, Lebrun A, Heller C, Lavery R, Viovy J-L, Chatenay D, Caron F. Science. 1996; 271(5250):792. [PubMed: 8628993]
52. Fu H, Chen H, Marko JF, Yan J. Nucleic Acids Res. 2010; 38(16):5594. [PubMed: 20435680]
53. Fu H, Chen H, Zhang X, Qu Y, Marko JF, Yan J. Nucleic Acids Res. 2011; 39(8):3473. [PubMed: 21177651]
54. Zhang X, Chen H, Fu H, Doyle PS, Yan J. Proc Natl Acad Sci USA. 2012; 109:8103. [PubMed: 22532662]
55. Ke C-H, Humeniuk M, S-Gracz H, Marszalek PE. Phys Rev Lett. 2007; 99(1) 018302.
56. Essevaz-Roulet B, Bockelmann U, Heslot F. Proc Natl Acad Sci USA. 1997; 94(22):11935. [PubMed: 9342340]
57. Danilowicz C, Coljee VW, Bouzigues C, Lubensky DK, Nelson DR, Prentiss M. Proc Natl Acad Sci USA. 2003; 100(4):1694. [PubMed: 12574500]
58. Hatch K, Danilowicz C, Coljee V, Prentiss M. Phys Rev E. 2007; 75(5) 051908.

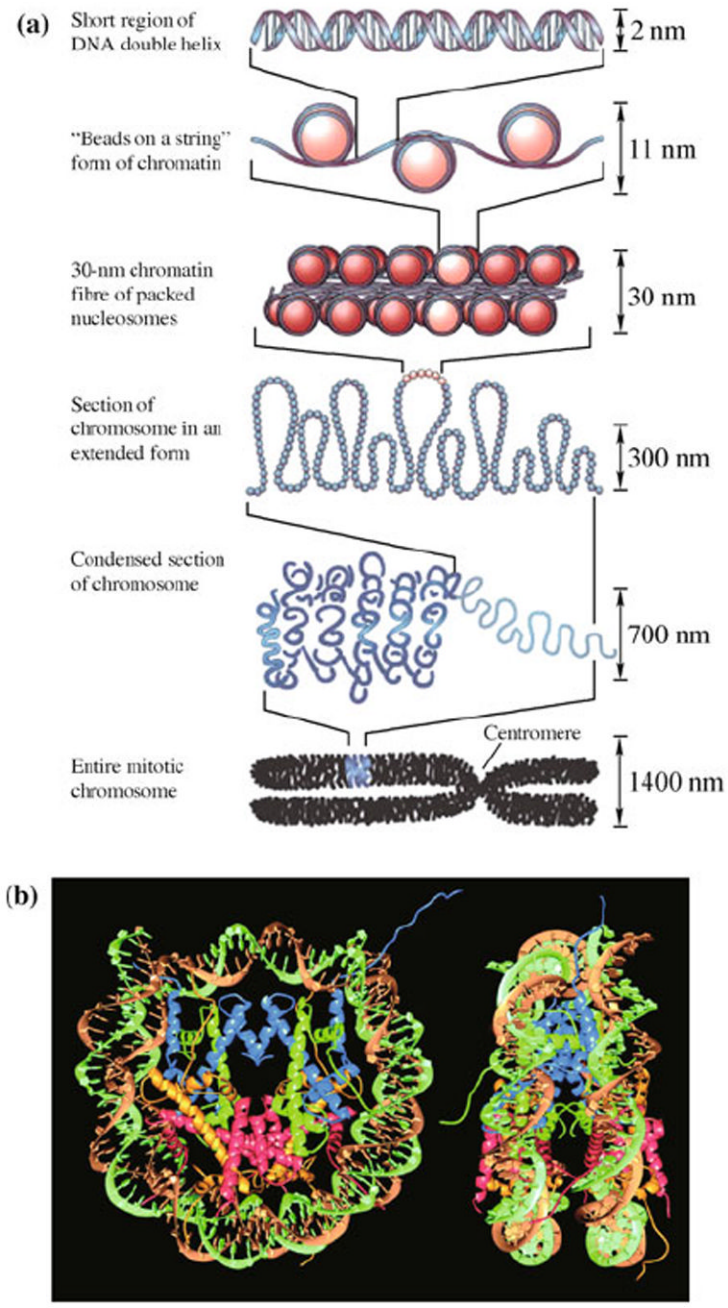

Fig. 1.

(a) Hierarchical organization of DNA packaged into a chromosome. The nucleosomes are formed by histones which bend DNA into small loops. Reproduced from Ref. [11], Copyright © 2003 Nature Publishing Group. **(b)** Structure of the nucleosome. Two superhelical turns of the DNA double helix wrap around an octamer of histones through hydrogen bonds and electrostatic interactions. Reproduced from Ref. [16], Copyright © 1997 Nature Publishing Group.

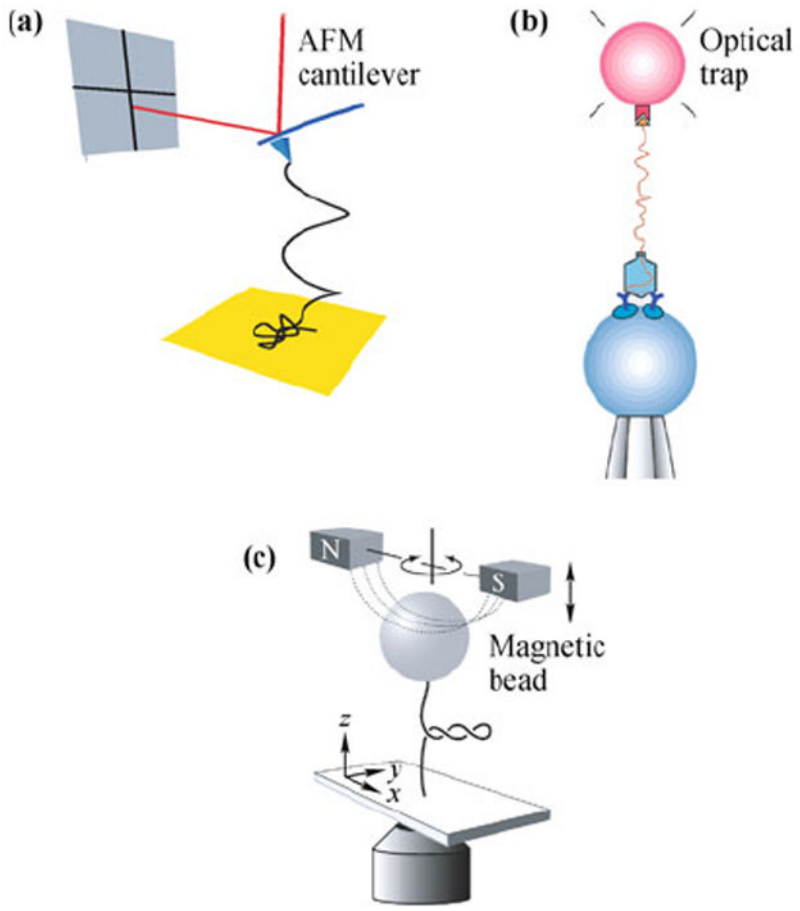

Fig. 2.

Illustrations of single-molecule manipulation techniques. **(a)** AFM. The molecule is held by the tip and the substrate surface. The force on the attached molecule is determined based on the deflection of the cantilever. Reproduced from Ref. [21], Copyright © 2010 American Physical Society. **(b)** Optical tweezers. One end of a DNA molecule is attached to a bead trapped by a laser beam, while the other end is attached to a DNA-virus capsid complex on a second bead, held by a micropipette tip. Reproduced from Ref. [8], Copyright © 2001 Nature Publishing Group. **(c)** Magnetic tweezers. A force is exerted on the molecule by an attached super-paramagnetic bead in a magnetic field. The molecule can be twisted as well as stretched by the applied field. Reproduced from Ref. [22], Copyright © 2006 American Physical Society.

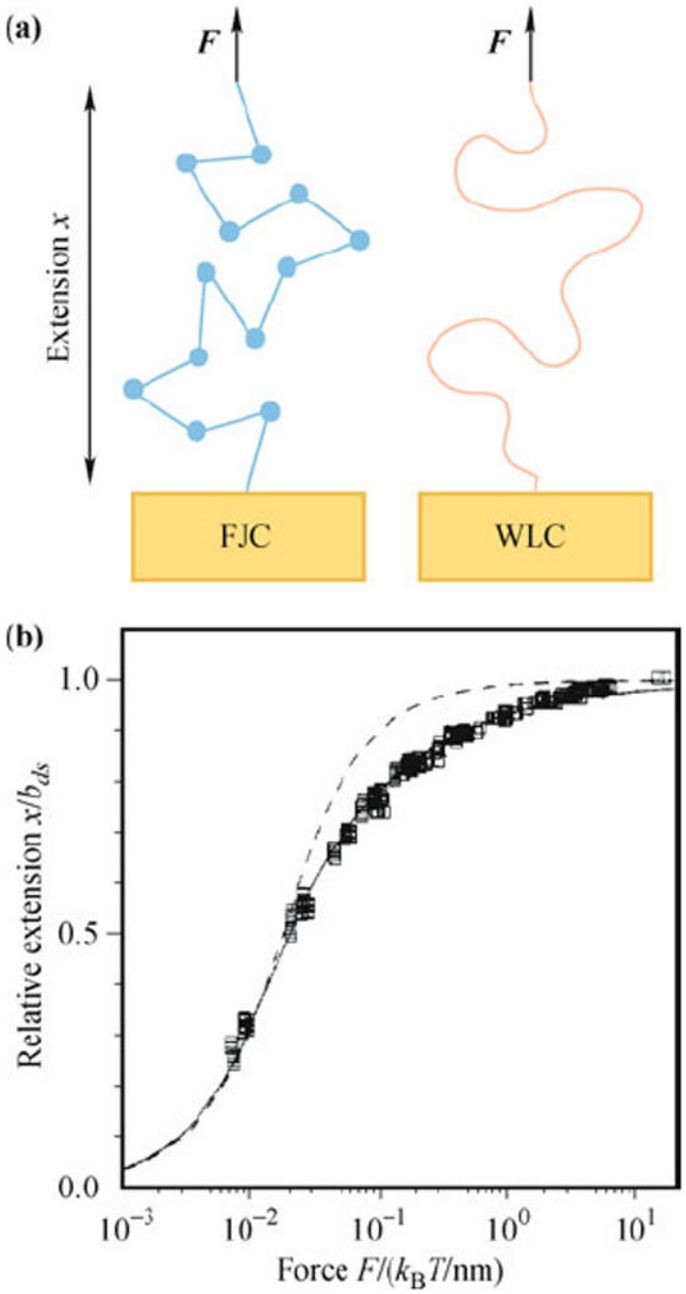

Fig. 3.

The polymer physics models that describe DNA. **(a)** Illustration of the FJC and WLC models. **(b)** Force-extension behavior of a single dsDNA molecule. dsDNA can be described accurately by the WLC model (*solid curve*), but not the FJC model (*dashed curve*). Reproduced from Ref. [45], Copyright © 1995 American Chemical Society.

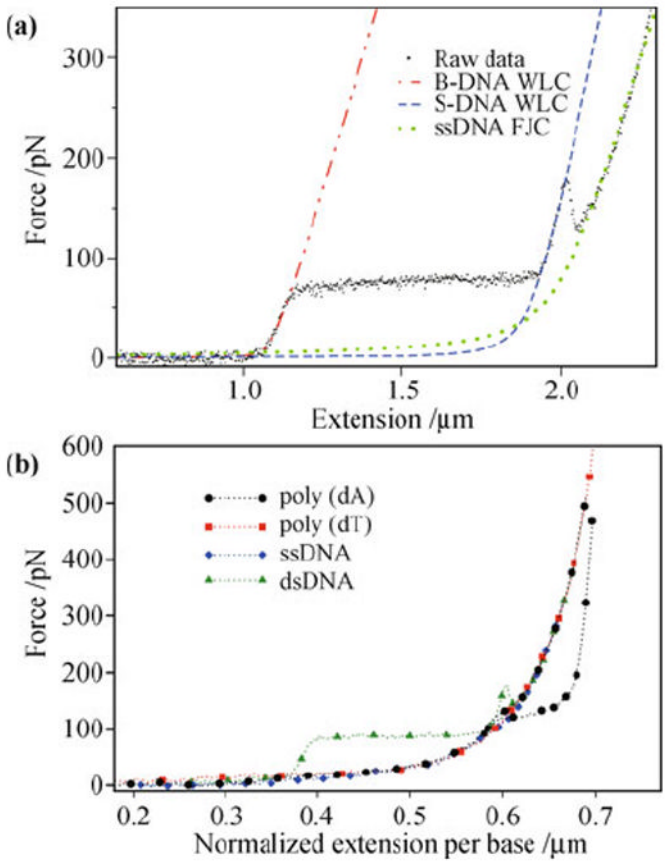

Fig. 4.

Force-induced transitions of DNA. **(a)** Force-extension data showing stretching, melting, and overstretching of a λ-DNA. The data are fit for extensible WLC and FJC models. Reproduced from Ref. [49], Copyright © 2009 IOP Publishing. **(b)** Force-extension pathways for poly(dA) compared to dsDNA and other ssDNA. Reproduced from Ref. [21], Copyright © 2010 American Physical Society.

Appendix B

- Postdoctoral Fellow Awardees: Dev Chatterjee, Kyle Hammerick, and Elizabeth McCullum

Alliance for NanoHealth (ANH) DOE Training Program
Post-Doctoral Research Training Fellowship 2009
Final Report

Name: Dev Kumar Chatterjee
Institution: The University of Texas MD Anderson Cancer Center
Project Title: Multifunctional Gold Nanoparticles for Cancer Therapy

I. **Summary of Research**: My research deals with the activation of gold nanoparticles (nanorods and nanoshells) with electromagnetic radiation for management of cancer.

II. **Reportable Outcomes:**
   a. Publications
      i. **Chatterjee DK,** Diagaradjane P and Krishnan S, Nanoparticle mediated hyperthermia in cancer therapy. ***Therapeutic Delivery*** Vol. 2(8) (2011), 1001–1014
      ii. **Chatterjee DK**, Cho S and Krishnan S (2013) Clinical Translations of Nanotechnology: Present and Future Outlook. *Cancer Nanotechnology: Principles and Applications in Radiation Oncology*. Ed(s) Cho SH, Krishnan S. Taylor and Francis
      iii. **Chatterjee DK**, and Krishnan S (2013) Gold Nanoparticle–Mediated Hyperthermia in Cancer Therapy. *Cancer Nanotechnology: Principles and Applications in Radiation Oncology*. Ed(s) Cho SH, Krishnan S. Taylor and Francis.
      iv.
   b. Patents
   c. Invited Presentations
      i. 'Nanomedicine - an introduction'. @ Seminars in Health Care: School of Health Professions, Programs in Cytogenetic Technology (CGT). USA, January 10, 2013

III. **Conclusion**
IV. **References**
V. **Appendices**

Current Career Profile (optional):

- Briefly describe your career profile
  - Dev Chatterjee is the NASA/DoE Alliance for Nanohealth postdoctoral fellow at MD Anderson Cancer Center's Department of Experimental Radiation Oncology, where he leads or supports several research projects related to the radiosensitization of cancers using gold nanoparticles. He has several first author publications in major peer-reviewed journals, has contributed multiple chapters to books on nanotechnology and cancer, and given invited lectures on the subject. He also serves as an associate editor of the American Journal of Cancer Therapy and Pharmacology, and as a member of Ambassadors of Cheer, a cancer patient support group at MD Anderson.

Published in final edited form as:
Ther Deliv. 2011 August 1; 2(8): 1001–1014.

Nanoparticle-mediated hyperthermia in cancer therapy

Dev Kumar Chatterjee[1], **Parmeswaran Diagaradjane**[1], and **Sunil Krishnan**[1,†]
[1]Department of Radiation Oncology, MD Anderson Cancer Center, Houston, TX 77030, USA

Abstract

A small rise in tumor temperature (hyperthermia) makes cancer cells more susceptible to radiation and chemotherapy. The means of achieving this is not trivial, and traditional methods have certain drawbacks. Loading tumors with systematically asministered energy-transducing nanoparticles can circumvent several of the obstacles to achieve tumor hyperthermia. However, nanoparticles also face unique challenges prior to clinical implementation. This article summarizes the state-of-the-art current technology and discusses the advantages and challenges of the three major nanoparticle formulations in focus: gold nanoshells and nanorods, superparamagnetic iron oxide particles and carbon nanotubes.

Hyperthermia in cancer therapy

Clinical rationale & biological basis for hyperthermia

Hyperthermia has a long history in the annals of cancer management. A correlation between erysipelas (a streptococcal skin infection) and tumor regression had been observed for over a century before William Coley first documented evidence of a relationship between infection and cancer regression in sarcoma patients in 1891 [1]. His attempts to recreate this phenomenon for the treatment of cancers culminated in the generation of cocktails of bacteria (Coley's toxin) that intentionally induced a fever to effect an antitumor response. While this probably represents among the first instances of the clinical use of hyperthermia for cancer therapy, it was also among the first demonstrations of the efficacy of immunotherapy. Since then, more localized and relatively safer methods of hyperthermia, either singly or in combination with conventional therapy, have been employed by many investigators to treat cancer (Box 1) [2–11].

Box 1

Definitions

- Hyperthermia, in a medical setting, is a rise in temperature of body tissues, globally or locally. In the field of cancer therapy where this elevation in temperature is induced intentionally, this definition can be further qualified based on the desired effect of this temperature rise on the tissue. If the temperature is raised high enough to cause immediate cellular death, largely

†Author for correspondence: Tel.: +1 713 563 2377, Fax: +1 713 563 2366, skrishnan@mdanderson.org.

Financial & competing interests disclosure
This work was funded in part by NIH grants KL2 RR024149 05, 1R21CA133691–01, 1R01CA132032 and U01CA151886 to Sunil Krishnan. The authors have no other relevant affiliations or financial involvement with any organization or entity with a financial interest in or financial conflict with the subject matter or materials discussed in the manuscript apart from those disclosed.
No writing assistance was utilized in the production of this manuscript.

through necrosis mediated by irreparable coagulation of proteins and other biological macromolecules, the more accurate term to use is *thermoablation*. In contrast to thermoablation, hyperthermia refers to smaller temperature rises, usually to 40–45°C, initiating a series of subcellular events, rendering the cells susceptible to various forms of damage including apoptosis, leading to subsequent cell death [70,71]. Other effects associated with hyperthermia include activation of immunological responses, enhancement of tumor blood flow and oxygenation via greater vascular perfusion and permeability, and a shift toward anaerobic metabolism resulting in decreased oxygen consumption and increased tissue oxygenation, all leading to an altered extracellular microenvironment.

- Nanoparticle is an umbrella term encompassing a variety of materials all sharing the common feature of having the longest dimension less than 100 nm. This limitation is generally relaxed in the scientific parlance, with particles not greatly exceeding 100 nm also earning the sobriquet ‘nano’ (Figure 1). Nanoparticles can be solid, hollow or branching, and made from a very diverse selection of materials. The development of means to control and characterize at the nanoscale allows a degree of design unsurpassed by single-molecule entities. In the field of cancer therapy, nanoparticles afford many advantages over conventional therapeutic methods and are an ongoing research focus on a global scale.

Heat as a curative modality (thermoablation) has been explored in cancer by many researchers. The challenge facing thermoablation therapies mirrors that of surgery: the destruction of the tumor needs to be as complete as possible, while sparing normal tissues. Thermoablation became a topic of high interest with the advent of electromagnetic heating. However, despite demonstrations of delayed tumor regrowth following thermoablation, in general, the therapy falls short in curative prowess owing to the difficulties in precise control of temperature rise in different regions of the tumor resulting in residual cancerous tissue and tumor recurrence. By contrast, sub-ablative heating has a bigger therapeutic window since cell destruction is not desired. Mild temperature rise throughout the tumor may be accompanied by some heating of surrounding normal tissue, but since non-malignant cells have unimpaired heat-shock protection mechanisms, the toxicity profile for mild hyperthermia is usually very good.

The increasing interest in hyperthermia has been paralleled by an increasing understanding of the mechanism of action of this treatment modality. It is now known that tumor cells, tumor vascular endothelial cells, and normal cells are not inherently different in their sensitivity to heat-induced cytotoxicity. However, owing to inefficient blood flow and oxygen transport through the newly formed immature blood vessels within tumors, tumor cells reside in an acidotic and nutrient-deprived milieu that confers them with greater thermosensitivity [12]. This greater sensitivity of hypoxic areas to heat provides a compelling rationale for the combination of hyperthermia with radiation therapy since poorly perfused tumor cores are generally resistant to the effects of ionizing radiation, which depends on the generation of toxic oxygen radicals in well-perfused regions. The complementary effects of radiation and hyperthermia is further accentuated by the fact that tumor cells in the S phase of the cell cycle are relatively radioresistant. However, it is precisely in this phase that tumor cells are most sensitive to the effect of heat and become radio-sensitized. Thus hyperthermia acts as a potent and selective radiosensitizer by affecting those cancer cells that are naturally radioresistant.

Hyperthermia can also be used to chemosensitize cancer cells. The degree of chemosensitization varies with the type and concentration of drug, the tumor type, the increase in tumor temperature and the time differential between the delivery of heat and chemotherapy. However, prior drug resistance does not appear to be a factor in the sensitivity to heat. Chemosensitization is highest when heat and chemotherapy are administered simultaneously, the effect diminishing at greater intervals between delivery of the two therapies [13]. In general, enhanced cytotoxicity of many chemotherapeutic agents increases in the range of 40.5–43°C [14]. However, clinically, temperatures above 41°C have been associated with higher toxicity and a low benefit:risk ratio. In general, hyperthermia with milder temperatures increases the destruction of cancer cells with chemotherapy, but not that of normal cells (i.e., chemotherapeutic side effects are minimized). However, there is a potentially wide variation in the thermal enhancement of a given agent among the different types of tumors. Also, different agents have different enhancement ratios for the same degree of temperature elevation in the same tumor type, indicating that the drug of choice at physiological temperatures may not be the drug of choice at elevated temperatures [14]. In general, however, even for drugs with good thermal enhancement for a particular tumor type, the enhancement of tumor toxicity due to heat is only seen at higher drug concentrations in the tumor. Hence, isolated perfusion of tumors with heated solutions of chemotherapeutics, providing a higher tumor drug concentration demonstrates a better response than systemic administration of the same drug. Several mechanisms have been proposed for this observed effect. Temperatures bordering on 42–43°C have some cancer-specific cytotoxicity resulting from the impaired mechanisms of cancer cells to handle heat shock. Prolonged (>1 h) heating at lower temperatures increases tumor perfusion, and this results in greater delivery of chemotherapeutics especially to the poorly vascularized core. The lack of enhanced drug toxicity with loco-regional hyperthermia with potential improvement in response to advanced disease suggests that thermochemotherapy is a viable and important alternative to drug treatment alone.

Unfortunately, it is not often possible to elevate tumor temperature uniformly to the 42–43°C required for direct cytotoxicity. Fortuitously, it is fairly well established now that clinically achievable elevations of tumor temperature to approximately 40–42°C (mild temperature hyperthermia), although less effective as monotherapy against cancer, has potent efficacy as an adjunct to radiation therapy. This is largely driven by an increase in blood flow (often sustained for 1–2 days) [15] and oxygen delivery and a decrease in oxygen demand (due to hyperthermia-induced cell death and metabolic suppression) that converge to increase tumor tissue oxygenation. Increased perfusion also directly translates to increased delivery of chemotherapeutic drugs to the poorly vascularized tumor cores [16]. Such a complementary role for hyperthermia has been demonstrated in numerous clinical and preclinical studies of hyperthermia combined with chemotherapy or radiation therapy, with significant improvements in outcome demonstrated for tumors of the prostate, breast, bladder, brain, cervix, head and neck, lung, rectum and esophagus, among others. Typically, adding hyperthermia to the treatment regimen has not resulted in increased toxicity (especially for radiation therapy), but has contributed to better control, cure and/or palliation [17–24].

Hyperthermia techniques

While the rationale for adding hyperthermia to clinical regimens is compelling, the means to do so are not as straightforward. Three types of hyperthermia are traditionally employed in clinical practice – whole-body, regional and local hyperthermia (Figure 1). Whole-body hyperthermia is achieved by such methods as hot water blankets and thermal chambers. In theory, it should be used for metastatic cancer where focal hyperthermia would be ineffective. Regional hyperthermia depends on perfusing with heated liquids – the two

popular techniques are perfusing the peritoneum with a heated solution of anticancer drugs for peritoneal cancers such as mesothelioma, and the perfusion of a part of the patient's blood, taken out and warmed *ex vivo*, into an artery supplying the limb containing the tumor [25,26]. Both whole-body and regional hyperthermia in general result in poor tumor specificity of treatment. While the toxic effects of hyperthermia are usually not severe, whole-body hyperthermia often causes gastrointestinal symptoms, such as diarrhea, nausea and vomiting, and may occasionally have serious cardiovascular side effects, such as myocardial ischemia, thrombosis and cardiac failure. Regional hyperthermia is invasive and involves significant challenges in set-up.

Local hyperthermia, in theory, has the advantage of being tumor focused. The three major methods of generation of local hyperthermia, in order of increasing invasiveness, are external, luminal and interstitial. Luminal hyperthermia uses special probes placed as close to the tumor as possible, such as in the lumen of the rectum for treatment of rectal cancers, whereas interstitial hyperthermia uses a grid of applicators/probes placed into tumor parenchyma for more uniform tumor heating. Heat sources can be inserted into the probes and applicators, or the probes can be heated by external heating sources. Generally, these methods also suffer from moderate to high invasiveness, while the heating of the tumor is non-uniform, being concentrated more on the probe than elsewhere. Another way in which this can be achieved is by placing metal **antennas** ('seeds') in the tumor interstitium before exposure to an external magnetic field. These antennas are elongated devices made of ferromagnetic material (e.g., iron), which heat up in an alternating electromagnetic field (detailed later). In this way, the heat for hyperthermia is actually generated inside the tumor rather than filtering through from outside, and can be readily controlled by simply controlling the strength of the magnetic field. However, implanting the relatively large seeds requires an invasive procedure, which adds to the morbidity of the treatment. The seeds may focus the heating in the immediate locality of the implantation area, with resultant cold spots elsewhere in the tumor. Placing the seeds in a deep tumor may be difficult and require image guidance. Finally, it often requires large investments of money because of the requirements for special electromagnetically shielded rooms and compliance with other federal regulations. External heating can be achieved either with electromagnetic radiation (e.g., **microwave**, laser and **radio-frequency**) or high-intensity focused ultrasound, all of which transduce energy from an external source to pass through the body. One disadvantage of this method is that energy is deposited in the normal tissues along its path and can result in hot spots within these tissues. In summary, despite the beneficial effects of adding hyperthermia to the cancer management regimen, current methods to achieve it are often invasive, nonuniform or non-specific to the tumor. Clearly, there are opportunities to improve uniformity and target specificity of heat in a non-invasive or minimally invasive manner.

Nanoparticles for local hyperthermia

The foregoing discussion outlines the promises and pitfalls of established methods of generating hyperthermia. The continuing quest for a method of hyperthermia that is tumor focused, minimally invasive, and uniform has led to the investigation of nanoparticles as conduits for generating hyperthermia (Figure 2). To maximize the energy deposited in the tumor while limiting the exposure in healthy tissues, tumors can be preferentially loaded with systemically administered nanoparticles that have a high-absorption cross section for transduction of an extrinsic energy source to heat. Hyperthermia achieved by this method has several potential advantages over both global and focal hyperthermia achieved without nanoparticles.

Localization of nanoparticles

It has been widely recognized that intravenously administered nanoparticles passively extravasate from vasculature and preferentially accumulate in tumors but not in normal tissues. This phenomenon, often referred to as the enhanced permeability and retention (EPR) effect, is a consequence of the leakiness of immature tumor neovasculature with large fenestrations and inefficient lymphatic drainage [27,28]. To ensure long circulation times of nanoparticles for efficient accumulation within tumors, evasion of non-specific reticuloendothelial capture of these particles can be achieved by rendering them 'stealth' properties via coating them with polyethylene glycol (a process known as PEGylation), dextran or other biocompatible coatings [29,30]. Additionally, nanoparticles can be decorated with targeting molecules homing to cancer-specific and cancer-associated antigens to achieve even greater tumor sensitivity [31–34]. It is to be noted that these techniques of tumor-specific localization of nanoparticles leads to tumor specific dose delivery that is independent of invasive procedures adopted in other localized dose-delivery strategies such as interstitial hyperthermia. Targeted nanoparticles also result in less non-specific accumulation in the body, enabling a lowering of injected dose of nanoparticles for the same therapeutic effect and lessening the probability of nanoparticle-mediated toxicity.

'Inside-out' hyperthermia

All sources of heat create a temperature gradient in the tissues with the temperature falling off sharply with distance from the heat source. All external sources of heat-like focused ultrasound or infrared lamps have a narrow window of effectiveness where the skin surface is significantly affected before the temperature in the tumor reaches therapeutic levels. However, unlike all other means of external hyperthermia, the primary source of the heat – the nanoparticle – is located inside the tumor. This reverses the direction of heat loss – from inside out and reduces damage to normal tissues while heating up the tumor. Furthermore, most of the nanoparticles are metallic and consequently have excellent thermal conductivity that couples and instantly transmits the heat they generate to the surrounding tumor tissue. Interstitial hyperthermia also relies on generation of heat from within the tumor but uses larger and more invasively inserted probes within tumors to achieve this.

Vascular-focused hyperthermia

Although all forms of hyperthermia seek to achieve fairly uniform temperatures globally within tumor parenchyma, a unique feature of nanoparticle-mediated hyperthermia is the location of nanoparticles in close proximity to tumor vasculature [35]. This results in a temperature gradient that is maximal at the vascular wall and falls off with distance from the perivascular space. Consequently, a global tumor parenchymal hyperthermic temperature is associated with considerably higher focal temperatures (hot spots) along tumor vasculature. By contrast, other forms of hyperthermia resulting in global tumor parenchymal hyperthermic temperatures are usually associated with focal cold spots along tumor vasculature that serve as 'heat sinks' for dissipation of heat from tumors. Consequently, the preferential vascular-focused hyperthermia achievable with nanoparticles has the advantage of not only causing heat-induced tissue damage of tumor cells but also vascular endothelia, which, in turn, sensitizes these endothelial cells and tumor cells to subsequent radiation therapy.

Theranostics

Compared to other forms of hyperthermia, nanoparticle-mediated hyperthermia has the potential to simultaneously image and treat tumors, an attribute referred to as **theranostics**, where therapy and diagnostics are integrated into a single platform. Since nanoparticles preferentially concentrate in tumors, detecting their presence can potentially be used as a

means of diagnosing the presence and extent of tumors. The same nanoparticles can then be used for hyperthermia as part of tumor management. Furthermore, when the nanoparticle is decorated with tumor-specific targeting molecules that permit precise sensing and imaging of tumors, subsequent therapy (hyperthermia or thermoablation) can be image-guided.

Combination with other therapies

The fact that nanoparticles afford immense opportunities for engineering their structure – more, in fact, than any other forms of injectable therapy – can be exploited to combine the hyperthermia with other therapeutic modalities. For instance, nanoparticles can be laden with or decorated with drugs, such that near-simultaneous hyperthermia and chemotherapy (drug release) can be triggered via an extrinsic energy source. Similarly, binding radioactive tracers to the nanoparticles to achieve a form of brachytherapy serves as a means of combining hyperthermia and radiation therapy.

These advantages have fueled the quest for ideal nanoparticles for achieving tumor hyperthermia. The major ones under investigation are reviewed here and include various forms of gold nanoparticles and superparamagnetic iron oxide nanoparticles (SPIONs) while carbon nanotubes (CNTs) are a more recent entrant to this field.

Hyperthermia using gold nanoparticles

Characteristics of gold nanoparticles

Many bulk metals, when reduced to a nanoscale, exhibit optical resonances of their surface plasmons, a characteristic wavelength (**surface plasmon resonance**) at which they strongly absorb and scatter incident light and convert resonant energy to heat. When fabricated in certain geometries, these plasmon resonances of gold can be tuned to near infrared (NIR) wavelengths, where this light penetrates deepest within human tissues due to minimal absorbance by native tissue chromophores [36]. Gold nanoparticles fabricated to have strong absorption cross sections in the NIR wavelength (up to a million-fold greater than the US FDA-approved dye indocyanine green) are also highly efficient at converting the absorbed light into heat. These photothermally activatable gold nanoparticles have many distinct advantages for clinical applications. First, gold is an inert noble metal that does not react with biological tissues and is molecularly stable. Second, long-term toxicity concerns are low due to extensive, decades-long clinical experience with the use of gold for the treatment of rheumatoid arthritis. Some caution is necessary, however, with extrapolating from larger microparticles to nanoparticles, as highlighted by a recent study that demonstrated that administration of large quantities of gold nanoparticles stimulates host immune complement activation, an effect that was dependent on other factors such as nanoparticle surface characteristics and structure [37]. Third, NIR activatable gold nanoparticles are within size regimens that permit tumor-specific accumulation via the EPR effect based on average vascular fenestrations of 60–400 nm in tumors. Fourth, in addition to passive accumulation in tumors via the EPR effect, surface bioconjugation for tumor-specific targeting or PEGylation for reticuloendothelial evasion can be readily performed via thiol linkages on the surface of these gold nanoparticles. Lastly, gold nanoparticles have the potential for FDA approval as a device rather than a drug, an attribute that could save significant time and money for clinical translation. Among a variety of gold nano-structures in use, the most commonly employed ones are nanoshells and nanorods.

Gold nanoshells—Nanoshells have a core of a different material coated by a thin layer of gold. The core material is dielectric, with silica being the most common material used. The resonance frequency is determined by the **core:shell ratio**. Gold nanoshells (GNSs) are usually close to 50–150 nm in the diameter and are generally moderately stable in solution,

especially if stored at low temperatures. Silica-GNSs that are activatable by NIR light tend to be roughly 150 nm in diameter, with a 120-nm diameter silica core. Extensive investigations into the safety and tolerability of GNSs have led to greater acceptance of the biocompatibility of these particles, paving the way for human clinical testing. GNSs are currently in clinical trials for head and neck cancer and prostate cancer using interstitial illumination with NIR lasers for thermoablation applications.

Gold nanorods—Gold nanorods (GNRs) are cylindrical nanoparticles made of solid gold with one dimension several times longer than the other. If the solid gold nanostructure is a sphere, the optical absorption maximum is in the region of 540 nm and cannot be tuned to other wavelengths. Hence this formulation is not of much use clinically. However, oblong forms, with large length:diameter aspect ratios, are tunable to higher wavelengths of light. The resonant frequency is determined by the aspect ratio, and can be calibrated to the NIR region. NIR activatable GNRs are much smaller than nanoshells, with typical sizes ranging approximately 4–5 nm in the longest dimension, usually with an aspect ratio of approximately 3. To facilitate anisotropic formation of rod-shaped structures during seed-mediated chemical synthesis of GNRs from spherical gold seed particles and to make them stable without aggregation in solution, a strongly charged surfactant such as cetyl trimethylammonium bromide (CTAB) is commonly employed. Since the CTAB dispersed in solution can be cytotoxic, it is often removed by serial centrifugation or dialysis, processes that involve a reduction in yield of GNRs or considerable expense. Furthermore, the CTAB on the surface of the GNRs is also shielded by a biocompatible compound such as PEG or by cross-linking a polysaccharide (chitosan) with ethylene/propylene-based block copolymers [38]. Despite some potential challenges with toxicity, GNRs – weight for weight of gold – possess a superior spectral bandwidth, are better than GNSs in heat generation from NIR light [39] and have a longer circulation half-life, improving chances for tumor accumulation.

Gold nanoparticles in cancer therapy

Hirsch *et al.* [40] were the first to demonstrate the effectiveness of GNS-mediated thermoablation in a mouse tumor model. While initial efforts used direct injection of GNSs into subcutaneous tumors, subsequent papers demonstrated that intravenously administered GNSs accumulated in tumors as early as 6 h after inoculation. Treatment of these animals with a 800 mW NIR laser emitting at 808 nm at 4 W/cm^2 for only 3 min resulted in significant survival difference over non-radiated mice [41]. Improvements in survival have been demonstrated when the gold nanoparticles are actively targeted to tumors in mice over passively targeted nanoparticles [42,43]. Several similar results have been demonstrated for GNRs [44,45]. However, despite promising results, thermoablative monotherapy of tumors with gold nanoparticles is associated with the possibility of considerable collateral damage of tissues adjacent to the tumor that are also ablated and lacks a clear advantage over established techniques such as radiofrequency ablation if interstitial laser fibers are required for photothermal ablation. Hence, combination therapy of hyperthermia (non-ablative temperatures) with other modalities is worth investigating.

In our laboratory, we have investigated the effect of modulating ionizing radiation on tumor-bearing mice using GNS-mediated hyperthermia. When tumors in mice pre-treated with GNSs are subject to mild temperature hyperthermia (~41°C for 20 min) followed immediately by a single dose of radiation (10 Gy with 125 kV X-rays) the tumor volume doubling time was nearly twice that with radiation alone [35]. Tumor volume doubling time is a metric used to represent tumor growth, which is independent of the initial size of the tumor; comparison of time taken for tumors to double in volume in the radiation-alone group versus tumors in a combined treatment group is a commonly employed technique for

evaluating effectiveness of putative radiation sensitization strategies. The reasons for the *in vivo* response were postulated to be caused by an early increase in vascular perfusion of tumors following hyperthermia. This can be seen using dynamic contrast enhancement of MRI. However, the results also indicate that it is possible that nanoparticle-mediated hyperthermia may modulate radiation response by other mechanisms. Relatively large GNSs leak out of tumor vasculature but fail to penetrate deep into the parenchyma of tumors, remaining sequestered in the perivascular region. Heating these sequestered GNSs to generate 'inside-out' hyperthermia can possibly result in vascular disruption. This was demonstrated by a loss of microvessel density in the tumor, disruption of normal stromal architecture and regional areas of necrosis (Figures 3A & B).

A third reason for the effectiveness of the GNS-mediated hyperthermia could be its effect on cancer stem cells. These tumor-initiating cells are hypothesized to be the primary reason for treatment failure of tumors as well as being responsible for metastatic spread. In a recent paper, it was demonstrated that radiation of breast cancer xenografts results in a reduction of tumor volume but an increase in the proportion of stem cells in the residual tumor whereas GNS-mediated hyperthermia coupled with radiation resulted in not only a greater reduction of tumor volume but also a reduction of the proportion of stem cells in the residual tumor. Furthermore, limiting dilution transplantation of the cancer cells from residual tumors following combined treatment resulted in a lower frequency of tumor formation than similar transplantation of cells from residual tumors following radiation alone (Figure 3c). Overcoming the inherent radio-resistance of cancer stem cells, which are thought to be the primary reason for therapy failure, provide another important rationale for the addition of hyperthermia to radiation therapy of tumors [46].

Hyperthermia using SPIONs

Characteristics of SPIONs

Magnetic materials are either permanent magnets (ferromagnetic, like iron) or which only demonstrate magnetism under the influence of an external magnetic field (paramagnetic). A new property is obtained when ferromagnetic materials are fabricated on the nanoscale – that of **superparamagnetism**. On the nanoscale, the ferromagnetic nanoparticles can randomly flip the orientation of their magnetic dipoles, a phenomenon that makes them appear paramagnetic. However, under the influence of an external magnetic field, they align in the direction of the field, and the resultant magnetic susceptibility is orders of magnitude higher than that of standard paramagnetic material. When the material for the nanoparticles is iron oxide (the most common), the nanoparticles are called SPIONs.

In theory, alternating the external magnetic field rapidly would cause the particles to rapidly flip their magnetic polarity. However, there is some hysteretic loss involved in the flipping, which manifests as heat. If a tissue (say, a tumor) is pre-loaded with SPIONs and then subjected to alternating magnetic field (AMF), it will heat up. Several factors will affect the extent of this heating – the magnitude of the field, the size and characteristic of the SPIONs, the depth of the tumor within the body and the concentration of SPIONs in the tumor.

The first instance of the treatment of cancer using magnetic iron oxide particles was probably in 1957 [47]. Since then the synthesis and design of SPIONs have progressed much. At the heart of the SPION is the magnetic core of iron oxide. Synthesis is usually by the precipitation of iron salts in the presence of various chemicals, for example ammonia [48], sodium nitrate/sodium hydroxide [49] or by photochemical methods [50].

Bare SPIONs are rapidly cleared from the blood after intravenous injection and accumulate in the liver, spleen, and lymph nodes. When biocompatible dextran magnetite nanoparticles

are injected intravenously in rats, clearance was initially very rapid (half-life of 10 min) followed by a slower decrease (half-life of 92 min) [51]. In the first 2 h, the particles spread throughout the body including the liver and the spleen [52]. However, over time, the particles are scavenged by the reticuloendothelial system and accumulate in the macrophages of the splenic marginal zone, where there is a steady and rapid increase in accumulated particles for up to 48 h, followed by a decrease until the end of the observed period of 25 days. The iron oxide cores sequester as granules in the Kupffer cells of the liver, leading to a slow increase in accumulated amount.

To enable tumor accumulation, SPIONs need to be coated with or embedded in a polymer shell. The most common method for this is to embed the SPIONs in a polymeric nanoparticle that is hydrophilic. A common polymer for this purpose is dextran [53], although other polymeric blends, such as β-cyclodextrin and pluronic polymer combination [48], and chitosan [54], can also be used. Apart from polymers, iron/iron oxide core-shell nanoparticles are also popular [55,56]. Silica is a popular coat for many varieties of nanoparticles, including SPIONs [49,57]. However, the resultant particles are often micro-spheres rather than nanoparticles, with diameters of approximately 20–30 μm. These are used as *in situ* implants into tumors rather than as intravenous formulations.

Subsequently, to enhance circulation half-life, the dextran coat is often covered by a monolayer of PEG [55]. Finally, targeting molecules can be attached to enhance specificity of uptake by cancer cells. For example, folic acid [54,58] can be attached to target folate receptors in several solid tumors. Addition of folic acid was found to increase the cytotoxicity against the folate receptor over-expressing KB cells but had little adverse impact on the A549 cells, which do not possess these receptors. In addition, a novel way of coating the SPIONs is the use of gold [59]. The thin gold shell can itself be heated up by AMF, thus adding to the hyperthermic effect. Indeed, gold-coated SPIONs demonstrated several-fold higher increases in heat release compared with SPIONs alone. Furthermore, SPION-mediated hyperthermia can be combined with other strategies to further enhance the therapeutic outcome. For example, the SPIONs can be coated with thermosensitive polymers that are loaded with anti-cancer drugs [48,58]. Application of AMF after accumulation of the SPIONs in tumors would raise the local temperature of the SPIONs sufficiently to exceed the critical temperature of the polymers, resulting in drug release.

SPIONs in cancer therapy

Delivery of adequate amounts of SPIONs into tumors is a prerequisite for successful hyperthermia. These can be delivered to possible nests of metastatic cells in lymph nodes by direct injection into the lymphatic channels draining into the lymph nodes [47]. Subsequently, a number of investigators injected the SPIONs directly into the tumor as proof-of-principle experiments. The SPIONs can be injected in solution, or loaded into hydrogels and organogels [57].

However, this more invasive method of SPION delivery is not favorable, owing to obvious difficulties in translating to clinical usage. The favored delivery route is intravenous; however, successful concentration of nanoparticles into tumors by this route is not easily achievable. A novel route of delivery is by loading the SPIONs into cells [56]. In the experiment described, tumor-tropic neural progenitor cells were loaded with SPIONs and transplanted into melanoma-bearing mice, whence the cells made their way into the tumors. Subsequent AMF exposure resulted in tumor regression.

To achieve adequate concentrations in the tumor, SPIONs are sometimes conjugated to targeting molecules. Triton BioSystems, Inc. (Chelmsford, MA) have developed one such system of AMF-responsive nanoparticles and targeted these to cancerous tissues by

conjugating with monoclonal antibodies. The combination of molecular targeting and the focused AMF field aims to achieve highly sensitive tumor hyperthermia.

The use of heat for cancer can be ablative or sub-ablative. When sub-ablative, it can be used either as a standalone therapy to delay tumor growth [50] or as a means of radiosensitization [46]. The degree of heating of the tumor can be controlled by the AMF field. However, increasing the current in the AMF generator, and thus increasing the AMF field strength, generates heat in tissues by inductive tissue heating from eddy current losses. This is independent of the presence of SPIONs and affects normal tissues in the AMF field. The raised temperature in the normal tissues limits the extent to which the AMF field can be increased. In mouse experiments, for example, radiofrequency exposures at 25 kW for 20 min raised the tumor core temperature to 47°C [50].

Another limitation of the use of SPIONs is the toxicity to normal cells in the absence of AMF. Biocompatibility studies with dextran and citric acid-coated SPIONs on human umbilical-vein endothelial cells [53] demonstrated the expected endocytotic uptake by the cells, followed by cell death through suspected apoptotic pathways. Even at concentrations as low as 0.1 mM, the coated SPIONs managed to inhibit migration/invasion functions of the cells. While cytotoxic effects are strongly dependent on the coating/matrix of the SPIONs, the results demonstrated the necessity of thorough cytotoxicity evaluation of any proposed therapy involving these nanoparticles.

Hyperthermia with CNTs

Characteristics of CNTs

CNTs are unique, (almost) 1D nanomaterials composed of single sheets of **graphene** rolled into the shape of a tube. Since the aspect ratio and the direction of rolling can be controlled at synthesis, the optical properties can also be tuned. Similar to gold nanoparticles, single-walled CNTs (SWCNTs) also strongly absorb electromagnetic waves to generate heat. Instead of plasmon resonance, absorption of light by CNTs results in excitation of electronic transitions within the nanostructure with relaxation resulting in amplified vibrational modes within the carbon lattice. There is neither an absorption threshold nor is the absorption a continuous function of energy, but absorption occurs as discrete tunable and sharp spikes. Also, unlike gold, CNTs can absorb over a broad frequency range including visible light, NIR light and even radiofrequency irradiation. The extinction coefficient of such absorption is much higher than that of common tissue chromophores, such as melanins, hemoglobin and water [49].

CNTs are very thin cylinders of graphene, which can be synthesized to considerable variations in aspect ratios. The diameter of the tubes can vary from the nano- to the micro-scales [60]. Usually the cylinders are SWCNTs, but more recently multi-walled CNTs (MWCNTs) have also been investigated for their optical properties. They have been shown to have enhanced absorption cross-sections when compared with SWCNTs [61].

CNTs in cancer therapy

Following in the footsteps of the GNRs and SPIONs, the enhanced optical cross section of CNTs has been investigated for photothermal ablation of cancer cells [61]. This has been demonstrated *in vitro* using SWCNTs [61–63]. Tumor destruction in mouse models of cancer have also been demonstrated using intratumoral injection of SWCNTs followed by NIR irradiation for only 3 min [64]. Similar to gold, not only NIR, but also radiofrequency fields have been used to generate hyperthermia using SWCNTs. The required radiofrequency field was in the megahertz region (13.56 mHz). The *in vitro* study was succeeded by *in vivo* studies using direct intratumoral injection of the nanotubes.

Hyperthermia using the radiofrequency field resulted in complete necrosis of tumors [65]. Not only SWCNTs, MWCNTs have also been demonstrated to be effective in tumor ablation using NIR light. However, unlike SWCNTs, MWCNTs achieve thermal ablation of tumors after exposure to only a 30 s burst of NIR light at a relatively low laser power of 3 W/cm^2 [66].

The major stumbling block to more widespread adoption of CNTs is a concern regarding their toxicity. Exposure of mesothelial and pleural lining to CNTs can result in granulomas reminiscent of mesotheliomas arising from asbestos exposure [67]. Several factors, including their propensity to aggregate, and the nature of the surface and functional groups attached thereof, affect the toxicity of these nanostructures. Although it has been demonstrated that at low doses CNTs are non-toxic to mice, more detailed studies are necessary prior to adopting these for clinical use.

There are reports of other nanoparticles beyond these three types, which can potentially be exploited for hyperthermia. For example, fluorescent quantum dots [68], silver and zinc nanoparticles and lanthanum manganite particles with impregnated silver ions [69] have been explored. However, the general principles discussed for the three nanoparticles hold true in most cases.

Conclusion & future perspective

Hyperthermia results in increasing perfusion of tumors. This results in less hypoxic areas and a better response to radiation, while also aiding chemotherapy. However, beyond these traditional effects, nanoparticle-mediated hyperthermia is proving to have additional roles to play in cancer therapy – from disruption of microvasculature to sensitization of recalcitrant cancer stem cells to radiation. All this makes quick addition of this therapeutic modality to the oncologist's repetoire an important priority.

However, despite the potential role that hyperthermia can play in cancer management it has not been adequately exploited clinically. There are several reasons for this. Historical methods of achieving global hyperthermia were cumbersome, non-standardized and non-specific. More recent methods of generating hyperthermia are still frequently invasive and/or result in non-uniform temperature elevations within tumors and possible hot spots in surrounding normal tissues. The breakthrough has been the introduction of injectable nanoparticles like SPIONs, GNSs and CNTs that made it possible to achieve ablative temperatures inside highly localized areas of the body, while maintaining other areas at normal or near-normal temperatures. Nanoparticles provide a promising alternative to the older techniques to attain tumor hyperthermia.

However, there are several challenges facing the use of nanoparticles for tumor hyperthermia. A major problem is adequacy and uniformity of accumulation of nanoparticles at the tumor site. Even with very small nanoparticles, uniform temperature throughout the core and mantle of the tumor is still difficult to obtain [16]. Nanoparticles do not readily penetrate uniformly into the poorly vascularized tumor core. Other avenues need to be explored to find means of raising temperature uniformly in the core.

A second issue hampering the clinical translation of nanoparticles is the issue of quality control. Nanoparticles made in the laboratory often suffer from intra-batch and inter-batch variations in size and composition. As nanoparticles become more complex in composition, the risk of variation increases proportionally. Size distribution of nanoparticles are typically assessed using dynamic light scattering (e.g., with the zetasizer), but this provides an estimate of hydrodynamic radius rather than actual diameter. The actual diameter can be seen from electron microscopy, but only a very small number of nanoparticles can be seen

per image and extrapolating size of the full sample from the images can lead to errors. When nanoparticles are coated with targeting ligands, presence and quantification of the ligands, and in some cases testing of the functional capabilities, need to be done. Obviously, scaling up of production for industry will be an issue for complex nanoparticles. However, despite these obstacles, better methods of nanoparticle synthesis are constantly being reported. Most commercially available nanoparticles (e.g., the GNSs from Nanospectra, Inc.) are now available in batches with less than 1% variation in diameters. It is expected that in the near future we will have more complex nanoparticles being produced with equivalent quality controls.

A third obstacle in the clinical acceptance of nanoparticles is biocompatibility. The problem might be considered to be twofold: one of immediate toxicity and one of delayed effects of retained nanoparticles. Immediate and direct toxicity issues can be resolved using standardized testing on appropriate animal models. Indeed, most nanoparticles have been shown to be relatively nontoxic in the doses required for therapeutic effect. Gold, in particular, has a long history of usage in medical conditions, and GNS have been demonstrated to be safe in the administered quantities. As a result, clinical trials have been launched for human testing. However, GNRs have a unique challenge; as mentioned above, the persistent CTAB in the solution needs to be removed or neutralized before clinical usage is possible. The more difficult challenge is the question of the long-term fate of the nanoparticles sequestered in the body. Hepatic and splenic macrophages ingest and store much of the injected nanoparticles; the long-term consequences of this storage are as yet uncertain.

Similar to other treatment modalities, such as chemotherapy and radiation, hyperthermia is most effective when confined to the tumor. While enhanced permeation and retention allows passive accumulation at tumors, there is also concurrent accumulation in some other tissues, most notably the liver. This makes use of this technique less effective when dealing with tumors of the liver and surrounding areas. Accumulation at other areas, though less prominent, argues for thorough investigation of the biodistribution for each particle proposed for clinical use.

In conclusion, nanoparticles hold promise as a novel means of generating hyperthermia with distinct advantages over traditional methods. Comprehensive toxicity evaluations, optimized methods to ensure uniform, adequate and specific intratumoral delivery and greater dose deposition at tumors are the challenges that face effective clinical exploitation of nanoparticle-mediated hyperthermia in tumor treatment.

Key Terms

Antenna	An antenna (as used in medical hyperthermia) is a small metal piece which absorbs radio waves and consequently heats up
Radiofrequency and microwaves	Radiofrequency waves are electromagnetic waves with the rate of oscillation in the range of approximately 3 kHz to 300 GHz; microwaves are a subset at the higher energy end of this spectrum (300 MHz to 300 GHz)
Theranostic	A combination of the terms therapeutic and diagnostic; usually refers to a device which can perform both functions
Surface plasmon resonance	Plasmons are quantized oscillations of free electrons. These electron waves propagate along the surface of metal

	nanoparticles, and can resonate when photons of certain wavelength are incident on them
Core:shell ratio	Ratio of the diameter of the core to the thickness of the shell of core shell nanoparticles. A higher core:shell ratio means a thinner shell
Superparamagnetism	Small nanometer-sized ferro- and ferri-magnetic particles demonstrate no magnetization in the absence of a magnetic field (unlike similar material in the meso- and macroscopic scales). These are magnetized in the presence of a magnetic field (such as paramagnetic material, e.g., gadolinium) but much more strongly than compared with conventioanl paramagnets
Graphene	Graphene is an allotrope of carbon, where the carbon atoms are bonded in a honeycomb pattern to form 2D crystalline planar sheets. The sheet can be rolled into tubes (carbon nanotubes) or stacked into a 3D sheet (graphite)

Bibliography

1. Coley WB II. Contribution to the Knowledge of Sarcoma. Ann Surg. 1891; 14(3):199–220.
2. Friedenthal E, Mendecki J, Botstein C, Sterzer F, Nowogrodzki M, Paglione R. Some practical considerations for the use of localized hyperthermia in the treatment of cancer. J Microw Power. 1981; 16(2):199–204. [PubMed: 6915106]
3. Lele PP. Induction of deep, local hyperthermia by ultrasound and electromagnetic fields: problems and choices. Radiat Environ Biophys. 1980; 17(3):205–217. [PubMed: 7443976]
4. Magin RL, Johnson RK. Effects of local tumor hyperthermia on the growth of solid mouse tumors. Cancer Res. 1979; 39(11):4534–4539. [PubMed: 498085]
5. Kim JH, Hahn EW, Ahmed SA. Combination hyperthermia and radiation therapy for malignant melanoma. Cancer. 1982; 50(3):478–482. [PubMed: 7093890]
6. Luk KH, Francis ME, Perez CA, Johnson RJ. Combined radiation and hyperthermia: comparison of two treatment schedules based on data from a registry established by the Radiation Therapy Oncology Group (RTOG). Int J Radiat Oncol Biol Phys. 1984; 10(6):801–809. [PubMed: 6735765]
7. Stewart JR, Gibbs FA Jr. Hyperthermia in the treatment of cancer. Perspectives on its promise and its problems. Cancer. 1984; 54(11 Suppl):2823–2830. [PubMed: 6388817]
8. Thrall DE. Clinical requirements for localized hyperthermia in the patient. Radiat Environ Biophys. 1980; 17(3):229–232. [PubMed: 7443978]
9. Doss JD, Mccabe CW. A technique for localized heating in tissue: an adjunct to tumor therapy. Med Instrum. 1976; 10(1):16–21. [PubMed: 1250180]
10. Irish CE, Brown J, Galen WP, et al. Thermoradiotherapy for persistent cancer in previously irradiated fields. Cancer. 1986; 57(12):2275–2279. [PubMed: 3697929]
11. Seegenschmiedt MH, Sauer R, Miyamoto C, Chalal JA, Brady LW. Clinical experience with interstitial thermoradiotherapy for localized implantable pelvic tumors. Am J Clin Oncol. 1993; 16(3):210–222. [PubMed: 8338055]
12. Bass H, Moore JL, Coakley WT. Lethality in mammalian cells due to hyperthermia under oxic and hypoxic conditions. Int J Radiat Biol Relat Stud Phys Chem Med. 1978; 33(1):57–67. [PubMed: 304850]
13. Storm FK. Clinical hyperthermia and chemotherapy. Radiol Clin North Am. 1989; 27(3):621–627. [PubMed: 2648463]
14. Urano M, Kuroda M, Nishimura Y. For the clinical application of thermochemotherapy given at mild temperatures. Int J Hyperthermia. 1999; 15(2):79–107. [PubMed: 10323618]

15. Shakil A, Osborn JL, Song CW. Changes in oxygenation status and blood flow in a rat tumor model by mild temperature hyperthermia. Int J Radiat Oncol Biol Phys. 1999; 43(4):859–865. [PubMed: 10098442]
16. Johannsen M, Thiesen B, Wust P, Jordan A. Magnetic nanoparticle hyperthermia for prostate cancer. Int J Hyperthermia. 2010; 26(8):790–795. [PubMed: 20653418]
17. Hurwitz MD, Hansen JL, Prokopios-Davos S, et al. Hyperthermia combined with radiation for the treatment of locally advanced prostate cancer: long-term results from Dana-Farber Cancer Institute study 94–153. Cancer. 2011; 117(3):510–516. [PubMed: 20886629]
18. Moros EG, Penagaricano J, Novak P, Straube WL, Myerson RJ. Present and future technology for simultaneous superficial thermoradiotherapy of breast cancer. Int J Hyperthermia. 2010; 26(7): 699–709. [PubMed: 20849263]
19. Van Den Berg CA, Van De Kamer JB, De Leeuw AA, et al. Towards patient specific thermal modelling of the prostate. Phys Med Biol. 2006; 51(4):809–825. [PubMed: 16467580]
20. Zagar TM, Oleson JR, Vujaskovic Z, et al. Hyperthermia combined with radiation therapy for superficial breast cancer and chest wall recurrence: a review of the randomised data. Int J Hyperthermia. 2010; 26(7):612–617. [PubMed: 20849256]
21. Franckena M, Van Der Zee J. Use of combined radiation and hyperthermia for gynecological cancer. Curr Opin Obstet Gynecol. 2010; 22(1):9–14. [PubMed: 20019611]
22. Vasanthan A, Mitsumori M, Park JH, et al. Regional hyperthermia combined with radiotherapy for uterine cervical cancers: a multi-institutional prospective randomized trial of the international atomic energy agency. Int J Radiat Oncol Biol Phys. 2005; 61(1):145–153. [PubMed: 15629605]
23. Huilgol NG, Gupta S, Sridhar CR. Hyperthermia with radiation in the treatment of locally advanced head and neck cancer: a report of randomized trial. J Cancer Res Ther. 2010; 6(4):492–496. [PubMed: 21358087]
24. Huilgol NG, Gupta S, Dixit R. Chemoradiation with hyperthermia in the treatment of head and neck cancer. Int J Hyperthermia. 2010; 26(1):21–25. [PubMed: 20100049]
25. Chang E, Alexander HR, Libutti SK, et al. Laparoscopic continuous hyperthermic peritoneal perfusion. J Am Coll Surg. 2001; 193(2):225–229. [PubMed: 11491455]
26. Feldman AL, Libutti SK, Pingpank JF, et al. Analysis of factors associated with outcome in patients with malignant peritoneal mesothelioma undergoing surgical debulking and intraperitoneal chemotherapy. J Clin Oncol. 2003; 21(24):4560–4567. [PubMed: 14673042]
27. Maeda H. The enhanced permeability and retention (EPR) effect in tumor vasculature: the key role of tumor-selective macromolecular drug targeting. Adv Enzyme Regul. 2001; 41:189–207. [PubMed: 11384745]
28. Maeda H, Wu J, Sawa T, Matsumura Y, Hori K. Tumor vascular permeability and the EPR effect in macromolecular therapeutics: a review. J Control Release. 2000; 65(1–2):271–284. [PubMed: 10699287]
29. Kah JC, Wong KY, Neoh KG, et al. Critical parameters in the pegylation of gold nanoshells for biomedical applications: an *in vitro* macrophage study. J Drug Target. 2009; 17(3):181–193. [PubMed: 19016072]
30. Wang J, Sui M, Fan W. Nanoparticles for tumor targeted therapies and their pharmacokinetics. Curr Drug Metab. 2010; 11(2):129–141. [PubMed: 20359289]
31. El-Sayed IH, Huang X, El-Sayed MA. Selective laser photo-thermal therapy of epithelial carcinoma using anti-EGFR antibody conjugated gold nanoparticles. Cancer Lett. 2006; 239(1): 129–135. [PubMed: 16198049]
32. Waldman SA, Fortina P, Surrey S, Hyslop T, Kricka LJ, Graves DJ. Opportunities for near-infrared thermal ablation of colorectal metastases by guanylyl cyclase C-targeted gold nanoshells. Future Oncol. 2006; 2(6):705–716. [PubMed: 17155897]
33. Patra CR, Bhattacharya R, Mukhopadhyay D, Mukherjee P. Fabrication of gold nanoparticles for targeted therapy in pancreatic cancer. Adv Drug Deliv Rev. 2010; 62(3):346–361. [PubMed: 19914317]
34. Hosta-Rigau L, Olmedo I, Arbiol J, Cruz LJ, Kogan MJ, Albericio F. Multifunctionalized gold nanoparticles with peptides targeted to gastrin-releasing peptide receptor of a tumor cell line. Bioconjug Chem. 2010; 21(6):1070–1078. [PubMed: 20476781]

35. Diagaradjane P, Shetty A, Wang JC, et al. Modulation of *in vivo* tumor radiation response via gold nanoshell-mediated vascular-focused hyperthermia: characterizing an integrated antihypoxic and localized vascular disrupting targeting strategy. Nano Lett. 2008; 8(5):1492–1500. [PubMed: 18412402]
36. Hirsch LR, Gobin AM, Lowery AR, et al. Metal nanoshells. Ann Biomed Eng. 2006; 34(1):15–22. [PubMed: 16528617]
37. Hulander M, Hong J, Andersson M, et al. Blood interactions with noble metals: coagulation and immune complement activation. ACS Appl Mater Interfaces. 2009; 1(5):1053–1062. [PubMed: 20355891]
38. Choi WI, Kim JY, Kang C, Byeon CC, Kim YH, Tae G. Tumor regression *in vivo* by photothermal therapy based on gold-nanorod-loaded, functional nanocarriers. ACS Nano. 2011; 5(3):1995–2003. [PubMed: 21344891]
39. Von Maltzahn G, Park JH, Agrawal A, et al. Computationally guided photothermal tumor therapy using long-circulating gold nanorod antennas. Cancer Res. 2009; 69(9):3892–3900. [PubMed: 19366797]
40. Hirsch LR, Stafford RJ, Bankson JA, et al. Nanoshell-mediated near-infrared thermal therapy of tumors under magnetic resonance guidance. Proc Natl Acad Sci USA. 2003; 100(23):13549–13554. [PubMed: 14597719]
41. O'neal DP, Hirsch LR, Halas NJ, Payne JD, West JL. Photo-thermal tumor ablation in mice using near infrared-absorbing nanoparticles. Cancer Lett. 2004; 209(2):171–176. [PubMed: 15159019]
42. Bernardi RJ, Lowery AR, Thompson PA, Blaney SM, West JL. Immunonanoshells for targeted photothermal ablation in medulloblastoma and glioma: an *in vitro* evaluation using human cell lines. J Neurooncol. 2008; 86(2):165–172. [PubMed: 17805488]
43. Cheng FY, Chen CT, Yeh CS. Comparative efficiencies of photothermal destruction of malignant cells using antibody-coated silica–Au nanoshells, hollow Au/Ag nanospheres and Au nanorods. Nanotechnology. 2009; 20(42):425104. [PubMed: 19779243]
44. Dickerson EB, Dreaden EC, Huang X, et al. Gold nanorod assisted near-infrared plasmonic photothermal therapy (PPTT) of squamous cell carcinoma in mice. Cancer Lett. 2008; 269(1):57–66. [PubMed: 18541363]
45. Skrabalak SE, Au L, Lu X, Li X, Xia Y. Gold nanocages for cancer detection and treatment. Nanomedicine (Lond). 2007; 2(5):657–668. [PubMed: 17976028]
46. Atkinson RL, Zhang M, Diagaradjane P, et al. Thermal enhancement with optically activated gold nanoshells sensitizes breast cancer stem cells to radiation therapy. Sci Transl Med. 2010; 2(55):55ra79.
47. Gilchrist RK, Medal R, Shorey WD, Hanselman RC, Parrott JC, Taylor CB. Selective inductive heating of lymph nodes. Ann Surg. 1957; 146(4):596–606. [PubMed: 13470751]
48. Yallapu MM, Othman SF, Curtis ET, Gupta BK, Jaggi M, Chauhan SC. Multi-functional magnetic nanoparticles for magnetic resonance imaging and cancer therapy. Biomaterials. 2011; 32(7):1890–1905. [PubMed: 21167595]
49. Huang N, Wang H, Zhao J, Lui H, Korbelik M, Zeng H. Single-wall carbon nanotubes assisted photothermal cancer therapy: animal study with a murine model of squamous cell carcinoma. Lasers Surg Med. 42(9):638–648. [PubMed: 20949599]
50. Elsherbini AA, Saber M, Aggag M, El-Shahawy A, Shokier HA. Magnetic nanoparticle-induced hyperthermia treatment under magnetic resonance imaging. Magn Reson Imaging. 2011; 29(2):272–280. [PubMed: 21145190]
51. Majumdar S, Zoghbi SS, Gore JC. Pharmacokinetics of superparamagnetic iron-oxide MR contrast agents in the rat. Invest Radiol. 1990; 25(7):771–777. [PubMed: 2391194]
52. Okon E, Pouliquen D, Okon P, et al. Biodegradation of magnetite dextran nanoparticles in the rat. A histologic and biophysical study. Lab Invest. 1994; 71(6):895–903. [PubMed: 7807971]
53. Wu X, Tan Y, Mao H, Zhang M. Toxic effects of iron oxide nanoparticles on human umbilical vein endothelial cells. Int J Nanomedicine. 2010; 5:385–399. [PubMed: 20957160]
54. Fan C, Gao W, Chen Z, et al. Tumor selectivity of stealth multi-functionalized superparamagnetic iron oxide nanoparticles. Int J Pharm. 2011; 404(1–2):180–190. [PubMed: 21087660]

55. Balivada S, Rachakatla RS, Wang H, et al. A/C magnetic hyperthermia of melanoma mediated by iron(0)/iron oxide core/shell magnetic nanoparticles: a mouse study. BMC Cancer. 2010; 10:119. [PubMed: 20350328]
56. Rachakatla RS, Balivada S, Seo GM, et al. Attenuation of mouse melanoma by A/C magnetic field after delivery of bi-magnetic nanoparticles by neural progenitor cells. ACS Nano. 2010; 4(12): 7093–7104. [PubMed: 21058696]
57. Le Renard PE, Jordan O, Faes A, et al. The *in vivo* performance of magnetic particle-loaded injectable, *in situ* gelling, carriers for the delivery of local hyperthermia. Biomaterials. 2010; 31(4):691–705. [PubMed: 19878991]
58. Hayashi K, Ono K, Suzuki H, et al. High-frequency, magnetic-field-responsive drug release from magnetic nanoparticle/organic hybrid based on hyperthermic effect. ACS Appl Mater Interfaces. 2010; 2(7):1903–1911. [PubMed: 20568697]
59. Mohammad F, Balaji G, Weber A, Uppu RM, Kumar CS. Influence of gold nanoshell on hyperthermia of superparamagnetic iron oxide nanoparticles (SPIONs). J Phys Chem C Nanomater Interfaces. 2010; 1(20):3141–3146. [PubMed: 21103390]
60. Zheng LX, O'connell MJ, Doorn SK, et al. Ultralong single-wall carbon nanotubes. Nat Mater. 2004; 3(10):673–676. [PubMed: 15359345]
61. Kam NW, O'Connell M, Wisdom JA, Dai H. Carbon nanotubes as multifunctional biological transporters and near-infrared agents for selective cancer cell destruction. Proc Natl Acad Sci USA. 2005; 102(33):11600–11605. [PubMed: 16087878]
62. Biris AS, Boldor D, Palmer J, et al. Nanophotothermolysis of multiple scattered cancer cells with carbon nanotubes guided by time-resolved infrared thermal imaging. J Biomed Opt. 2009; 14(2): 021007. [PubMed: 19405720]
63. Torti SV, Byrne F, Whelan O, et al. Thermal ablation therapeutics based on CN(x) multi-walled nanotubes. Int J Nanomedicine. 2007; 2(4):707–714. [PubMed: 18203437]
64. Moon HK, Lee SH, Choi HC. *In vivo* near-infrared mediated tumor destruction by photothermal effect of carbon nanotubes. ACS Nano. 2009; 3(11):3707–3713. [PubMed: 19877694]
65. Gannon CJ, Cherukuri P, Yakobson BI, et al. Carbon nanotube-enhanced thermal destruction of cancer cells in a noninvasive radiofrequency field. Cancer. 2007; 110(12):2654–2665. [PubMed: 17960610]
66. Burke A, Ding X, Singh R, et al. Long-term survival following a single treatment of kidney tumors with multiwalled carbon nanotubes and near-infrared radiation. Proc Natl Acad Sci USA. 2009; 106(31):12897–12902. [PubMed: 19620717]
67. Poland CA, Duffin R, Kinloch I, et al. Carbon nanotubes introduced into the abdominal cavity of mice show asbestos-like pathogenicity in a pilot study. Nat Nanotechnol. 2008; 3(7):423–428. [PubMed: 18654567]
68. Glazer ES, Curley SA. Radiofrequency field-induced thermal cytotoxicity in cancer cells treated with fluorescent nanoparticles. Cancer. 2010; 116(13):3285–3293. [PubMed: 20564640]
69. Melnikov OV, Gorbenko OY, Markelova MN, et al. Ag-doped manganite nanoparticles: new materials for temperature-controlled medical hyperthermia. J Biomed Mater Res A. 2009; 91(4): 1048–1055. [PubMed: 19127514]
70. Fuller KJ, Issels RD, Slosman DO, Guillet JG, Soussi T, Polla BS. Cancer and the heat-shock response. Eur J Cancer. 1994; 30A(12):1884–1891. [PubMed: 7880622]
71. Harmon BV, Takano YS, Winterford CM, Gobe GC. The role of apoptosis in the response of cells and tumours to mild hyperthermia. Int J Radiat Biol. 1991; 59(2):489–501. [PubMed: 1671698]

Executive summary

- Hyperthermia, a small rise in tumor temperature, alters the cancer cells (especially the cancer stem cells) and the microenvironment to increase susceptibility to radiation and chemotherapy.
- Specific and uniform elevation of tumor temperature is difficult with whole-body and regional hyperthermia. Luminal and interstitial local hyperthermia are invasive, while external radiation may cause skin burns.
- Preferential loading of tumors with systemically administered, energy-transducing nanoparticles allows tumor specificity, heating from within the tumor, vascular disruption, simultaneous imaging and therapy (theranostics) and single-platform combination with other therapies.
- Three major nanoparticles for generating hyperthermia are gold nanoparticles, superparamagnetic iron oxide nanoparticles (SPIONs) and carbon nanotubes (CNTs).
- Gold nanoparticles with strong absorption cross sections in the near infrared wavelength due to surface plasmon resonance, efficiently generate heat upon illumination and are inert, stable and readily conjugated to biomolecules for specific tumor targeting. Two major types are nanoshells and nanorods.
- SPIONs heat up rapidly in an alternating magnetic field depending on the field strength and frequency, particle concentration and characteristics and the depth of the tumor within the body.
- CNTs are largely unidimensional nanomaterials composed of rolled sheets of graphene with tunable absorption of electromagnetic waves over a broad frequency range to generate heat.
- Obstacles to clinical exploitation of hyperthermia can potentially be overcome with nanoparticles providing more efficient methods of generating uniform heating in tumors with minimal effect on normal tissue.
- Challenges facing nanoparticle-mediated tumor hyperthermia include inadequacy and non-uniformity of accumulation in tumors, especially the core; lack of quality control in production; perceived toxicity issues; concurrent accumulation in the liver and other tissues; and thermal modeling/dosimetry.

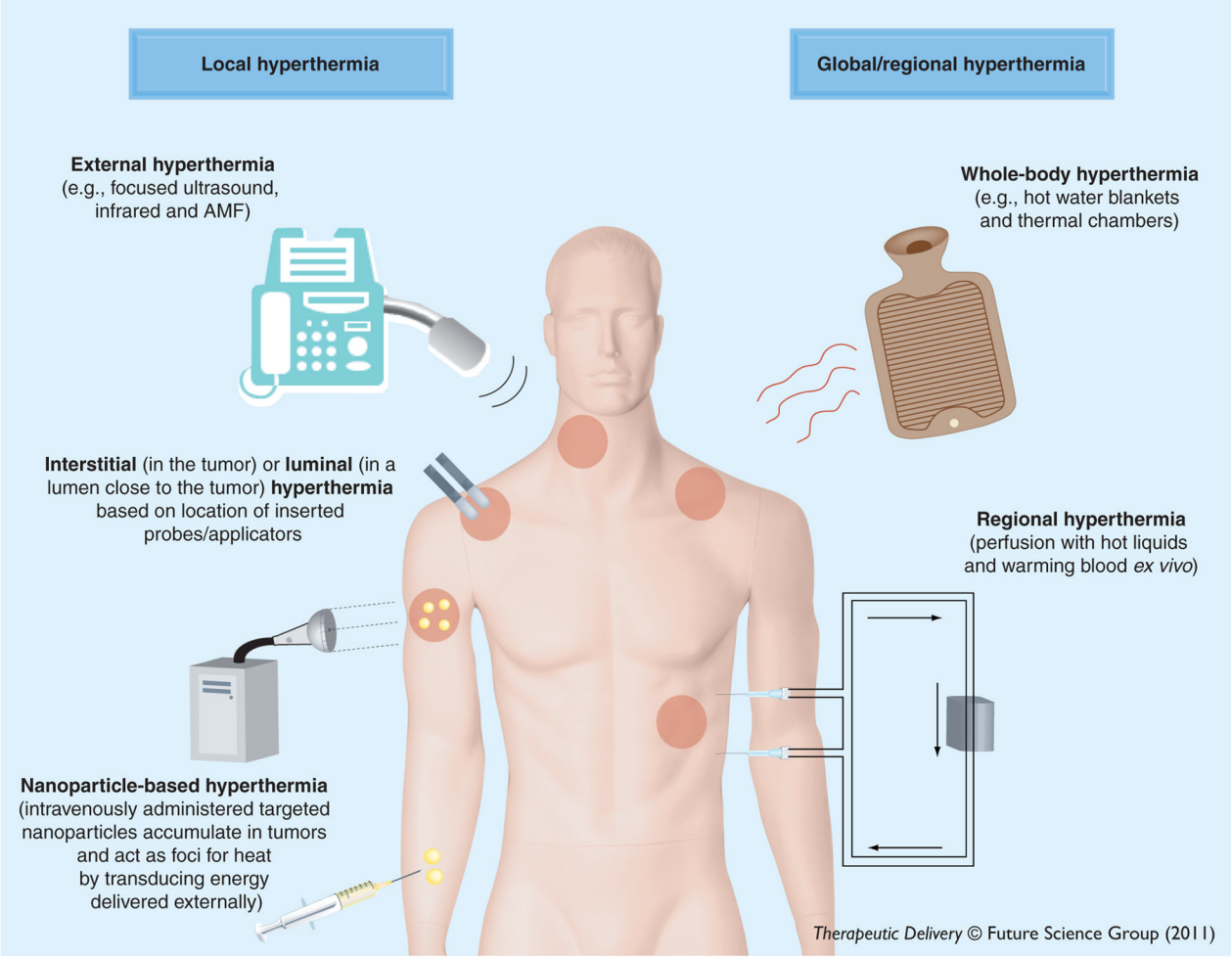

Figure 1. Methods of achieving tumor hyperthermia
AMF: Alternating magnetic field

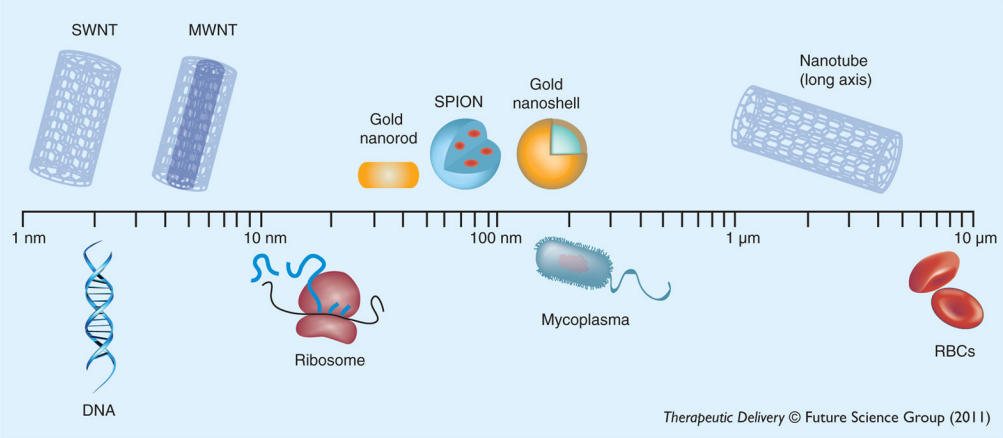

Figure 2. Relative scale of synthetic nanomaterials as compared with naturally occurring biomacromolecules and cells

MWNT: Multiwalled carbon nanotubes; RBC: Red blood cell; SPION: Superparamagnetic iron oxide nanoparticle; SWNT: Single-walled carbon nanotubes.

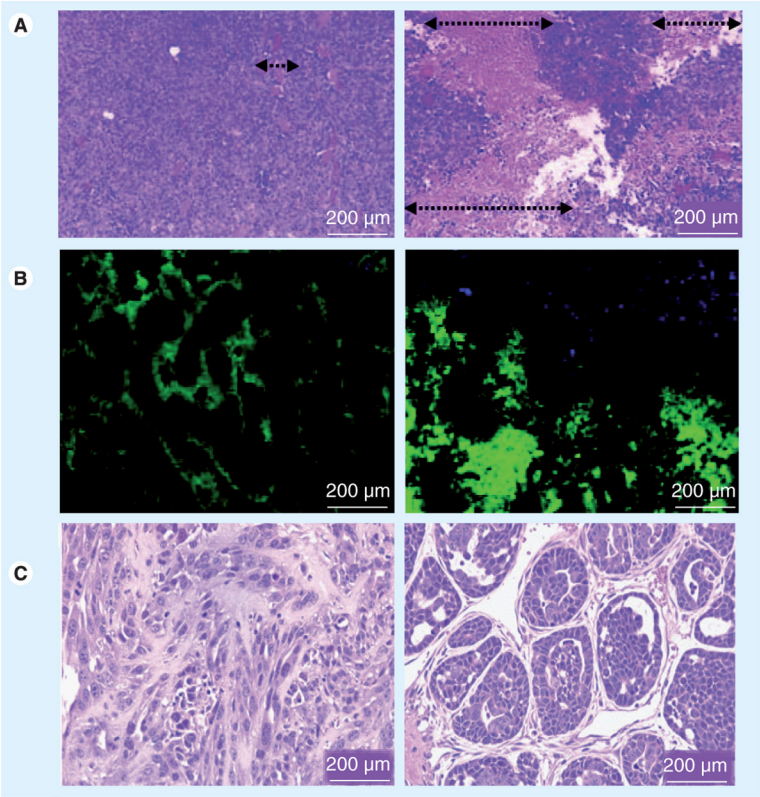

Figure 3. Effects of nanoparticle-mediated hyperthermia on tumors *in vivo*.

(A) In mice with subcutaneously inoculated human colorectal cancer cells, 90 min following a single 10 Gy dose of radiation therapy using 125 kV x-rays, hematoxylin and eosin-stained slides of the tumor core show minimal necrosis (left), but addition of gold nanoshell-mediated hyperthermia (41°C for 20 min immediately prior to radiation) results in significantly more necrosis (right). Arrows denote size of areas of necrosis within tumors [35]. **(B)** On further investigation, the tumor core of mice treated with radiation alone (left) has classical tissue architecture with central vascular channels surrounded by orderly layers of cells with decreasing levels of oxygenation with increasing distance – hypoxic areas (further from vasculature) are stained green and perfused areas are stained blue in this immunofluorescence image. However, the mice treated with combined hyperthermia and radiation (right) have tumor cores with complete disruption of normal stromal structure, suggestive of vascular collapse [35]. **(C)** In a mouse model of breast cancer, treatment with a single dose of 6 Gy with or without post-treatment hyperthermia (42°C for 20 min) was followed by tumor digestion 48 h later and re-implantation in syngeneic mice in limiting dilutions. For reappearance of tumors, the combined treatment group required more cells re-implanted in mice than the radiation alone group, suggestive of a greater effect of combined treatment on putative cancer stem cells. Furthermore, the tumors reappeared as a more aggressive phenotype in the radiation alone group (left) than the combined treatment group (right). These results suggest that more efficient elimination of cancer stem cells by nanoshell-mediated hyperthermia and radiation compared with radiation alone results in lesser ability to recreate tumors as well as appearance of more differentiated, less aggressive and more treatable tumors [46].

Figures reproduced with permission from the referenced sources.

Published in final edited form as:
Ther Deliv. 2011 August 1; 2(8): 1001–1014.

Nanoparticle-mediated hyperthermia in cancer therapy

Dev Kumar Chatterjee[1], **Parmeswaran Diagaradjane**[1], and **Sunil Krishnan**[1,†]
[1]Department of Radiation Oncology, MD Anderson Cancer Center, Houston, TX 77030, USA

Abstract

A small rise in tumor temperature (hyperthermia) makes cancer cells more susceptible to radiation and chemotherapy. The means of achieving this is not trivial, and traditional methods have certain drawbacks. Loading tumors with systematically asministered energy-transducing nanoparticles can circumvent several of the obstacles to achieve tumor hyperthermia. However, nanoparticles also face unique challenges prior to clinical implementation. This article summarizes the state-of-the-art current technology and discusses the advantages and challenges of the three major nanoparticle formulations in focus: gold nanoshells and nanorods, superparamagnetic iron oxide particles and carbon nanotubes.

Hyperthermia in cancer therapy

Clinical rationale & biological basis for hyperthermia

Hyperthermia has a long history in the annals of cancer management. A correlation between erysipelas (a streptococcal skin infection) and tumor regression had been observed for over a century before William Coley first documented evidence of a relationship between infection and cancer regression in sarcoma patients in 1891 [1]. His attempts to recreate this phenomenon for the treatment of cancers culminated in the generation of cocktails of bacteria (Coley's toxin) that intentionally induced a fever to effect an antitumor response. While this probably represents among the first instances of the clinical use of hyperthermia for cancer therapy, it was also among the first demonstrations of the efficacy of immunotherapy. Since then, more localized and relatively safer methods of hyperthermia, either singly or in combination with conventional therapy, have been employed by many investigators to treat cancer (Box 1) [2–11].

Box 1

Definitions

- Hyperthermia, in a medical setting, is a rise in temperature of body tissues, globally or locally. In the field of cancer therapy where this elevation in temperature is induced intentionally, this definition can be further qualified based on the desired effect of this temperature rise on the tissue. If the temperature is raised high enough to cause immediate cellular death, largely

†Author for correspondence: Tel.: +1 713 563 2377, Fax: +1 713 563 2366, skrishnan@mdanderson.org.

Financial & competing interests disclosure
This work was funded in part by NIH grants KL2 RR024149 05, 1R21CA133691–01, 1R01CA132032 and U01CA151886 to Sunil Krishnan. The authors have no other relevant affiliations or financial involvement with any organization or entity with a financial interest in or financial conflict with the subject matter or materials discussed in the manuscript apart from those disclosed.
No writing assistance was utilized in the production of this manuscript.

through necrosis mediated by irreparable coagulation of proteins and other biological macromolecules, the more accurate term to use is *thermoablation*. In contrast to thermoablation, hyperthermia refers to smaller temperature rises, usually to 40–45°C, initiating a series of subcellular events, rendering the cells susceptible to various forms of damage including apoptosis, leading to subsequent cell death [70,71]. Other effects associated with hyperthermia include activation of immunological responses, enhancement of tumor blood flow and oxygenation via greater vascular perfusion and permeability, and a shift toward anaerobic metabolism resulting in decreased oxygen consumption and increased tissue oxygenation, all leading to an altered extracellular microenvironment.

- Nanoparticle is an umbrella term encompassing a variety of materials all sharing the common feature of having the longest dimension less than 100 nm. This limitation is generally relaxed in the scientific parlance, with particles not greatly exceeding 100 nm also earning the sobriquet ‘nano’ (Figure 1). Nanoparticles can be solid, hollow or branching, and made from a very diverse selection of materials. The development of means to control and characterize at the nanoscale allows a degree of design unsurpassed by single-molecule entities. In the field of cancer therapy, nanoparticles afford many advantages over conventional therapeutic methods and are an ongoing research focus on a global scale.

Heat as a curative modality (thermoablation) has been explored in cancer by many researchers. The challenge facing thermoablation therapies mirrors that of surgery: the destruction of the tumor needs to be as complete as possible, while sparing normal tissues. Thermoablation became a topic of high interest with the advent of electromagnetic heating. However, despite demonstrations of delayed tumor regrowth following thermoablation, in general, the therapy falls short in curative prowess owing to the difficulties in precise control of temperature rise in different regions of the tumor resulting in residual cancerous tissue and tumor recurrence. By contrast, sub-ablative heating has a bigger therapeutic window since cell destruction is not desired. Mild temperature rise throughout the tumor may be accompanied by some heating of surrounding normal tissue, but since non-malignant cells have unimpaired heat-shock protection mechanisms, the toxicity profile for mild hyperthermia is usually very good.

The increasing interest in hyperthermia has been paralleled by an increasing understanding of the mechanism of action of this treatment modality. It is now known that tumor cells, tumor vascular endothelial cells, and normal cells are not inherently different in their sensitivity to heat-induced cytotoxicity. However, owing to inefficient blood flow and oxygen transport through the newly formed immature blood vessels within tumors, tumor cells reside in an acidotic and nutrient-deprived milieu that confers them with greater thermosensitivity [12]. This greater sensitivity of hypoxic areas to heat provides a compelling rationale for the combination of hyperthermia with radiation therapy since poorly perfused tumor cores are generally resistant to the effects of ionizing radiation, which depends on the generation of toxic oxygen radicals in well-perfused regions. The complementary effects of radiation and hyperthermia is further accentuated by the fact that tumor cells in the S phase of the cell cycle are relatively radioresistant. However, it is precisely in this phase that tumor cells are most sensitive to the effect of heat and become radio-sensitized. Thus hyperthermia acts as a potent and selective radiosensitizer by affecting those cancer cells that are naturally radioresistant.

Hyperthermia can also be used to chemosensitize cancer cells. The degree of chemosensitization varies with the type and concentration of drug, the tumor type, the increase in tumor temperature and the time differential between the delivery of heat and chemotherapy. However, prior drug resistance does not appear to be a factor in the sensitivity to heat. Chemosensitization is highest when heat and chemotherapy are administered simultaneously, the effect diminishing at greater intervals between delivery of the two therapies [13]. In general, enhanced cytotoxicity of many chemotherapeutic agents increases in the range of 40.5–43°C [14]. However, clinically, temperatures above 41°C have been associated with higher toxicity and a low benefit:risk ratio. In general, hyperthermia with milder temperatures increases the destruction of cancer cells with chemotherapy, but not that of normal cells (i.e., chemotherapeutic side effects are minimized). However, there is a potentially wide variation in the thermal enhancement of a given agent among the different types of tumors. Also, different agents have different enhancement ratios for the same degree of temperature elevation in the same tumor type, indicating that the drug of choice at physiological temperatures may not be the drug of choice at elevated temperatures [14]. In general, however, even for drugs with good thermal enhancement for a particular tumor type, the enhancement of tumor toxicity due to heat is only seen at higher drug concentrations in the tumor. Hence, isolated perfusion of tumors with heated solutions of chemotherapeutics, providing a higher tumor drug concentration demonstrates a better response than systemic administration of the same drug. Several mechanisms have been proposed for this observed effect. Temperatures bordering on 42–43°C have some cancer-specific cytotoxicity resulting from the impaired mechanisms of cancer cells to handle heat shock. Prolonged (>1 h) heating at lower temperatures increases tumor perfusion, and this results in greater delivery of chemotherapeutics especially to the poorly vascularized core. The lack of enhanced drug toxicity with loco-regional hyperthermia with potential improvement in response to advanced disease suggests that thermochemotherapy is a viable and important alternative to drug treatment alone.

Unfortunately, it is not often possible to elevate tumor temperature uniformly to the 42–43°C required for direct cytotoxicity. Fortuitously, it is fairly well established now that clinically achievable elevations of tumor temperature to approximately 40–42°C (mild temperature hyperthermia), although less effective as monotherapy against cancer, has potent efficacy as an adjunct to radiation therapy. This is largely driven by an increase in blood flow (often sustained for 1–2 days) [15] and oxygen delivery and a decrease in oxygen demand (due to hyperthermia-induced cell death and metabolic suppression) that converge to increase tumor tissue oxygenation. Increased perfusion also directly translates to increased delivery of chemotherapeutic drugs to the poorly vascularized tumor cores [16]. Such a complementary role for hyperthermia has been demonstrated in numerous clinical and preclinical studies of hyperthermia combined with chemotherapy or radiation therapy, with significant improvements in outcome demonstrated for tumors of the prostate, breast, bladder, brain, cervix, head and neck, lung, rectum and esophagus, among others. Typically, adding hyperthermia to the treatment regimen has not resulted in increased toxicity (especially for radiation therapy), but has contributed to better control, cure and/or palliation [17–24].

Hyperthermia techniques

While the rationale for adding hyperthermia to clinical regimens is compelling, the means to do so are not as straightforward. Three types of hyperthermia are traditionally employed in clinical practice – whole-body, regional and local hyperthermia (Figure 1). Whole-body hyperthermia is achieved by such methods as hot water blankets and thermal chambers. In theory, it should be used for metastatic cancer where focal hyperthermia would be ineffective. Regional hyperthermia depends on perfusing with heated liquids – the two

popular techniques are perfusing the peritoneum with a heated solution of anticancer drugs for peritoneal cancers such as mesothelioma, and the perfusion of a part of the patient's blood, taken out and warmed *ex vivo*, into an artery supplying the limb containing the tumor [25,26]. Both whole-body and regional hyperthermia in general result in poor tumor specificity of treatment. While the toxic effects of hyperthermia are usually not severe, whole-body hyperthermia often causes gastrointestinal symptoms, such as diarrhea, nausea and vomiting, and may occasionally have serious cardiovascular side effects, such as myocardial ischemia, thrombosis and cardiac failure. Regional hyperthermia is invasive and involves significant challenges in set-up.

Local hyperthermia, in theory, has the advantage of being tumor focused. The three major methods of generation of local hyperthermia, in order of increasing invasiveness, are external, luminal and interstitial. Luminal hyperthermia uses special probes placed as close to the tumor as possible, such as in the lumen of the rectum for treatment of rectal cancers, whereas interstitial hyperthermia uses a grid of applicators/probes placed into tumor parenchyma for more uniform tumor heating. Heat sources can be inserted into the probes and applicators, or the probes can be heated by external heating sources. Generally, these methods also suffer from moderate to high invasiveness, while the heating of the tumor is non-uniform, being concentrated more on the probe than elsewhere. Another way in which this can be achieved is by placing metal **antennas** ('seeds') in the tumor interstitium before exposure to an external magnetic field. These antennas are elongated devices made of ferromagnetic material (e.g., iron), which heat up in an alternating electromagnetic field (detailed later). In this way, the heat for hyperthermia is actually generated inside the tumor rather than filtering through from outside, and can be readily controlled by simply controlling the strength of the magnetic field. However, implanting the relatively large seeds requires an invasive procedure, which adds to the morbidity of the treatment. The seeds may focus the heating in the immediate locality of the implantation area, with resultant cold spots elsewhere in the tumor. Placing the seeds in a deep tumor may be difficult and require image guidance. Finally, it often requires large investments of money because of the requirements for special electromagnetically shielded rooms and compliance with other federal regulations. External heating can be achieved either with electromagnetic radiation (e.g., **microwave**, laser and **radio-frequency**) or high-intensity focused ultrasound, all of which transduce energy from an external source to pass through the body. One disadvantage of this method is that energy is deposited in the normal tissues along its path and can result in hot spots within these tissues. In summary, despite the beneficial effects of adding hyperthermia to the cancer management regimen, current methods to achieve it are often invasive, nonuniform or non-specific to the tumor. Clearly, there are opportunities to improve uniformity and target specificity of heat in a non-invasive or minimally invasive manner.

Nanoparticles for local hyperthermia

The foregoing discussion outlines the promises and pitfalls of established methods of generating hyperthermia. The continuing quest for a method of hyperthermia that is tumor focused, minimally invasive, and uniform has led to the investigation of nanoparticles as conduits for generating hyperthermia (Figure 2). To maximize the energy deposited in the tumor while limiting the exposure in healthy tissues, tumors can be preferentially loaded with systemically administered nanoparticles that have a high-absorption cross section for transduction of an extrinsic energy source to heat. Hyperthermia achieved by this method has several potential advantages over both global and focal hyperthermia achieved without nanoparticles.

Localization of nanoparticles

It has been widely recognized that intravenously administered nanoparticles passively extravasate from vasculature and preferentially accumulate in tumors but not in normal tissues. This phenomenon, often referred to as the enhanced permeability and retention (EPR) effect, is a consequence of the leakiness of immature tumor neovasculature with large fenestrations and inefficient lymphatic drainage [27,28]. To ensure long circulation times of nanoparticles for efficient accumulation within tumors, evasion of non-specific reticuloendothelial capture of these particles can be achieved by rendering them 'stealth' properties via coating them with polyethylene glycol (a process known as PEGylation), dextran or other biocompatible coatings [29,30]. Additionally, nanoparticles can be decorated with targeting molecules homing to cancer-specific and cancer-associated antigens to achieve even greater tumor sensitivity [31–34]. It is to be noted that these techniques of tumor-specific localization of nanoparticles leads to tumor specific dose delivery that is independent of invasive procedures adopted in other localized dose-delivery strategies such as interstitial hyperthermia. Targeted nanoparticles also result in less non-specific accumulation in the body, enabling a lowering of injected dose of nanoparticles for the same therapeutic effect and lessening the probability of nanoparticle-mediated toxicity.

'Inside-out' hyperthermia

All sources of heat create a temperature gradient in the tissues with the temperature falling off sharply with distance from the heat source. All external sources of heat-like focused ultrasound or infrared lamps have a narrow window of effectiveness where the skin surface is significantly affected before the temperature in the tumor reaches therapeutic levels. However, unlike all other means of external hyperthermia, the primary source of the heat – the nanoparticle – is located inside the tumor. This reverses the direction of heat loss – from inside out and reduces damage to normal tissues while heating up the tumor. Furthermore, most of the nanoparticles are metallic and consequently have excellent thermal conductivity that couples and instantly transmits the heat they generate to the surrounding tumor tissue. Interstitial hyperthermia also relies on generation of heat from within the tumor but uses larger and more invasively inserted probes within tumors to achieve this.

Vascular-focused hyperthermia

Although all forms of hyperthermia seek to achieve fairly uniform temperatures globally within tumor parenchyma, a unique feature of nanoparticle-mediated hyperthermia is the location of nanoparticles in close proximity to tumor vasculature [35]. This results in a temperature gradient that is maximal at the vascular wall and falls off with distance from the perivascular space. Consequently, a global tumor parenchymal hyperthermic temperature is associated with considerably higher focal temperatures (hot spots) along tumor vasculature. By contrast, other forms of hyperthermia resulting in global tumor parenchymal hyperthermic temperatures are usually associated with focal cold spots along tumor vasculature that serve as 'heat sinks' for dissipation of heat from tumors. Consequently, the preferential vascular-focused hyperthermia achievable with nanoparticles has the advantage of not only causing heat-induced tissue damage of tumor cells but also vascular endothelia, which, in turn, sensitizes these endothelial cells and tumor cells to subsequent radiation therapy.

Theranostics

Compared to other forms of hyperthermia, nanoparticle-mediated hyperthermia has the potential to simultaneously image and treat tumors, an attribute referred to as **theranostics**, where therapy and diagnostics are integrated into a single platform. Since nanoparticles preferentially concentrate in tumors, detecting their presence can potentially be used as a

means of diagnosing the presence and extent of tumors. The same nanoparticles can then be used for hyperthermia as part of tumor management. Furthermore, when the nanoparticle is decorated with tumor-specific targeting molecules that permit precise sensing and imaging of tumors, subsequent therapy (hyperthermia or thermoablation) can be image-guided.

Combination with other therapies

The fact that nanoparticles afford immense opportunities for engineering their structure – more, in fact, than any other forms of injectable therapy – can be exploited to combine the hyperthermia with other therapeutic modalities. For instance, nanoparticles can be laden with or decorated with drugs, such that near-simultaneous hyperthermia and chemotherapy (drug release) can be triggered via an extrinsic energy source. Similarly, binding radioactive tracers to the nanoparticles to achieve a form of brachytherapy serves as a means of combining hyperthermia and radiation therapy.

These advantages have fueled the quest for ideal nanoparticles for achieving tumor hyperthermia. The major ones under investigation are reviewed here and include various forms of gold nanoparticles and superparamagnetic iron oxide nanoparticles (SPIONs) while carbon nanotubes (CNTs) are a more recent entrant to this field.

Hyperthermia using gold nanoparticles

Characteristics of gold nanoparticles

Many bulk metals, when reduced to a nanoscale, exhibit optical resonances of their surface plasmons, a characteristic wavelength (**surface plasmon resonance**) at which they strongly absorb and scatter incident light and convert resonant energy to heat. When fabricated in certain geometries, these plasmon resonances of gold can be tuned to near infrared (NIR) wavelengths, where this light penetrates deepest within human tissues due to minimal absorbance by native tissue chromophores [36]. Gold nanoparticles fabricated to have strong absorption cross sections in the NIR wavelength (up to a million-fold greater than the US FDA-approved dye indocyanine green) are also highly efficient at converting the absorbed light into heat. These photothermally activatable gold nanoparticles have many distinct advantages for clinical applications. First, gold is an inert noble metal that does not react with biological tissues and is molecularly stable. Second, long-term toxicity concerns are low due to extensive, decades-long clinical experience with the use of gold for the treatment of rheumatoid arthritis. Some caution is necessary, however, with extrapolating from larger microparticles to nanoparticles, as highlighted by a recent study that demonstrated that administration of large quantities of gold nanoparticles stimulates host immune complement activation, an effect that was dependent on other factors such as nanoparticle surface characteristics and structure [37]. Third, NIR activatable gold nanoparticles are within size regimens that permit tumor-specific accumulation via the EPR effect based on average vascular fenestrations of 60–400 nm in tumors. Fourth, in addition to passive accumulation in tumors via the EPR effect, surface bioconjugation for tumor-specific targeting or PEGylation for reticuloendothelial evasion can be readily performed via thiol linkages on the surface of these gold nanoparticles. Lastly, gold nanoparticles have the potential for FDA approval as a device rather than a drug, an attribute that could save significant time and money for clinical translation. Among a variety of gold nano-structures in use, the most commonly employed ones are nanoshells and nanorods.

Gold nanoshells—Nanoshells have a core of a different material coated by a thin layer of gold. The core material is dielectric, with silica being the most common material used. The resonance frequency is determined by the **core:shell ratio**. Gold nanoshells (GNSs) are usually close to 50–150 nm in the diameter and are generally moderately stable in solution,

especially if stored at low temperatures. Silica-GNSs that are activatable by NIR light tend to be roughly 150 nm in diameter, with a 120-nm diameter silica core. Extensive investigations into the safety and tolerability of GNSs have led to greater acceptance of the biocompatibility of these particles, paving the way for human clinical testing. GNSs are currently in clinical trials for head and neck cancer and prostate cancer using interstitial illumination with NIR lasers for thermoablation applications.

Gold nanorods—Gold nanorods (GNRs) are cylindrical nanoparticles made of solid gold with one dimension several times longer than the other. If the solid gold nanostructure is a sphere, the optical absorption maximum is in the region of 540 nm and cannot be tuned to other wavelengths. Hence this formulation is not of much use clinically. However, oblong forms, with large length:diameter aspect ratios, are tunable to higher wavelengths of light. The resonant frequency is determined by the aspect ratio, and can be calibrated to the NIR region. NIR activatable GNRs are much smaller than nanoshells, with typical sizes ranging approximately 4–5 nm in the longest dimension, usually with an aspect ratio of approximately 3. To facilitate anisotropic formation of rod-shaped structures during seed-mediated chemical synthesis of GNRs from spherical gold seed particles and to make them stable without aggregation in solution, a strongly charged surfactant such as cetyl trimethylammonium bromide (CTAB) is commonly employed. Since the CTAB dispersed in solution can be cytotoxic, it is often removed by serial centrifugation or dialysis, processes that involve a reduction in yield of GNRs or considerable expense. Furthermore, the CTAB on the surface of the GNRs is also shielded by a biocompatible compound such as PEG or by cross-linking a polysaccharide (chitosan) with ethylene/propylene-based block copolymers [38]. Despite some potential challenges with toxicity, GNRs – weight for weight of gold – possess a superior spectral bandwidth, are better than GNSs in heat generation from NIR light [39] and have a longer circulation half-life, improving chances for tumor accumulation.

Gold nanoparticles in cancer therapy

Hirsch *et al.* [40] were the first to demonstrate the effectiveness of GNS-mediated thermoablation in a mouse tumor model. While initial efforts used direct injection of GNSs into subcutaneous tumors, subsequent papers demonstrated that intravenously administered GNSs accumulated in tumors as early as 6 h after inoculation. Treatment of these animals with a 800 mW NIR laser emitting at 808 nm at 4 W/cm^2 for only 3 min resulted in significant survival difference over non-radiated mice [41]. Improvements in survival have been demonstrated when the gold nanoparticles are actively targeted to tumors in mice over passively targeted nanoparticles [42,43]. Several similar results have been demonstrated for GNRs [44,45]. However, despite promising results, thermoablative monotherapy of tumors with gold nanoparticles is associated with the possibility of considerable collateral damage of tissues adjacent to the tumor that are also ablated and lacks a clear advantage over established techniques such as radiofrequency ablation if interstitial laser fibers are required for photothermal ablation. Hence, combination therapy of hyperthermia (non-ablative temperatures) with other modalities is worth investigating.

In our laboratory, we have investigated the effect of modulating ionizing radiation on tumor-bearing mice using GNS-mediated hyperthermia. When tumors in mice pre-treated with GNSs are subject to mild temperature hyperthermia (~41°C for 20 min) followed immediately by a single dose of radiation (10 Gy with 125 kV X-rays) the tumor volume doubling time was nearly twice that with radiation alone [35]. Tumor volume doubling time is a metric used to represent tumor growth, which is independent of the initial size of the tumor; comparison of time taken for tumors to double in volume in the radiation-alone group versus tumors in a combined treatment group is a commonly employed technique for

evaluating effectiveness of putative radiation sensitization strategies. The reasons for the *in vivo* response were postulated to be caused by an early increase in vascular perfusion of tumors following hyperthermia. This can be seen using dynamic contrast enhancement of MRI. However, the results also indicate that it is possible that nanoparticle-mediated hyperthermia may modulate radiation response by other mechanisms. Relatively large GNSs leak out of tumor vasculature but fail to penetrate deep into the parenchyma of tumors, remaining sequestered in the perivascular region. Heating these sequestered GNSs to generate 'inside-out' hyperthermia can possibly result in vascular disruption. This was demonstrated by a loss of microvessel density in the tumor, disruption of normal stromal architecture and regional areas of necrosis (Figures 3A & B).

A third reason for the effectiveness of the GNS-mediated hyperthermia could be its effect on cancer stem cells. These tumor-initiating cells are hypothesized to be the primary reason for treatment failure of tumors as well as being responsible for metastatic spread. In a recent paper, it was demonstrated that radiation of breast cancer xenografts results in a reduction of tumor volume but an increase in the proportion of stem cells in the residual tumor whereas GNS-mediated hyperthermia coupled with radiation resulted in not only a greater reduction of tumor volume but also a reduction of the proportion of stem cells in the residual tumor. Furthermore, limiting dilution transplantation of the cancer cells from residual tumors following combined treatment resulted in a lower frequency of tumor formation than similar transplantation of cells from residual tumors following radiation alone (Figure 3c). Overcoming the inherent radio-resistance of cancer stem cells, which are thought to be the primary reason for therapy failure, provide another important rationale for the addition of hyperthermia to radiation therapy of tumors [46].

Hyperthermia using SPIONs

Characteristics of SPIONs

Magnetic materials are either permanent magnets (ferromagnetic, like iron) or which only demonstrate magnetism under the influence of an external magnetic field (paramagnetic). A new property is obtained when ferromagnetic materials are fabricated on the nanoscale – that of **superparamagnetism**. On the nanoscale, the ferromagnetic nanoparticles can randomly flip the orientation of their magnetic dipoles, a phenomenon that makes them appear paramagnetic. However, under the influence of an external magnetic field, they align in the direction of the field, and the resultant magnetic susceptibility is orders of magnitude higher than that of standard paramagnetic material. When the material for the nanoparticles is iron oxide (the most common), the nanoparticles are called SPIONs.

In theory, alternating the external magnetic field rapidly would cause the particles to rapidly flip their magnetic polarity. However, there is some hysteretic loss involved in the flipping, which manifests as heat. If a tissue (say, a tumor) is pre-loaded with SPIONs and then subjected to alternating magnetic field (AMF), it will heat up. Several factors will affect the extent of this heating – the magnitude of the field, the size and characteristic of the SPIONs, the depth of the tumor within the body and the concentration of SPIONs in the tumor.

The first instance of the treatment of cancer using magnetic iron oxide particles was probably in 1957 [47]. Since then the synthesis and design of SPIONs have progressed much. At the heart of the SPION is the magnetic core of iron oxide. Synthesis is usually by the precipitation of iron salts in the presence of various chemicals, for example ammonia [48], sodium nitrate/sodium hydroxide [49] or by photochemical methods [50].

Bare SPIONs are rapidly cleared from the blood after intravenous injection and accumulate in the liver, spleen, and lymph nodes. When biocompatible dextran magnetite nanoparticles

are injected intravenously in rats, clearance was initially very rapid (half-life of 10 min) followed by a slower decrease (half-life of 92 min) [51]. In the first 2 h, the particles spread throughout the body including the liver and the spleen [52]. However, over time, the particles are scavenged by the reticuloendothelial system and accumulate in the macrophages of the splenic marginal zone, where there is a steady and rapid increase in accumulated particles for up to 48 h, followed by a decrease until the end of the observed period of 25 days. The iron oxide cores sequester as granules in the Kupffer cells of the liver, leading to a slow increase in accumulated amount.

To enable tumor accumulation, SPIONs need to be coated with or embedded in a polymer shell. The most common method for this is to embed the SPIONs in a polymeric nanoparticle that is hydrophilic. A common polymer for this purpose is dextran [53], although other polymeric blends, such as β-cyclodextrin and pluronic polymer combination [48], and chitosan [54], can also be used. Apart from polymers, iron/iron oxide core-shell nanoparticles are also popular [55,56]. Silica is a popular coat for many varieties of nanoparticles, including SPIONs [49,57]. However, the resultant particles are often micro-spheres rather than nanoparticles, with diameters of approximately 20–30 μm. These are used as *in situ* implants into tumors rather than as intravenous formulations.

Subsequently, to enhance circulation half-life, the dextran coat is often covered by a monolayer of PEG [55]. Finally, targeting molecules can be attached to enhance specificity of uptake by cancer cells. For example, folic acid [54,58] can be attached to target folate receptors in several solid tumors. Addition of folic acid was found to increase the cytotoxicity against the folate receptor over-expressing KB cells but had little adverse impact on the A549 cells, which do not possess these receptors. In addition, a novel way of coating the SPIONs is the use of gold [59]. The thin gold shell can itself be heated up by AMF, thus adding to the hyperthermic effect. Indeed, gold-coated SPIONs demonstrated several-fold higher increases in heat release compared with SPIONs alone. Furthermore, SPION-mediated hyperthermia can be combined with other strategies to further enhance the therapeutic outcome. For example, the SPIONs can be coated with thermosensitive polymers that are loaded with anti-cancer drugs [48,58]. Application of AMF after accumulation of the SPIONs in tumors would raise the local temperature of the SPIONs sufficiently to exceed the critical temperature of the polymers, resulting in drug release.

SPIONs in cancer therapy

Delivery of adequate amounts of SPIONs into tumors is a prerequisite for successful hyperthermia. These can be delivered to possible nests of metastatic cells in lymph nodes by direct injection into the lymphatic channels draining into the lymph nodes [47]. Subsequently, a number of investigators injected the SPIONs directly into the tumor as proof-of-principle experiments. The SPIONs can be injected in solution, or loaded into hydrogels and organogels [57].

However, this more invasive method of SPION delivery is not favorable, owing to obvious difficulties in translating to clinical usage. The favored delivery route is intravenous; however, successful concentration of nanoparticles into tumors by this route is not easily achievable. A novel route of delivery is by loading the SPIONs into cells [56]. In the experiment described, tumor-tropic neural progenitor cells were loaded with SPIONs and transplanted into melanoma-bearing mice, whence the cells made their way into the tumors. Subsequent AMF exposure resulted in tumor regression.

To achieve adequate concentrations in the tumor, SPIONs are sometimes conjugated to targeting molecules. Triton BioSystems, Inc. (Chelmsford, MA) have developed one such system of AMF-responsive nanoparticles and targeted these to cancerous tissues by

conjugating with monoclonal antibodies. The combination of molecular targeting and the focused AMF field aims to achieve highly sensitive tumor hyperthermia.

The use of heat for cancer can be ablative or sub-ablative. When sub-ablative, it can be used either as a standalone therapy to delay tumor growth [50] or as a means of radiosensitization [46]. The degree of heating of the tumor can be controlled by the AMF field. However, increasing the current in the AMF generator, and thus increasing the AMF field strength, generates heat in tissues by inductive tissue heating from eddy current losses. This is independent of the presence of SPIONs and affects normal tissues in the AMF field. The raised temperature in the normal tissues limits the extent to which the AMF field can be increased. In mouse experiments, for example, radiofrequency exposures at 25 kW for 20 min raised the tumor core temperature to 47°C [50].

Another limitation of the use of SPIONs is the toxicity to normal cells in the absence of AMF. Biocompatibility studies with dextran and citric acid-coated SPIONs on human umbilical-vein endothelial cells [53] demonstrated the expected endocytotic uptake by the cells, followed by cell death through suspected apoptotic pathways. Even at concentrations as low as 0.1 mM, the coated SPIONs managed to inhibit migration/invasion functions of the cells. While cytotoxic effects are strongly dependent on the coating/matrix of the SPIONs, the results demonstrated the necessity of thorough cytotoxicity evaluation of any proposed therapy involving these nanoparticles.

Hyperthermia with CNTs

Characteristics of CNTs

CNTs are unique, (almost) 1D nanomaterials composed of single sheets of **graphene** rolled into the shape of a tube. Since the aspect ratio and the direction of rolling can be controlled at synthesis, the optical properties can also be tuned. Similar to gold nanoparticles, single-walled CNTs (SWCNTs) also strongly absorb electromagnetic waves to generate heat. Instead of plasmon resonance, absorption of light by CNTs results in excitation of electronic transitions within the nanostructure with relaxation resulting in amplified vibrational modes within the carbon lattice. There is neither an absorption threshold nor is the absorption a continuous function of energy, but absorption occurs as discrete tunable and sharp spikes. Also, unlike gold, CNTs can absorb over a broad frequency range including visible light, NIR light and even radiofrequency irradiation. The extinction coefficient of such absorption is much higher than that of common tissue chromophores, such as melanins, hemoglobin and water [49].

CNTs are very thin cylinders of graphene, which can be synthesized to considerable variations in aspect ratios. The diameter of the tubes can vary from the nano- to the micro-scales [60]. Usually the cylinders are SWCNTs, but more recently multi-walled CNTs (MWCNTs) have also been investigated for their optical properties. They have been shown to have enhanced absorption cross-sections when compared with SWCNTs [61].

CNTs in cancer therapy

Following in the footsteps of the GNRs and SPIONs, the enhanced optical cross section of CNTs has been investigated for photothermal ablation of cancer cells [61]. This has been demonstrated *in vitro* using SWCNTs [61–63]. Tumor destruction in mouse models of cancer have also been demonstrated using intratumoral injection of SWCNTs followed by NIR irradiation for only 3 min [64]. Similar to gold, not only NIR, but also radiofrequency fields have been used to generate hyperthermia using SWCNTs. The required radiofrequency field was in the megahertz region (13.56 mHz). The *in vitro* study was succeeded by *in vivo* studies using direct intratumoral injection of the nanotubes.

Hyperthermia using the radiofrequency field resulted in complete necrosis of tumors [65]. Not only SWCNTs, MWCNTs have also been demonstrated to be effective in tumor ablation using NIR light. However, unlike SWCNTs, MWCNTs achieve thermal ablation of tumors after exposure to only a 30 s burst of NIR light at a relatively low laser power of 3 W/cm^2 [66].

The major stumbling block to more widespread adoption of CNTs is a concern regarding their toxicity. Exposure of mesothelial and pleural lining to CNTs can result in granulomas reminiscent of mesotheliomas arising from asbestos exposure [67]. Several factors, including their propensity to aggregate, and the nature of the surface and functional groups attached thereof, affect the toxicity of these nanostructures. Although it has been demonstrated that at low doses CNTs are non-toxic to mice, more detailed studies are necessary prior to adopting these for clinical use.

There are reports of other nanoparticles beyond these three types, which can potentially be exploited for hyperthermia. For example, fluorescent quantum dots [68], silver and zinc nanoparticles and lanthanum manganite particles with impregnated silver ions [69] have been explored. However, the general principles discussed for the three nanoparticles hold true in most cases.

Conclusion & future perspective

Hyperthermia results in increasing perfusion of tumors. This results in less hypoxic areas and a better response to radiation, while also aiding chemotherapy. However, beyond these traditional effects, nanoparticle-mediated hyperthermia is proving to have additional roles to play in cancer therapy – from disruption of microvasculature to sensitization of recalcitrant cancer stem cells to radiation. All this makes quick addition of this therapeutic modality to the oncologist's repetoire an important priority.

However, despite the potential role that hyperthermia can play in cancer management it has not been adequately exploited clinically. There are several reasons for this. Historical methods of achieving global hyperthermia were cumbersome, non-standardized and non-specific. More recent methods of generating hyperthermia are still frequently invasive and/or result in non-uniform temperature elevations within tumors and possible hot spots in surrounding normal tissues. The breakthrough has been the introduction of injectable nanoparticles like SPIONs, GNSs and CNTs that made it possible to achieve ablative temperatures inside highly localized areas of the body, while maintaining other areas at normal or near-normal temperatures. Nanoparticles provide a promising alternative to the older techniques to attain tumor hyperthermia.

However, there are several challenges facing the use of nanoparticles for tumor hyperthermia. A major problem is adequacy and uniformity of accumulation of nanoparticles at the tumor site. Even with very small nanoparticles, uniform temperature throughout the core and mantle of the tumor is still difficult to obtain [16]. Nanoparticles do not readily penetrate uniformly into the poorly vascularized tumor core. Other avenues need to be explored to find means of raising temperature uniformly in the core.

A second issue hampering the clinical translation of nanoparticles is the issue of quality control. Nanoparticles made in the laboratory often suffer from intra-batch and inter-batch variations in size and composition. As nanoparticles become more complex in composition, the risk of variation increases proportionally. Size distribution of nanoparticles are typically assessed using dynamic light scattering (e.g., with the zetasizer), but this provides an estimate of hydrodynamic radius rather than actual diameter. The actual diameter can be seen from electron microscopy, but only a very small number of nanoparticles can be seen

per image and extrapolating size of the full sample from the images can lead to errors. When nanoparticles are coated with targeting ligands, presence and quantification of the ligands, and in some cases testing of the functional capabilities, need to be done. Obviously, scaling up of production for industry will be an issue for complex nanoparticles. However, despite these obstacles, better methods of nanoparticle synthesis are constantly being reported. Most commercially available nanoparticles (e.g., the GNSs from Nanospectra, Inc.) are now available in batches with less than 1% variation in diameters. It is expected that in the near future we will have more complex nanoparticles being produced with equivalent quality controls.

A third obstacle in the clinical acceptance of nanoparticles is biocompatibility. The problem might be considered to be twofold: one of immediate toxicity and one of delayed effects of retained nanoparticles. Immediate and direct toxicity issues can be resolved using standardized testing on appropriate animal models. Indeed, most nanoparticles have been shown to be relatively nontoxic in the doses required for therapeutic effect. Gold, in particular, has a long history of usage in medical conditions, and GNS have been demonstrated to be safe in the administered quantities. As a result, clinical trials have been launched for human testing. However, GNRs have a unique challenge; as mentioned above, the persistent CTAB in the solution needs to be removed or neutralized before clinical usage is possible. The more difficult challenge is the question of the long-term fate of the nanoparticles sequestered in the body. Hepatic and splenic macrophages ingest and store much of the injected nanoparticles; the long-term consequences of this storage are as yet uncertain.

Similar to other treatment modalities, such as chemotherapy and radiation, hyperthermia is most effective when confined to the tumor. While enhanced permeation and retention allows passive accumulation at tumors, there is also concurrent accumulation in some other tissues, most notably the liver. This makes use of this technique less effective when dealing with tumors of the liver and surrounding areas. Accumulation at other areas, though less prominent, argues for thorough investigation of the biodistribution for each particle proposed for clinical use.

In conclusion, nanoparticles hold promise as a novel means of generating hyperthermia with distinct advantages over traditional methods. Comprehensive toxicity evaluations, optimized methods to ensure uniform, adequate and specific intratumoral delivery and greater dose deposition at tumors are the challenges that face effective clinical exploitation of nanoparticle-mediated hyperthermia in tumor treatment.

Key Terms

Antenna	An antenna (as used in medical hyperthermia) is a small metal piece which absorbs radio waves and consequently heats up
Radiofrequency and microwaves	Radiofrequency waves are electromagnetic waves with the rate of oscillation in the range of approximately 3 kHz to 300 GHz; microwaves are a subset at the higher energy end of this spectrum (300 MHz to 300 GHz)
Theranostic	A combination of the terms therapeutic and diagnostic; usually refers to a device which can perform both functions
Surface plasmon resonance	Plasmons are quantized oscillations of free electrons. These electron waves propagate along the surface of metal

	nanoparticles, and can resonate when photons of certain wavelength are incident on them
Core:shell ratio	Ratio of the diameter of the core to the thickness of the shell of core shell nanoparticles. A higher core:shell ratio means a thinner shell
Superparamagnetism	Small nanometer-sized ferro- and ferri-magnetic particles demonstrate no magnetization in the absence of a magnetic field (unlike similar material in the meso- and macroscopic scales). These are magnetized in the presence of a magnetic field (such as paramagnetic material, e.g., gadolinium) but much more strongly than compared with conventioanl paramagnets
Graphene	Graphene is an allotrope of carbon, where the carbon atoms are bonded in a honeycomb pattern to form 2D crystalline planar sheets. The sheet can be rolled into tubes (carbon nanotubes) or stacked into a 3D sheet (graphite)

Bibliography

1. Coley WB II. Contribution to the Knowledge of Sarcoma. Ann Surg. 1891; 14(3):199–220.
2. Friedenthal E, Mendecki J, Botstein C, Sterzer F, Nowogrodzki M, Paglione R. Some practical considerations for the use of localized hyperthermia in the treatment of cancer. J Microw Power. 1981; 16(2):199–204. [PubMed: 6915106]
3. Lele PP. Induction of deep, local hyperthermia by ultrasound and electromagnetic fields: problems and choices. Radiat Environ Biophys. 1980; 17(3):205–217. [PubMed: 7443976]
4. Magin RL, Johnson RK. Effects of local tumor hyperthermia on the growth of solid mouse tumors. Cancer Res. 1979; 39(11):4534–4539. [PubMed: 498085]
5. Kim JH, Hahn EW, Ahmed SA. Combination hyperthermia and radiation therapy for malignant melanoma. Cancer. 1982; 50(3):478–482. [PubMed: 7093890]
6. Luk KH, Francis ME, Perez CA, Johnson RJ. Combined radiation and hyperthermia: comparison of two treatment schedules based on data from a registry established by the Radiation Therapy Oncology Group (RTOG). Int J Radiat Oncol Biol Phys. 1984; 10(6):801–809. [PubMed: 6735765]
7. Stewart JR, Gibbs FA Jr. Hyperthermia in the treatment of cancer. Perspectives on its promise and its problems. Cancer. 1984; 54(11 Suppl):2823–2830. [PubMed: 6388817]
8. Thrall DE. Clinical requirements for localized hyperthermia in the patient. Radiat Environ Biophys. 1980; 17(3):229–232. [PubMed: 7443978]
9. Doss JD, Mccabe CW. A technique for localized heating in tissue: an adjunct to tumor therapy. Med Instrum. 1976; 10(1):16–21. [PubMed: 1250180]
10. Irish CE, Brown J, Galen WP, et al. Thermoradiotherapy for persistent cancer in previously irradiated fields. Cancer. 1986; 57(12):2275–2279. [PubMed: 3697929]
11. Seegenschmiedt MH, Sauer R, Miyamoto C, Chalal JA, Brady LW. Clinical experience with interstitial thermoradiotherapy for localized implantable pelvic tumors. Am J Clin Oncol. 1993; 16(3):210–222. [PubMed: 8338055]
12. Bass H, Moore JL, Coakley WT. Lethality in mammalian cells due to hyperthermia under oxic and hypoxic conditions. Int J Radiat Biol Relat Stud Phys Chem Med. 1978; 33(1):57–67. [PubMed: 304850]
13. Storm FK. Clinical hyperthermia and chemotherapy. Radiol Clin North Am. 1989; 27(3):621–627. [PubMed: 2648463]
14. Urano M, Kuroda M, Nishimura Y. For the clinical application of thermochemotherapy given at mild temperatures. Int J Hyperthermia. 1999; 15(2):79–107. [PubMed: 10323618]

15. Shakil A, Osborn JL, Song CW. Changes in oxygenation status and blood flow in a rat tumor model by mild temperature hyperthermia. Int J Radiat Oncol Biol Phys. 1999; 43(4):859–865. [PubMed: 10098442]
16. Johannsen M, Thiesen B, Wust P, Jordan A. Magnetic nanoparticle hyperthermia for prostate cancer. Int J Hyperthermia. 2010; 26(8):790–795. [PubMed: 20653418]
17. Hurwitz MD, Hansen JL, Prokopios-Davos S, et al. Hyperthermia combined with radiation for the treatment of locally advanced prostate cancer: long-term results from Dana-Farber Cancer Institute study 94–153. Cancer. 2011; 117(3):510–516. [PubMed: 20886629]
18. Moros EG, Penagaricano J, Novak P, Straube WL, Myerson RJ. Present and future technology for simultaneous superficial thermoradiotherapy of breast cancer. Int J Hyperthermia. 2010; 26(7): 699–709. [PubMed: 20849263]
19. Van Den Berg CA, Van De Kamer JB, De Leeuw AA, et al. Towards patient specific thermal modelling of the prostate. Phys Med Biol. 2006; 51(4):809–825. [PubMed: 16467580]
20. Zagar TM, Oleson JR, Vujaskovic Z, et al. Hyperthermia combined with radiation therapy for superficial breast cancer and chest wall recurrence: a review of the randomised data. Int J Hyperthermia. 2010; 26(7):612–617. [PubMed: 20849256]
21. Franckena M, Van Der Zee J. Use of combined radiation and hyperthermia for gynecological cancer. Curr Opin Obstet Gynecol. 2010; 22(1):9–14. [PubMed: 20019611]
22. Vasanthan A, Mitsumori M, Park JH, et al. Regional hyperthermia combined with radiotherapy for uterine cervical cancers: a multi-institutional prospective randomized trial of the international atomic energy agency. Int J Radiat Oncol Biol Phys. 2005; 61(1):145–153. [PubMed: 15629605]
23. Huilgol NG, Gupta S, Sridhar CR. Hyperthermia with radiation in the treatment of locally advanced head and neck cancer: a report of randomized trial. J Cancer Res Ther. 2010; 6(4):492–496. [PubMed: 21358087]
24. Huilgol NG, Gupta S, Dixit R. Chemoradiation with hyperthermia in the treatment of head and neck cancer. Int J Hyperthermia. 2010; 26(1):21–25. [PubMed: 20100049]
25. Chang E, Alexander HR, Libutti SK, et al. Laparoscopic continuous hyperthermic peritoneal perfusion. J Am Coll Surg. 2001; 193(2):225–229. [PubMed: 11491455]
26. Feldman AL, Libutti SK, Pingpank JF, et al. Analysis of factors associated with outcome in patients with malignant peritoneal mesothelioma undergoing surgical debulking and intraperitoneal chemotherapy. J Clin Oncol. 2003; 21(24):4560–4567. [PubMed: 14673042]
27. Maeda H. The enhanced permeability and retention (EPR) effect in tumor vasculature: the key role of tumor-selective macromolecular drug targeting. Adv Enzyme Regul. 2001; 41:189–207. [PubMed: 11384745]
28. Maeda H, Wu J, Sawa T, Matsumura Y, Hori K. Tumor vascular permeability and the EPR effect in macromolecular therapeutics: a review. J Control Release. 2000; 65(1–2):271–284. [PubMed: 10699287]
29. Kah JC, Wong KY, Neoh KG, et al. Critical parameters in the pegylation of gold nanoshells for biomedical applications: an *in vitro* macrophage study. J Drug Target. 2009; 17(3):181–193. [PubMed: 19016072]
30. Wang J, Sui M, Fan W. Nanoparticles for tumor targeted therapies and their pharmacokinetics. Curr Drug Metab. 2010; 11(2):129–141. [PubMed: 20359289]
31. El-Sayed IH, Huang X, El-Sayed MA. Selective laser photo-thermal therapy of epithelial carcinoma using anti-EGFR antibody conjugated gold nanoparticles. Cancer Lett. 2006; 239(1): 129–135. [PubMed: 16198049]
32. Waldman SA, Fortina P, Surrey S, Hyslop T, Kricka LJ, Graves DJ. Opportunities for near-infrared thermal ablation of colorectal metastases by guanylyl cyclase C-targeted gold nanoshells. Future Oncol. 2006; 2(6):705–716. [PubMed: 17155897]
33. Patra CR, Bhattacharya R, Mukhopadhyay D, Mukherjee P. Fabrication of gold nanoparticles for targeted therapy in pancreatic cancer. Adv Drug Deliv Rev. 2010; 62(3):346–361. [PubMed: 19914317]
34. Hosta-Rigau L, Olmedo I, Arbiol J, Cruz LJ, Kogan MJ, Albericio F. Multifunctionalized gold nanoparticles with peptides targeted to gastrin-releasing peptide receptor of a tumor cell line. Bioconjug Chem. 2010; 21(6):1070–1078. [PubMed: 20476781]

35. Diagaradjane P, Shetty A, Wang JC, et al. Modulation of *in vivo* tumor radiation response via gold nanoshell-mediated vascular-focused hyperthermia: characterizing an integrated antihypoxic and localized vascular disrupting targeting strategy. Nano Lett. 2008; 8(5):1492–1500. [PubMed: 18412402]
36. Hirsch LR, Gobin AM, Lowery AR, et al. Metal nanoshells. Ann Biomed Eng. 2006; 34(1):15–22. [PubMed: 16528617]
37. Hulander M, Hong J, Andersson M, et al. Blood interactions with noble metals: coagulation and immune complement activation. ACS Appl Mater Interfaces. 2009; 1(5):1053–1062. [PubMed: 20355891]
38. Choi WI, Kim JY, Kang C, Byeon CC, Kim YH, Tae G. Tumor regression *in vivo* by photothermal therapy based on gold-nanorod-loaded, functional nanocarriers. ACS Nano. 2011; 5(3):1995–2003. [PubMed: 21344891]
39. Von Maltzahn G, Park JH, Agrawal A, et al. Computationally guided photothermal tumor therapy using long-circulating gold nanorod antennas. Cancer Res. 2009; 69(9):3892–3900. [PubMed: 19366797]
40. Hirsch LR, Stafford RJ, Bankson JA, et al. Nanoshell-mediated near-infrared thermal therapy of tumors under magnetic resonance guidance. Proc Natl Acad Sci USA. 2003; 100(23):13549–13554. [PubMed: 14597719]
41. O'neal DP, Hirsch LR, Halas NJ, Payne JD, West JL. Photo-thermal tumor ablation in mice using near infrared-absorbing nanoparticles. Cancer Lett. 2004; 209(2):171–176. [PubMed: 15159019]
42. Bernardi RJ, Lowery AR, Thompson PA, Blaney SM, West JL. Immunonanoshells for targeted photothermal ablation in medulloblastoma and glioma: an *in vitro* evaluation using human cell lines. J Neurooncol. 2008; 86(2):165–172. [PubMed: 17805488]
43. Cheng FY, Chen CT, Yeh CS. Comparative efficiencies of photothermal destruction of malignant cells using antibody-coated silica–Au nanoshells, hollow Au/Ag nanospheres and Au nanorods. Nanotechnology. 2009; 20(42):425104. [PubMed: 19779243]
44. Dickerson EB, Dreaden EC, Huang X, et al. Gold nanorod assisted near-infrared plasmonic photothermal therapy (PPTT) of squamous cell carcinoma in mice. Cancer Lett. 2008; 269(1):57–66. [PubMed: 18541363]
45. Skrabalak SE, Au L, Lu X, Li X, Xia Y. Gold nanocages for cancer detection and treatment. Nanomedicine (Lond). 2007; 2(5):657–668. [PubMed: 17976028]
46. Atkinson RL, Zhang M, Diagaradjane P, et al. Thermal enhancement with optically activated gold nanoshells sensitizes breast cancer stem cells to radiation therapy. Sci Transl Med. 2010; 2(55):55ra79.
47. Gilchrist RK, Medal R, Shorey WD, Hanselman RC, Parrott JC, Taylor CB. Selective inductive heating of lymph nodes. Ann Surg. 1957; 146(4):596–606. [PubMed: 13470751]
48. Yallapu MM, Othman SF, Curtis ET, Gupta BK, Jaggi M, Chauhan SC. Multi-functional magnetic nanoparticles for magnetic resonance imaging and cancer therapy. Biomaterials. 2011; 32(7):1890–1905. [PubMed: 21167595]
49. Huang N, Wang H, Zhao J, Lui H, Korbelik M, Zeng H. Single-wall carbon nanotubes assisted photothermal cancer therapy: animal study with a murine model of squamous cell carcinoma. Lasers Surg Med. 42(9):638–648. [PubMed: 20949599]
50. Elsherbini AA, Saber M, Aggag M, El-Shahawy A, Shokier HA. Magnetic nanoparticle-induced hyperthermia treatment under magnetic resonance imaging. Magn Reson Imaging. 2011; 29(2):272–280. [PubMed: 21145190]
51. Majumdar S, Zoghbi SS, Gore JC. Pharmacokinetics of superparamagnetic iron-oxide MR contrast agents in the rat. Invest Radiol. 1990; 25(7):771–777. [PubMed: 2391194]
52. Okon E, Pouliquen D, Okon P, et al. Biodegradation of magnetite dextran nanoparticles in the rat. A histologic and biophysical study. Lab Invest. 1994; 71(6):895–903. [PubMed: 7807971]
53. Wu X, Tan Y, Mao H, Zhang M. Toxic effects of iron oxide nanoparticles on human umbilical vein endothelial cells. Int J Nanomedicine. 2010; 5:385–399. [PubMed: 20957160]
54. Fan C, Gao W, Chen Z, et al. Tumor selectivity of stealth multi-functionalized superparamagnetic iron oxide nanoparticles. Int J Pharm. 2011; 404(1–2):180–190. [PubMed: 21087660]

55. Balivada S, Rachakatla RS, Wang H, et al. A/C magnetic hyperthermia of melanoma mediated by iron(0)/iron oxide core/shell magnetic nanoparticles: a mouse study. BMC Cancer. 2010; 10:119. [PubMed: 20350328]
56. Rachakatla RS, Balivada S, Seo GM, et al. Attenuation of mouse melanoma by A/C magnetic field after delivery of bi-magnetic nanoparticles by neural progenitor cells. ACS Nano. 2010; 4(12): 7093–7104. [PubMed: 21058696]
57. Le Renard PE, Jordan O, Faes A, et al. The *in vivo* performance of magnetic particle-loaded injectable, *in situ* gelling, carriers for the delivery of local hyperthermia. Biomaterials. 2010; 31(4):691–705. [PubMed: 19878991]
58. Hayashi K, Ono K, Suzuki H, et al. High-frequency, magnetic-field-responsive drug release from magnetic nanoparticle/organic hybrid based on hyperthermic effect. ACS Appl Mater Interfaces. 2010; 2(7):1903–1911. [PubMed: 20568697]
59. Mohammad F, Balaji G, Weber A, Uppu RM, Kumar CS. Influence of gold nanoshell on hyperthermia of superparamagnetic iron oxide nanoparticles (SPIONs). J Phys Chem C Nanomater Interfaces. 2010; 1(20):3141–3146. [PubMed: 21103390]
60. Zheng LX, O'connell MJ, Doorn SK, et al. Ultralong single-wall carbon nanotubes. Nat Mater. 2004; 3(10):673–676. [PubMed: 15359345]
61. Kam NW, O'Connell M, Wisdom JA, Dai H. Carbon nanotubes as multifunctional biological transporters and near-infrared agents for selective cancer cell destruction. Proc Natl Acad Sci USA. 2005; 102(33):11600–11605. [PubMed: 16087878]
62. Biris AS, Boldor D, Palmer J, et al. Nanophotothermolysis of multiple scattered cancer cells with carbon nanotubes guided by time-resolved infrared thermal imaging. J Biomed Opt. 2009; 14(2): 021007. [PubMed: 19405720]
63. Torti SV, Byrne F, Whelan O, et al. Thermal ablation therapeutics based on CN(x) multi-walled nanotubes. Int J Nanomedicine. 2007; 2(4):707–714. [PubMed: 18203437]
64. Moon HK, Lee SH, Choi HC. *In vivo* near-infrared mediated tumor destruction by photothermal effect of carbon nanotubes. ACS Nano. 2009; 3(11):3707–3713. [PubMed: 19877694]
65. Gannon CJ, Cherukuri P, Yakobson BI, et al. Carbon nanotube-enhanced thermal destruction of cancer cells in a noninvasive radiofrequency field. Cancer. 2007; 110(12):2654–2665. [PubMed: 17960610]
66. Burke A, Ding X, Singh R, et al. Long-term survival following a single treatment of kidney tumors with multiwalled carbon nanotubes and near-infrared radiation. Proc Natl Acad Sci USA. 2009; 106(31):12897–12902. [PubMed: 19620717]
67. Poland CA, Duffin R, Kinloch I, et al. Carbon nanotubes introduced into the abdominal cavity of mice show asbestos-like pathogenicity in a pilot study. Nat Nanotechnol. 2008; 3(7):423–428. [PubMed: 18654567]
68. Glazer ES, Curley SA. Radiofrequency field-induced thermal cytotoxicity in cancer cells treated with fluorescent nanoparticles. Cancer. 2010; 116(13):3285–3293. [PubMed: 20564640]
69. Melnikov OV, Gorbenko OY, Markelova MN, et al. Ag-doped manganite nanoparticles: new materials for temperature-controlled medical hyperthermia. J Biomed Mater Res A. 2009; 91(4): 1048–1055. [PubMed: 19127514]
70. Fuller KJ, Issels RD, Slosman DO, Guillet JG, Soussi T, Polla BS. Cancer and the heat-shock response. Eur J Cancer. 1994; 30A(12):1884–1891. [PubMed: 7880622]
71. Harmon BV, Takano YS, Winterford CM, Gobe GC. The role of apoptosis in the response of cells and tumours to mild hyperthermia. Int J Radiat Biol. 1991; 59(2):489–501. [PubMed: 1671698]

Executive summary

- Hyperthermia, a small rise in tumor temperature, alters the cancer cells (especially the cancer stem cells) and the microenvironment to increase susceptibility to radiation and chemotherapy.
- Specific and uniform elevation of tumor temperature is difficult with whole-body and regional hyperthermia. Luminal and interstitial local hyperthermia are invasive, while external radiation may cause skin burns.
- Preferential loading of tumors with systemically administered, energy-transducing nanoparticles allows tumor specificity, heating from within the tumor, vascular disruption, simultaneous imaging and therapy (theranostics) and single-platform combination with other therapies.
- Three major nanoparticles for generating hyperthermia are gold nanoparticles, superparamagnetic iron oxide nanoparticles (SPIONs) and carbon nanotubes (CNTs).
- Gold nanoparticles with strong absorption cross sections in the near infrared wavelength due to surface plasmon resonance, efficiently generate heat upon illumination and are inert, stable and readily conjugated to biomolecules for specific tumor targeting. Two major types are nanoshells and nanorods.
- SPIONs heat up rapidly in an alternating magnetic field depending on the field strength and frequency, particle concentration and characteristics and the depth of the tumor within the body.
- CNTs are largely unidimensional nanomaterials composed of rolled sheets of graphene with tunable absorption of electromagnetic waves over a broad frequency range to generate heat.
- Obstacles to clinical exploitation of hyperthermia can potentially be overcome with nanoparticles providing more efficient methods of generating uniform heating in tumors with minimal effect on normal tissue.
- Challenges facing nanoparticle-mediated tumor hyperthermia include inadequacy and non-uniformity of accumulation in tumors, especially the core; lack of quality control in production; perceived toxicity issues; concurrent accumulation in the liver and other tissues; and thermal modeling/dosimetry.

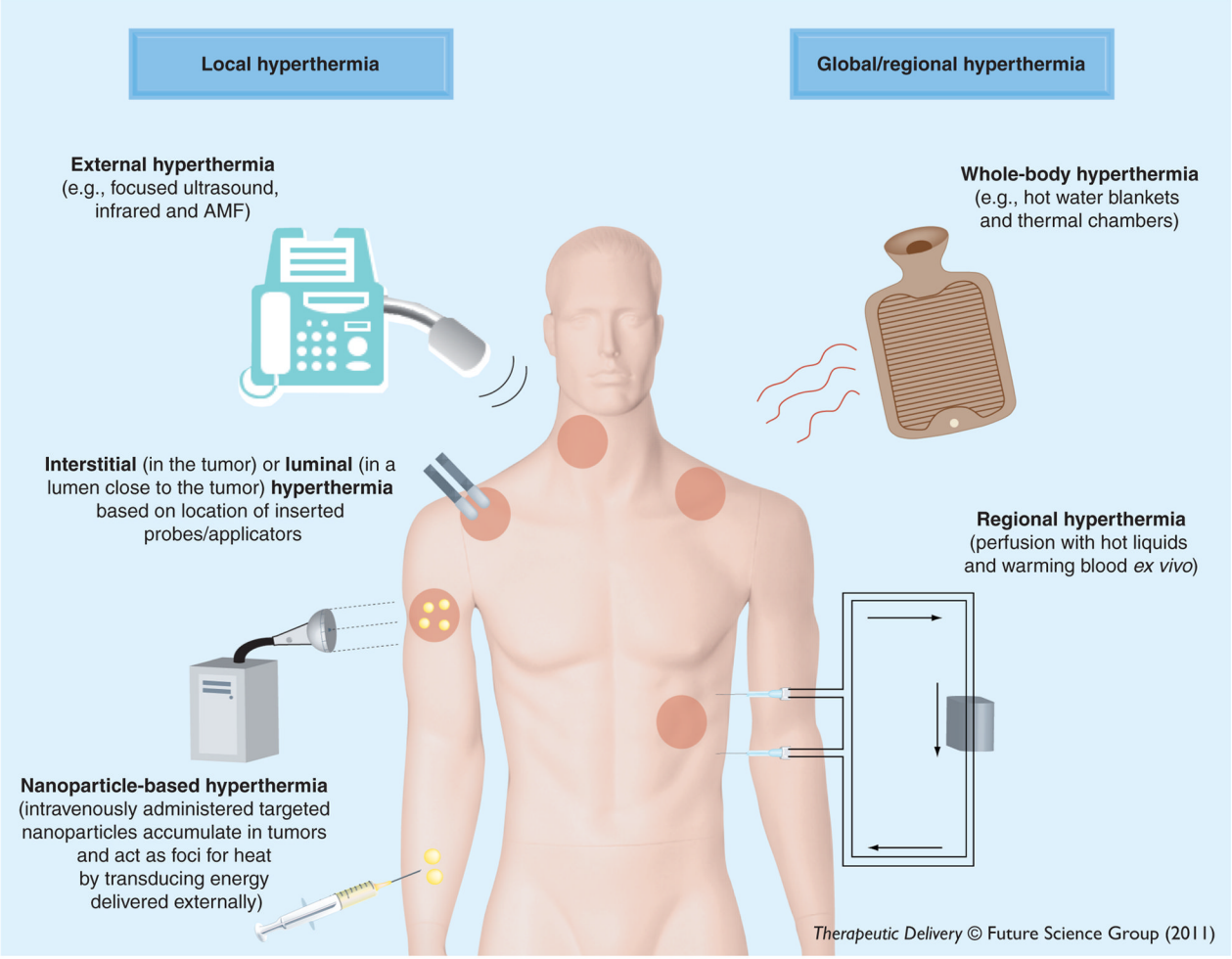

Figure 1. Methods of achieving tumor hyperthermia
AMF: Alternating magnetic field

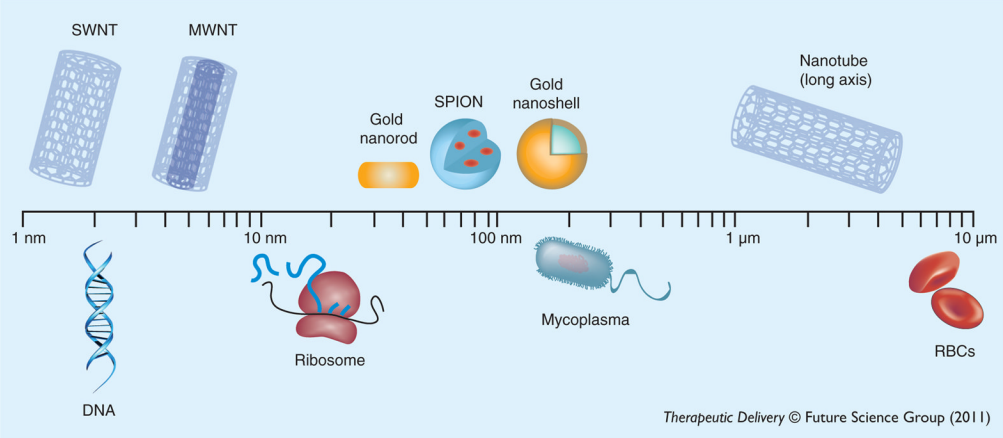

Figure 2. Relative scale of synthetic nanomaterials as compared with naturally occurring biomacromolecules and cells

MWNT: Multiwalled carbon nanotubes; RBC: Red blood cell; SPION: Superparamagnetic iron oxide nanoparticle; SWNT: Single-walled carbon nanotubes.

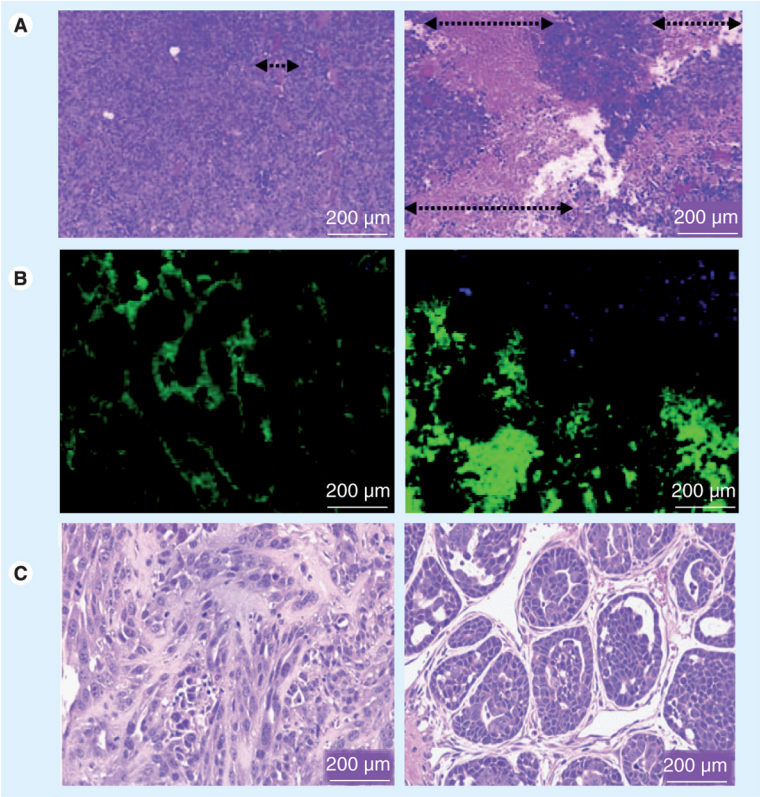

Figure 3. Effects of nanoparticle-mediated hyperthermia on tumors *in vivo*.

(A) In mice with subcutaneously inoculated human colorectal cancer cells, 90 min following a single 10 Gy dose of radiation therapy using 125 kV x-rays, hematoxylin and eosin-stained slides of the tumor core show minimal necrosis (left), but addition of gold nanoshell-mediated hyperthermia (41°C for 20 min immediately prior to radiation) results in significantly more necrosis (right). Arrows denote size of areas of necrosis within tumors [35]. **(B)** On further investigation, the tumor core of mice treated with radiation alone (left) has classical tissue architecture with central vascular channels surrounded by orderly layers of cells with decreasing levels of oxygenation with increasing distance – hypoxic areas (further from vasculature) are stained green and perfused areas are stained blue in this immunofluorescence image. However, the mice treated with combined hyperthermia and radiation (right) have tumor cores with complete disruption of normal stromal structure, suggestive of vascular collapse [35]. **(C)** In a mouse model of breast cancer, treatment with a single dose of 6 Gy with or without post-treatment hyperthermia (42°C for 20 min) was followed by tumor digestion 48 h later and re-implantation in syngeneic mice in limiting dilutions. For reappearance of tumors, the combined treatment group required more cells re-implanted in mice than the radiation alone group, suggestive of a greater effect of combined treatment on putative cancer stem cells. Furthermore, the tumors reappeared as a more aggressive phenotype in the radiation alone group (left) than the combined treatment group (right). These results suggest that more efficient elimination of cancer stem cells by nanoshell-mediated hyperthermia and radiation compared with radiation alone results in lesser ability to recreate tumors as well as appearance of more differentiated, less aggressive and more treatable tumors [46].

Figures reproduced with permission from the referenced sources.

Alliance for NanoHealth (ANH) DOE Training Program
Post-Doctoral Research Training Fellowship 2009
Final Report

Name: Kyle Hammerick
Institution: Rice University (Postdoctoral Fellowship)
Project Title: Nanostructured polymer matrices to direct osteogenic differentiation of human induced pluripotent stem cells

I. Summary of Research:

Introduction: Nanoscale features interact with cells at the level of focal adhesion complexes influencing cell adhesion. In so doing, they can alter cytoskeletal tension and cell differentiation.[1] Alterations in nanostructures that induce spreading and increase focal adhesion signaling seem to enhance osteogenic differentiation.[2] Nanostructures can also directly impact organization of the cytoskeleton ultimately affecting cellular phenotype, and therefore explicit parameters may be defined that promote osteogenesis. For instance, cell adhesive motifs spaced 58-73 nm apart proved optimal for osteoblast adhesion and activation.[3] Although this was demonstrated in osteoblasts, it suggests that certain nanostructures may bias mesenchymal and osteogenic differentiation in populations of pluripotent cells. The objective of this study was to utilize scaffolds with nanostructures to direct differentiation of human induced pluripotent stem cells (hiPSCs) toward mesenchymal and ultimately osteogenic fates.
Materials and Methods: Different feature sizes were probed for their ability to elicit mesenchymal cell differentiation from hiPSCs. Randomly organized nano- and microscaffolds were fabricated by electrospinning poly(ε-caprolactone) (PCL) to fiber dimensions of 400 nm, 5 μm, and 10 μm in diameter. Human iPSCs reprogrammed from IMR-90 human fibroblasts were cultured on structured scaffolds and on flat, feature-free, PCL for up to three weeks. The cell morphology was characterized with respect to focal adhesion formation and cytoskeletal organization. The cells were immunophenotyped for expression of mesenchymal markers such as CD73, CD90, and CD105. The degree of departure from embryonic-like expression patterns was also characterized by expression of alkaline phosphatase as well as typical stem cell markers Oct4 and SSEA-4.
Results and Discussion: Scaffold feature size caused morphological differences in hiPSCs and hiPSC colony formation. Nanostructures seemed to cause focal adhesion clustering and compact cellular morphologies while microstructured and flat PCL surfaces promoted cell spreading and larger focal adhesion complexes. (**Figure 1**) In addition, the microstructures induced expression of typical mesenchymal stem cell markers (CD73, CD90, CD105), while the nanostructures appeared to inhibit differentiation of hiPSCs toward mesenchymal lineages.

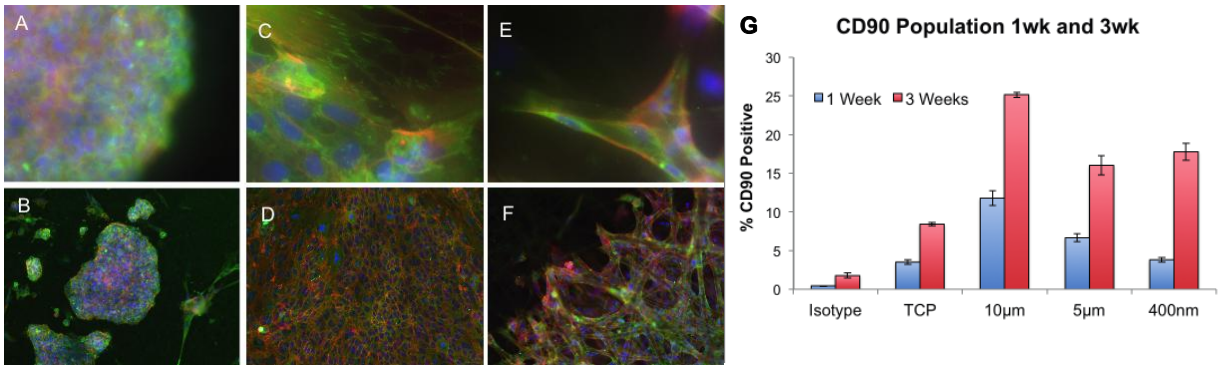

Figure 3 Human induced pluripotent stem cells on nanostructured PCL surfaces (A and B), flat PCL surface (C and D), and 10 µm diameter PCL scaffolds (E and F). Vinculin in the focal adhesion sites can be seen in green with F-actin in red and the nuclei blue, stained with DAPI. CD90 Expression levels after 1 and 3 weeks cultured on micro-and nanostructured PCL compared to tissue culture plastic controls (G).

II. **Reportable Outcomes:**

a. Publications

Liao, J., **Hammerick, K.E**., Challen, G.A., Goodell, M.A., Kasper, F.K., and Mikos, A.G. Investigating the role of hematopoietic stem and progenitor cells in regulating the osteogenic differentiation of mesenchymal stem cells in vitro. J Orthop Res. 2011. **9**: 3325-3335.

Hammerick, **K.E.,** Mikos, A.G., and F.K. Kasper, "Drug Delivery Strategies for Bone Regeneration," in Nanostructured Biomaterials for Overcoming Biological Barriers, M.J. Alonso and N.S. Csaba, Eds., Royal Society of Chemistry, Cambridge, United Kingdom, 2012, pp. 526-547.

Presentations

Hammerick, K.E. and Mikos, A.G. Nanostructured polymer matrices direct mesenchymal differentiation of human induced pluripotent stem cells. Alliance for Nanohealth Annual Meeting, February 23, 2010. Houston, TX, USA.

Hammerick, K.E. Kasper, F.K., and Mikos, A.G. Nanostructures inhibit mesenchymal differentiation of human induced pluripotent stem cells. International Society for Stem Cell Research 9th Annual Meeting. June 15-18, 2011. Toronto, Ontario, Canada.

Hammerick, K.E., Kasper, F.K. and Mikos, A.G. Nanostructured Scaffolds for Regulating Osteogenic Differentiation of Induced Pluripotent Stem Cells. Biomedical Engineering Society Annual Meeting. October 12-15, 2011. Hartford, CT, USA.

b. Patents

N/A

c. Invited Presentations

Hammerick, K.E., Engineering the stem cell microenvironment: Electrically and mechanically directed differentiation of stem cells. February 18, 2011. Santa Clara University, Santa Clara, CA, USA

Hammerick, K.E. Engineering the stem cell microenvironment. June 9, 2011. Purdue University, West Lafayette, IN, USA.

III. Conclusion

The goal of this study was to investigate the influence of scaffolds with nanoscale features on the generation of mesenchymal stem cells and ultimately osteogenic constructs from hiPSCs. While it was expected that nanostructures would promote cell differentiation by increasing cell adhesion signaling due to increased generation of adhesion sites, it appears that nanostructured scaffolds inhibited spreading and expression of mesenchymal stem cell markers in hiPSCs. Therefore, judicious incorporation of nanostructures should be observed in the quest for regenerating mesenchymal tissues like bone.

IV. References

1. McBeath R, Pirone DM, Nelson CM, Bhadriraju K, & Chen CS *Dev Cell*, 2004, **6**, 483-495.
2. Biggs MJ, *et al. J Biomed Mater Res A*, 2009, **91**, 195-208.
3. Arnold M, *et al. Chemphyschem*, 2004, **5**, 383-388.

V. Appendices

Published in final edited form as:
J Orthop Res. 2011 October ; 29(10): 1544–1553. doi:10.1002/jor.21436.

INVESTIGATING THE ROLE OF HEMATOPOIETIC STEM AND PROGENITOR CELLS IN REGULATING THE OSTEOGENIC DIFFERENTIATION OF MESENCHYMAL STEM CELLS IN VITRO

Jiehong Liao[1], **Kyle E. Hammerick**[1], **Grant A. Challen**[2], **Margaret A. Goodell**[2], **F. Kurtis Kasper**[1], and **Antonios G. Mikos**[1,*]

[1]Department of Bioengineering, Rice University, Houston, TX

[2]Center for Cell and Gene Therapy, Baylor College of Medicine, Houston, TX

Abstract

Significant progress has been made in understanding the hematopoietic supportive capacity of both mesenchymal stem cells (MSCs) and osteogenic cells in maintaining hematopoietic stem and progenitor cells (HSPCs) *in vitro*. However the role of HSPCs in regulating their bone marrow niche environment through influencing the function of neighboring cell populations to complete this reciprocal relationship is not well understood. In this study, we investigated the influence of HSPCs on the osteogenic differentiation of MSCs *in vitro*, using a highly enriched population of hematopoietic cells with the phenotype c-Kit$^+$Sca-1$^+$Lineage$^-$ (KSL) and bone marrow derived mesenchymal stromal cells in direct contact co-culture in medium with or without the addition of the osteogenic supplement dexamethasone. The data suggest that a low dose of HSPCs in co-culture with MSCs in combination with dexamethasone treatment accelerates the osteogenic progression of MSCs, as evidenced in the earlier peak in alkaline phosphatase activity and enhanced calcium deposition compared to cultures of MSCs alone. We observed a longer persistence of functional primitive hematopoietic stem and progenitor cells in the population treated with dexamethasone, and this observation was positively correlated with enhanced osteogenic differentiation of MSCs. Therefore, our findings further support the concept that HSPCs are actively involved in regulating the development and maintenance of the stem cell niche environment in which they reside.

Keywords

Marrow stromal cell; Co-culture; Niche; Osteoblast; Dexamethasone

Introduction

Strategies to effect bone regeneration often seek to leverage select elements of native bone tissue, such as bone marrow derived stem cell populations or processed bone matrix components, to provide engines to drive tissue regeneration or structures to support tissue formation. Experimental approaches commonly employ mesenchymal stem cells (MSCs) harvested from the marrow to promote bone regeneration, yet other cellular components of the bone marrow may play an active role in promoting osteogenesis. Indeed, recent evidence suggests that MSCs together with hematopoietic stem cells form a unique niche in the bone marrow and function in strong cooperation with each other [1]. Accordingly, key elements

*Corresponding Author: Antonios G. Mikos, Professor, Department of Bioengineering, Rice University, MS-142, P.O. Box 1892, Houston, TX 77251, Tel: (713) 348-5355, Fax: (713) 348-4244, mikos@rice.edu.

of the marrow microenvironment present the potential to be harnessed in combination to promote bone osteogenesis. Understanding the bone marrow microenvironment and recreating key components or interactions *in vitro* may enable approaches utilizing culture expanded stem cells for bone regeneration.

To effectively engineer the marrow microenvironment, it is essential to understand the interactions between resident cell populations, as intimate contact between supporting cells, growth factors, and extracellular matrix cues provides a specific microenvironment that balances stem cell self-renewal versus differentiation and quiescence versus proliferation. The cellular components comprising the stem cell niche contain a heterogeneous population of cells, and in addition to hematopoietic progenitors, include multipotent mesenchymal progenitor cells and osteoblastic cells that may play an integral role within the stem cell niche. While significant progress has been made in understanding the hematopoietic supportive capacity of both MSCs and osteogenic cells [2–5], little is known about the ability of HSPCs to regulate the development and maintenance of their own niche environment by influencing neighboring cells. Since hematopoietic cells and mesenchymal populations reside in such close proximity [1], it is widely believed that there is substantial crosstalk between HSPCs and the other cellular components of the niche [6–8].

HSPCs and their primitive progeny are primarily located proximal to the endosteal surface of trabecular bone [9, 10]. The exact spatial relationship of HSPCs and stromal progenitor cells within the marrow is not well defined, but both cell populations coexist in close proximity within the marrow, suggesting that they play an interactive role in regulating their microenvironment and influencing the function of the other. HSPC development and localization is directly influenced by factors synthesized during the osteogenic program of MSCs. The differentiation of bone marrow stromal cells toward the osteogenic lineage results in a cascade of events, from the early expression of osteopontin to the development of a mineralized extracellular matrix. For example, osteopontin which is a potent regulator of mineralization and one of the most abundant non-collagenous proteins in bone [11], has been shown as a negative regulator of HSPC proliferation [12, 13], presumably facilitating the maintenance of a pool of hematopoietic progenitor cells within the marrow. Also, the mineral phase of bone is integral to the localization and adhesion of HSPCs within the endosteal niche, as HSPCs lacking the calcium-sensing receptor to detect the ionic content of the mineral phase do not function normally upon transplantation [14]. These examples support the concept that MSCs and osteoblastic cells actively regulate the function of HSPCs. The question remains whether HSPCs participate in completing this reciprocal relationship and how they influence the development and maintenance of the bone marrow niche.

Recent reports suggest that HSPCs regulate bone formation through the production of BMP-2 and BMP-6 [15, 16]. However, these studies emphasize the effect of soluble signaling as the cell populations were physically separated in culture. Here we investigate the role of HSPCs in regulating the osteogenic differentiation of MSCs *in vitro* by examining the progression of osteogenesis through incorporating direct cell-cell interactions. Specifically, we evaluated the osteogenic differentiation of MSCs induced by dexamethasone treatment, in order to direct cells toward the osteoblastic lineage prior to establishing experimental cultures as with our previous osteogenic studies using rat MSCs [17, 18], and hypothesized that both cell-cell interactions and paracrine signaling provided by HSPCs would augment the osteogenic response of MSCs. To investigate our hypothesis, MSCs were co-cultured in direct contact with HSPCs in medium with or without the addition of dexamethasone, in order to explore the progression of osteogenesis and examine how HSPCs participate in the physical development of a mineralized niche environment *in vitro*.

Materials and Methods

Mesenchymal stem cell isolation and expansion

MSCs were isolated from bone marrow collected and pooled from the femurs and tibias of twenty 8–10 week old C57BL/6 mice (Jackson Laboratory, Bar Harbor, ME) according to previously established methods [19] and approved by the Institutional Animal Care and Use Committee of Baylor College of Medicine. Mice were anesthetized with isoflurane, euthanized via cervical dislocation, and then immersed in 70% ethanol. Femurs and tibias were excised and cleared of soft tissue. Bones were crushed using a mortar and pestle with Hanks Balanced Salt Solution (HBSS) (Invitrogen, Carlsbad, CA), supplemented with 2% fetal bovine serum (FBS) (Gemini Bio-Products, West Sacramento, CA), also with the addition of 1% antibiotics containing 10,000 U/mL penicillin and 10,000 μg/mL streptomycin (Invitrogen, Carlsbad, CA). The bone marrow suspension was filtered through a 100 μm cell strainer to remove bone debris, followed by a 40 μm cell strainer to obtain a single-cell suspension. Whole bone marrow was plated in tissue culture flasks with general expansion medium consisting of α-MEM, supplemented with 10% FBS, also with the addition of 1% antibiotics containing penicillin and streptomycin. Adherent cells were cultured for 7 days in general expansion medium with medium changes every 3 days. Following the primary culture period, MSCs were lifted with 0.25% trypsin and plated at low density for subculture expansion [20]. When confluent, MSCs were lifted and frozen in aliquots of medium containing 20% FBS and 10% dimethyl sulfoxide (DMSO). The adherent cells isolated from whole bone marrow and expanded through subculture will be referred to as the MSC population in subsequent co-cultures.

Hematopoietic stem and progenitor cell isolation

Following the same procedure described above to collect bone marrow from C57BL/6 mice, the marrow was alternatively suspended in phosphate buffered saline (PBS), supplemented with 2% FBS, 2 mM EDTA, and 10 mM HEPES, also with the addition of 1% antibiotics containing penicillin and streptomycin, then filtered through a 40 μm cell strainer to obtain a single-cell suspension. Whole bone marrow was enriched immunomagnetically for Sca-1+ cells using the EasySep Mouse SCA1 Positive Selection Kit (Stemcell Technologies, Vancouver, BC, Canada) according to the manufacturer's instructions. In addition to labeling cells with phycoerythrin (PE) conjugated Sca-1 as part of the EasySep Kit, cells were incubated on ice for 20 min with the following antibodies all at 1:100 dilution; fluorescein isothiocyanate (FITC) conjugated c-Kit (BD Pharmingen, Franklin Lakes, NJ), PE-Cy5 conjugated Mac-1, Gr-1, CD4, CD8, B220, and Ter-119 (eBioscience, San Diego, CA, USA) as previously described [21]. Cells were sorted for the cell surface phenotype c-$Kit^{+}Sca\text{-}1^{+}Lineage^{-}$ (KSL), comprised of hematopoietic stem and progenitor cells, using a Cytomation MoFlo cell sorter (Dako, Carpinteria, CA). The hematopoietic stem and progenitor cells isolated and purified from whole bone marrow will be referred to as the HSPC population in subsequent co-cultures.

MSC-HSPC direct contact co-culture

Cryopreserved MSCs were thawed at 37 °C and plated in tissue culture flasks with general medium for 24 h, then changed to complete osteogenic medium for an additional 6 days with medium changes every 2 days for osteogenic pre-culture [17, 18]. Complete osteogenic medium for osteogenic pre-culture consisted of α-MEM, supplemented with 10% FBS, 10 nM dexamethasone, 10 mM β-glycerophosphate, and 50 mg/L ascorbic acid, also with the addition of 1% antibiotics containing penicillin and streptomycin. In preparation for cell seeding, individual wells of 12-well plates were filled with 1 mL of complete osteogenic medium either with or without the addition of 10 nM dexamethasone. Following the osteogenic pre-culture period, MSCs were lifted with 0.25% trypsin and seeded into 12-well

plates at a density of 4×10^4 cells/well, where each well was 3.8 cm^2. After allowing 24 h for MSCs to attach and form a monolayer, HSPCs were isolated as described above and seeded into wells designated for direct contact co-culture at either 400 cells/well or 1000 cells/well. The first medium change was performed after 4 days with subsequent medium changes every 2 days thereafter. Sixteen wells were cultured for each culture group (MSC, CC400, CC1000) and dexamethasone treatment (−DEX and +DEX) for each culture time (8, 16, 24 days), at the end of which wells were rinsed with PBS in preparation for analysis. Two wells were fixed for scanning electron microscopy, two wells were stained to visualize alkaline phosphatase activity, and two wells were stained to visualize calcium deposition. Four wells were prepared to quantitatively assess cellularity and alkaline phosphatase activity, four wells to assess calcium content, and two wells to assess colony-forming capacity in methylcellulose medium.

Scanning electron microscopy

Culture wells for scanning electron microscopy were fixed with 10% neutral-buffered formalin (Fisher Scientific, Pittsburgh, PA) then rinsed with ddH_2O and air-dried. Wells were cut out from the culture plates using an X-660 Laser Platform laser cutter (Universal Laser Systems, Morningside, QLD, Australia) and mounted on aluminum stubs with conductive copper tape. Samples were sputter coated with gold for 1 min prior to imaging using a Quanta 400 SEM (FEI, Hillsboro, OR).

Staining and light microscopy

Alkaline phosphatase activity was visualized by staining culture wells using a Blue Alkaline Phosphatase Substrate Kit (Vector Laboratories, Burlingame, CA) according to the manufacturer's instructions. Reagents provided with the kit were mixed in recommended proportions into 100 mM Tris-HCl buffer with pH adjusted to 8.2. Cells were incubated with 500 μL of the substrate solution and developed in the dark for 30 min at 37 °C. Following the staining procedure where cells expressing alkaline phosphatase were stained blue, wells were fixed with 10% neutral-buffered formalin then rinsed with ddH_2O. Plates were placed at an angle to air-dry then stored at 4 °C. Cells were imaged using an Imager.Z2 light microscope with an AxioCam MRc 5 video camera attachment (Zeiss, Thornwood, New York).

Calcium deposition was visualized by staining culture wells with 40 mM Alizarin Red S (Sigma-Aldrich, St. Louis, MO) with pH adjusted to 4.1 using ammonium hydroxide [22]. Cells were fixed with 10% neutral-buffered formalin then rinsed with ddH_2O. Wells were incubated with 500 μL of the Alizarin Red S solution for 30 min at room temperature. Wells were washed four times with 2 mL of ddH_2O to remove any unincorporated dye. Calcium deposits indicative of matrix mineralization on differentiating cells were stained red. Plates were placed at an angle to air-dry then stored at 4 °C. Cells were imaged using an Imager.Z2 light microscope with an AxioCam MRc 5 video camera attachment.

Biochemical assays

Cells from individual culture wells were lifted with 0.25% trypsin and placed in separate microcentrifuge tubes. Cell pellets were washed with PBS then 500 μL of ddH_2O was added. Cells were lysed via three repetitions of a freeze and thaw cycle, where samples were frozen in liquid nitrogen for 10 min, thawed in a 37 °C water bath for 10 min, and sonicated for 10 min.

As a measure of cellularity, double-stranded DNA was quantified using the fluorometric PicoGreen assay (Invitrogen, Carlsbad, CA) with DNA standards [23]. Fluorescence was measured on an FL ×800 plate reader (BioTek, Winooski, VT). DNA content is reported as

μg of DNA per well to assess cellularity. Alkaline phosphatase activity was determined by quantifying the enzyme-mediated dephosphorylation of the substrate p-nitrophenol phosphate to p-nitrophenol in a colorimetric assay (Sigma-Aldrich, St. Louis, MO) with p-nitrophenol standards [24]. Absorbance was measured on a PowerWave ×340 plate reader (BioTek, Winooski, VT), with concentrated samples diluted as necessary to ensure absorbance readings within the linear range of the assay. Normalized alkaline phosphatase activity (ALP/DNA) was calculated by dividing alkaline phosphatase activity over DNA content for each sample and is reported as pmol per h per μg DNA as an early marker for osteogenic differentiation.

Calcium content was determined by quantifying free calcium ions in a colorimetric assay by first adding 500 μL of 1 N acetic acid directly into each culture well. After allowing calcium deposits to dissolve, samples were collected and wells were rinsed with an additional 200 μL of 1 N acetic acid. Calcium was quantified using the calcium assay (Genzyme, Cambridge, MA) with calcium chloride standards [25]. Absorbance was measured on a PowerWave ×340 plate reader, with concentrated samples diluted as necessary to ensure absorbance readings within the linear range of the assay. Fold change in calcium content at each time point was calculated by normalizing calcium content to that of MSCs alone within each respective dexamethasone treatment to assess matrix mineralization as a late marker for osteogenic differentiation.

Colony-forming assay

Cells from individual culture wells were lifted with 0.25% trypsin and placed in separate microcentrifuge tubes. The colony-forming capacity of HSPCs after each co-culture period was assessed by plating cells in Methocult GF M3434 methylcellulose-based medium (Stemcell Technologies, Vancouver, BC, Canada), then counting the number of colonies formed after 14 days [26]. Individual samples were first counted using a hemocytometer, aliquots of 10^4 total cells were plated in 35 mm low attachment culture dishes (Stemcell Technologies, Vancouver, BC, Canada) with 1.1 mL of Methocult GF M3434, and then incubated for 14 days. Following the incubation period, colonies were counted using gridded scoring transparencies on a Stemi 2000 C stereomicroscope (Zeiss, Thornwood, New York). Colony-forming unit counts are reported as colonies per 10^4 total cells to assess the number of functional hematopoietic stem and progenitor cells remaining within the total cell population after co-culture.

Statistical analysis

Biochemical assay results to assess cellularity, alkaline phosphatase activity, and calcium content are reported as mean ± standard deviation for n = 4. A three-factor ANOVA was first performed to determine significant main effects or interactions between culture group (MSC, CC400, CC1000), dexamethasone treatment (−DEX and +DEX), and culture time (8, 16, 24 days). Multiple pairwise comparisons were then made using the Tukey procedure to determine significant differences. All statistical analyses were performed at a significance level of 5%.

Colony-forming assay results are reported as mean ± standard deviation for n = 4. A two-factor ANOVA was first performed to determine significant main effects or interaction between dexamethasone treatment (−DEX and +DEX) and culture time (8, 16, 24 days). Multiple pairwise comparisons were then made using the Tukey procedure to determine significant differences. All statistical analyses were performed at a significance level of 5%.

Results

The influence of HSPCs on the osteogenic differentiation of MSCs *in vitro* was evaluated through direct contact co-culture with or without the addition of dexamethasone. Total DNA content per culture well was used to assess overall cellularity and proliferation throughout the culture period (Figure 1). Cellularity remained constant over time at approximately the initial seeding density for cultures of MSCs alone with dexamethasone (MSC+), whereas an increase in cellularity was observed from 8 to 16 days for cultures of MSCs alone without dexamethasone (MSC−). Unlike cultures of MSCs alone, cellularity increased over time for all co-cultures regardless of dexamethasone treatment, with significant differences compared to MSCs alone at 16 and 24 days within both dexamethasone treatments. Co-cultures with dexamethasone (CC400+ and CC1000+) resulted in lower cellularity at 16 and 24 days compared to those without dexamethasone (CC400− and CC1000−).

Scanning electron micrographs were taken to visualize the surface morphology of culture wells with MSCs alone and MSCs and HSPCs in co-culture, as well as changes in the overall topography over time (Figure 2). MSCs spread over the surface of culture wells forming a monolayer while HSPCs maintained a rounded phenotype. In short-term co-culture over 8 days, HSPCs appeared to grow on the surface of MSCs. In long-term co-culture over 24 days, HSPCs seemed to incorporate into the cell layer with MSCs. The cultures acquired a rough texture after 24 days with the development of mineralized extracellular matrix containing mineral nodules.

Alkaline phosphatase expression and activity was used to assess early osteogenic differentiation of cells in culture. Light micrographs were taken of culture wells stained blue to visualize qualitatively the ALP expression of MSCs alone and MSCs and HSPCs in co-culture after 8 days (Figure 3). All cultures showed positive expression of ALP with fairly even distribution within the culture wells overall. Microscopy images revealed that most of the spread MSCs express ALP with varying intensities of blue staining, while the rounded HSPCs did not appear to express ALP as evident in the lack of blue staining macroscopically. The alkaline phosphatase activity was also measured for each group and normalized to DNA content (ALP/DNA) to quantitatively reflect early osteogenic differentiation (Figure 4). ALP/DNA remained constant over time at approximately the initial level at seeding for cultures of MSCs alone without dexamethasone, whereas ALP/DNA increased significantly in the first 8 days and peaked at 16 days for cultures of MSCs alone with dexamethasone. Although co-cultures without dexamethasone showed the same trend and ALP/DNA levels as MSCs alone, those with dexamethasone resulted in a peak in ALP/DNA at 8 days.

Calcium content as compared to MSCs within each respective dexamethasone treatment was used to assess late osteogenic differentiation of cells in culture qualitatively by microscopy (Figure 5) and quantitatively via a calcium assay (Figure 6). Light micrographs were taken of culture wells stained red to visualize qualitatively the calcium deposition of MSCs alone and MSCs and HSPCs in co-culture after 24 days (Figure 5). Although all cultures showed calcium deposition with varying intensities of red staining, the distribution of calcium deposits within the culture wells varied overall. Blank regions lacking calcium deposits were most apparent for co-cultures without dexamethasone, whereas calcium deposition appeared more evenly distributed for co-cultures with dexamethasone. Microscopy images revealed that the blank regions indeed had functional cells growing which did not stain red for calcium deposits. Further, a calcium assay was applied to determine quantitatively the fold change in calcium content as compared to MSCs within each respective dexamethasone treatment (Figure 6). Only the low dose co-culture group with dexamethasone (CC400+) showed a significant difference in calcium content compared to MSCs alone with

dexamethasone (MSC+). Fold change in calcium deposition for CC400+ was 5.8 ± 1.2 fold higher than MSC+ at 8 days and 5.5 ± 2.8 fold higher than MSC+ at 16 days. Interestingly, there was no significant difference at 24 days.

Colony-forming cell growth in methylcellulose medium was used to assess the colony-forming capacity of HSPCs after co-culture (Figure 7). Although the number of hematopoietic stem and progenitor cells significantly decreased in the first week of co-culture as compared to the initial HSPC population following FACS analysis prior to seeding (99.4 ± 11.6 colony-forming units per 10^4 total cells), more colonies remained with dexamethasone treatment in short-term co-culture. After 8 days of co-culture, colony-forming unit counts per 10^4 total cells for CC400+ was 35.3 ± 12.4 and for C400− was 3.3 ± 1.3. While dexamethasone treatment resulted in this significant difference in colony counts at 8 days, the number of colonies decreased over extended culture periods.

Discussion

The objective of this study was to investigate the influence of HSPCs on the osteogenic differentiation of MSCs through direct contact co-culture, to better understand the interactions of cellular components comprising the stem cell niche under *in vitro* culture conditions. This study was designed to evaluate the osteogenic differentiation of MSCs *in vitro* induced by dexamethasone treatment, and to examine how the inclusion of HSPCs in co-culture would augment this differentiation response by providing a niche microenvironment consisting of both direct cell-cell interactions and paracrine signaling.

Recent studies have reported that HSPCs actively participate in bone formation by producing BMP-2 and BMP-6 [15], especially when activated by elevated erythropoietin levels induced by acute bleeding [16]. Frequently in studies investigating the crosstalk between HSPCs and MSCs, the effect of soluble signaling is emphasized as HSPCs are cultured separately from MSCs in the top chambers of transwell plates then assessed for osteoblastic colony formation at the end of culture [15, 27]. Although inclusion in the present study of non-contact co-cultures of MSCs osteogenically induced by dexamethasone treatment and HSPCs may have provided a base-line regarding the effects of soluble signaling between HSPCs and MSCs *in vitro*, it is known that HSPCs and MSCs reside in close physical association to form a unique niche in the bone marrow [1]. Accordingly, the focus of the present study was to mimic the direct HSPC-MSC contact in the stem cell niche under *in vitro* conditions, and to examine osteogenic differentiation of MSCs in contact co-culture with HSPCs following induction via dexamethasone treatment. Indeed, here we investigated the progression of osteogenesis from induction to mineralized matrix production by incorporating direct cell-cell interactions in addition to paracrine signaling, which allowed us to examine the extent to which HSPCs participate in the physical development of a mineralized niche environment *in vitro*.

Our results showed that HSPCs influenced the osteogenic differentiation of MSCs under *in vitro* culture conditions with dexamethasone. We observed that low doses of HSPCs co-cultured in direct contact with MSCs and exposed to dexamethasone treatment, reduced overall cellular proliferation, stimulated early alkaline phosphatase activity, and enhanced calcium deposition, thus supporting the progression of osteogenic differentiation *in vitro*. Additionally, qualitative morphological observations from light microscopy and scanning electron microscopy suggest the presence of physical interactions between HSPCs and differentiating MSCs throughout the progression of osteogenesis *in vitro*, which may be examined in greater detail in future studies.

Cellularity and proliferation throughout the culture period was evaluated by quantifying total DNA content per culture well. Cultures of MSCs alone, particularly with dexamethasone treatment, maintained similar cellularity over 24 days of culture. Since cells were induced toward osteogenic differentiation *in vitro* with dexamethasone, we expect to see minimal proliferative activity as cells transition to an osteoblastic phenotype [28]. Although in all co-culture groups, the overall cell population rapidly proliferated, dexamethasone treatment significantly reduced cellularity after 16 and 24 days of culture. Qualitative morphological observations from light microscopy and scanning electron microscopy suggest that the HSPC population proliferated quickly in co-culture, while the MSC population maintained a confluent cell layer, which may have supported the growth and retention of HSPCs *in vitro*. Over an extended culture period, however, HSPCs appeared to incorporate into the cell layer with MSCs, where they could possibly outcompete MSCs for space and nutrients. While in this study, the contribution of each cell population to the overall change in cellularity over time was not specifically assessed, we consider that HSPCs proliferate much more rapidly than MSCs in co-culture, as MSCs and osteogenic cells are often used as feeder layers to expand hematopoietic cell numbers *ex vivo* due to their supportive role in the stem cell niche [2–5]. However in those applications, dexamethasone is not included as a culture supplement, and thus the effects of co-culture in combination with dexamethasone on HSPCs *in vitro* are not known. Studies investigating glucocorticoid treatment through intraperitoneal injections have shown hematoprotective effects of dexamethasone, promoting the quiescence of stem cells as seen in the maintenance of high colony-forming cell numbers even after cytotoxic chemotherapy [29, 30]. In exploring how HSPCs affect the progression of MSCs initiated toward osteogenic differentiation via dexamethasone exposure, we observed that dexamethasone may play a role in maintaining hematopoietic stem and progenitor cells *in vitro*. This is evidenced in the higher number of functional hematopoietic stem and progenitor cells within the total cell population that remain following short-term co-culture with dexamethasone, albeit those colony-forming cells decrease significantly in number over extended culture periods. Although the expansion of HSPCs *ex vivo* was not the focus of this current study, we found that dexamethasone as a culture supplement may be worth exploring in order to optimize co-culture conditions to permit the sustained expansion of HSPCs *ex vivo*.

Alkaline phosphatase activity was used as an early marker for osteogenic differentiation as enzyme levels peak during the onset of osteogenic differentiation then decrease as cells progress toward an osteoblastic phenotype [28]. Dexamethasone treatment induced a significant increase in ALP/DNA in the first 8 days for all culture groups. While MSCs alone showed a clear peak in ALP/DNA at 16 days, the data suggest that the peak in ALP/DNA for co-culture groups may have occurred sooner within the first 8 days of culture, since ALP/DNA levels were already declining after 8 days. Thus, these trends in ALP/DNA imply that dexamethasone indeed promotes osteogenic differentiation with a characteristic peak in the profile of alkaline phosphatase expression we typically observe in our osteogenic cultures [31–33], and that co-culture with HSPCs accelerates the osteogenic differentiation of MSCs in their transition to an osteoblastic phenotype.

Since cell populations were not separated following co-culture, total alkaline phosphatase activity of the entire cell population as a whole was evaluated qualitatively via microscopy. Through macroscopic inspection following the staining procedure to visualize ALP expression at 8 days, HSPCs did not appear to stain for ALP activity, as most of the staining was much more apparent and intense for the MSCs. While we do not know how the HSPC population contributes to quantitative ALP measurements, ALP expression has been documented for rare hematopoietic cells, particularly plasma cells as terminally differentiated B-cells [34]. This may account for the higher levels of total ALP detected qualitatively for co-cultures without dexamethasone, as the colony-forming assay revealed

that cells rapidly differentiated into mature hematopoietic lineages within the first week of culture without dexamethasone treatment, as evident in the lower numbers of functional hematopoietic stem and progenitor cells remaining within the total cell population after co-culture.

Calcium deposition was used as a late marker for osteogenic differentiation, as cells with an osteoblastic phenotype deposit increasing amounts of extracellular matrix, which mineralizes over time [28]. Since mouse MSCs were expanded through a brief osteogenic pre-culture period with dexamethasone in order to direct cells toward the osteoblastic lineage prior to establishing experimental cultures as with our previous osteogenic studies using rat MSCs [17, 18], this transient exposure may have initiated osteogenic progression with sustained effects even after the removal of dexamethasone in subsequent experimental cultures, similar to what has been documented for human MSCs [35]. Thus, the sustained effects of dexamethasone in initiating a pre-osteoblastic phenotype likely contributed to the calcium deposition qualitatively observed in our experimental cultures without dexamethasone. Interestingly, there is a qualitative difference in the distribution of cell populations and calcium deposits within co-cultures not treated with dexamethasone. Mineralized extracellular matrix appears to be localized to the MSC population, with large regions of the cultures wells occupied by the HSPC population that did not stain for calcium, in contrast to the more even staining seen for co-cultures treated with dexamethasone.

When the quantitative calcium data for co-culture groups are normalized to that of MSCs alone within each respective dexamethasone treatment and considered as fold change in calcium content, it is apparent that, in combination with dexamethasone treatment, a low dose of HSPCs in fact enhance calcium deposition at early time points. Over an extended culture period, the signaling effects of HSPCs, which seem to accelerate osteogenic progression, dissipate as MSCs in all culture groups treated with dexamethasone converge to an osteoblastic phenotype. From the colony-forming assay, we see that it is the primitive hematopoietic stem and progenitor cells remaining in the total cell population following co-culture that exert this stimulatory effect on the osteogenic differentiation of MSCs. On the contrary, if HSPCs differentiate into mature hematopoietic lineages in co-culture, then those hematopoietic cells lose their ability to augment the osteogenic progression of MSCs. Our findings in this study support the concept that not only do osteoblastic cells play a supportive role in maintaining hematopoietic cells, but that there is a reciprocal relationship whereby hematopoietic cells regulate osteoblastic cell function as active participants in the maintenance and development of the stem cell niche [15, 27]. Interestingly, there appears to be an optimal cell density to achieve enhanced mineralization under co-culture conditions, as may be the case in the physiological environment where the balance between cell populations affects overall cell function and tissue morphology. Furthermore, in modeling the osteogenic development of MSCs through dexamethasone exposure, we observed that not only does dexamethasone assist in directing cells towards recreating a mineralized microenvironment *in vitro* via brief exposure in pre-culture, but dexamethasone may also promote the maintenance of functional hematopoietic stem and progenitor cells in short-term co-culture, perhaps through direct action on HSPCs or indirectly through promoting the osteogenic development of MSCs that in turn act upon HSPCs. However, further investigation is warranted to determine whether MSCs or osteogenically differentiated MSCs constitute a sufficient environment to support the hematopoietic function of HSPCs [2, 3, 36]. Nevertheless, our investigation into the reciprocal relationship between the two major cell populations comprising the bone marrow niche under *in vitro* culture conditions may facilitate the development of tissue engineering strategies further optimizing co-culture parameters to achieve expansion of hematopoietic cells *ex vivo*. Understanding the development of the bone marrow microenvironment and recreating key components or

interactions *in vitro* brings us a step closer towards the realization of medical therapies utilizing culture expanded stem cells.

Conclusion

In this work, we demonstrated that primitive hematopoietic stem and progenitor cells enhance the osteogenic differentiation of mesenchymal stem cells through both cell-cell interactions and paracrine signaling as facilitated through dexamethasone treatment *in vitro*. We were able to examine how HSPCs participate in the physical development of a mineralized niche environment through direct contact co-culture with MSCs. This study further supports the concept that HSPCs actively regulate the development and maintenance of the stem cell niche environment in which they reside.

Acknowledgments

This work has been supported by the National Institutes of Health (R01 AR057083 and R01 EB005173). KE Hammerick was supported by an Alliance for NanoHealth Postdoctoral Fellowship. GA Challen was supported by the National Institutes of Health (K99 DK084259) and is an American Society of Hematology Scholar. We thank Christopher Threeton of the Texas Children's Hospital Flow Cytometry Core Laboratory for cell sorting and analysis.

References

1. Mendez-Ferrer S, Michurina TV, Ferraro F, et al. Mesenchymal and haematopoietic stem cells form a unique bone marrow niche. Nature. 466:829–834. [PubMed: 20703299]
2. Calvi LM, Adams GB, Weibrecht KW, et al. Osteoblastic cells regulate the haematopoietic stem cell niche. Nature. 2003; 425:841–846. [PubMed: 14574413]
3. Jing D, Fonseca AV, Alakel N, et al. Hematopoietic stem cells in co-culture with mesenchymal stromal cells--modeling the niche compartments in vitro. Haematologica. 2010; 95:542–550. [PubMed: 20145267]
4. Mishima S, Nagai A, Abdullah S, et al. Effective ex vivo expansion of hematopoietic stem cells using osteoblast-differentiated mesenchymal stem cells is cxcl12 dependent. Eur J Haematol. 2010; 84:538–546. [PubMed: 20088916]
5. Taichman RS, Reilly MJ, Emerson SG. Human osteoblasts support human hematopoietic progenitor cells in vitro bone marrow cultures. Blood. 1996; 87:518–524. [PubMed: 8555473]
6. Li Z, Li L. Understanding hematopoietic stem-cell microenvironments. Trends Biochem Sci. 2006; 31:589–595. [PubMed: 16911868]
7. Wilson A, Trumpp A. Bone-marrow haematopoietic-stem-cell niches. Nat Rev Immunol. 2006; 6:93–106. [PubMed: 16491134]
8. Yin T, Li L. The stem cell niches in bone. J Clin Invest. 2006; 116:1195–1201. [PubMed: 16670760]
9. Balduino A, Hurtado SP, Frazao P, et al. Bone marrow subendosteal microenvironment harbours functionally distinct haemosupportive stromal cell populations. Cell Tissue Res. 2005; 319:255–266. [PubMed: 15578225]
10. Taichman RS. Blood and bone: Two tissues whose fates are intertwined to create the hematopoietic stem-cell niche. Blood. 2005; 105:2631–2639. [PubMed: 15585658]
11. Denhardt DT, Guo X. Osteopontin: A protein with diverse functions. Faseb J. 1993; 7:1475–1482. [PubMed: 8262332]
12. Nilsson SK, Johnston HM, Whitty GA, et al. Osteopontin, a key component of the hematopoietic stem cell niche and regulator of primitive hematopoietic progenitor cells. Blood. 2005; 106:1232–1239. [PubMed: 15845900]
13. Stier S, Ko Y, Forkert R, et al. Osteopontin is a hematopoietic stem cell niche component that negatively regulates stem cell pool size. J Exp Med. 2005; 201:1781–1791. [PubMed: 15928197]

14. Adams GB, Chabner KT, Alley IR, et al. Stem cell engraftment at the endosteal niche is specified by the calcium-sensing receptor. Nature. 2006; 439:599–603. [PubMed: 16382241]
15. Jung Y, Song J, Shiozawa Y, et al. Hematopoietic stem cells regulate mesenchymal stromal cell induction into osteoblasts thereby participating in the formation of the stem cell niche. Stem Cells. 2008; 26:2042–2051. [PubMed: 18499897]
16. Shiozawa Y, Jung Y, Ziegler AM, et al. Erythropoietin couples hematopoiesis with bone formation. PLoS One. 2010; 5:e10853. [PubMed: 20523730]
17. Liao J, Guo X, Nelson D, et al. Modulation of osteogenic properties of biodegradable polymer/extracellular matrix scaffolds generated with a flow perfusion bioreactor. Acta Biomater. 2010; 6:2386–2393. [PubMed: 20080214]
18. Peter SJ, Liang CR, Kim DJ, et al. Osteoblastic phenotype of rat marrow stromal cells cultured in the presence of dexamethasone, beta-glycerolphosphate, and l-ascorbic acid. J Cell Biochem. 1998; 71:55–62. [PubMed: 9736454]
19. Haylock DN, Williams B, Johnston HM, et al. Hemopoietic stem cells with higher hemopoietic potential reside at the bone marrow endosteum. Stem Cells. 2007; 25:1062–1069. [PubMed: 17420230]
20. Kretlow JD, Jin YQ, Liu W, et al. Donor age and cell passage affects differentiation potential of murine bone marrow-derived stem cells. BMC Cell Biol. 2008; 9:60. [PubMed: 18957087]
21. Challen GA, Goodell MA. Runx1 isoforms show differential expression patterns during hematopoietic development but have similar functional effects in adult hematopoietic stem cells. Exp Hematol. 2010; 38:403–416. [PubMed: 20206228]
22. Gregory CA, Gunn WG, Peister A, Prockop DJ. An alizarin red-based assay of mineralization by adherent cells in culture: Comparison with cetylpyridinium chloride extraction. Anal Biochem. 2004; 329:77–84. [PubMed: 15136169]
23. Singer VL, Jones LJ, Yue ST, Haugland RP. Characterization of picogreen reagent and development of a fluorescence-based solution assay for double-stranded DNA quantitation. Anal Biochem. 1997; 249:228–238. [PubMed: 9212875]
24. Bretaudiere, JP.; Spillan, T. Alkaline phosphatases. In: Bergmeyer, HU.; Bergmeyer, J.; Grassl, M., editors. Methods of enzymatic analysis. Verlag Chemie: Deerfield Beach; 1984. p. 75-92.
25. Holtorf HL, Jansen JA, Mikos AG. Flow perfusion culture induces the osteoblastic differentiation of marrow stroma cell-scaffold constructs in the absence of dexamethasone. J Biomed Mater Res A. 2005; 72:326–334. [PubMed: 15657936]
26. Ogawa, M.; Livingston, AG. Hematopoietic colony-forming cells. In: Klug, CA.; Jordan, CT., editors. Hematopoietic stem cell protocols. Totowa: Humana Press; 2002. p. 113-122.
27. Taichman RS, Reilly MJ, Verma RS, Emerson SG. Augmented production of interleukin-6 by normal human osteoblasts in response to cd34+ hematopoietic bone marrow cells in vitro. Blood. 1997; 89:1165–1172. [PubMed: 9028938]
28. Owen TA, Aronow M, Shalhoub V, et al. Progressive development of the rat osteoblast phenotype in vitro: Reciprocal relationships in expression of genes associated with osteoblast proliferation and differentiation during formation of the bone extracellular matrix. J Cell Physiol. 1990; 143:420–430. [PubMed: 1694181]
29. Kim H, Choi JY, Lee JM, et al. Dexamethasone increases angiopoietin-1 and quiescent hematopoietic stem cells: A novel mechanism of dexamethasone-induced hematoprotection. FEBS Lett. 2008; 582:3509–3514. [PubMed: 18804469]
30. Kriegler AB, Bernardo D, Verschoor SM. Protection of murine bone marrow by dexamethasone during cytotoxic chemotherapy. Blood. 1994; 83:65–71. [PubMed: 8274755]
31. Datta N, Holtorf HL, Sikavitsas VI, et al. Effect of bone extracellular matrix synthesized in vitro on the osteoblastic differentiation of marrow stromal cells. Biomaterials. 2005; 26:971–977. [PubMed: 15369685]
32. Holtorf HL, Datta N, Jansen JA, Mikos AG. Scaffold mesh size affects the osteoblastic differentiation of seeded marrow stromal cells cultured in a flow perfusion bioreactor. J Biomed Mater Res A. 2005; 74:171–180. [PubMed: 15965910]

33. Sikavitsas VI, Bancroft GN, Holtorf HL, et al. Mineralized matrix deposition by marrow stromal osteoblasts in 3d perfusion culture increases with increasing fluid shear forces. Proc Natl Acad Sci U S A. 2003; 100:14683–14688. [PubMed: 14657343]

34. Borgen E, Beiske K, Trachsel S, et al. Immunocytochemical detection of isolated epithelial cells in bone marrow: Non-specific staining and contribution by plasma cells directly reactive to alkaline phosphatase. J Pathol. 1998; 185:427–434. [PubMed: 9828843]

35. Jaiswal N, Haynesworth SE, Caplan AI, Bruder SP. Osteogenic differentiation of purified, culture-expanded human mesenchymal stem cells in vitro. J Cell Biochem. 1997; 64:295–312. [PubMed: 9027589]

36. Askmyr M, Sims NA, Martin TJ, Purton LE. What is the true nature of the osteoblastic hematopoietic stem cell niche? Trends Endocrinol Metab. 2009; 20:303–309. [PubMed: 19595609]

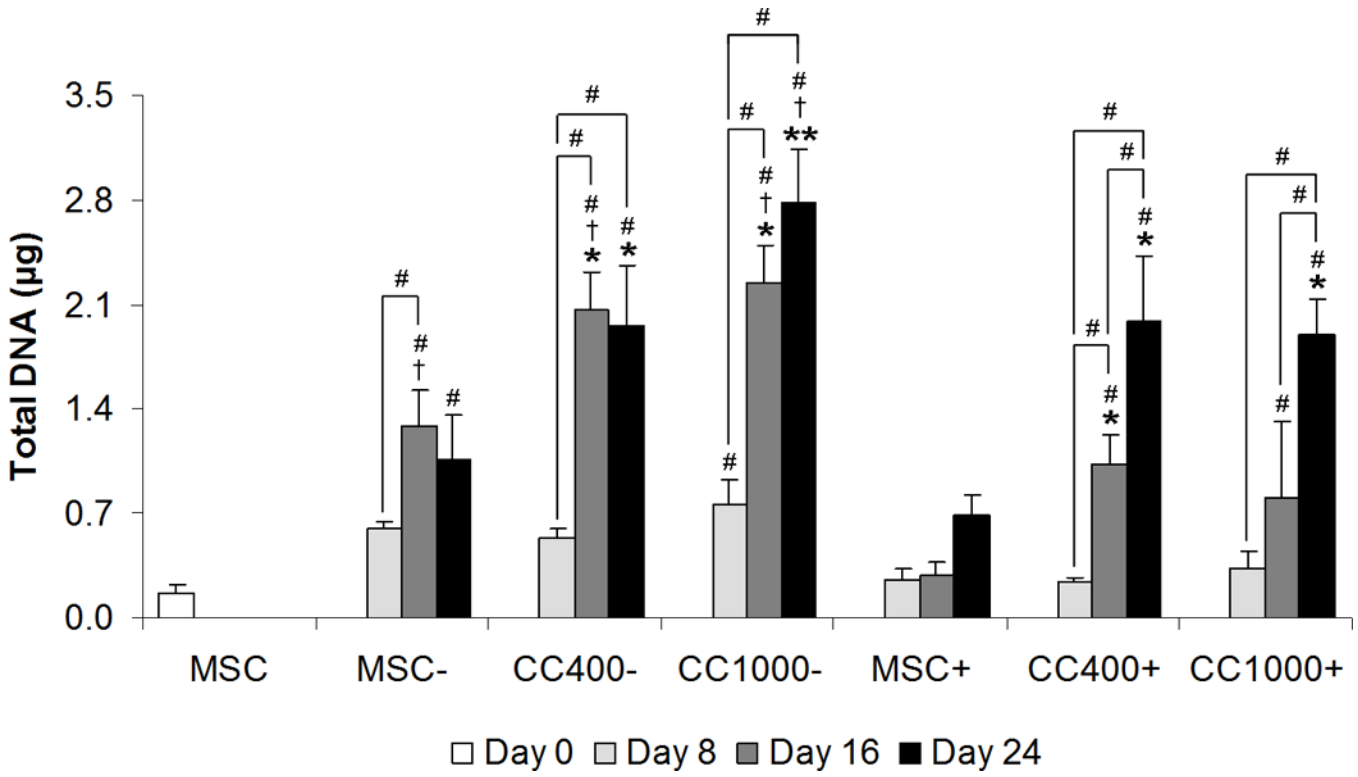

Figure 1.

Total DNA content of wells cultured with MSCs alone (MSC) or MSCs and HSPCs in co-culture (CC) at specified seeding densities (400 or 1000 HSPCs seeded onto 40,000 MSCs) either with (+) or without (−) the addition of dexamethasone. Data are presented as mean ± standard deviation for n = 4. Within a specific treatment group, significant difference ($p < 0.05$) compared to MSCs at seeding and between time points is noted with (#). Within each culture group at a specific time point, significant difference ($p < 0.05$) between dexamethasone treatment is noted with (†). Within each dexamethasone group at a specific time point, significant difference ($p < 0.05$) compared to MSCs alone is noted with (*), with significant difference ($p < 0.05$) compared to all other groups noted with (**).

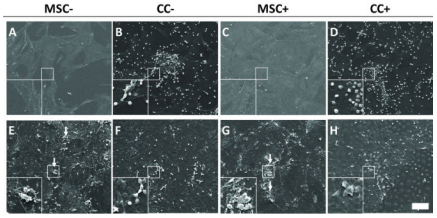

Figure 2.

Representative scanning electron micrographs of wells cultured with MSCs alone (MSC) or MSCs and HSPCs in co-culture (CC) either with (+) or without (−) the addition of dexamethasone after 8 days (A–D) and 24 days (E–H). Arrows indicate areas of mineralization showing mineral nodules. The scale bar represents 100 μm for all images with insets showing a 3× magnified view of HSPCs (B, D, F and H) and MSCs or mineral nodules (A, C, E and G) in more detail.

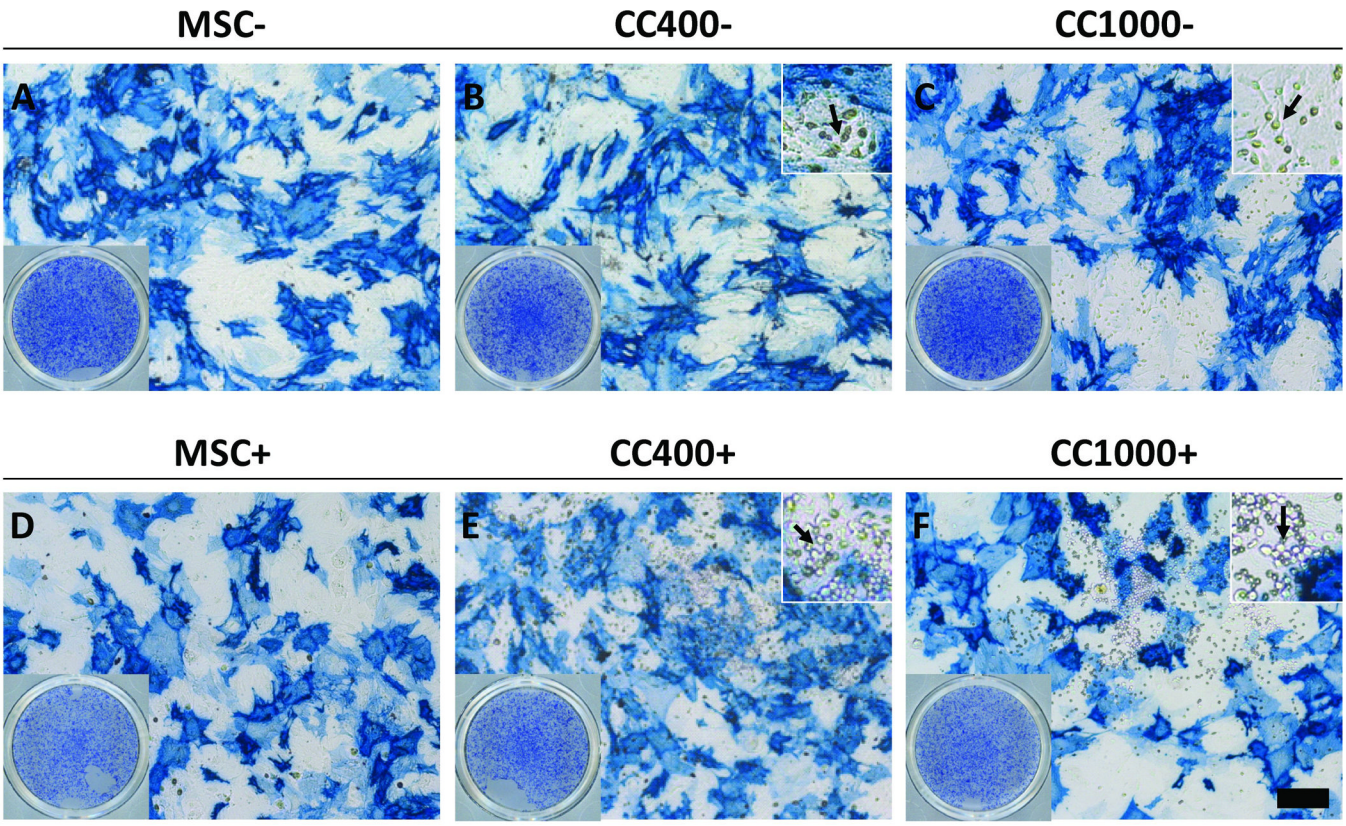

Figure 3.

Alkaline phosphatase staining of wells after 8 days of culture with MSCs alone (MSC) or MSCs and HSPCs in co-culture (CC) at specified seeding densities (400 or 1000 HSPCs seeded onto 40,000 MSCs) either with (+) (D–F) or without (−) (A–C) the addition of dexamethasone. The scale bar represents 200 μm for all microscopy images, save insets. Bottom-left insets (A–F) show the overall alkaline phosphatase staining of the wells, and top-right insets (B, C, E and F) show a 3× magnified view (with respect to the respective main images) of co-cultures, with arrows indicating apparent HSPCs.

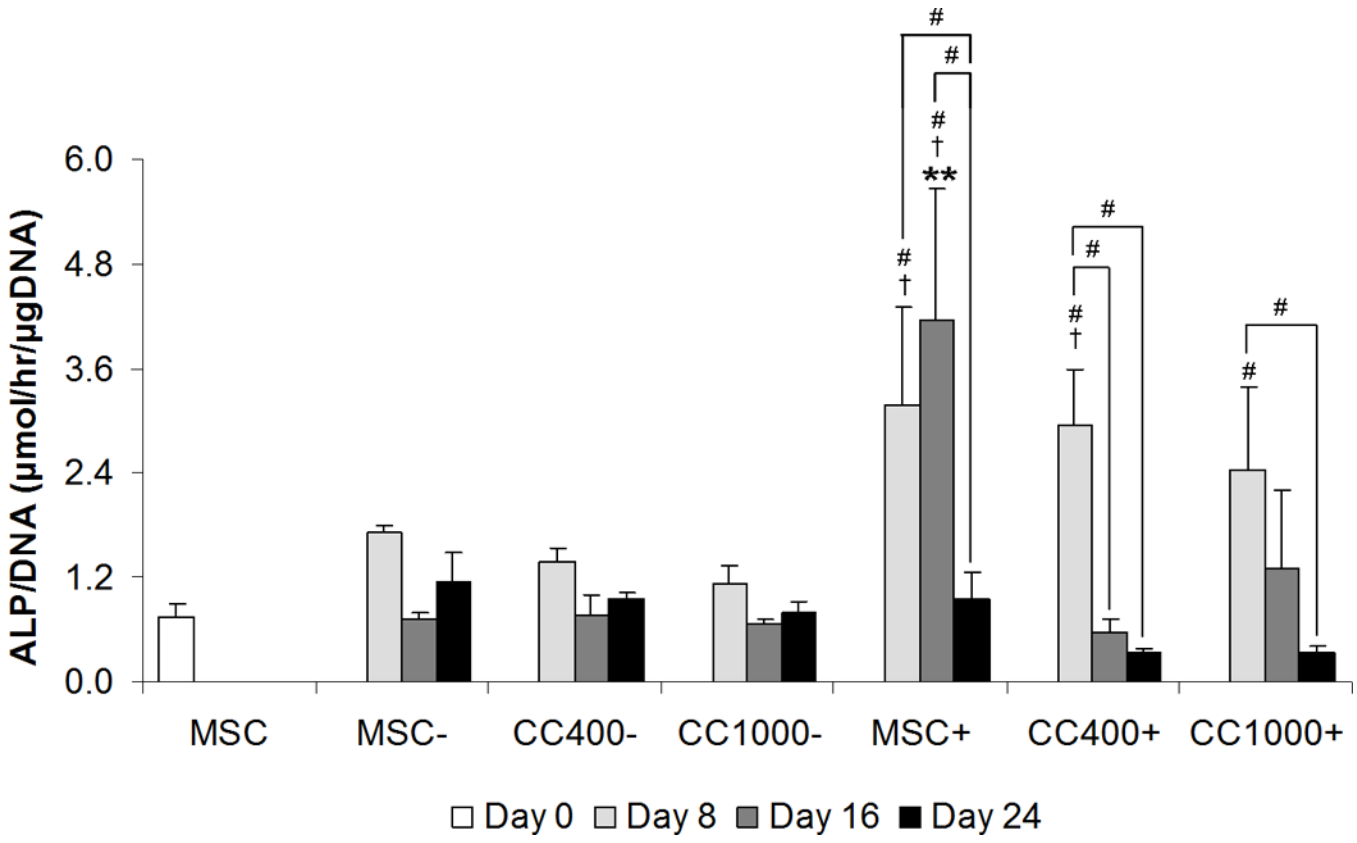

Figure 4.

Alkaline phosphatase activity MSCs alone (MSC) or MSCs and HSPCs in co-culture (CC) at specified seeding densities (400 or 1000 HSPCs seeded onto 40,000 MSCs) either with (+) or without (−) the addition of dexamethasone. Plots show alkaline phosphatase activity normalized to DNA content. Data are presented as mean ± standard deviation for n = 4. Within a specific treatment group, significant difference ($p < 0.05$) compared to MSCs at seeding and between time points is noted with (#). Within each culture group at a specific time point, significant difference ($p < 0.05$) between dexamethasone treatment is noted with (†). Within each dexamethasone group at a specific time point, significant difference ($p < 0.05$) compared to MSCs alone is noted with (*), with significant difference ($p < 0.05$) compared to all other groups noted with (**).

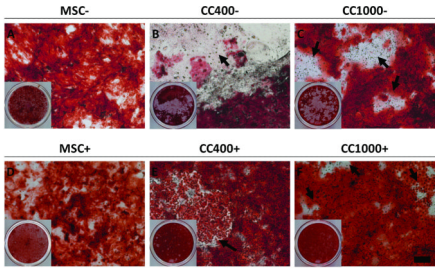

Figure 5.

Alizarin Red staining of wells after 24 days of culture with MSCs alone (MSC) or MSCs and HSPCs in co-culture (CC) at specified seeding densities (400 or 1000 HSPCs seeded onto 40,000 MSCs) either with (+) (D–F) or without (−) (A–C) the addition of dexamethasone. The scale bar represents 200 μm for all microscopy images, and arrows indicate apparent HSPCs. Insets show the overall Alizarin Red staining of the wells.

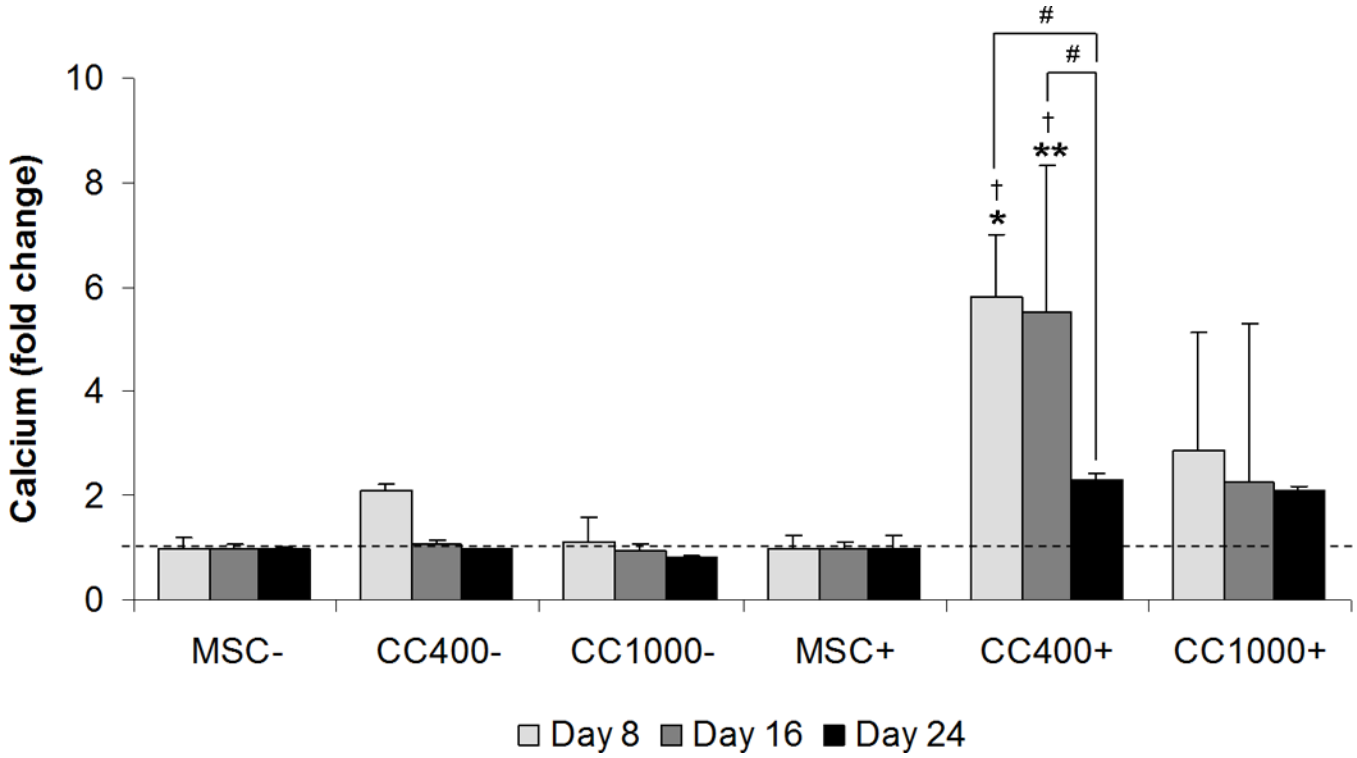

Figure 6.

Calcium content of wells cultured with MSCs alone (MSC) or MSCs and HSPCs in co-culture (CC) at specified seeding densities (400 or 1000 HSPCs seeded onto 40,000 MSCs) either with (+) or without (−) the addition of dexamethasone. Plots show fold change in calcium content as compared to cultures with MSCs for each dexamethasone treatment at each time point. Data are presented as mean ± standard deviation for n = 4. Within a specific treatment group, significant difference ($p < 0.05$) between time points is noted with (#). Within each culture group at a specific time point, significant difference ($p < 0.05$) between dexamethasone treatment is noted with (†). Within each dexamethasone group at a specific time point, significant difference ($p < 0.05$) compared to MSCs alone is noted with (*), with significant difference ($p < 0.05$) compared to all other groups noted with (**).

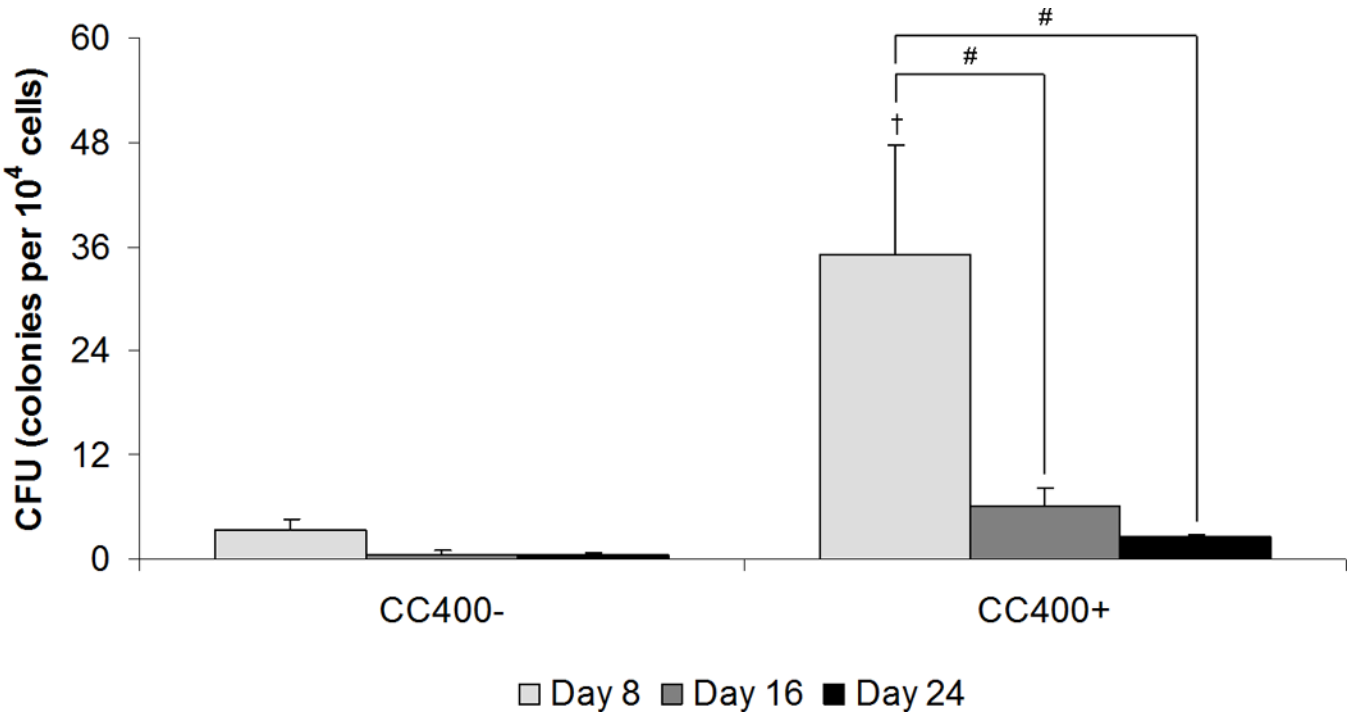

Figure 7.
Colony-forming unit counts of colonies derived in methylcellulose medium from the total cell population after co-culture (CC) at the specified seeding density (400 HSPCs seeded onto 40,000 MSCs) either with (+) or without (−) the addition of dexamethasone. Data are presented as mean ± standard deviation for n = 4. Within a specific treatment group, significant difference ($p < 0.05$) between time points is noted with (#). Significant difference ($p < 0.05$) between dexamethasone treatment is noted with (†).

Alliance for NanoHealth (ANH) NASA/DOE
Graduate Student Research Training Fellowship 2009
Final Report

Name: Elizabeth O. McCullum
Institution: Baylor College of Medicine
Project Title: De novo Evolution of Anti-breast Cancer Peptide Therapeutics for Nano-based Drug Delivery

The preparation to begin research aims began with the organization, ordering and design of the immediate planned experiments. This includes the purchasing of equipment, chemicals and other materials pertinent to fulfilling immediate experiments. The first several months were spent designing the library that would be used to select Rad21 peptide mimics, designing the mock library that would be used to test the mRNA display experiments in the lab and finally performing and optimizing preliminary experiments that would set the foundation for future work. In order to move the project forward to gain insight into specific aims two and three, we decided to use a peptide from the evolutionary trace experiment to test following the aforementioned experimental design.

Experiments:

Western blotting

The Western blotting technique is commonly used to identify proteins as a result of their ability to recognize and bind specific antibodies. This analysis of a reaction mixture can specifically detect a protein of interest. Regardless of the source, this technique will provide information on protein size and the amount that is expressed. However, the antibody used for detection must be specific for the protein of interest to overcome the possible discrepancies associated with non-specific proteins in the mixture. Furthermore, a secondary antibody with a fluorescent tag, binds to the primary antibody to indicate the presence of the initial protein in the solution.

WB analysis of the Rad21 Smc1 interaction in solution this pull-down assay was used to demonstrate the positive control used to compare the Rad21 mimic inhibition with the standard Rad21 Smc1 interaction. (Figure 1.) Both proteins, Rad21 and Smc1, were synthesized in a coupled transcription/translation (T_NT) reaction. The Rad21 protein is encoded with a HA-tag on the N-terminus, while the SMC1 has a Myc tag at its C-terminus. These constructions allowed for the two proteins to interact with their respective C- and N- termini. Moreover, this allows for blotting with a variety

of antibodies. The antibodies used consisted of Rad21 monoclonal (mAb) and polyclonal antibodies (pAb), Myc mAb, HA pAb and SMC1 pAb.

The assay will also be able to contribute to other lab endeavors as means to probe for other key Rad21 protein interactors, which play a critical role in cancer cell proliferation.

This was a learning endeavor for me considering I have not preformed an experimental WB in quite some time. I was also responsible for determining buffer conditions for providing the proteins with an environment conducive to binding. Although, this took more time than expected I was able to successfully generate data.

Molecular Cloning: Constructing the solid phase selection molecule: SMC1-GST plasmid

This series of experiments required use of several molecular biology techniques. I decided to use a SMC1-GST tagged protein to serve as the selection step. This could possibly be the most important step of the selection, therefore a large amount of this construct is needed with high purity. As a result, I designed two plasmid construction strategies to get optimal amounts and quality of this target.

Mock Selection:

mRNA display is an in vitro selection technique that allows for the identification of peptide and protein sequences with desired properties from either a natural protein library or a combinatorial peptide library. The defining feature of this technique is the ability to covalently link the polypeptide chain to the 3' end of its encoding mRNA sequences. This is accomplished by synthesis and in vitro translation of an mRNA template with puromycin attached to its 3' end using a short DNA linker. Upon the puromycin entering the ribosome a peptide bond is made between the molecule and the nascent peptide. Since the genotype coding sequence and the phenotype polypeptide are now covalently linked, each will present at the selection step despite stringent conditions. Furthermore, the ability for this system to sift through large diverse libraries increases the probability of isolating a rare functional sequence.

The mock selection is in the process of being preformed with a single modified Rad21 sequence containing the conserved region of the protein sequence. Using this single sequence I have generated the DNA template using a

traditional enzymatic Klenow extension reaction. Using this DNA template, I optimized PCR conditions for a fully functional DNA template to be used in the subsequent *in vitro* transcription reaction. After transcription, I have preformed a cross-linking reaction. This is one of the more challenging steps

of any selection. This reaction is approximately 50% efficient and therefore generates only small amounts of cross-linked mRNA. (Figure 3)

Due to the slow progression of overcoming some of the challenges of working with RNA, a fragile molecule, my advisor and I have discussed using the evolutionary trace experiments to generate peptides for preliminary tests and optimization for planned experiments in specific aims two and three. Unfortunately, resources and time would prevent me from identifying peptides to fulfill the entire research proposal. It is my hope that the work completed will continue with in my postdoctoral lab as initially written to complete the selection for identification of Rad21 mimics that will disrupt the Rad21-SMC1 interaction of the Cohesin complex and couple them to a nano-delivery system.

Reportable Outcomes:

Publications – n/a

Patents – n/a

Invited Presentations – n/a

Appendices: Figure's 1 – 3

A.

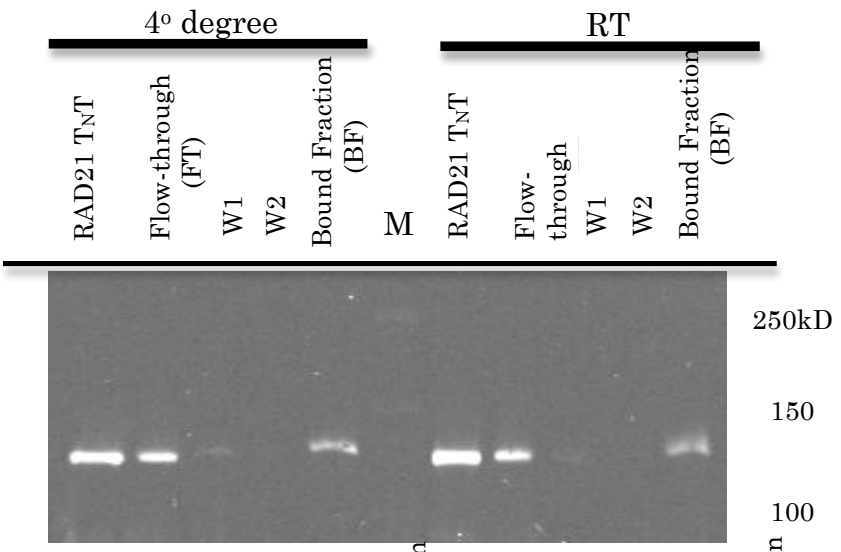

B.

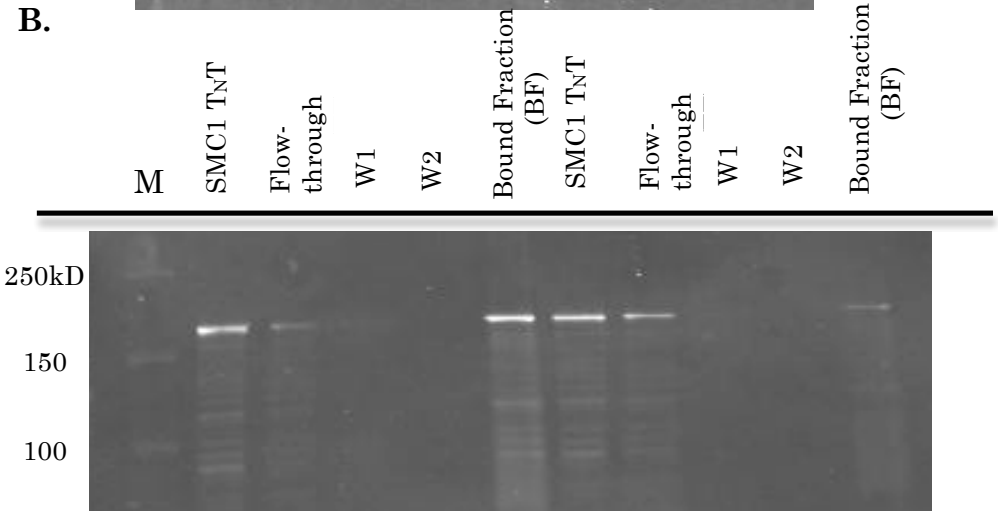

C.

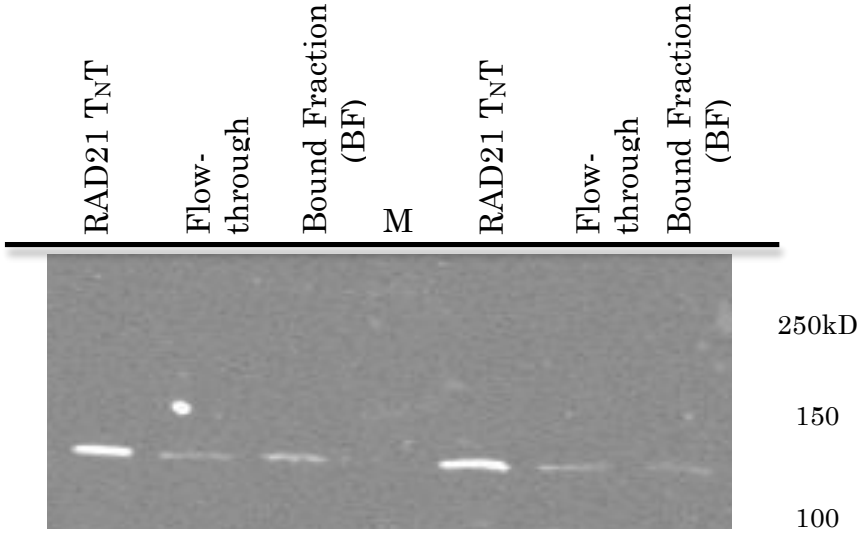

D.

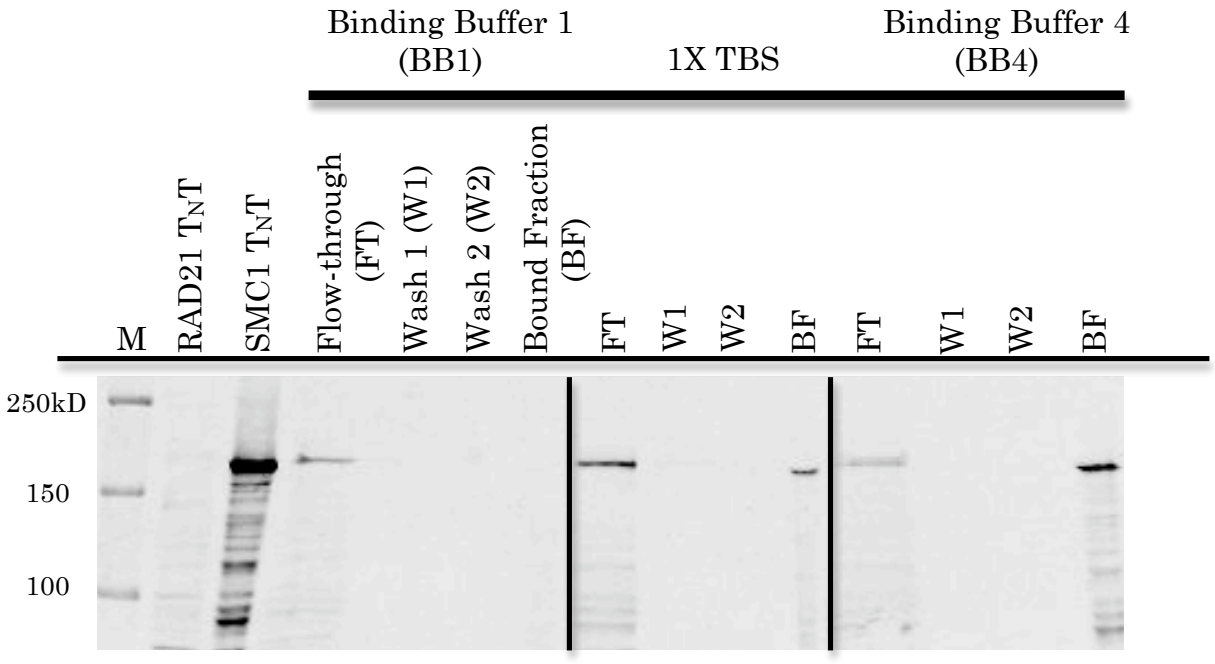

Fig. 1. (a) Rad21 positive ctrl 4deg/RT in 1X TBS (b) SMC1 post. Ctrl w/ Myc beads/Negt. Ctrl with HA beads in 1X TBS (c) HA-RAD21 incubation with Myc beads used for a negative control in 1X TBS (d) Smc1-MT pull down with HA-Rad21 beads in a variety of buffer conditions for optimal binding conditions.

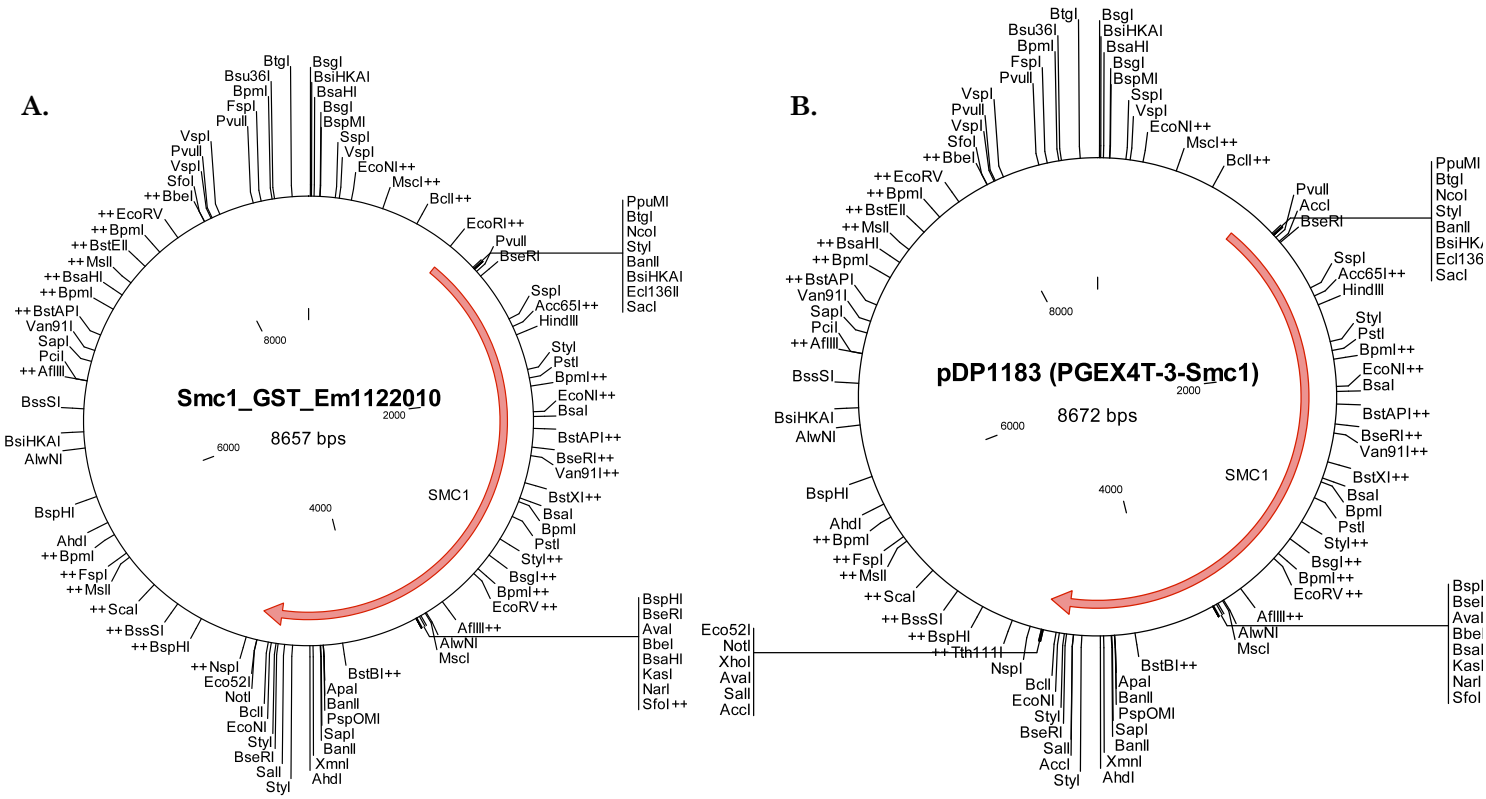

pGex-4T-1 vector and SMC1 insert

pGex-4T-3 vector and SMC1 insert

Fig 2. SMC1-GST tag construction strategies. (a) Insertion of the SMC1 sequence using sticky end ligation. (b) Insertion of SMC1 protein using blunt end ligation.

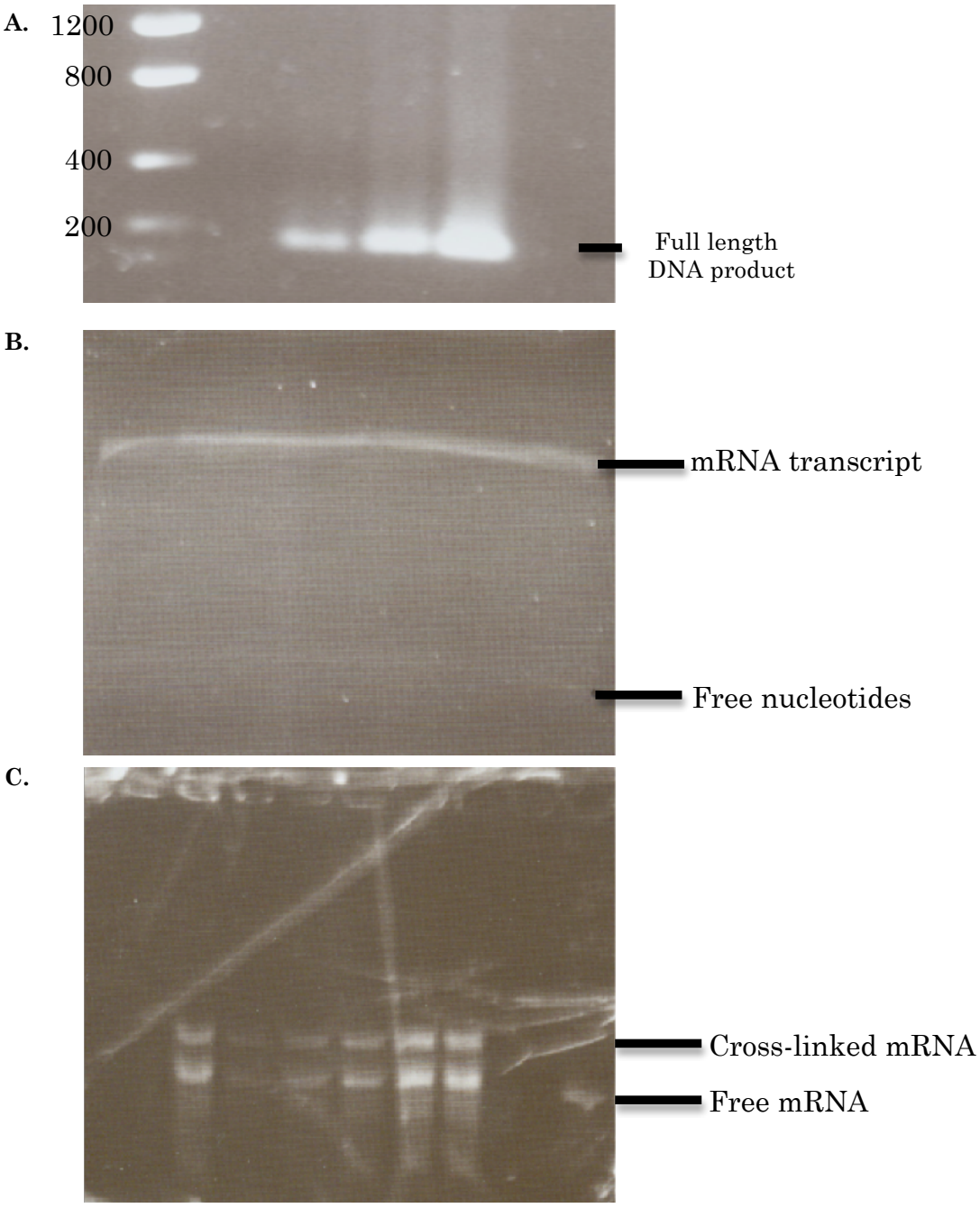

Fig. 3. (a) PCR amplification of the full-length DNA from Klenow extension reaction run on a 1% agarose gel for quantification. (b) mRNA transcript during denaturing PAGE purification after an *in vitro* transcription reaction. (c) Cross-linked mRNA during denaturing PAGE purification.

Appendix C

- ANH Distinguished Investigator Program

ALLIANCE *for* NANOHEALTH

SPECIAL EVENT

Distinguished Lectureship

"Developing Biomedical Technology for the Developing World"

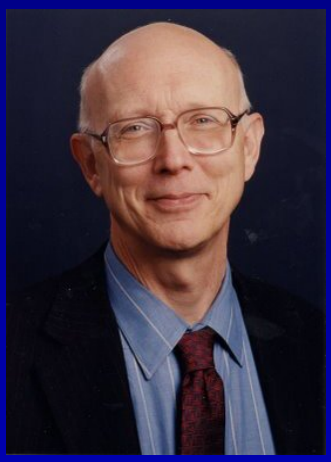

George M. Whitesides , Ph.D.

Woodford L. and Ann A. Flowers University Professor
Department of Chemistry & Chemical Biology
Harvard University

Thursday, December 18, 2008
4:00-5:00pm

Beth Robertson Auditorium
Fayez S. Sarofim Research Building
The Brown Foundation Institute of Molecular Medicine
1825 Pressler Street, Houston Texas

For More Information Contact: Jason Sakamoto, Ph.D.
Tel: 713-500-2466 ~ Jason.Sakamoto@UTH.TMC.EDU
WWW.NANOHEALTHALLIANCE.ORG

ALLIANCE *for* NANOHEALTH

"What You Need to Know About the FDA from the Very Beginning of Your Company's Existence: Regulatory 101 for Startup Companies"

MAX TALBOTT LLC
HEALTH PRODUCT CONSULTING

Max Talbott

Owner, Max Talbott, LLC

Previously: - Senior Vice President at DuPont/BMS Biopharmaceuticals,
- Senior Vice President at Aventis/Rhone Poulenc Rorer,
- Director at Eli Lilly and
- Director at the Food and Drug Administration

Monday, September 21st, 2009
1:00 – 2:00 pm

Refreshments will be provided on a first-come first-served basis

Beth Robertson Auditorium

Fayez S. Sarofim Research Building
The Brown Foundation Institute of Molecular Medicine
1825 Pressler Street, Houston, Texas

For More Information Contact: Damian Walsh
Tel: 713-500-3768 ~ damian.walsh@uth.tmc.edu
www.nanohealthalliance.org

ALLIANCE *for* NANOHEALTH

"Removing Gravity: A New Tool for Medical Research."

Neal Pellis, Ph.D.

Senior Scientist in the Space Life Sciences Directorate (SLSD) at NASA Johnson Space Center

Thursday, January 21, 2010
1:00 pm – 2:00 pm

Refreshments will be provided on a first-come first-served basis

Beth Robertson Auditorium

Fayez S. Sarofim Research Building
The Brown Foundation Institute of Molecular Medicine
1825 Pressler Street, Houston, Texas

Please RSVP with Damian Walsh
Tel: 713-500-3768 ~ damian.walsh@uth.tmc.edu
www.nanohealthalliance.org

ALLIANCE *for* NANOHEALTH

Alliance for NanoHealth Distinguished Lectureship

Nanomedicine and Nanotoxicity: From Basic Studies to Clinical Applications

Yuliang Zhao, Ph.D.

Professor and Director

CAS Key Lab for Biomedical Effects of Nanomaterials & Nanosafety,
Institute of High Energy Physics, Chinese Academy of Sciences; and
National Center for Nanosciences and Technology of China,
zhaoyuliang@ihep.ac.cn or zhaoyl@nanoctr.cn

Wednesday, February 10, 2010
3:00 pm – 4:00 pm

Fayez S. Sarofim Research Building

Rooms: IMM 109/110

The Brown Foundation Institute of Molecular Medicine
1825 Pressler Street, Houston, Texas

For More Information Contact: Damian Walsh
Tel: 713-500-3768 ~ damian.walsh@uth.tmc.edu
www.nanohealthalliance.org

ALLIANCE *for* NANOHEALTH

*n*BME
Department *of* NanoMedicine *and* BioMedical Engineering

The Alliance of NanoHealth (ANH) & The UTHealth Department of Nanomedicine and Biomedical Engineering (nBME)

Welcomes you to a seminar series:

Mathematical Engines of Nanomedicine Day (MEND)

May 20 2010, 11:30am to 6:00pm

Mathematical Engines of Nanomedicine Day (MEND) is the first meeting dedicated to the increasing role of mathematics in nanomedicine. MEND brings distinguished researchers together to combine efforts of the math, computational and medical communities in developing advanced, predicted and rational solutions in clinics.

Presentations by Invited Guests:

- **Wing Kam Liu, PhD** (Professor, Department of Mechanical Engineering, Northwestern University)
- **Markus Buehler, PhD** (Associate Professor, Department of Civil and Environmental Engineering, MIT)
- **Eric Demain, PhD** (Associate Professor, Department of Civil and Environmental Engineering, MIT)

TMC Presentations:

- **Mauro Ferrari, PhD** (Professor and Chairman, Department of Nanomedicine and Biomedical Engineering (nBME); Professor of Internal Medicine, UTHealth)
- **Miloc Kojic, PhD** (Professor, Department of Nanomedicine and Biomedical Engineering (nBME); UTHealth)
- **Paolo Decuzzi, PhD** (Associate Professor, Department of Nanomedicine and Biomedical Engineering (nBME); UTHealth)
- **Vittorio Cristini, PhD** (Associate Professor, School of Health Information Sciences; UTHealth

The program starts with lunch from 11.30am to 1:00pm. Talks are from 1:00pm to 6:00pm.

Fayez S. Sarofim Research Building
Beth Robinson Auditorium
The Brown Foundation Institute of Molecular Medicine
1825 Pressler Street, Houston, Texas

For Free Registration Contact: Damian Walsh
Tel: 713-500-3768 ~ damian.walsh@uth.tmc.edu

The Alliance for Nanohealth

Presents a Distinguished Lectureship Special Event

NANOFLUIDIC SYSTEMS FOR DNA ANALYSIS

Harold G. Craighead, Ph.D.

Professor

School of Applied and Engineering Physics

Cornell University

Member of the National Academy of Engineering

TUESDAY

May 24

2011

11:30 am - 1 pm

THE METHODIST HOSPITAL RESEARCH INSTITUTE AUDITORIUM

Methodist® The Methodist Hospital Research Institute®

ALLIANCE *for* NANOHEALTH

The Methodist Hospital Research Institute and The Alliance for NanoHealth present:

Institute Special Seminar:
NanoTherm® Therapy

THURSDAY
September 1
2011
11:30 a.m. - 1:00 p.m.

The Methodist Hospital
Research Institute
Auditorium

Andreas Jordan
Chief Scientific Officer
MagForce AG
Berlin, Germany

ALLIANCE *for* NANOHEALTH

www.methodisthealth.com/TMHRI_Events

Methodist® The Methodist Hospital Research Institute®

LEADING MEDICINE®

Dr. rer. nat. Andreas Jordan (CSO)

Short Bio

Dr. Andreas Jordan founded MagForce Nanotechnologies AG and serves on its management board as chief scientific officer, with responsibility for all research and development activities. He began his career with studies in biology at the Free University of Berlin, followed by further studies in biochemistry at the Technical University of Berlin. His doctoral dissertation in 1993 addressed the production of nanoparticles and their application for cancer therapy. This pioneering work was based on research which began in 1987, long before the subject of nanotechnology had achieved any international significance. He subsequently managed scientific projects for the Berlin's Virchow Clinic (now Charité) as well as for the Institute for Diagnostic Research, a subsidiary of Schering.

Dr. Jordan has already delivered more than 500 scientific lectures about Nano-Cancer® therapy. He has authored more than 45 articles for peer-reviewed scientific journals and has cleared the way for twelve families of international patents, some of which have been licensed. His contacts to NASA, the National Cancer Institute (NCI), the Institute of Nanotechnology (IoN), the U.S. Food and Drug Administration (FDA), and such renowned U.S. hospitals as the University of California, San Francisco (UCSF), the Cleveland Clinic Foundation (CCF) and Duke University, as well as throughout Asia, continue to provide an essential foundation for his professional activities through the world.

NanoTherm® Therapy

Andreas Jordan

MagForce Nanotechnologies AG, Max-Dohrn-Str. 8-10, 10589 Berlin, Germany,

Thermotherapy using magnetic nanoparticles (NanoTherm® therapy) is a new approach for the local treatment of solid tumors and one of the first clinical applications of nanotechnology in cancer therapy. The principle of the method is the direct introduction of a dispersion of magnetic nanoparticles (NanoTherm®) into a tumour and their subsequent activation by an 100 kHz alternating magnetic field (NanoActivator™) to produce heat. The magnetic fluid consists of superparamagnetic iron-oxide nanoparticles (iron concentration 112 mg/ml) with a mean diameter of 12 nm and an aminosilane type shell.

In a phase II clinical trial, 59 patients with glioblastoma recurrences received local thermotherapy combined with fractionated stereotactic radiotherapy with a median dose of 30 Gy in a median fractionation of 5x2 Gy/week.

Median overall survival after diagnosis of first tumour recurrence was 13.4 months (95% CI: 10.6–16.2 months) and 23.2 months (95% CI 17.2 – 29.2 months) after primary tumour diagnosis compared to 6.2 and 13.4 resp. of a historical control. Due to this positive outcome, MagForce received European regulatory approval for its medical products NanoTherm and NanoActivator for the treatment of brain tumours.

Two other clinical trials are currently recruiting patients: A feasibility study for the treatment of non resectable pancreatic carcinoma in combination with chemotherapy and an efficacy study on prostate carcinoma in combination with low dose rate brachytherapy.

Currently a new generation of nanoparticles is being developed, which can offer even greater therapeutic potential to the NanoTherm therapy. Through modification of the nanoparticle surface with functional drug delivery systems, it is possible to combine hyperthermia with chemotherapy. Additionally, in order to develop multifunctional nanocarriers with multiple therapeutic applications, MagForce is also exploring the use of targeting ligands with tumour localizing properties along with stealth coatings for systemic administration.

The Alliance for Nanohealth

Presents a Distinguished Lectureship Special Event

AFM TECHNOLOGIES IN LIFE SCIENCES

Christoph Gerber, Ph.D.

Director of Scientific Communications
National Center of Competence in Research Nanoscale
Science University of Basel

THURSDAY

October 27

2 0 1 1

3:45 pm - 5 pm

Pioneer of atomic force microscopy Christoph Gerber was instrumental in the invention of both the scanning tunneling microscope and the atomic force microscope. The atomic force microscope and Atomic Force Microscope (AFM) offers a resolution, you can use to represent individual atoms. It works on many, even non-conductive materials, which is why it took the world in many disciplines such as physics, biology, nanotechnology, chemistry, medicine and engineering dissemination. The invention of new microscopes in the eighties was groundbreaking and has revolutionized research in many areas sustainably. Today, Gerber explores with his research group at the Swiss Nanoscience Institute various applications and developments of the atomic force microscope cantilever and the associated technology for the measurement of features and properties in the nano world of biology and chemistry.

THE METHODIST HOSPITAL
DUNN RIO GRANDE, D1-059

Methodist The Methodist Hospital Research Institute

ALLIANCE *for* NANOHEALTH

Christoph Gerber

Co-founder of the Basel nanoscience Born in 1942 in Basel physicist started his scientific career in the research department of the company Contraves in Sweden. He then worked for many years in the IBM research laboratory in Switzerland, Germany and the United States. In 2001 he founded together with Prof. Dr. Hans-Joachim Güntherodt the NCCR Nanoscience in the Department of Physics, University of Basel, is from 2006, the Swiss Nanoscience Institute (SNI) emerged. Since then he has the SNI the University of Basel as a research group leader and director of scientific communication.

Pioneer of atomic force microscopy Christoph Gerber was instrumental in the invention of both the scanning tunneling microscope and the atomic force microscope. The atomic force microscope and Atomic Force Microscope (AFM) offers a resolution, you can use to represent individual atoms. It works on many, even non-conductive materials, which is why it took the world in many disciplines such as physics, biology, nanotechnology, chemistry, medicine and engineering dissemination. The invention of new microscopes in the eighties was groundbreaking and has revolutionized research in many areas sustainably. Today, Gerber explores with his research group at the Swiss Nanoscience Institute various applications and developments of the atomic force microscope cantilever and the associated technology for the measurement of features and properties in the nano world of biology and chemistry.

The cantilever technique allows to understand the precision and accuracy the nature of molecular dimensions in the laboratory. By measuring tiny forces, it was possible, for example, to determine specific interactions between molecules. This also enabled new approaches for studies on genetic material and to partially vital proteins. Thus a completely new research area has been developed that gives a deeper insight into the nano world. The utilization of the cantilever technique for highly sensitive nano-thermal sensors or for the detection of magnetic resonance allows to investigate much

smaller areas with higher accuracy than with conventional magnetic resonance imaging. Thus, for example, bacteria and demonstrate their resistance to antibiotics, making the traditional Petri dish can be efficiently replaced.

Internationally renowned scientist Prof. Dr. Christoph Gerber is highly regarded internationally, and his scientific excellence has been recognized with a variety of academic titles and memberships. The University of Basel, honored the outstanding scientific achievements of Prof. Gerber in 1987 with the award of an honorary doctorate from the Faculty of Natural Sciences.

Gerber's pioneering work has been cited over 21,000 times. He is one of the world's hundred most cited physicists. About his immediate scientific work, he has been heavily involved through newspaper articles, television programs and participation in public events to communicate scientific findings to a wider public.

The Alliance for Nanohealth Presents:

A Distinguished Lectureship Special Event

Targeted Nanodrugs: The Drugs of the 21st Century

Yechezkel Barenholz, Ph.D.

Head of Membrane and Liposome Research Lab
Hebrew University Hadassah Medical School

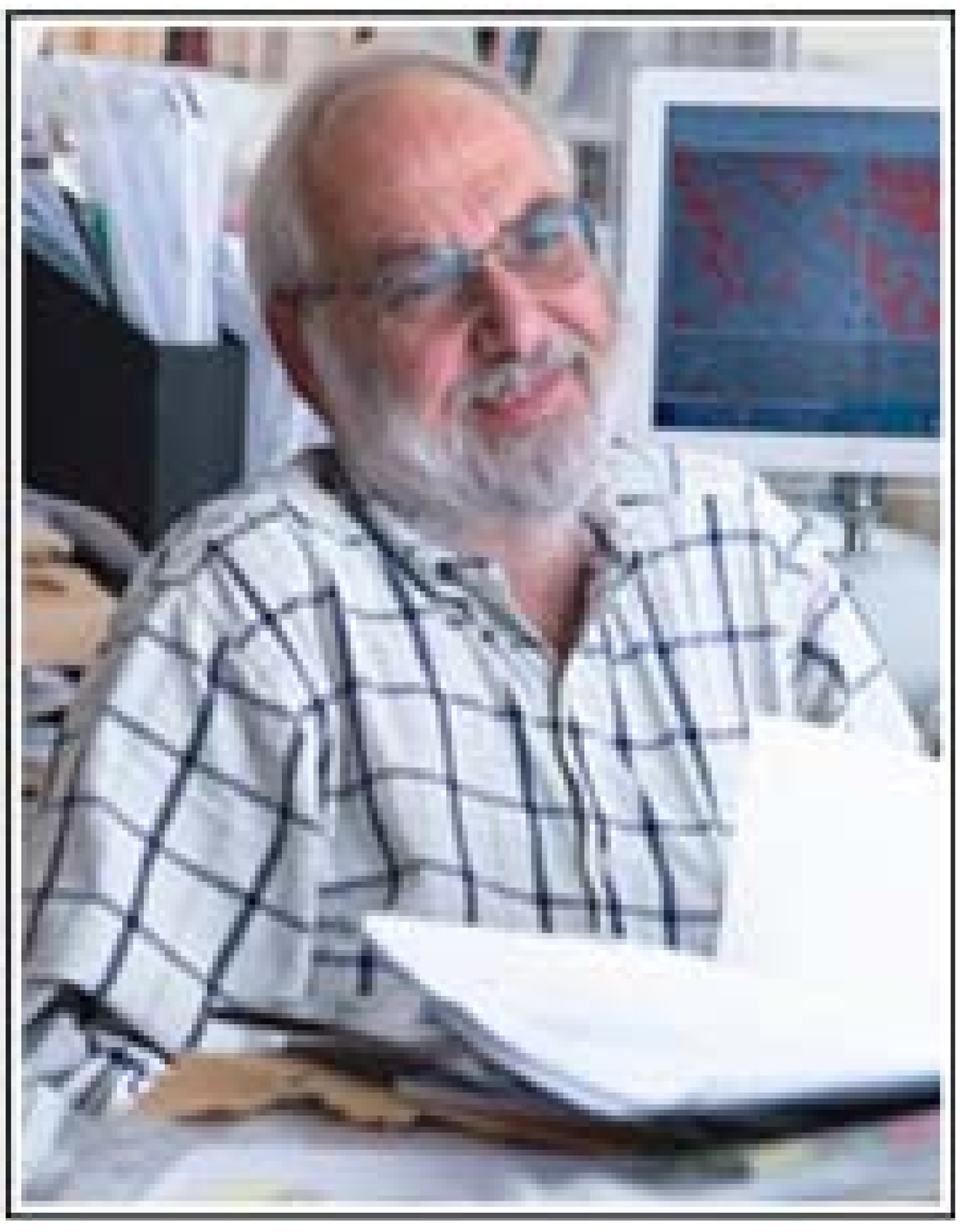

MONDAY

November 28

2011

4:00 p.m.– 5:00 p.m.

The Methodist Hospital
Research Institute
RI Auditorium, R2-306
www.methodisthealth.com/tmhri_events

Most drugs available today for treatment of major diseases such as cancer and inflammation have a limited therapeutic efficacy as they need to reach higher levels at the disease sites in order to improve therapeutic efficacy, and a lower level at the normal-healthy tissues so they will be less toxic. Such achievement will bring us closer to the "Magic Bullet" concept suggested by the famous scientist Paul Ehrlich.

Recent developments of novel Nanotechnology based approaches enables to load high level of many drugs into various types of nanoparticles and especially into nano (~100 nm) liposomes leading to the development of nano-drugs. These nano-liposomes are sacs in which an envelope (a membrane) composed of phospholipids surround small amount of water in which high level of drug is encapsulated. The mechanism of drug loading allows achieving a controlled drug release. Our better understanding of the micro-anatomy of diseased tissues and blood vessels in these tissues combined with and of lipid biophysics enable to improve nanoparticles selectivity (passive targeting) leading them to concentrate at the disease sites, slowly releasing their drugs there, thereby improving therapeutic efficacy, and reducing toxicity. This presentation will focus on few such nano-drugs based on ~100 nm liposomes as DDS. The first one is our nano liposomes based anticancer drug Doxil™, which is the first nano-drug approved by the US FDA. Doxil shows superior pharmacokinetics, improved therapeutic efficacy and reduced toxicity when used to treat ovarian, breast, Kaposi sarcoma and multiple myeloma cancers. Means to improve Doxil performance, as well as other liposomal anti cancer nano-drugs and anti-inflammatory liposomal nano-drug (all at the last stages of preclinical development) will also be discussed. If time permit, the presentation will also deal with the scientist (inventor / developer) selection of the optimal commercialization venue of novel nano-drugs.

ALLIANCE *for* NANOHEALTH

Methodist® The Methodist Hospital Research Institute®

LEADING MEDICINE®

Professor Yechezkel (Chezy) Barenholz

Head of Membrane and Liposome Research Lab, Hebrew University Hadassah Medical School, POB 12272, Jerusalem 91120, Israel,

Short Biography

Professor Barenholz (Daniel G. Miller Professor in Cancer Research) received his Ph.D. at the Hebrew University-Hadassah Medical School, Jerusalem in 1971. He is on the faculty of the Hebrew University since 1968 and was promoted to a Professor on 1981. He was a visiting Professor at the Department of Biochemistry, University of Virginia School of Medicine, Charlottesville VA, USA from 1973 to 2005; a Donders Chair Professor at The Faculty of Pharmacy, University of Utrecht, The Netherlands, on 1992; a Visiting Professor at the University Kyoto University (Kyoto, Japan, 1998); at La Sapeinza University (Roma, Italy, 2006); Jaiotung University (Shanghai, China, 2006); Kings College (London, UK, 2006);and, Danish Technical University (DTU, Copenhagen, 2010). His current basic research focuses on composition, structure, function relationships of biological membranes with special focus and contributions related to sphingolipids. His applied research deals with development of drug delivery systems (DDS) and drugs based on such DDS including vaccines and nucleic acids' delivery systems. This is exemplified by Doxil™ development (together with Professor Alberto Gabizon and SEQUUS Pharmaceuticals, Menlo Park CA, USA).The anticancer drug Doxil™ (Caelyx™ in Europe) is the first FDA approved nano drug and the first FDA approved liposomal drug (1995). It is distributed today all over the world by Johnson and Johnson. Doxil is having yearly sales exceeding half a Billion dollars. Professor Barenholz with help of others founded based on Barenholz inventions the following start up companies:1. NasVax Ltd (now a public company on the Israeli stock market), a vaccines' developing company now in clinical trials of Influenza vaccine which is based on VaxiSome™, which is based on Barenholz invented polycationic sphingolipid adjuvant; 2. Moebius medical which develops liposomes' based medical device for treatment of osteoarthritis; and 3. LipoCure Ltd for the development of liposomal nano drugs for treatment of cancer and inflammatory diseases [rheumatoid arthritis (RA) and multiple sclerosis (MS)]. Professor Barenholz is a coauthor in more than 350 scientific publications and a co-inventor in more than 30 approved patent families. He was an executive editor of Progress in Lipid Research and he is on the editorial board of 4 scientific journals. Professor Barenholz was awarded few prizes including twice the Kaye award (1995 & 1997), Alec D. Bangham (the Liposome field founder) award (1998), and Teva Founders Prize (2001). On 2003 Professor Barenholz founded (from Doxil royalties) the "Barenholz Prize" for Israeli Ph.D. students to encourage excellence and innovation in applied science of Israeli students.

Targeted Nanodrugs: the Drugs of the 21 Century?

Most drugs available today for treatment of major diseases such as cancer and inflammation have a limited therapeutic efficacy as they need to reach higher levels at the disease sites in order to improve therapeutic efficacy, and a lower level at the normal-healthy tissues so they will be less toxic. Such achievement will bring us closer to the "Magic Bullet" concept suggested by the famous scientist Paul Ehrlich.

Recent developments of novel Nanotechnology based approaches enables to load high level of many drugs into various types of nanoparticles and especially into nano (~100 nm) liposomes leading to the development of nano-drugs. These nano-liposomes are sacs in which an envelope (a membrane) composed of phospholipids surround small amount of water in which high level of drug is encapsulated. The mechanism of drug loading allows achieving a controlled drug release. Our better understanding of the micro-anatomy of diseased tissues and blood vessels in these tissues combined with and of lipid biophysics enable to improve nanoparticles selectivity (passive targeting) leading them to concentrate at the disease sites, slowly releasing their drugs there, thereby improving therapeutic efficacy, and reducing toxicity. This presentation will focus on few such nano-drugs based on ~100 nm liposomes as DDS. The first one is our nano liposomes based anticancer drug Doxil^{TM}, which is the first nano-drug approved by the US FDA. Doxil shows superior pharmacokinetics, improved therapeutic efficacy and reduced toxicity when used to treat ovarian, breast, Kaposi sarcoma and multiple myeloma cancers. Means to improve Doxil performance, as well as other liposomal anti cancer nano-drugs and anti-inflammatory liposomal nano-drug (all at the last stages of preclinical development) will also be discussed. If time permit, the presentation will also deal with the scientist (inventor / developer) selection of the optimal commercialization venue of novel nano-drugs.

The Alliance for Nanohealth Presents:

ALLIANCE *for* NANOHEALTH

Microengineered Hydrogels for Stem Cell Bioengineering and Tissue Regeneration

Monday
August 13
2012

12:00 p.m.– 1:00 p.m.

The Methodist Hospital
Research Institute
Boardroom, R2-311

www.methodisthealth.com/tmhri_events

Ali Khademhosseini, Ph.D.

Associate Professor,
Center for Biomedical Engineering, Department of Medicine, Brigham and Women's Hospital, Harvard Medical School, Cambridge, MA
Harvard-MIT Division of Health Sciences and Technology, MIT, Cambridge, MA
Wyss Institute for Biologically Inspired Engineering, Harvard University, Boston, MA

Micro- and nanoscale technologies are emerging as powerful tools for controlling the interaction between cells and their surroundings for biological studies, tissue engineering, and cell-based screening. In addition, hydrogel biomaterials have been increasingly used in various tissue engineering applications since they provide cells with a hydrated 3D microenvironment that mimics the native extracellular matrix. In our lab we have developed various approaches to merge microscale techniques with hydrogel biomaterials for directing stem cell differentiation and generating complex 3D tissues. In this talk, I will outline our work in controlling the cell-microenvironment interactions by using patterned hydrogels to direct the differentiation of stem cells. In addition, I will describe the fabrication and the use of microscale hydrogels for tissue engineering by using a 'bottom-up' and a 'top-down' approach. Top-down approaches for fabricating complex engineered tissues involve the use of miniaturization techniques to control cell-cell interactions or to recreate biomimetic microvascular networks within mesoscale hydrogels. Our group has also pioneered bottom-up approaches to generate tissues by the assembly of shape-controlled cell-laden microgels (i.e. tissue building blocks), that resemble functional tissue units. In this approach, microgels were fabricated and seeded with different cell types and induced to self assemble to generate 3D tissue structures with controlled microarchitecture and cell-cell interactions.

Methodist® The Methodist Hospital Research Institute®

LEADING MEDICINE®

Ali Khademhosseini Biosketch

Ali Khademhosseini is an Associate Professor at Harvard-MIT's Division of Health Sciences and Technology (HST), Brigham and Women's Hospital (BWH) and Harvard Medical School (HMS) as well as an Associate Faculty at the Wyss Institute for Biologically Inspired engineering. He is also a Junior Principal Investigator at Japan's World Premier International – Advanced Institute for Materials Research (WPI-AIMR) at Tohoku University where he directs a satellite laboratory. In addition he is an adjunct faculty at the Biomedical Engineering Department at the University of Texas at Austin and an eminent scholar at Kyung Hee University in Korea.

His research is based on developing micro- and nanoscale technologies to control cellular behavior with particular emphasis in developing microscale biomaterials and engineering systems for tissue engineering. Currently, his laboratory is developing technologies to control the formation of vascularized tissues with appropriate microarchitectures as well as regulating stem cell differentiation within microengineered systems. He has edited 4 books and 4 journal special issues and is an author on over 200 articles in peer reviewed journals, 39 book chapters, 160 abstracts, and 16 patent/disclosure applications. His work has been published in journals such as *PNAS*, *JACS*, *Advanced Materials*, *Nature Materials*, *Biomaterials* and *Lab on a chip* and highlighted in *Nature*, *Scientific American* and *Technology Review* Magazines. As of June 2012, he has been cited over 6800 times and has an H-index of 43. Also, he has been invited to give nearly 150 seminars and keynote lectures.

Dr. Khademhosseini's interdisciplinary research has been recognized by over 30 major national and international awards. He has received early career awards from three major engineering discipline societies: electrical (IEEE Engineering in Medicine and Biology Society (EMBS) award and IEEE Nanotechnology award), chemical (Colburn award from the American Institute of Chemical Engineers) and mechanical engineering (Y.C. Fung award from the American Society of Mechanical Engineers). He is also the recipient of the Presidential Early Career Award for Scientists and Engineers (PECASE), the highest honor given by the US government for early career investigators. In 2011, he received the Pioneers of Miniaturization Prize from the Royal Society of Chemistry for his contribution to microscale tissue engineering and microfluidics. In addition, he has received the young investigator awards of the Society for Biomaterials (SFB), the Tissue Engineering and Regenerative Medicine International Society-North America (TERMIS-NA) and the American Society for Engineering Education (ASEE). He has also received the Viktor K. Lamer award, the Unilever award and the BIOT Young Investigator award of the American Chemical Society, the International Union of Pure and Applied Chemistry (IUPAC) Polymer Award and has been recognized by major governmental awards including the NSF Career award and the Office of Naval Research young investigator award. In 2007, he was named a TR35 recipient by the Technology Review Magazine as one of the world's top young innovators. He has also received major recognitions from other organizations including the Society for Laboratory Automation and Screening (SLAS) Innovation Award, a Sloan fellowship as well as the IAMBE and the Coulter foundation early career awards. For his PhD work he received the BMW Scientific Award, considered as one of the most prestigious international prizes for a young scientist of any field. He is also a fellow of the American Institute of Medical and Biological Engineering (AIMBE) reserved for the top 2% of the biomedical engineers in the United States.

Dr. Khademhosseini is highly interested in training students and postdoctoral fellows for which he received the MIT's Outstanding Undergraduate mentor. Seventeen of his previous trainees remain as faculty in academia at institutions including Harvard University-Massachusetts General Hospital, Brigham and Women's Hospital, University of California-Riverside, University of Pittsburgh, INSERM, National Hsin-Chu University, Hanyang University, Singapore National University, Inha University and Tsinghua University.

Dr. Khademhosseini is an Associate Editor for the *International Journal of Nanomedicine*, as well as *Biomedical Microdevices* and a Principal Editor of the journal *Nano LIFE*. He is also the Associate editor for research highlights for *Lab on a Chip*. He also serves as a member of the editorial boards of numerous journals including the *Small*, *Tissue Engineering* (Parts A, B and C), *Journal of Tissue Engineering and Regenerative Medicine*, *Reviews on Biomedical Engineering*, *Biomicrofluidics*, *Biomedical Materials*, *Journal of Biomaterials Science-Polymer Edition* and *Biofabrication*. He is the chair of the Bionanotechnology Technical Activities Committee for the IEEE-EMBS. He received his Ph.D. in bioengineering from MIT (2005), and MASc (2001) and BASc (1999) degrees from University of Toronto both in chemical engineering.